

**UNIVERSIDADE FEDERAL DE MINAS GERAIS**  
**PROGRAMA DE PÓS-GRADUAÇÃO EM SANEAMENTO,**  
**MEIO AMBIENTE E RECURSOS HÍDRICOS**

**APPLICATION OF TiO<sub>2</sub> THIN FILMS COATED  
ON PET BY HIGH POWER IMPULSE  
MAGNETRON SPUTTERING FOR WATER  
TREATMENT**

**Rafaela Brito Portela Marcelino**

**Belo Horizonte**

**2018**

**APPLICATION OF TiO<sub>2</sub> THIN FILMS COATED  
ON PET BY HIGH POWER IMPULSE  
MAGNETRON SPUTTERING FOR WATER  
TREATMENT**

**Rafaela Brito Portela Marcelino**

**Rafaela Brito Portela Marcelino**

**APPLICATION OF TiO<sub>2</sub> THIN FILMS COATED  
ON PET BY HIGH POWER IMPULSE  
MAGNETRON SPUTTERING FOR WATER  
TREATMENT**

Thesis presented to the Postgraduate Program in Sanitation, Environment and Water Resources of Universidade Federal de Minas Gerais, as a partial requirement to obtain the title of Doctor in Sanitation, Environment and Water Resources.

Research field: Environment

Research line: Characterization, prevention and control of pollution

Supervisor: Prof.<sup>a</sup> Dr.<sup>a</sup> Camila Costa de Amorim

Belo Horizonte

Escola de Engenharia da UFMG

2018

M314a

Marcelino, Rafaela Brito Portela.

Application of TiO<sub>2</sub> thin films coated on PET by high power impulse magnetron sputtering for water treatment [manuscrito] / Rafaela Brito Portela Marcelino. - 2018.  
xviii, 183 f., enc.: il.

Orientadora: Camila Costa de Amorim.

Tese (doutorado) - Universidade Federal de Minas Gerais, Escola de Engenharia.

Bibliografia: f. 148-183.

1. Engenharia sanitária - Teses. 2. Meio ambiente - Teses. 3. Cafeína - Teses. 4. Carbendazim - Teses. 5. Fotocatálise - Teses. I. Amorim, Camila Costa de. II. Universidade Federal de Minas Gerais. Escola de Engenharia. III. Título.

CDU: 628(043)



FOLHA DE APROVAÇÃO

Application Of  $TiO_2$  Thin Films Coated On Pet By High Power Impulse Magnetron  
Sputtering For Water Treatment

**RAFAELA BRITO PORTELA MARCELINO**

Tese defendida e aprovada pela banca examinadora constituída pelos Senhores:

Profª CAMILA COSTA DE AMORIM AMARAL

Profª MÔNICA MARIA DINIZ LEÃO

Prof. LUIZ CARLOS ALVES DE OLIVEIRA

Profª REGINA DE FATIMA PERALTA MUNIZ MOREIRA

Profª ROSA MARIA RABELO JUNQUEIRA

Aprovada pelo Colegiado do PG SMARH

Prof. Antonio Teixeira de Matos  
Coordenador

Versão Final aprovada por

Profª Camila Costa de Amorim Amaral  
Orientadora

Belo Horizonte, 26 de outubro de 2018.

## AGRADECIMENTOS

Primeiramente agradeço a Deus. Essa jornada foi uma das mais difíceis de minha vida e sem a ajuda e direção de Deus eu não estaria aqui.

Agradeço, em seguida, a minha família. Preciso agradecer a meu esposo que foi a minha maior fonte de apoio para a realização desse projeto, ele quem me aguentou e me ajudou nos momentos mais difíceis dessa caminhada. Agradeço também ao meu filho Artur que me inspira diariamente a ser uma pessoa melhor. Agradeço, de coração, aos meus queridos pais e meus irmãos que, mesmo estando fisicamente distantes, sempre me apoiam, me sustentam e me iluminam.

Gostaria de expressar minha gratidão e admiração a todos os que me direcionaram e me transmitiram conhecimentos valiosos nessa jornada (professores, doutorandos, mestrandos, ICs, servidores, palestrantes, amigos, etc.), em especial a orientadora prof. Camila Amorim, ao prof. Peter Kelly da MMU, a Monique Cotrim e ao prof. Rodrigo Lambert Oréface, do Programa de Pós-Graduação em Engenharia Metalúrgica, Materiais e de Minas que me ajudaram com os ensaios de ângulo de contato, a prof. Ana Paula Carvalho do Departamento de Química e Ariete Righi que me ajudaram com as medidas de Raman, e a toda equipe do Centro de Microscopia que me ajudou com as análises de MEV, MET e AFM, principalmente aos funcionários Raquel Maria Souza, Henrique Limborço, Douglas Rodrigues Miquita, Jéssica de Paula e Marcelo da Cruz Costa de Souza.

Agradeço imensamente a meus queridos colegas e amigos do PPGSMARH, do GruPOA, da salinha 4626 e dos laboratórios. Eliz, Cacá, Má, Dri, Luiz, Nic, Lídia Roberts, Pedrinho, Raissa, Rodrigo e San, muito obrigada pela ajuda, amizade, confiança, e pelos conhecimentos transmitidos durante todo esse período. Agradeço também a valiosa ajuda de todos os ICs (Flávia, Yukimi, Karoline, Joanna, Natália) que passaram pelo grupo de pesquisa, principalmente aos que tiveram contato direto com esse trabalho.

Finalmente, gostaria de agradecer à CAPES pela bolsa recebida e aos membros da banca examinadora por terem aceitado o convite e se disponibilizado a avaliar essa tese e contribuir com o trabalho.

## RESUMO

A fotocatalise solar é um processo promissor e ambientalmente sustentável de tratamento de águas e efluentes, pois utiliza os fótons da radiação solar como força motriz para o processo de degradação de poluentes. Uma das maiores dificuldades na implementação desse tipo de processo é a separação e recuperação de catalisadores na forma de pó. Nesse contexto, o uso de catalisadores imobilizados em materiais sólidos de baixo custo, tais como polímeros orgânicos, pode ser uma solução interessante. Avanços recentes no campo de engenharia de superfícies, como o processo *High Power Impulse Magnetron Sputtering* (HiPIMS), provaram poder depositar revestimentos fotocataliticamente ativos diretamente em substratos poliméricos flexíveis (polietileno tereftalato - PET, por exemplo) em um processo de uma única etapa. Nesse sentido, este trabalho visa a aplicação de superfícies fotocatalíticas formadas por filme fino de  $\text{TiO}_2$  recoberto em folhas de PET para o tratamento solar de água contaminada com dois poluentes modelo: cafeína (estimulante do sistema nervoso central e indicadora de poluição antropogênica) e carbendazim (fungicida tóxico e recalcitrante amplamente utilizado no Brasil). O trabalho inclui a parceria com a *Manchester Metropolitan University* para a deposição de filme fino fotocatalítico em folhas de PET; a caracterização do material quanto a composição elementar (EDS, EELS) e propriedades cristalográficas (Raman), morfológicas (MEV, MET, AFM), texturais (MEV, MET, AFM), ópticas (transmitância UV-Vis) e tribológicas (profilometria e hidrofobicidade); o teste das propriedades fotocatalíticas das superfícies contra poluentes modelo em escala de bancada utilizando reator UV-A/Vis e simulador de irradiação solar; e o estudo da integração dos materiais fotocatalíticos em reatores de tratamento de água em escala semi-piloto (CPC e RPR). Os resultados obtidos indicam que as superfícies fotocatalíticas, na presença de um fotossensibilizante natural (cúrcuma), foram capazes de minimizar a concentração dos contaminantes de preocupação emergente (cafeína e carbendazim) em até 40% em soluções aquosas e que a superfície catalítica pode ser reutilizada mantendo sua atividade fotocatalítica constante. Os resultados também mostraram uma mineralização de matéria orgânica de até 79% e a redução da toxicidade aguda para *Aliivibrio fischeri* de soluções de poluentes tratadas, o que descarta a possibilidade de formação de sub-produtos de degradação mais tóxico do que os poluentes originais. Além disso, o estudo de espécies radicalares de oxigênio mostrou a prevalência da lacuna eletrogerada ( $\text{h}^+$ ) no processo fotocatalítico puro enquanto no processo com fotossensibilizante o radical superóxido ( $\text{O}_2^-$ ) se mostrou mais importante. Em conclusão, o processo de imobilização do semicondutor  $\text{TiO}_2$  em polímero PET se mostrou eficiente e o material proposto se mostrou ativo para a degradação de poluentes orgânicos recalcitrantes.

**Palavras chave:** engenharia de superfícies; engenharia de *band-gap*; carbendazim; cafeína; fotocatalise.

## ABSTRACT

Solar photocatalysis is a promising and environmentally sustainable process of water and wastewater treatment, as it uses solar radiation photons as the driving force for the pollutant degradation process. One of the greatest drawbacks in implementing this type of process is the separation and recovery of powdered catalysts. In this context, the use of catalysts immobilized on low-cost solid materials, such as organic polymers, may be an interesting solution. Recent advances in the field of surface engineering, such as the High Power Impulse Magnetron Sputtering (HiPIMS) process, have proven able to deposit photocatalytic active coatings directly on flexible polymer substrates (polyethylene terephthalate - PET, for example) in a single phase process. In this sense, this project aims at the application of photocatalytic surfaces formed by TiO<sub>2</sub> thin film coated on PET sheets for the solar treatment of water contaminated with two model pollutants: caffeine (central nervous system stimulant and an indicator of anthropogenic pollution) and carbendazim (toxic and recalcitrant fungicide widely used in Brazil). This work includes the partnership with Manchester Metropolitan University for the deposition of thin photocatalytic film on PET sheets; the characterization of the material regarding its elemental composition (EDS, EELS) as well as its crystallographic (Raman), morphological (SEM, STEM), textural (SEM, STEM, AFM), optic (UV-Vis transmittance) and tribological (profilometry and hydrophilicity) properties; the assessment of its photocatalytic properties against model pollutants in bench scale using UV-A/Vis reactor and solar irradiation simulator; and the study of the integration of photocatalytic materials into semi-pilot scale water treatment reactors (CPC and RPR). The obtained results indicate that the photocatalytic surfaces, in the presence of a natural photosensitizer (turmeric), were able to minimize the concentration of contaminants of emerging concern (caffeine and carbendazim) by up to 40% in aqueous solutions and that the catalytic surfaces can be reused without significant loss of activity. The results also showed organic matter mineralization of up to 79% and the reduction of acute toxicity to *Aliivibrio fischeri* from treated pollutants solutions, which eliminates the possibility of formation of degradation by-products more toxic than the original pollutants. In addition, the study of reactive oxygen species showed the prevalence of the electrogenerated hole (h<sup>+</sup>) in the pure photocatalytic process, while in the photosensitized process, the superoxide radical (<sup>•</sup>O<sub>2</sub><sup>-</sup>) played a more important role. In conclusion, the immobilization process of the TiO<sub>2</sub> semiconductor on PET polymer was efficient and the proposed material proved to be active for the degradation of recalcitrant organic pollutants.

**Keywords:** surface engineering; band-gap engineering; carbendazim; caffeine; photocatalysis.



# TABLE OF CONTENTS

LIST OF FIGURES.....	IX
LIST OF TABLES.....	XV
NOMENCLATURE.....	XVII
<b>CHAPTER 1. INTRODUCTION .....</b>	<b>1</b>
1.1 BACKGROUND AND MOTIVATION .....	1
1.2 OBJECTIVES .....	5
1.2.1 General objective.....	5
1.2.2 Specific objectives.....	5
1.3 DOCUMENT STRUCTURE .....	6
<b>CHAPTER 2. FUNDAMENTALS.....</b>	<b>7</b>
2.1 PHOTOCATALYSIS AND TITANIA .....	7
2.1.1 Environmental photocatalysis and context.....	7
2.1.2 Photocatalysis fundamentals and key aspects .....	8
2.2 BAND-GAP ENGINEERING: ENHANCING VISIBLE LIGHT PHOTOCATALYSIS.....	13
2.3 OVERVIEW OF SOLAR PHOTOREACTORS .....	23
2.3.1 Photocatalytic efficiency measurement .....	23
2.3.2 Reactors designs.....	25
2.3.3 Solar photoreactors for water and wastewater treatment .....	32
2.4 SURFACE ENGINEERING AND PHOTOCATALYTIC SURFACES.....	35
2.5 MODEL CONTAMINANTS OF EMERGING CONCERN: CARBENDAZIM AND CAFFEINE.....	38
2.6 PHOTOCATALYTIC THIN FILM CHARACTERIZATION .....	46
2.6.1 Crystallographic characterization by Grazing Incidence X-ray Diffraction (GIXRD).....	46
2.6.2 Crystallographic characterization by Raman spectroscopy.....	48
2.6.3 Elementary composition by Energy Dispersive Spectroscopy (EDS).....	52
2.6.4 Electron Energy-Loss Spectroscopy (EELS) microanalysis .....	53
2.6.5 Coating morphology by Scanning Electron Microscopy (SEM).....	55
2.6.6 Coating superficial morphology, roughness and specific area by Atomic Force Microscopy (AFM) .....	56
2.6.7 Morphology, composition and thickness determination by Transmission Electron Microscopy (TEM) .....	57
2.6.8 Thickness measurement with Profilometry .....	57
2.6.9 Optical band-gap calculation by Tauc-Plot method.....	58
2.6.10 Photoinduced wettability via water droplet contact angle.....	59
<b>CHAPTER 3. CHARACTERIZATION OF TiO<sub>2</sub> THIN FILMS COATED ON PET BY HIGH POWER IMPULSE MAGNETRON SPUTTERING .....</b>	<b>61</b>
3.1 THIN FILM DEPOSITION.....	62
3.2 CRYSTALLOGRAPHIC CHARACTERIZATION AND ELEMENTARY COMPOSITION .....	63
3.2.1 X-ray diffraction (XRD and GIXRD).....	63
3.2.2 Raman spectroscopy.....	63
3.2.3 Energy Dispersive Spectroscopy (EDS) .....	63
3.2.4 Electron Energy-Loss Spectroscopy (EELS) .....	64
3.3 MORPHOLOGICAL AND TEXTURAL CHARACTERIZATION .....	65
3.3.1 Scanning Electron Microscopy (SEM) .....	65
3.3.2 Atomic Force Microscopy (AFM).....	65
3.3.3 Transmission Electron Microscopy (TEM).....	65
3.3.4 Coating thickness.....	66
3.4 OPTICAL CHARACTERIZATION .....	67
3.4.1 UV-Vis transmittance and Tauc-Plot method.....	67
3.4.2 Photoinduced wettability via water droplet contact angle .....	67
3.5 RESULTS AND DISCUSSION .....	68
3.5.1 X-ray diffraction (XRD and GIXRD).....	68

3.5.2	<i>Raman spectroscopy</i> .....	68
3.5.3	<i>Scanning Electron Microscopy (SEM) coupled with Energy Dispersive Spectroscopy (EDS)</i> .....	72
3.5.4	<i>Transmission Electron Microscopy (TEM) coupled with Electron Energy-Loss Spectroscopy (EELS)</i> 75	
3.5.5	<i>Atomic Force Microscopy (AFM)</i> .....	79
3.5.6	<i>UV-Vis transmittance and Tauc-Plot method for optical band-gap calculation</i> .....	80
3.5.7	<i>Photoinduced Wettability via Water droplet contact angle</i> .....	81
3.5.8	<i>Thickness, phase, surface and optical properties of the photocatalytic surface</i> .....	82
3.6	CONCLUSIONS.....	85
<b>CHAPTER 4. APPLICATION OF TiO<sub>2</sub> THIN FILMS COATED ON PET BY HIGH POWER IMPULSE MAGNETRON SPUTTERING AT LABORATORY SCALE FOR CARBENDAZIM DEGRADATION.....</b>		<b>86</b>
4.1	INTRODUCTION .....	86
4.2	MATERIAL AND METHODS .....	89
4.2.1	<i>HiPIMS thin film deposition</i> .....	89
4.2.2	<i>Photocatalytic activity assessment</i> .....	89
4.2.3	<i>Organic matter assessment</i> .....	91
4.2.4	<i>CBZ oxidation study via ESI-MS</i> .....	91
4.2.5	<i>Acute ecotoxicity assessment</i> .....	92
4.3	RESULTS AND DISCUSSION .....	93
4.3.1	<i>Photocatalytic degradation of CBZ under UV-A/Vis irradiation</i> .....	93
4.3.2	<i>Organic matter removal</i> .....	97
4.3.3	<i>CBZ oxidation study via ESI-MS</i> .....	99
4.3.4	<i>Acute ecotoxicity assessment</i> .....	101
4.4	CONCLUDING REMARKS .....	102
<b>CHAPTER 5. APPLICATION OF TiO<sub>2</sub> THIN FILMS COATED ON PET BY HIGH POWER IMPULSE MAGNETRON SPUTTERING AT LABORATORY SCALE FOR CAFFEINE DEGRADATION.....</b>		<b>103</b>
5.1	INTRODUCTION .....	103
5.2	MATERIAL AND METHODS .....	105
5.2.1	<i>Photocatalytic degradation of CAF under UV-A/Vis irradiation</i> .....	105
5.2.2	<i>Photocatalytic degradation of CAF under simulated solar irradiation</i> .....	106
5.2.3	<i>Elucidation of involved radical species via trapping reactions</i> .....	107
5.2.4	<i>Organic matter assessment</i> .....	107
5.2.5	<i>Acute toxicity assessment</i> .....	107
5.3	RESULTS AND DISCUSSION .....	108
5.3.1	<i>Photocatalytic degradation of caffeine under UV-A/Vis irradiation</i> .....	108
5.3.2	<i>Study of CAF oxidation via ESI-MS</i> .....	111
5.3.3	<i>Organic matter removal</i> .....	113
5.3.4	<i>Acute ecotoxicity assessment</i> .....	114
5.3.5	<i>Photocatalytic degradation of CAF under simulated solar irradiation</i> .....	114
5.3.6	<i>Elucidation of involved radical species via trapping reactions</i> .....	117
5.4	CONCLUDING REMARKS .....	122
<b>CHAPTER 6. APPLICATION OF THE PHOTOCATALYTIC SURFACES AT SEMI-PILOT SCALE UNDER SOLAR IRRADIATION FOR WATER TREATMENT .....</b>		<b>123</b>
6.1	INTRODUCTION .....	123
6.2	MATERIAL AND METHODS .....	125
6.2.1	<i>Semi-pilot water treatment assay at RPR solar reactor</i> .....	126
6.2.2	<i>Semi-pilot water treatment assay at CPC solar reactor</i> .....	127
6.2.3	<i>Organic matter assessment</i> .....	128
6.2.4	<i>Acute toxicity assessment</i> .....	128
6.3	RESULTS AND DISCUSSION .....	129
6.3.1	<i>Semi-pilot water treatment assay at RPR solar reactor</i> .....	129
6.3.2	<i>Semi-pilot water treatment assay at CPC solar reactor</i> .....	134
6.3.3	<i>Organic matter assessment</i> .....	141

6.3.4	<i>Acute ecotoxicity assessment</i> .....	142
<b>CHAPTER 7.</b>	<b>CONCLUSIONS AND FUTURE WORK SUGGESTIONS</b> .....	<b>144</b>
7.1	CONCLUSIONS.....	144
7.2	FUTURE WORK SUGGESTIONS.....	146
<b>LIST OF PUBLICATIONS</b>	.....	<b>147</b>
<b>REFERENCES</b>	.....	<b>149</b>

## LIST OF FIGURES

<b>Figure 2.1</b> - Schematic illustration of the TiO <sub>2</sub> photocatalytic processes.	9
<b>Figure 2.2</b> - The structure of (a) anatase, (b) brookite, (c) rutile, and (d) TiO <sub>2</sub> -B.	10
<b>Figure 2.3</b> - Phase diagram for nanocrystalline titania (rutile and anatase) considering both grain boundary and surface areas as contributions for the total energy of the system.	12
<b>Figure 2.4</b> - Schematic mechanism of TiO <sub>2</sub> photocatalysis with Fe(III) doping.	15
<b>Figure 2.5</b> - Behavior of incident solar radiation on a CPC reactor (upper), and CPC solar photoreactor schematic illustration (lower).	32
<b>Figure 2.6</b> - Schematic view of direct and diffuse sunlight paths in RPR photocatalytic reactor.	33
<b>Figure 2.7</b> - Proposition of photodegradation pathway of carbendazim in aqueous solution.	39
<b>Figure 2.8</b> – Photodegradation pathway.	43
<b>Figure 2.9</b> – Schematic illustration of XRD (a) and GIXRD (b) incident X-ray beam on the sample surface and detector positioning.	47
<b>Figure 2.10</b> - Schematic illustration of electron beam interaction with the sample in a Scanning Electron Microscope. Characteristic X-rays are used by EDS detector.	52
<b>Figure 2.11</b> - Schematic illustration of electron beam interaction with the sample in a Transmission Electron Microscope. Inelastically scattered electrons are used for microanalysis by EELS detector.	54
<b>Figure 3.1</b> - Raman spectra excited using 785 nm laser of PET-TiO <sub>2</sub> thin film and uncoated PET sheet. Anatase (A), rutile (R) and PET main characteristic peaks are	69

highlighted.

**Figure 3.2** - Raman spectra excited using 532 nm laser of the uncoated PET sheet. PET main characteristic peaks are highlighted. 70

**Figure 3.3** - Raman spectra excited using 532 nm laser of the PET-TiO<sub>2</sub> sample. 71

**Figure 3.4** - SEM micrograph of the brand new titania-coated PET surface with corresponding EDS spectrum and results. 72

**Figure 3.5** - SEM micrograph of the 5 times used titania-coated PET surface with corresponding EDS spectrum and results. 73

**Figure 3.6** - SEM secondary electrons micrograph of the titania-coated PET surface for surface morphology evaluation. 74

**Figure 3.7** - SEM chemical mapping micrographs of the titania-coated PET surface: (a) Titanium map, (b) Oxygen map, (c) secondary electron, titanium, oxygen, and carbon mixed map with corresponding EDS spectrum. 75

**Figure 3.8** - TEM micrograph of the cross-sectioned TiO<sub>2</sub> thin film coated onto PET substrate with detailed titanium (Ti), oxygen (O) and carbon (C) mapping. 76

**Figure 3.9** - Electron Energy-Loss Spectroscopy (EELS) spectrum of the cross-sectioned TiO<sub>2</sub> thin film coated onto PET substrate. 77

**Figure 3.10** - Selected nanometric micrographs of the cross-sectioned TiO<sub>2</sub> thin film coated onto PET substrate: (a) example of heterogeneous coating thickness distribution and (b) tendency of crystallinity on the surface of the analyzed cross-section image with near-atomic resolution. 78

**Figure 3.11** - Selected AFM 3D topography micrographs of two different 900µm<sup>2</sup> regions of the brand new TiO<sub>2</sub>-coated PET. 79

**Figure 3.12** - Selected AFM 3D topography micrographs of two different 900µm<sup>2</sup> regions of the five times used TiO<sub>2</sub>-coated PET. 79

<b>Figure 3.13</b> - Tauc-Plot graphical obtaining of band-gap energy of the titania thin film deposited on PET substrate.	81
<b>Figure 4.1</b> – (a) The interior of the UV-A/Vis photocatalytic reactor and (b) the corresponding lamps emission spectrum.	89
<b>Figure 4.2</b> - CBZ removal during adsorption (PET-TiO <sub>2</sub> + Dark), photocatalysis (PET-TiO <sub>2</sub> + UV-A/Vis), photolysis assisted by turmeric (Turmeric - UV-A/Vis) and photocatalysis assisted by turmeric (Turmeric - PET-TiO <sub>2</sub> - UV-A/Vis) (n=3).	92
<b>Figure 4.3-</b> UV-Vis spectrum of CBZ aqueous solution.	93
<b>Figure 4.4-</b> UV-Vis spectrum of CBZ aqueous solution during the photocatalytic reaction assisted by turmeric and detail of the CBZ peak reduction.	94
<b>Figure 4.5</b> - Turmeric removal during photolysis (Turmeric - UV-A/Vis) and photocatalysis assisted by turmeric (Turmeric - PET-TiO <sub>2</sub> - UV-A/Vis) (n=3).	95
<b>Figure 4.6</b> - UV-Vis spectrum of turmeric aqueous solution.	95
<b>Figure 4.7</b> - The reusability of the titania-coated thin film: carbendazim decay curves of the 5 cycles of use with detail to the pseudo-first-order rate constants.	96
<b>Figure 4.8</b> - ESI-(+)-MS spectrum from the Carbendazim standard solution.	98
<b>Figure 4.9</b> - ESI-(+)-MS spectrum from the turmeric solution.	99
<b>Figure 4.10</b> - ESI-(+)-MS spectrum from the photocatalytically-treated solution of carbendazim assisted with turmeric.	99
<b>Figure 5.1</b> – (a) The benchtop solar simulator chamber and (b) the detail of the xenon lamps with daylight filters.	105
<b>Figure 5.2-</b> CAF removal during adsorption (PET-TiO <sub>2</sub> + Dark), photocatalysis (PET-TiO <sub>2</sub> + UV-A/Vis), photolysis assisted by turmeric (Turmeric - UV-A/Vis) and photocatalysis assisted by turmeric (Turmeric - PET-TiO <sub>2</sub> - UV-A/Vis) (n=3).	107

<b>Figure 5.3</b> - UV-Vis spectrum of the caffeine aqueous solution.	108
<b>Figure 5.4</b> – ESI-(+)-MS spectrum from the caffeine standard solution.	111
<b>Figure 5.5</b> - ESI-(+)-MS spectrum from the photocatalytically-treated solution of caffeine and turmeric.	111
<b>Figure 5.6</b> - CAF removal during adsorption (PET-TiO <sub>2</sub> + Dark), photolysis (Suntest) and photocatalysis (PET-TiO <sub>2</sub> + Suntest) (n=3).	114
<b>Figure 5.7</b> - CAF removal during photolysis (Suntest), photolysis assisted by turmeric (Turmeric + Suntest), photocatalysis (PET-TiO <sub>2</sub> + Suntest) and photocatalysis assisted by turmeric (Turmeric + PET-TiO <sub>2</sub> + Suntest) (n=3).	115
<b>Figure 5.8</b> - CAF removal during photocatalysis (PET-TiO <sub>2</sub> + Suntest), photocatalysis with the $\cdot\text{O}_2^-$ trapping agent (PET-TiO <sub>2</sub> + Suntest + BQ), photocatalysis with the $\text{HO}\cdot$ trapping agent (PET-TiO <sub>2</sub> + Suntest + DMSO), and photocatalysis with the $\text{h}^+$ trapping agent (PET-TiO <sub>2</sub> + Suntest + EDTA) (n=3).	116
<b>Figure 5.9</b> - CAF removal during photocatalysis assisted by turmeric (Turmeric + PET-TiO <sub>2</sub> + Suntest), photocatalysis assisted by turmeric with the $\cdot\text{O}_2^-$ trapping agent (Turmeric + PET-TiO <sub>2</sub> + Suntest + BQ), photocatalysis assisted by turmeric with the $\text{HO}\cdot$ trapping agent (Turmeric + PET-TiO <sub>2</sub> + Suntest + DMSO), and photocatalysis assisted by turmeric with the $\text{h}^+$ trapping agent (Turmeric + PET-TiO <sub>2</sub> + Suntest + EDTA) (n=3).	118
<b>Figure 5.10</b> - Simplified illustration of the photocatalysis assisted by turmeric process.	120
<b>Figure 6.1</b> - RPR and CPC reactors (GruPOA)	123
<b>Figure 6.2</b> - RPR reactor with the photocatalytic surface coated with TiO <sub>2</sub> .	125
<b>Figure 6.3</b> – Illustration of RPR reactor with its main dimensions and components.	125

<b>Figure 6.4</b> – CPC reactor with cylinder coated with TiO <sub>2</sub> .	126
<b>Figure 6.5</b> – Illustration of CPC reactor with its main components.	127
<b>Figure 6.6</b> – CAF removal during photolysis (CAF+ RPR) and photocatalysis (CAF+ PET-TiO <sub>2</sub> + RPR) under natural sunlight in the RPR photoreactor (n=3) in a temporal scale.	128
<b>Figure 6.7</b> – Evolution of accumulated solar UV radiation (Q <sub>UV</sub> ) during each photocatalysis (CAF + PET-TiO <sub>2</sub> + RPR) experiment (E1, E2, and E3) with reaction time.	129
<b>Figure 6.8</b> – Evaluation of CAF removal per accumulated solar UV radiation (Q <sub>UV</sub> ) during each photocatalysis (CAF + PET-TiO <sub>2</sub> + RPR) experiment (E1, E2, and E3).	130
<b>Figure 6.9</b> – CAF removal during photolysis assisted by turmeric (CAF/Turmeric + RPR) and photocatalysis assisted by turmeric (CAF/Turmeric + PET-TiO <sub>2</sub> + RPR) under natural sunlight in the RPR photoreactor (n=3) in a temporal scale.	131
<b>Figure 6.10</b> – Evolution of accumulated solar UV radiation (Q <sub>UV</sub> ) during each photocatalysis assisted by turmeric (CAF/Turmeric + PET-TiO <sub>2</sub> + RPR) experiment (E1, E2, and E3) with reaction time.	132
<b>Figure 6.11</b> – Evaluation of CAF removal per accumulated solar UV radiation (Q <sub>UV</sub> ) during each photocatalysis assisted by turmeric (CAF/Turmeric + PET-TiO <sub>2</sub> + RPR) experiment (E1, E2, and E3).	133
<b>Figure 6.12</b> – CAF removal during photolysis (CAF+ CPC) and photocatalysis (CAF + Tube-TiO <sub>2</sub> + CPC) under natural sunlight in the RPR photoreactor (n=3) in a temporal scale.	134
<b>Figure 6.13</b> – Evolution of accumulated solar UV radiation (Q <sub>UV</sub> ) during each photocatalysis (CAF + Tube-TiO <sub>2</sub> + CPC) experiment (E1, E2, and E3) with reaction time.	135



<b>Figure 6.14</b> – Evaluation of CAF removal per accumulated solar UV radiation ( $Q_{UV}$ ) during each photocatalysis (CAF + Tube-TiO <sub>2</sub> + CPC) experiment (E1, E2, and E3).	136
<b>Figure 6.15</b> – CAF removal during photolysis assisted by turmeric (CAF/Turmeric + CPC) and photocatalysis assisted by turmeric (CAF/Turmeric + Tube-TiO <sub>2</sub> + CPC) under natural sunlight in the CPC photoreactor (n=3) in a temporal scale.	137
<b>Figure 6.16</b> – Evolution of accumulated solar UV radiation ( $Q_{UV}$ ) during each photocatalysis assisted by turmeric (CAF/Turmeric + Tube-TiO <sub>2</sub> + CPC) experiment (E1, E2, and E3) with reaction time.	138
<b>Figure 6.17</b> – Evaluation of CAF removal per accumulated solar UV radiation ( $Q_{UV}$ ) during each photocatalysis assisted by turmeric (CAF/Turmeric + Tube-TiO <sub>2</sub> + CPC) experiment (E1, E2, and E3).	138
<b>Figure 6.18</b> – Evaluation of CAF removal per accumulated solar UV radiation ( $Q_{UV}$ ) during each photocatalysis assisted by turmeric experiment in Suntest CPS+ (Suntest1, Suntest2, and Suntest3), RPR reactor (RPR1, RPR2 and RPR3) and CPC reactor (CPC1, CPC2 and CPC3).	139
<b>Figure 6.19</b> – Summary of toxicity assessment results from the CAF solutions treated by solar photocatalysis assisted by turmeric: CPC reactor, RPR reactor, and Suntest CPS+ solar simulator.	141

## LIST OF TABLES

<b>Table 2.1</b> - Summary of selected work on heteroatom doping for improved visible-light sensitivity.	17
<b>Table 2.2</b> - Summary of selected work on sensitized photocatalysis for improved visible-light sensitivity.	22
<b>Table 2.3</b> - Selected examples of conventional slurry and fixed bed photocatalytic reactors used in environmental applications.	26
<b>Table 2.4</b> - Examples of new trends of photocatalytic reactors for environmental applications.	30
<b>Table 2.5</b> - Summary of selected data on photocatalytic coatings deposited by HiPIMS.	37
<b>Table 2.6</b> – Physico-chemical properties of carbendazim.	38
<b>Table 2.7</b> – Summary of selected data on the occurrence of Carbendazim in diverse water matrices.	39
<b>Table 2.8</b> - Summary of selected data on the occurrence of caffeine in diverse water matrices.	41
<b>Table 2.9</b> - Physico-chemical properties of caffeine.	42
<b>Table 2.10</b> - Summary of selected data on photocatalytic degradation of the studied model pollutants (carbendazim or caffeine) aqueous solutions.	44
<b>Table 2.11</b> - The vibrational spectrum of PET referenced in the literature.	50

<b>Table 3.1-</b> Water droplet contact angles and wettability classification.	82
<b>Table 3.2 -</b> Phase, surface and optical properties of the TiO <sub>2</sub> photocatalytic surface coated onto 100 µm PET by HiPIMS.	83
<b>Table 4.1 –</b> Summary of organic matter removal of the CBZ aqueous solution through DOC measurements by the different processes.	97
<b>Table 5.1 –</b> Summary of organic matter removal of the CAF aqueous solution through DOC measurements by the different processes.	112
<b>Table 6.1 –</b> Summary of organic matter removal of the CAF aqueous solution through DOC measurements by the different processes.	140

## NOMENCLATURE

AAS	Atomic Absorption Spectrometry
AFM	Atomic Force Microscopy
aTU	Acute Toxicity Unit
BOD	Biochemical Oxygen Demand
BSE	Backscattered electrons
CAF	Caffeine
CAS	Chemical American Society
CB	Conduction band
CBZ	Carbendazim
CEC	Contaminants of emerging concern
COD	Chemical Oxygen Demand
CPC	Compound Parabolic Collector
DOC	Dissolved Organic Carbon
DRS	UV–Vis Diffuse Reflectance Spectroscopy
EC <sub>50</sub>	The concentration that has an effect on 50% of the population
EDS	Energy Dispersive Spectroscopy
EELS	Electron energy-loss spectroscopy
E <sub>g</sub>	Optical band-gap energy
EPR	Electron paramagnetic resonance
FEG	Field emission gun
FTIR	Fourier Transform Infrared Spectroscopy
GIXRD	Grazing Incidence X-ray Diffraction

GruPOA	Research Group on Environmental Applications of Advanced Oxidation Processes
HiPIMS	High Power Impulse Magnetron Sputtering
LED	Light emitting diode
LP	Lamp power
MMU	Manchester Metropolitan University
Mw	Molecular weight
m/z	Mass-to-charge ratio
NMR	Solid-state Nuclear Magnetic Resonance
PET	Polyethylene terephthalate
PSTY	Photocatalytic Space-Time Yield
PVD	Physical vapor deposition
QY	Quantum Yield
RPR	Raceway pond reactors
R <sub>rms</sub>	Root-mean-squared roughness
SE	Secondary electrons
SEM	Scanning Electron Microscopy
STEM	Scanning Transmission Electron Microscopy
TEM	Transmission Electron Microscopy
TOC	Total Organic Carbon
UFMG	<i>Universidade Federal de Minas Gerais</i>
UK	United Kingdom
UV	Ultraviolet radiation
UV-A/Vis	Ultraviolet A and visible radiation
UV-Vis	Ultraviolet and visible radiation
VB	Valence band

wt%	Weight percent
WWTP	Wastewater treatment plants
XPS	X-ray photoelectron spectroscopy
XRD	X-ray Diffraction

## CHAPTER 1. INTRODUCTION

This chapter provides an overview of the performed work, including information on background and justification (section 1.1), a description of the general and specific research objectives to be achieved (section 1.2), and information about the thesis layout (section 1.3).

### 1.1 *Background and Motivation*

Heterogeneous photocatalysis can be defined as the change of velocity of a photoreaction in the liquid or gas phase in the presence of a solid catalyst that simultaneously adsorbs both reactants and photons in an efficient manner. Photocatalysis is known as a promising and environmentally sustainable process of water treatment as it is initiated simply by light irradiation.

The photocatalytic activity of titanium dioxide ( $\text{TiO}_2$  - also known as titania) was perceived almost a century ago. Since then, heterogeneous photocatalysis has been widely studied for multiple environmental applications (REDDY *et al.*, 2016). Additionally, endocrine disruptors and other contaminants of emerging concern (CEC) have been detected in surface waters and in treated wastewaters (GROS *et al.*, 2017), at concentrations varying between some  $\text{ng L}^{-1}$  and several  $\mu\text{g L}^{-1}$ . Owing to the development and dissemination of analytical techniques, the world has become aware of the occurrence of CECs. This awareness, coupled with the fact that the removal rates of CECs in urban wastewater treatment plants (WWTP) are rather low, compounds the need for improvements in treatment techniques in order to achieve improved water quality (BUTKOVSKYI *et al.*, 2016; GROS *et al.*, 2017; LOOS, ROBERT *et al.*, 2017) and provide a safe aquatic environment (RODRÍGUEZ-GIL *et al.*, 2018; THOMAIDI *et al.*, 2015; VAN DEN BRINK *et al.*, 2000) and advanced treatment based on photocatalysis is a potential solution for CEC removal.

The industrial application of artificially irradiated photocatalytic processes for the treatment of water and wastewaters, however, is still limited by the operational cost associated with these technologies and the difficulty of separating the catalysts used in suspension in the treatment process. The use of natural sunlight, especially in locations with high insolation rates, not only reduces the electricity-related costs but also the hazards of mercury contamination from UV lamps (MARCELINO *et al.*, 2015). Moreover, most of the works are performed exclusively in laboratory scale and therefore scaling-up is essential to reach the utilization of photocatalytic processes for

water purification at industrial scale (GHAFOORI; MEHRVAR; CHAN, 2014; MAUČEC *et al.*, 2017).

In photocatalytic processes, the use of a catalyst in its powdered form results in a higher surface area but poses some difficulties to recover the powder after treatment. In order to recover the catalyst after photocatalytic treatment, many studies have been made of ways to support the catalysts in different matrices (DE BRITES-NÓBREGA *et al.*, 2013; MUNOZ *et al.*, 2017; RAMASUNDARAM *et al.*, 2017; YI *et al.*, 2015). It is important to study and develop different methodologies to support solar-activated photocatalysts onto inexpensive substrates in addition to enabling scale-up in order to extend credibility to photocatalytic processes for water purification in real scale situations.

Surface engineering is playing an important role, while providing a wide range of different techniques for photocatalytic film deposition on different substrates, including physical vapor deposition processes (RATOVA *et al.*, 2017; ROSSNAGEL, 2003) chemical vapor deposition techniques (UR RASHID *et al.*, 2015) and photocatalytic organic paints (HOMA *et al.*, 2017; SUAVE *et al.*, 2017), creating a wide range of photocatalytic surfaces. Magnetron sputtering is a physical vapor deposition technique which is being used for the deposition of a wide range of functional films, including photocatalytic coatings (KELLY *et al.*, 2014; QUYNH *et al.*, 2016; RATOVA *et al.*, 2017).

Titania coatings directly deposited by conventional magnetron sputtering, however, tend to have an amorphous microstructure. For the anatase (the most photoactive phase) structure to develop, substrate heating or postdeposition thermal treatment is usually required, with the anatase crystal phase generally forming at temperatures in excess of 400 °C (BANERJEE *et al.*, 2015; RATOVA *et al.*, 2014).

Consequently, conventional magnetron sputtering may not be able to deposit anatase materials onto polymeric supports, due to high temperature and/or post-deposition annealing requirements (SINGH *et al.*, 2013), since polymeric materials present melting point temperatures below 400 °C. Alternatively, high power impulse magnetron sputtering (HiPIMS), a relatively recently introduced variant of the process, has proven able to deposit photocatalytically active titania coatings directly



onto flexible polymeric substrates in a single stage process (KELLY *et al.*, 2014; KELLY *et al.*, 2012; RATOVA *et al.*, 2014; TIRON *et al.*, 2016), and it is studied in this work.

Organic polymers have wide applicability as substrates for photocatalytic thin films deposition (CÁMARA *et al.*, 2016; PASSERI *et al.*, 2013; SINGH *et al.*, 2013). These materials are inexpensive and easy to mold into different geometries because of their flexibility, which makes them an ideal solution for a wide range of applications. Polyethylene terephthalate (PET) is a thermoplastic polyester considered one of the most important engineering plastics owing to its interesting properties, such as excellent tensile and impact strength, chemical resistance, clarity, processability, colorability and reasonable thermal stability (AWAJA, 2005; OROMIEHIE, 2004). Moreover, PET it is reportedly the most recyclable polymer (JAMDAR *et al.*, 2017) and, therefore, transparent PET substrate was selected to support photocatalytic thin films used in this research.

In this context, this project is justified since it aims at studying the development of photocatalytic surfaces coated on flexible PET substrates in partnership with Surface Engineering Research Group from Manchester Metropolitan University (MMU, United Kingdom). The developed surfaces were characterized, studied in laboratory scale and then applied to internal parts of semi-pilot scale solar photoreactors in order to study the feasibility of the proposed material for the treatment of water contaminated with CECs.

The PET-coated surfaces have been developed in partnership with MMU from the work of Ratova *et al.* (2014) where the authors developed a methodology of low-temperature coating of TiO<sub>2</sub> thin films onto glass substrates in a single step process. Afterwards, the authors concluded that this methodology could be used to deposit photocatalytic films onto polymeric substrates, and assessed the feasibility with polyethylene terephthalate (PET) and polycarbonate substrates. It was found that titania coatings deposited by HiPIMS directly onto polymeric substrates showed relatively high levels of activity in their as-deposited state. In the current Ph.D. research, the deposition of the photocatalytic thin films was performed in partnership at MMU due to their know-how and laboratory structure. The surfaces were characterized and tested for water treatment at The surfaces were characterized and tested for water treatment at *Universidade Federal de Minas Gerais* (UFMG, Brazil).

Carbendazim and caffeine were selected as model CECs for water treatment assays due to their photostability, colorlessness, and relevant environmental impact (KAUR *et al.*, 2016; MAZELLIER *et al.*, 2002; RODRÍGUEZ-GIL *et al.*, 2018). Moreover, caffeine molecule has been used as an indicator of anthropogenic pollution (DANESHVAR *et al.*, 2012; PEELER *et al.*, 2006; RODRÍGUEZ-GIL *et al.*, 2018; SEILER *et al.*, 1999) due to its high consumption and recalcitrant nature. Therefore, it can be a good indicator of photocatalytic tertiary wastewater treatment performance.

Since this research is being performed in partnership between the Research Group on Environmental Applications of Advanced Oxidation Processes - GruPOA (UFMG, Brazil) and the Surface Engineering Research Group from MMU (United Kingdom), this project is also justified since it sponsors innovation in the research currently carried out by GruPOA (UFMG), contributing to the internationalization of the current postgraduate program and university, besides being an opportunity to transfer technological knowledge to UFMG and to Brazil.

## **1.2 Objectives**

### **1.2.1 General objective**

The general objective of the present project is to study the technical feasibility of the solar water treatment process promoted by the PET coated with TiO<sub>2</sub> photocatalytic material.

### **1.2.2 Specific objectives**

- To investigate the main characteristics of the material which affects its performance through phase, compositional and morphological characterization;
- To test photocatalytic properties of the HiPIMS-coated PET-TiO<sub>2</sub> surfaces in laboratory scale with carbendazim and with caffeine as model pollutants of emerging concern in aqueous solution;
- To study the photogenerated species and to propose a simplified mechanism through scavengers reactions;
- To study the scale-up and the integration of the photocatalytic materials into semi-pilot scale solar water treatment reactors.

### **1.3 Document Structure**

This thesis is composed of 7 chapters. Chapter 1 is introductory. It contains the context/justification and the main research aims of the present thesis project.

Chapter 2 provides an overview on the fundamental background and state-of-the-art of photocatalysis, photocatalytic TiO<sub>2</sub>-based applications, band-gap engineering (mainly sensitization), surface engineering, photocatalytic thin-films characterization, main solar photoreactors and of the selected model contaminants of emerging concern: carbendazim and caffeine.

The first specific objective is addressed in Chapter 3, where the characterization of the photocatalytic surfaces was addressed. The analytical techniques were presented, the methodology employed was detailed and the results were presented and discussed.

Chapter 4, entitled "Application of TiO<sub>2</sub> thin films coated onto PET by high power impulse magnetron sputtering at laboratory scale for carbendazim degradation", addresses the second specific objective.

Chapter 5 is entitled "Application of TiO<sub>2</sub> thin films coated onto PET by high power impulse magnetron sputtering at laboratory scale for caffeine degradation". It is associated with the third specific objective.

The scale-up of the studied technologies to a semi-pilot scale under natural solar irradiation was studied in Chapter 6, entitled "Application of photocatalytic surfaces at semi-pilot scale under solar irradiation for water treatment".

Finally, in Chapter 7, "Conclusions and future work suggestions", it can be found the main achievements of the study, conclusions, and suggestions of future work based on the insights obtained during this research project.

## CHAPTER 2. FUNDAMENTALS

This chapter introduces the main principles of photocatalysis and the use of titanium dioxide as a photocatalyst. It also presents a fundamental background of band-gap engineering, surface engineering and of the selected model contaminants of emerging concern: carbendazim and caffeine.

### 2.1 *Photocatalysis and Titania*

#### 2.1.1 Environmental photocatalysis and context

The continuous increase in population, urbanization, industrial growth and agricultural activities has a significant impact on the demand for natural resources. In parallel, the existence of a wide range of sources of contamination that may reach the aquatic environment and the atmosphere directly challenges the supply of clean water and air necessary to anthropogenic activities, besides being an important ecological and health risk. Therefore, the decline of water and air quality has progressively become a global issue of concern.

There is also a growing concern about the currently specifically unregulated groups of pollutants, which, because of their toxic effects on the environment and human health, coupled with their high occurrence, render them subject to future regulation (MIRALLES-CUEVAS *et al.*, 2013). Such groups of pollutants, called contaminants of emerging concern (CEC), may be found in the environment at low concentrations (i.e.  $\text{ng}\cdot\text{L}^{-1}$ ) include various globally widespread organic compounds, such as pesticides, pharmaceuticals, personal care products, polymers, amongst others (as well as their metabolites and transformation products) (MARTÍNEZ-HERNÁNDEZ *et al.*, 2018).

Pollution treatment technologies based on photocatalysis have proven effective for *in situ* degradation of biorecalcitrant organic compounds and inorganic contaminants, in addition to promotion of disinfection in different environmental matrices. These processes present the advantage of destroying the pollutants, in contrast to conventional techniques such as adsorption or flocculation that only transfer the contaminants from one phase to another.

Photocatalysis has therefore become of great environmental interest in the last century, as it has the potential to be used as a tertiary treatment technology which can couple both disinfection and

removal of contaminants of emerging concern (REDDY *et al.*, 2016; ROBERT *et al.*, 2017; CAI, 2017; GARZA-CAMPOS *et al.*, 2016; HERRMANN *et al.*, 2007; MALATO *et al.*, 2009; MARCELINO *et al.*, 2015; PEREIRA *et al.*, 2014; RATOVA *et al.*, 2017; SPASIANO *et al.*, 2015). To that purpose, a wide range of materials have been successfully applied as photocatalysts for air and water treatment (AUGUGLIARO *et al.*, 2009; CÁMARA *et al.*, 2016; LIN, Y.-C. *et al.*, 2015; MIARALIPOUR *et al.*, 2018; PETRONELLA *et al.*, 2017; PITRE *et al.*, 2017; SINGH *et al.*, 2013).

Nevertheless, the need for energetic ultraviolet radiation in most successful photocatalytic processes has limited both the feasibility and environmental benefits of photocatalysis on industrially relevant scales (SCHULTZ & YOON, 2014; YOON *et al.*, 2010). Therefore, the use of photocatalysts with band-gap narrow enough to absorb light in visible and near infrared regions is of great interest (BOYJOO *et al.*, 2017a). Many studies have been performed in order to design and develop visible-light activated photocatalysts and the main strategies involving band-gap engineering will be discussed in the following sections.

It is also understood that reactor configuration and design affect the photocatalytic treatment efficiency (BOYJOO *et al.*, 2017a; VAN GERVEN *et al.*, 2007a) since it affects photons absorption. In parallel with the band-gap engineering run, different studies were performed in order to better understand the effect of photons absorption in different reactors configurations, and therefore suggest improved reactor designs in order to maximize the efficiency of photocatalytic reactors (PASSALÍA *et al.*, 2017; BOYJOO *et al.*, 2017).

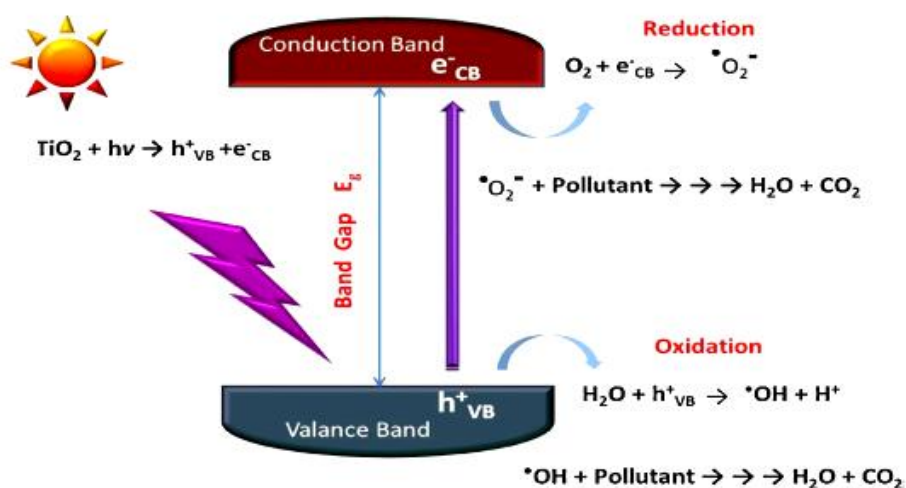
### **2.1.2 Photocatalysis fundamentals and key aspects**

Photocatalysis is a process involving both oxidation and reduction reactions promoted by a catalyst, which is activated by radiation with sufficient energy in the presence of water and electron acceptor (compound suitable for trapping the electron). In water treatment processes, photocatalysis can promote the formation of strong and non-selective oxygen-based radicals, such as hydroxyl radicals (HO•), and therefore degrade organic and inorganic pollutants (MILLS, 1997).

Photocatalytic materials are typically semiconductors, the electronic structures of which are characterized by a filled valence band and an empty conduction band. Absorption of a photon with energy greater than the band-gap energy leads to migration of the electron to the conduction band

and the formation of an electron/hole pair. If a compound or a defect state suitable for trapping the electron or hole is available, recombination is prevented and subsequent redox reactions are likely to occur. Valence band holes are good oxidants while conduction band electrons are good reductants (MALATO *et al.*, 2009a). Thus, photoinduced holes exhibit a high oxidation potential and are able, either directly or indirectly, to decompose stable organic pollutants and the photogenerated electrons are able to reduce ambient oxygen (BAUDYS *et al.*, 2015). The process is illustrated in Figure 2.1.

**Figure 2.1** - Schematic illustration of the TiO<sub>2</sub> photocatalytic processes. Extracted from Banerjee *et al.* (2015).



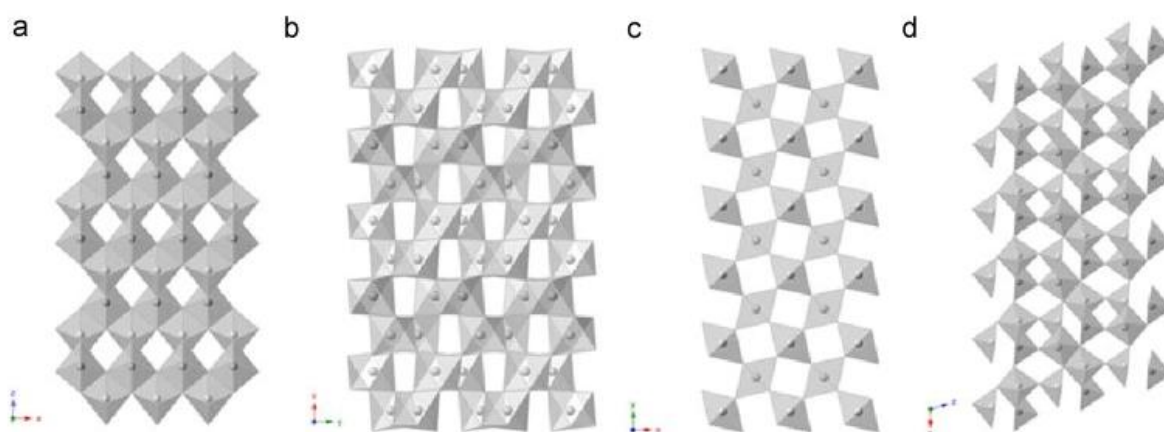
Titania-based photocatalysis has been studied for the degradation of a variety of bio-recalcitrant contaminants in water, including pesticides (BERBERIDOU *et al.*, 2017; KAUR *et al.*, 2015), pharmaceuticals (GAR ALALM *et al.*, 2016; VAIANO *et al.*, 2015) and hormones (MANASSERO *et al.*, 2013; OHKO *et al.*, 2001; OHKO *et al.*, 2002; SORNALINGAM *et al.*, 2018) in the presence of artificial or solar radiation (MARCELINO *et al.*, 2015). Technological development in photocatalysis has resulted in the development of catalysts with improved solar sensitivity in order to enhance the efficiency of pollutant decontamination under solar radiation (KAUR *et al.*, 2016; MALATO *et al.*, 2009a; MARCELINO *et al.*, 2015; REDDY *et al.*, 2016).

TiO<sub>2</sub> is the most widely used photocatalyst (SHAHAM-WALDMANN, 2016) mainly because it is inexpensive, chemically stable and biologically benign (LUTTRELL *et al.*, 2015), although it

presents some major drawbacks. Firstly, the photocatalytic activity of TiO<sub>2</sub> requires UV excitation to promote an electron from the valence band (VB) to the conduction band (CB), generating a short-term electron-hole pair that can participate in reductive (electron, e<sup>-</sup>) or oxidative (hole, h<sup>+</sup>) reactions, with high carrier recombination rates (PITRE *et al.*, 2017). In terms of solar irradiation utilization, titania-catalysts solar spectral efficiency is poorly around 3.5% (INFINITYPV, 2018). Moreover, it is typically difficult to achieve high reaction rates using TiO<sub>2</sub> due to this high carrier (electron/hole pairs) recombination rates that ultimately decreases photocatalyst effectiveness and photonic efficiency of the redox process (ILIEV *et al.*, 2018).

TiO<sub>2</sub> is typically an n-type semiconductor due to oxygen deficiency at its crystal lattice (PELAEZ *et al.*, 2012), which means that free electrons are the majority carriers and holes are the minority carriers. Titania exists mainly in four crystalline forms: anatase (tetragonal), brookite (orthorhombic), rutile (tetragonal) and monoclinic TiO<sub>2</sub>-B (HANAOR & SORRELL, 2011; MONAI *et al.*, 2017), which are shown in Figure 2.2.

**Figure 2.2** - The structure of (a) anatase, (b) brookite, (c) rutile, and (d) TiO<sub>2</sub>-B. Extracted from Liu *et al.* (2013).



Different polymorphs have different physicochemical properties, such as electronic and optical properties, which affect the material performance in photocatalytic applications. However, the role of crystal structure and morphology in photocatalytic processes is not straightforward, since it is difficult to synthesize single-phase material and many correlated factors influence the rate of photochemical reactions, such as particle size, shape, crystallinity, number/type of defects, electron-



hole recombination, surface area, reactant and intermediate species adsorption on the catalyst surface, for example (MONAI *et al.*, 2017; OHTANI, 2010).

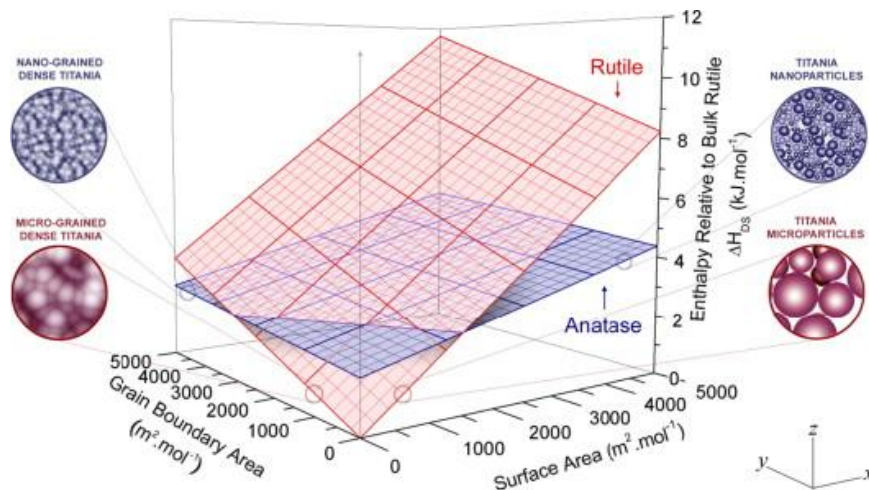
The two main photocatalytic polymorphs, the metastable anatase, and the stable rutile, present several structural and functional differences (HANAOR & SORRELL, 2011; HURUM *et al.*, 2003). Anatase particles are generally less than 50 nm in size and present band-gap energy around 3.2 eV, corresponding to a UV region wavelength ( $\lambda = 385$  nm). Anatase crystals present higher adsorptive affinity for organic compounds than that of rutile, coupled with lower rates of carrier recombination in comparison to rutile due to its 10-fold greater rate of hole trapping (HURUM *et al.*, 2003).

In contrast, the rutile phase usually exists as particles larger than 200 nm and presents smaller band-gap energy of 3.0 eV with excitation wavelengths that extend into the visible region ( $\lambda = 410$  nm). In the case of nanocrystalline titania materials, even though rutile polymorph is usually more stable in higher scale materials, it is established in the literature that nanosized anatase has a smaller surface energy (DA SILVA *et al.*, 2017; LEVCHENKO *et al.*, 2006).

With decreasing particle size (increasing surface area) the total free energy of rutile nanoparticles increases faster with the surface area than anatase, leading to a crossover between the phases at a critical size below which anatase is thermodynamically more stable than rutile (CASTRO, 2013). It is reported that there is an energy crossover at  $15.3 \text{ m}^2\text{g}^{-1}$  (or 63 nm), as from which the anatase phase is more stable than rutile (CASTRO, 2013; CASTRO & WANG, 2011).

Since the grain boundary energy for anatase and rutile are non-negligible (CASTRO, 2013) and therefore these titania materials may suffer coarsening (crystal size augmentation), a three-dimensional diagram was proposed by Castro (2013) and it is shown in Fig. 2.3. This diagram shows the stability trend for these two phases (anatase and rutile) as a function of both surface area and grain boundary area. The circles represent hypothetical microstructures at that interface area condition. To the left, there are nanograined samples, while to the right nanoparticles free of strong agglomerates.

**Figure 2.3** - Phase diagram for nanocrystalline titania (rutile and anatase) considering both grain boundary and surface areas as contributions for the total energy of the system. Extracted from Castro (2013).



Brookite and  $\text{TiO}_2\text{-B}$ , whose photocatalytic activity were once considered negligible, are now gaining attention due to their improved performance, in some cases showing enhanced activity with respect to anatase or rutile (MONAI *et al.*, 2017; YANG *et al.*, 2009), and they are now being studied both as single and mixed-phase catalysts.

$\text{TiO}_2$  is mainly used in slurry reactors (suspended catalyst), since these processes are usually more efficient, although the penetration depth of the light into the suspensions is limited, and the catalyst particles must be separated (filtration or sedimentation) prior to the discharge of the treated water. Supported photocatalyst should be preferred to scale up the wastewater treatment, although the overall reaction rate may decrease due to mass transfer resistance of the pollutant to the catalyst surface (MAUČEC *et al.*, 2017; SHI *et al.*, 2017).

Beyond titania photocatalysis, considerable effort has been made in order to enhance the optical adsorption abilities of photocatalytic materials in order to utilize visible (and solar) radiation, and the main band-gap engineering techniques applied to semiconductors are discussed in the next topic.

## **2.2 Band-gap Engineering: Enhancing Visible Light Photocatalysis**

Band-gap engineering is the process of shifting the band-gap of a material by controlling the composition or crystal structures of semiconductors or composites (CAPASSO, 1987). Different approaches have been taken to narrow the band-gap of photocatalysts in order to trigger its photoactivity under visible or near-infrared light, which is widely available and safer compared to UV radiation.

Before discussing the band-gap engineering processes, it is noteworthy that there are some definitions disagreements related to photocatalysis and visible-light irradiation that may lead to difficulty on reproducing the majority of the works reported on literature, as some of these aspects are discussed in sequence.

As an example, the boundary wavelength between ultraviolet light and visible light is not yet clear (OHTANI, 2010; SHAHAM-WALDMANN, 2016). Ohtani (2010) discussed that “visible light” limiting wavelength differs among researchers and that inadequate optical cut-off filters have been used in experimental works.

He also stated that adequate compounds should be used for the photocatalytic activity test (OHTANI, 2010; OHTANI, 2014). The use of dyes as model contaminants demonstrating the visible photocatalytic properties of materials may be inappropriate (OHTANI, 2010; SHAHAM-WALDMANN, 2016; YAN *et al.*, 2006). Dyes absorb visible light and, therefore, the photoreaction might be induced by visible-light dye sensitization and by photoabsorption of a photocatalyst (OHTANI, 2013; ROBERT *et al.*, 2017; SHAHAM-WALDMANN, 2016; YAN *et al.*, 2006). Therefore, colorless compounds should be preferred as model pollutants.

Moreover, photocatalytic activity depends strongly on the wavelength (and power) of incident light and differences between irradiation sources utilized are also important issues on reproducibility. Monochromatic light irradiation should be preferred in order to assay the photocatalytic activity of materials. However, a wide range of irradiation sources (mercury-vapor lamps, xenon lamps, light emitting diodes - LEDs, natural solar irradiation, etc.) is used and, even though grating-type monochromators and cutting-off filters are often used, the irradiation is mostly emitted in different wavelengths, which can only be precisely measured with spectral-radiometer devices, and therefore it may hinder the comparison of different experimental results.

Comparing experiments towards kinetic constants may be another issue. Many papers report *pseudo*-first order kinetic constants obtained from experimental data assuming simplified Langmuir–Hinshelwood mechanism, where kinetic data is usually analyzed by plotting the logarithm of the concentration of a substrate or a product against time of the reaction (OHTANI, 2010).

However, since it is a complex phenomenon and involves diverse heterogeneous processes (chemical/physical/optical), kinetic constants of experimental photocatalysis should be obtained considering pollutant concentration as a function of three different variables: time, incident radiation inside the reactor, and photonic flux absorbed by the catalyst (MALATO *et al.*, 2009; MANASSERO *et al.*, 2017; OHTANI, 2010; OHTANI, 2014). Obtaining these parameters is not a simple mission and may require mathematical modeling and advanced computational simulation (MANASSERO *et al.*, 2017).

The overall reaction rate of photocatalytic processes is usually slow compared to conventional chemical reaction rates, and therefore there is a need to provide large amounts of active catalyst sites inside the reactor (RAY, 2009). The number of photoactive sites increases with photon absorption until a maximum value is reached, and further absorption of photons does not affect the amount of solute photoadsorbed on the substrate. This limiting concentration should be a characteristic of the catalyst surface and the physicochemical characteristics of the solution (AUGUGLIARO *et al.*, 2009).

Therefore, despite the potential of this promising technology and great number of papers published, the environmental applications of photocatalysis are still very limited, published work may not be easily reproducible, and it still remains challenging to develop industrial-scale technologies based on photocatalysis (ROBERT *et al.*, 2017; VAN GERVEN *et al.*, 2007). Band-gap engineering and the development of visible-light efficient photocatalytic processes may increase the process efficiency and credibility.

Heteroatom doping is among the most popular band-gap engineering techniques. Doping introduces additional impurities that may act as charge carrier traps, and thus extend the lifetime of the photogenerated charge carriers. This can be achieved by adding controlled metal (COTTINEAU *et*

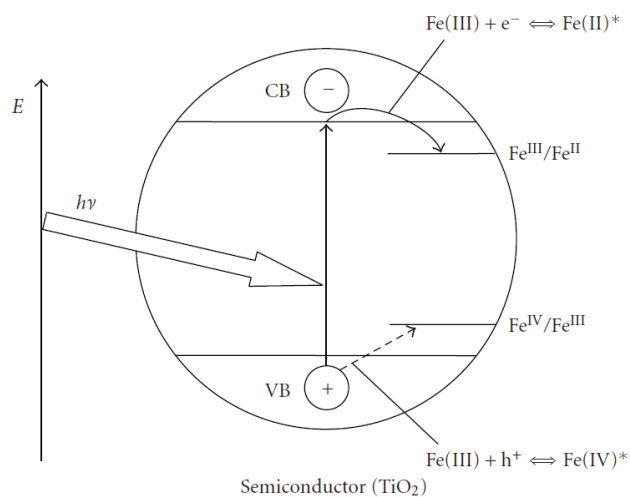
al., 2013; ZHANG et al., 2014) or nonmetal (RATOVA et al., 2017; YAN et al., 2017) impurities that generate donor or acceptor states in the band-gap.

Is noteworthy that cationic doping with transition metal ions is a popular process used to narrow the band-gap energies of photocatalysts. The improved response to visible light, in this case, is mainly due to high levels of impurities in the forbidden energy band of the photocatalysts, however, these impurities could also serve as recombination centers for photoinduced charge carriers and consequently reduce the photocatalytic activity. Therefore, this type of doping is currently being criticized and non-metal doping is usually preferred (MAZZOLINI *et al.*, 2016; YAN *et al.*, 2017).

N-doped TiO<sub>2</sub>, for example, have been attracting increasing attention and Di Valentin *et al.* (2007) reviewed the theory and experimental results obtained with this technique (DI VALENTIN *et al.*, 2007). The researchers concluded that N-doped anatase contains thermally stable single N-atom impurities that can occupy both interstitial and substitutional positions in the solid, with some evidence for a preference for interstitial sites. Electron paramagnetic resonance (EPR) spectra measured under irradiation show that the N centers are responsible for visible light absorption with the promotion of electrons from the localized N-impurity states to the conduction band or to electron scavengers like O<sub>2</sub> adsorbed on the surface (DI VALENTIN *et al.*, 2007).

Through heteroatom doping, the visible-light absorption characteristics of commonly used photocatalysts, such as TiO<sub>2</sub>, ZnO, and Fe<sub>x</sub>O<sub>x</sub> have being reported as improved. Tryba (2008), for example, proposed a schematic mechanism to show the effect if Fe(III) doping on the TiO<sub>2</sub> photocatalytic process, presented in Figure 2.4.

**Figure 2.4** - Schematic mechanism of TiO<sub>2</sub> photocatalysis with Fe(III) doping. Extracted from Tryba (2008).



The author concluded that, based on the favorable energy levels, Fe(III) impurities can act either as electron or hole traps (Figure 2.3). Therefore, photogenerated charge carriers can be temporarily separated more efficiently (TRYBA, 2008). Examples of successfully reported heteroatom doping are shown in Table 2.1.

**Table 2.1** - Summary of selected work on heteroatom doping for improved visible-light sensitivity.

Catalyst	Dopant	Main methodology	Main results	Reference
TiO <sub>2</sub> Nanofibers	Au, Pt, Pd, and Ag	The formation of active TiO <sub>2</sub> nanofibers in the microwave-assisted synthesis and their modification with Au, Pt, Pd, and Ag nanoparticles were studied. Microwave-assisted synthesis permitted to obtain TiO <sub>2</sub> nanofibers and nanowires with a diameter of 10nm and a specific surface area 158.5m <sup>2</sup> /g. Photocatalytic activity was determined by degradation of the methylene blue (MB) solution under visible light irradiation. High intensity LED lamp was used as the light source.	The obtained samples showed higher photocatalytic activity with respect to pure TiO <sub>2</sub> nanofibers. The doped TiO <sub>2</sub> nanofibers were appropriate for the degradation of harmful organic compounds as well as for hydrogen production by water splitting.	(DRUNKA <i>et al.</i> , 2018)
TiO <sub>2</sub> /graphene composite	N (N-TG)	Graphene oxide, TiO <sub>2</sub> and different amounts of urea (N source) were mixed to dope nitrogen into TiO <sub>2</sub> and RGO simultaneously.	Authors found that the best N-doping ratio was 1.46 at.% for N-TG which the band-gap is 2.86. Humic acid removal in dark is 18.0%, which would increase to 91.7% with the synergistic effect of photodegradation.	(YE <i>et al.</i> , 2018)
TiO <sub>2</sub> and TiO <sub>2</sub> coupled with magnetite (Fe <sub>3</sub> O <sub>4</sub> /TiO <sub>2</sub> )	S	TiO <sub>2</sub> -S photocatalyst is prepared using titanium sulfate as a dual precursor. In parallel, superparamagnetic Fe <sub>3</sub> O <sub>4</sub> magnetite nanoparticles were prepared. Subsequently, they were combined with hydrothermal treatment, which introduced a mass of hydroxyl groups on the photocatalyst surface. Xenon lamp (350 W) with optical filter ( $\lambda > 420$ nm) was used on the photocatalytic tests.	The electronic interaction between S and hydroxyls reduces the band-gap of TiO <sub>2</sub> . Fe <sub>3</sub> O <sub>4</sub> /TiO <sub>2</sub> -S with surface hydroxyls was shown an efficient visible light photocatalyst. Complete removal of model pollutants was achieved.	(YAN <i>et al.</i> , 2017)
TiO <sub>2</sub>	N and Mo	Doping of titania with N and Mo to enhance photocatalytic properties by reactive magnetron sputtering. Photocatalytic properties of the coatings were evaluated on the basis of the photodegradation rate of methylene blue dye under UV, fluorescent and visible light.	The photocatalytic activity of co-doped samples was significantly higher than that of N-doped coatings. Unlike N-doped titania films, co-doped coatings exhibited high photocatalytic activity under the fluorescent light source and noticeable activity under visible light.	(RATOVA <i>et al.</i> , 2015)

TiO <sub>2</sub>	W or Nb or ZnFe <sub>2</sub> O <sub>4</sub>	<p>Titania coatings doped with W, Nb, and ZnFe<sub>2</sub>O<sub>4</sub> were deposited from blended oxide powder targets onto glass substrates by pulsed magnetron sputtering. The as-deposited coatings were characterized. Selected coatings were then annealed at temperatures in the range of 400–700 °C and re-analyzed. The photocatalytic activity was assessed by methyl orange degradation under UV and fluorescent light sources.</p>	<p>It was found that, after annealing, coatings with photo-active surfaces were produced and that activity varied with dopant content.</p> <p>Activity levels under fluorescent light irradiation were up to 60% of the activity measured under UV irradiation.</p>	(FARAHANI <i>et al.</i> , 2013)
TiO <sub>2</sub>	N	<p>TiO<sub>2</sub>-based powder, including 0.1 at% of N doped in the rutile lattice, has been synthesized by oxidation of TiN.</p>	<p>Results showed an important shift of the band-gap to lower energy in the visible-light region. The substitutional doping of N into the TiO<sub>2</sub> lattice is found to be effective; its 2<i>p</i> states contribute to the band-gap narrowing by mixing with O 2<i>p</i> as shown in <i>ab initio</i> electronic structure calculations.</p>	(MORIKAWA <i>et al.</i> , 2001)



The heterojunction is another relevant process for photocatalyst band-gap engineering, and it is the combination of wide band-gap semiconductors, such as titanium dioxide, with narrow band semiconductors. This process can also enhance the photocatalytic efficiency by decreasing the recombination rate of the photogenerated electron-hole pairs (CHAI *et al.*, 2006; RTIMI *et al.*, 2013). The combination can compensate the drawbacks of the individual materials, and provoke a synergistic effect such as an efficient charge separation and improvement of photostability. Therefore, visible light-driven coupled photocatalysts that can decompose organic material are of great interest (PELAEZ *et al.*, 2012).

The development of different photocatalytic materials with strong visible-light-absorption ability, such as bismuth-containing photocatalysts (CHEN *et al.*, 2016; SEDDIGI *et al.*, 2017; WEI; YANG; GUO, 2009; ZHANG, L.; ZHU, 2012), is also of growing interest and these materials have also been coupled with TiO<sub>2</sub>. Ratova and coworkers (2017), for example, combined bismuth tungstate with TiO<sub>2</sub> in order to enhance visible light activity. The photocatalytic activity was measured by acetone degradation test which indicated that the deposition of bismuth tungstate resulted in a significant enhancement of visible light activity, for both anatase and rutile titania particle, due to more efficient photogenerated charge carrier separation, as well as to the contribution of the intrinsic photocatalytic properties of Bi<sub>2</sub>WO<sub>6</sub> (RATOVA *et al.*, 2017).

Photosensitization is a reaction to radiation that is mediated by a light-absorbing molecule, which is not the ultimate target. It can enhance the visible-light harvesting and promote charge separation by effective interface charge transfer between the photosensitizer and TiO<sub>2</sub> (GHAFOOR *et al.* 2017). The phenomenon was discovered in 1968 and, since then, dyes have been used in electrochemical energy converting cells: dye-sensitized solar cells (O'REGAN & GRÄTZEL, 1991) and photocatalytic processes.

For example, Grätzel and coworkers with a highly efficient ruthenium-complex sensitized nanocrystalline TiO<sub>2</sub>-based dye-sensitized solar cells –DSSCs (GRÄTZEL, 2001; O'REGAN & GRÄTZEL, 1991). Dye- photosensitization has been widely used to extend the photo-response of semiconductor photocatalysts into the visible region (PELAEZ *et al.* 2012; REDDY *et al.* 2016).

It begins with fast interfacial electron transfer from visible-light-excited chromophores of the dye into the conduction band of the photocatalyst, followed by interfacial electron transfer and is a

simple method that can extend catalysts activation to longer wavelengths (visible radiation, for example) (DUNCAN, 2007; PAN *et al.*, 2011). Selected examples of sensitized photocatalysis are presented in Table 2.2.

**Table 2.2** - Summary of selected work on sensitized photocatalysis for improved visible-light sensitivity.

Catalyst	Sensitizer	Main methodology	Main results	Reference
Carbon nitride (CN) nanosheets loaded with Pt nanoparticles	Dye Erythrosin B (ErB)	Carbon nitride (CN) nanosheets with a thickness of around 3 nm were prepared by pyrolysis of urea. Well-dispersed Pt nanoparticles of about 3 nm were pre-loaded on CN nanosheets as the co-catalyst by chemical reduction in ethylene glycol. The dye ErB was added in the photoreaction suspension.	Pt/CN sample showed an H <sub>2</sub> evolution rate of 45.1 μmol h <sup>-1</sup> from an aqueous solution of triethanolamine (TEOA) under visible light irradiation (λ > 420 nm). By simply adding a low-cost dye ErB in the photoreaction suspension, a remarkably enhanced H <sub>2</sub> evolution rate of 652.5 μmol h <sup>-1</sup> was observed, attributed to the extended light absorption to long wavelengths and efficient charge transfer from excited ErB to CN.	(WANG <i>et al.</i> , 2013)
Production of reduced GO and graphene-based TiO <sub>2</sub>	Rhodamine B (RhB)	The reduction of GO nanosheets was conducted in a mixing suspension solution of GO, RhB and TiO <sub>2</sub> nanoparticles under visible-light irradiation.	Based on the dye-sensitization mechanism, the photogenerated electrons are firstly produced on the excited dye molecule under visible light irradiation and then transferred to the GO via the conduction band of TiO <sub>2</sub> , leading to the effective reduction of GO to rGO.	(WANG <i>et al.</i> , 2013b)
Rhodamine B (RhB) and TiO <sub>2</sub>	Rhodamine B (RhB)	Photodegradation of RhB in a TiO <sub>2</sub> (P-25, Degussa, 80% anatase/20% rutile) suspension under visible-light irradiation.	Water significantly modulates the surface electronic structure of TiO <sub>2</sub> , switches the adsorption mode of dyes, and promotes dye sensitization of TiO <sub>2</sub> under visible-light irradiation. It provides a cheap and green way to improve environmental photocatalysis.	(PAN <i>et al.</i> , 2011)
Nanocrystalline TiO <sub>2</sub>	Symmetrical and unsymmetrical squaraine dyes	A series of novel symmetrical and unsymmetrical squaraine dyes have been synthesized and their comparative efficiencies as photosensitizers in dye-sensitized solar cells (DSSCs) containing nanocrystalline TiO <sub>2</sub> photoelectrodes have been investigated.	DSSCs employing unsymmetrical squaraines as sensitizers produced photocurrent with much higher efficiencies compared to DSSCs containing symmetrical squaraines.	(ALEX <i>et al.</i> , 2005)

In addition, there is also a wide range of extra modification techniques that have produced visible-light sensitive catalysts, such as self-doping ( $\text{Ti}^{3+}$  self-doping of  $\text{TiO}_2$ ), surface-modified catalysts, shape-controlled photocatalysts (with preferred exposed facets), etc.(BOYJOO *et al.* 2017; QI *et al.* 2014; XING *et al.* 2013; SUN *et al.* 2010).

Moreover, plasmonic photocatalysts have also received growing interest based on the plasmon effect of surface deposited noble metals (KALE *et al.*, 2014; ZHANG *et al.*, 2013). Lately, graphitic carbon nitride and other metal-free photocatalysts have also attracted extensive attention in visible light photocatalysis (NIDHEESH 2017; BOYJOO *et al.* 2017; BETHI *et al.* 2016; CAO *et al.* 2015; SUN *et al.* 2014).

Besides band-gap engineering, there are other two fundamental approaches for enhancement of photocatalytic activity: minimizing charge carrier recombination, and promotion of the forward reaction and adsorption of reactants through the provision of adequate quality and quantity of active sites (LEARY, 2011).

The combination of carbonaceous materials with conventional photocatalysts, like  $\text{TiO}_2$ , has proven to enhance visible-light activity by addressing these key areas: narrowing the band-gap, enhancing adsorption properties and extending the lifetimes of the photo-generated charge carriers (LEARY *et al.*, 2011; SUAVE *et al.*, 2017a; RATOVA *et al.*, 2018).  $\text{TiO}_2$ /carbon composites presented improved photocatalytic activity, in which carbon materials act as adsorbents, supports, electron sinks for the hindrance of charge carrier recombination or as the photosensitizer to generate a greater density of electron/hole pairs (LEARY & WESTWOOD, 2011; NGUYEN-PHAN *et al.*, 2011; SUAVE *et al.*, 2017b).

Conventional carbonaceous materials such as carbon black, graphite and graphitized materials have long been used as adsorbents and in heterogeneous catalysis particularly as supports for precious metal particles (BAHOME *et al.* 2005; MENG *et al.* 2011; LEARY & WESTWOOD 2011). Different opportunities increased with the advance of nanostructured carbons such as carbon nanotubes, [60]-fullerenes, graphene, etc. (MENG *et al.* 2011; BAHOME *et al.* 2005; CHUNG *et al.*, 2013; HAN *et al.* 2007; FARALDOS & BAHAMONDE 2017).

## 2.3 Overview of Solar Photoreactors

Conventional water (and wastewater) treatment photocatalytic reactors can be classified in two different groups regarding the catalyst distribution: in fluidized (or slurry) reactors, catalysts are freely suspended particles in aqueous solution, while in fixed bed reactors they are immobilized on rigid surfaces. It is consensual that slurry reactors are usually more efficient, although the penetration depth of the light into the suspensions may be limited, and the catalyst particles must be separated prior to the discharge of the treated water.

Despite the specific efficiency loss, the development of supported catalysts is of greater interest since the simple reutilization of the supported catalyst contributes to a higher performance of the overall process and publications in this field are increasing (MAUČEC *et al.*, 2017; MIARALIPOUR *et al.*, 2018; PASSALÍA *et al.*, 2017; SHI *et al.*, 2017; SINGH *et al.*, 2013), although the surface area is minimized and the reaction rate may be limited by mass transport of the pollutant to the catalyst surface (RAY, 2009; SPASIANO *et al.*, 2015).

Aside from conventional reactor design parameters, the major challenge in designing photocatalytic reactors is stated as the efficient illumination of the catalyst. This reactor configuration and design affect the absorption of photons, their distribution inside the reactor, and thus the photocatalytic treatment efficiency (ALFANO *et al.*, 2000; BOYJOO *et al.*, 2017; IBHADON *et al.*, 2013; RAY, 2009; SPASIANO *et al.*, 2015).

### 2.3.1 Photocatalytic efficiency measurement

It is therefore important to establish an efficiency parameter in order to compare the performance of different reactors configurations (DE LASA *et al.*, 2016; MANASSERO *et al.*, 2017). Finding a simple yet robust parameter to measure the efficiency of photocatalytic processes is not straightforward since it involves a multi-photon process in parallel with a radical chain reaction (OHTANI, 2010). Even though there is still not a clear consensus in the best option, the most used efficiency benchmarks are shortly defined and examined.

The quantum yield (QY) or quantum efficiency can be the most adequate parameter in order to evaluate the efficiency of the photocatalytic process (SATUF *et al.*, 2007). The

QY is expressed as the rate of a reaction (molecule s<sup>-1</sup> or mol s<sup>-1</sup>) induced by photon absorption divided by the flux of absorbed photons (photon s<sup>-1</sup> or Einstein s<sup>-1</sup>; an Einstein is a mole of photons); more simply, it is the number of molecules (or moles) reacted or produced divided by the number of photons (or Einsteins) absorbed (SPASIANO *et al.*, 2015).

Nonetheless, it can be difficult to determine the number of absorbed photons and therefore, apparent quantum efficiency (photonic efficiency) has often been used instead of quantum efficiency (OHTANI, 2010). The photonic efficiency relates the moles of reactant molecules degraded per mol of incident photons (MANASSERO *et al.*, 2013, MANASSERO *et al.*, 2017; MOTEGH *et al.*, 2012).

It is noteworthy that both quantum efficiency and photonic efficiency depend on the irradiation wavelength and occasionally on the irradiation intensity (DE LASA *et al.*, 2016; OHTANI, 2010), and thereby the efficiency data should be reported with corresponding wavelength and intensity.

In this sense, such measurement should be preferably performed by monochromatic irradiation (OHTANI, 2010). However, since a wide range of multi-wavelength radiation sources (mercury-vapor lamps, xenon lamps, light emitting diodes - LEDs, natural solar irradiation, etc.) is used in visible photocatalytic processes, efficiency comparison is often compromised.

Recently, Leblebici *et al.* (2015) used a new figure of merit, the photocatalytic space-time yield (*PSTY*), in order to compare 12 photocatalytic reactor designs. This benchmark measures the effects of reaction rate, mass and photon transfer rate, and light utilization efficiency on the specific volumetric yield of these reactors. The overall *PSTY* (eq. 2.1) is defined as the ratio of space-time yield (*STY*) to the lamp power, *LP*, the standardized electricity expenditure of lamps (LEBLEBICI *et al.*, 2015):

$$PSTY \left( \frac{m^3 \text{ wastewater}}{m^3 \text{ reactor} \cdot \text{day} \cdot kW} \right) = \frac{STY}{LP} \quad (2.1)$$

The *STY* can be calculated by the inverse of passage time and can be standardized to the desired pollutant removal extent (LEBLEBICI *et al.*, 2015). However, it may not be

easy to find data published with the same pollutant removal extent in order to perform this comparison.

### **2.3.2 Reactors designs**

This section addresses the main photocatalytic reactors designs and improved photons-absorption approaches. Table 2.3 provides selected examples of conventional slurry and fixed bed photocatalytic reactors used in environmental applications, highlighting the processes employed (catalyst and radiation source), the types of reactor, and the main results achieved.

**Table 2.3-** Selected examples of conventional slurry and fixed bed photocatalytic reactors used in environmental applications.

<i>Process employed</i>	<i>Reactor</i>	<i>Main Results</i>	<i>Ref.</i>
Photocatalytic degradation of the pharmaceutical drug clofibric acid (CA) under UV radiation with TiO <sub>2</sub>	(i) slurry reactor (SR); (ii) fixed-film reactor (FFR) with TiO <sub>2</sub> immobilized onto the reactor window; and (iii) fixed-bed reactor (FBR) filled with TiO <sub>2</sub> -coated glass rings.	In the best conditions, the quantum efficiency was SR: 4.59 %, FBR: 2.96% and FFR: 2.02%, while photonic efficiency was SR: 1.68%, FBR: 0.54% and FFR: 0.64%.	Manessero et al, 2017 a
Photocatalytic degradation of the pharmaceutical drug clofibric acid (CA) under UV radiation	Fixed-bed reactor filled with TiO <sub>2</sub> -coated glass rings	A kinetic model that takes into account radiation absorption by means of the local surface rate of photon absorption (LSRPA) has been developed. Degradation of CA reached 40 % in 660 min of reaction.	Manassero, 2017 b
UV-A and visible light irradiated processes (ZnO/H <sub>2</sub> O <sub>2</sub> ; Fe/TiO <sub>2</sub> /H <sub>2</sub> O <sub>2</sub> ) for photodegradation of commercial pesticides (neonicotinoids) in synthetic wastewater.	Annular slurry photoreactor.	Fe/TiO <sub>2</sub> /H <sub>2</sub> O <sub>2</sub> (Fe/TiO <sub>2</sub> catalyst with 7.2% Fe w/w) was the most efficient process studied, with conversions of 100% and 46% after two hours of irradiation with UV-A and visible light, respectively.	Banić et al, 2016
An immobilized photocatalytic system to remove pharmaceutical components (chlorhexidine digluconate, ibuprofen, atenolol, carbamazepine) from synthetic wastewater.	Packed bed photoreactor (PBPR) with TiO <sub>2</sub> nanoparticles immobilized on calcium alginate beads.	Lower degradation efficiency when compared with slurry photocatalysis; catalyst could be reused without losing its effectiveness for at least five cycles (the main advantage to making the process more cost-effective than the slurry system).	Sarkar, 2015



<p>Visible light active N-doped TiO<sub>2</sub> photocatalyst supported on glass spheres for the degradation of organic pollutants in wastewater</p>	<p>Continuous flat-plate fixed bed photoreactor with visible light active N-doped TiO<sub>2</sub> photocatalyst supported on glass spheres.</p>	<p>Design and implementation of the reactor; optimization of catalyst formulation; flat plate geometry was chosen to maximize the exposure of the catalyst to the light sources.</p>	<p>Vaiano et al, 2015</p>
<p>Degradation of pesticides (monocrotophos, endosulfan, chlorpyrifos) by solar photocatalysis with TiO<sub>2</sub> coated polystyrene beads.</p>	<p>Packed bed photoreactor with TiO<sub>2</sub> coated polystyrene beads.</p>	<p>50% of the initial pesticide concentration was removed in the early stage (1 h); aeration enhanced pesticide removal by 10–20%.</p>	<p>Sivagami et al. 2014</p>

Another significant impediment to the development of efficient photocatalytic reactors is the establishment of effective reactor designs for large-scale use, as demanded by industrial and commercial applications. Real-scale processes must be efficient yet cost-effective, and reaching an optimum point maybe challenging.

Therefore, different reactors designs have been studied in order to reach the desired equilibrium between efficiency and cost-effectiveness in artificial visible light processes and solar irradiated technologies. Optical fiber photoreactors have caught attention due to their illumination efficiency and the possibility of achieving effective light delivery to the catalyst particles while maintaining a uniform distribution of light (INDERMÜHLE *et al.*, 2016).

In optical fibers reactors, the catalyst is typically coated onto stripped fibers, therefore it is a variation of fixed bed reactors. As light is propagated along the fiber length by reflection by the fiber wall, a portion of the light is refracted rather than reflected. The refracted portion, which is dependent on the refractive index of the fiber wall and catalyst coating, will then be absorbed by the catalyst, which is subsequently activated (DIEHM *et al.*, 2014). Optical fibers thus act as both the light distributor and the photocatalyst support (DANION *et al.*, 2004).

Membrane photocatalytic reactors have also arisen as possible technologies for photocatalysis scaling-up. These hybrid systems couple photocatalysis with membrane separation processes, and therefore can achieve higher removal rates of organic pollutants (MOZIA, 2010; GANIYU *et al.*, 2015). These reactors, however, do not improve photons absorption and therefore will not be discussed with further details and examples in this section.

Recently, micro-photoreactors have gained special attention due to the rapid development and application of microfluidic devices (RUSSO *et al.* 2016). Besides being easily scalable (GORGES *et al.*, 2004; REIS & LI PUMA, 2015; ZHANG *et al.*, 2017), researchers stated that the advantages of microreactors include efficient heat and mass transfer, shorter reaction times, high surface-area-to-volume ratios, high yield and selectivity, reduced consumption of reagents and solvents, highly controlled process conditions (fluid behavior approaches the plug flow regime), reduced materials costs,

easiness of integration with laboratory analytical methodologies and increased safety (GORGES *et al.*, 2004; RUSSO *et al.*, 2016; RUSSO *et al.*, 2016b).

Microphotoreactors were used to perform photochemical transformations and to outperform classical photoreactor designs (COLMENARE *et al.*, 2017; ZHANG *et al.*, 2017). In environmental applications, however, they have been used for direct photolysis of contaminants under UV irradiation at 254 nm (RUSSO *et al.*, 2016; RUSSO *et al.*, 2016b) and there are few works reported using visible-light photocatalytic processes (STRAATHOF *et al.*, 2016; MARINHO *et al.*, 2017). However, researchers suggest that microreactors with immobilized catalysts can be the breakthrough which will lead to photocatalytic process at the industrial scale (LEBLEBICI *et al.*, 2015; RUSSO *et al.*, 2016; RUSSO *et al.*, 2016b).

Table 2.4 presents some examples of new trends of photocatalytic reactors used for environmental applications, highlighting the processes employed, the types of reactor, and the main results achieved.

Comparing the works of Marinho *et al.* (2017) and Machado *et al.* (2015), for example, we can see that both works studied the reduction of Cr(VI) although they were performed in completely different processes conditions. The photonic efficiency for the photochemical Cr(VI) reduction reported by Machado and coworkers in a spiral-shaped reactor was 2.52% while the TiO<sub>2</sub> photocatalytic process with the use of the innovative micro-mesostructured reactor achieved complete Cr(VI) reduction and 3.96% of photonic efficiency under simulated solar irradiation.

Even though the processes were performed in different conditions, the photocatalytic processes were performed at simulated solar irradiation while the photochemical was assessed at UV conditions. Although the microreactor presented a higher complexity design than the proposed SSR reactor, the photocatalytic process achieved higher efficiency and therefore the use of micro-reactors with immobilized catalysts could be a possible solution towards visible-light photocatalysis. In order to obtain conclusive information, further cost-benefit analysis must be performed to evaluate the economic feasibility of scaling-up such microreactors.

**Table 2.4-** Examples of new trends of photocatalytic reactors for environmental applications.

<i>Process employed</i>	<i>Reactor</i>	<i>Main Results</i>	<i>Ref.</i>
Cr(VI) reduction under simulated solar light ( $41 \text{ W}_{\text{UV}} \cdot \text{m}^{-2}$ ) TiO <sub>2</sub> photocatalysis, in the presence of different sacrificial agents	Micro-meso-structured-reactor (NETmix ) constructed with cellulose acetate sheet coated with a TiO <sub>2</sub> thin film. Illuminated surface per unit of volume inside the reactor of $470 \text{ m}^2 \text{ m}^{-3}$ and 1.36 g TiO <sub>2</sub> per liter of liquid inside the reactor.	Fast and complete Cr(VI) reduction: the maximum reduction rate was attained using tartaric acid and 3.96% of photonic efficiency was achieved.	(MARINHO <i>et al.</i> , 2017)
TiO <sub>2</sub> photocatalysis for <i>n</i> -decane oxidation at gas phase under simulated solar irradiation	Micro-meso-structured-reactor constructed with cellulose acetate sheet coated with a TiO <sub>2</sub> thin film with equivalent of 1.95 g of TiO <sub>2</sub> per liter of air and illuminated surface per unit of volume inside the reactor of $349 \text{ m}^2 \text{ m}^{-3}$ .	No catalyst deactivation was observed after 72 h of continuous use.	(DA COSTA FILHO <i>et al.</i> , 2017)
Photochemical reduction of Cr(VI) with UV tubular fluorescent lamps (Xelux 8 Watt, 16 mm diameter, $2.5 \text{ mW cm}^{-2}$ ) in the presence of ethanol	Spiral-shaped reactor (SSR) - only UV photolysis.	The designed reactor was effective when applied to real wastewater, showing a total Cr(VI) reduction of 51.8% and photonic efficiency of 2.52% and its configuration is	(MACHADO <i>et al.</i> , 2015)

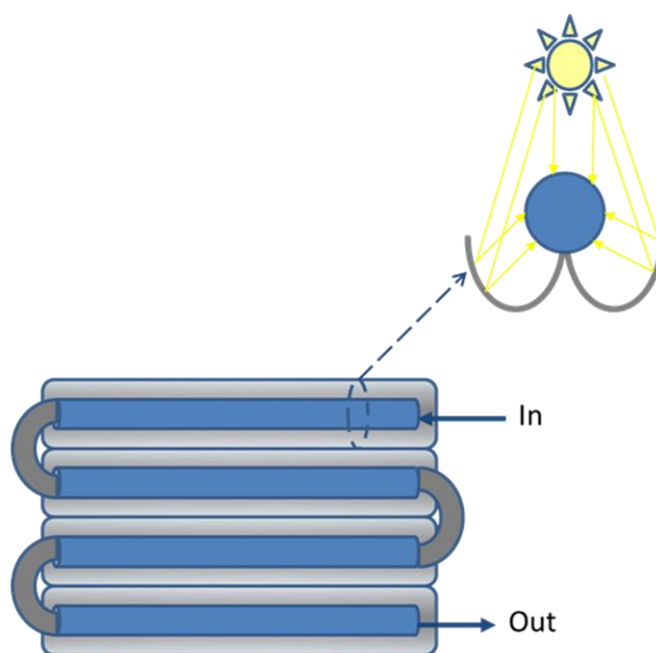
		suitable for scale up.	
Photocatalytic degradation of hydroxybutanedioic acid.	TiO <sub>2</sub> -coated optical fiber photoreactor.	30% degradation after 5 h irradiation in a multi-optical fiber reactor.	(DANION <i>et al.</i> , 2004)
Photocatalytic degradation of malic acid.	TiO <sub>2</sub> -coated optical fiber photoreactor.	75% maleic acid removal and 21% TOC removal after 20 h.	(DANION <i>et al.</i> , 2007)

### 2.3.3 Solar photoreactors for water and wastewater treatment

Solar reactors used for water and wastewater treatment can be categorized as concentrating solar reactors and non-concentrating solar reactors. In the late 1990s, researchers concluded that, for solar water treatment purposes, highly concentrated direct UV radiation was unnecessary, if both direct and diffuse light was used, and therefore came up with the Compound Parabolic Collector (CPC), which have been, since then, the most studied photoreactor for solar water and wastewater treatment (MALATO *et al.*, 2009b; SPASIANO *et al.*, 2015), although mainly by photo-Fenton based processes.

A schematic illustration of a CPC photoreactor is shown in Figure 2.5, where it is possible to see the details of the compound parabolic collectors and the schematic effect of utilization of both direct and diffuse irradiation.

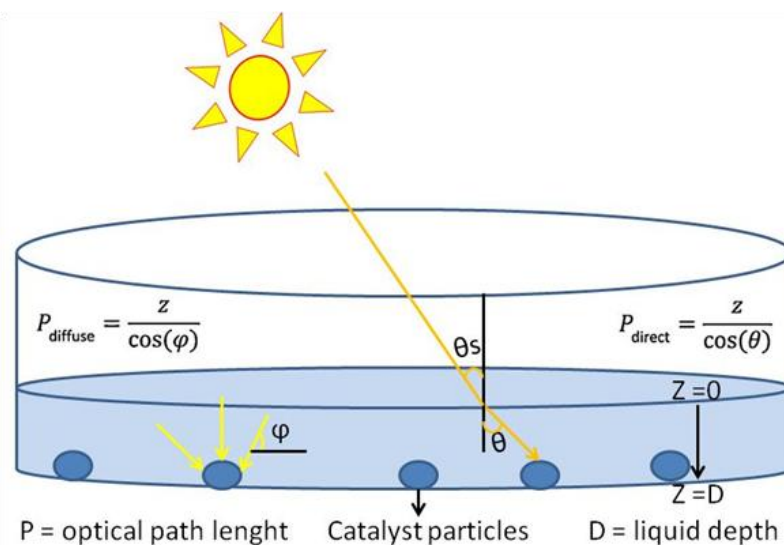
**Figure 2.5-** Behavior of incident solar radiation on a CPC reactor (upper), and CPC solar photoreactor schematic illustration (lower).



Nevertheless, the main drawback in the commercial-scale application of these techniques is the cost (CARRA *et al.*, 2014). In this context, raceway pond reactors (RPRs) have recently been studied as solar photo-Fenton reactors in order to degrade low concentration pollutants, such as contaminants of emerging concern in drinking waters or in wastewater treatment plant (WWTP) effluents (CARRA *et al.*, 2014).

As a tertiary treatment, the need for effective radiation distribution and sufficient radiation density decreases, since the pollutant concentration is at least a thousand times lower, and the usual concentration of HO<sup>•</sup> radicals attained in tubular CPC photoreactors would be higher than necessary. As a result, simpler and less costly photoreactors could be used for this application (RIVAS *et al.*, 2015). Figure 2.6 illustrates the paths of direct and diffuse sunlight in a photocatalytic reactor.

**Figure 2.6-** Schematic view of direct and diffuse sunlight paths in RPR photocatalytic reactor. Adapted from (RIVAS *et al.*, 2015).



RPRs are simple and extensive non-concentrating photoreactors with channels through which the water is recirculated (RIVAS *et al.*, 2015). They are made of low-cost materials, mainly plastic liners. Additionally, the power requirements for mixing are small, typically around 4 W m<sup>-3</sup>. Due to their flexibility and easy scale-up, raceway reactors are the most commonly used systems for microalgal applications.

Their reported production costs are markedly lower than those for tubular photobioreactors, such is the case for fuel production from microalgae, and much lower than traditional CPCs (RIVAS *et al.*, 2015). For example, Carra *et al.* (2014) reported that the cost for the installation and purchase of a large scale CPC plant has been estimated at 400 € m<sup>-2</sup>, while around 10 € m<sup>-2</sup> for RPR solar reactors (XU *et al.*, 2013).

RPR reactors have been mainly studied for photo-Fenton reactions (CABRERA-REINA *et al.*, 2019; CABRERA REINA *et al.*, 2015; CARRA *et al.*, 2015; DA COSTA *et al.*, 2018) and researchers have recently compared the feasibility of the treatment of industrial wastewater by solar

photo-Fenton in RPR and CPC reactors. While comparing the treatment capacity related to the photoreactor investment (mg of dissolved organic carbon removed/€ m<sup>2</sup>) the authors observed differences as much as two orders of magnitude favorable to the RPR, which demonstrates the potential application of these reactors for the treatment of industrial wastewater by solar photo-Fenton (CABRERA-REINA *et al.*, 2019).

Studies with photocatalytic processes in RPR reactors are scarce and recently, Amiri *et al.*, (2018) studied the solar TiO<sub>2</sub> photocatalytic degradation of Chlorpyrifos in a natural agriculture runoff at circumneutral pH and achieved 80% of the pollutant removal in slurry configuration (AMIRI *et al.*, 2018). Further researches involving the use of RPR reactors with fixed-bed (or fixed-film) photocatalytic configurations are necessary.



## **2.4 Surface engineering and photocatalytic surfaces**

Photocatalytic surfaces attracted growing interest and reached industrial application due to the wide range of possible applications, including self-cleaning surfaces (BANERJEE; DIONYSIOU; PILLAI, 2015; PAL *et al.*, 2016), anti-fogging coatings (KAYANI *et al.*, 2016), anti-reflective coatings (KAYANI *et al.*, 2016), antimicrobial surfaces (MURANYI; SCHRAML; WUNDERLICH, 2010), electrodes for hydrogen evolution (NAKATA & FUJISHIMA, 2012), catalysts for air purification (VERBRUGGEN, 2015) and catalysts for water treatment (RATOVA *et al.*, 2017).

Their self-cleaning properties, achieved via photo-induced hydrophilicity, may be the most famous achievement. When a photocatalytic surface is exposed to sufficient irradiation, its surface exhibits hydrophilicity (also known as wettability). Water droplets spread over hydrophilic surfaces and form a thin film of water. During the process of spreading, dirt on the surface is washed away and, therefore, these materials are known as self-cleaning surfaces (FUJISHIMA *et al.*, 2008). There is a variety of different physical and chemical processes that can be used to create a photocatalytic surface, mainly studied by surface engineering.

Surface engineering is the science that studies physical and chemical processes for the modification of the surface of a material in order to increase performance, reduce costs and/or control surface properties. It can be used to develop a wide range of functional properties, including physical, chemical, electrical, optical, electronic, magnetic, mechanical, wear-resistant and corrosion-resistant properties at the required substrate surfaces.

Creating a photocatalytic surface implies in changing the substrate superficial optical properties. There are several processes available for the deposition of photocatalytic coatings on a wide range of substrates (e.g. sol-gel, hydrothermal method, electron beam evaporation, sputtering, etc.), among which physical vapor deposition (PVD) processes are of growing interest. PVD process can be simplified as the evaporation (or sputtering) of coating material from a solid source (also known as the target) under a partial vacuum. The vapor phase created is transported to the substrate and the interest material condensates onto the substrate surface.

Magnetron sputtering is a well-established PVD technique for the deposition of metallic and ceramic coatings onto various supports. This process is widely used for the deposition of thin films

in both laboratories and industrial production facilities and is readily scalable. It presents a number of advantages, including large area uniformity, good control over chemical and morphological properties and high reproducibility (RATOVA *et al.* 2013).

Conventional magnetron sputtering, however, may not be able to deposit anatase crystalline materials onto polymeric supports due to high temperature and/or post-deposition annealing requirements (SINGH *et al.*, 2013). Alternatively, high power impulse magnetron sputtering (HiPIMS) has proven able to deposit photocatalytically active titania coatings directly onto flexible polymeric substrates in a single stage process (KELLY *et al.*, 2014; RATOVA *et al.*, 2014).

High Power Impulse Magnetron Sputtering (HiPIMS) is a relatively new technology that helps to avoid the limitation in maximum power applied to the target (KOUZNETSOV *et al.* 1999) observed in conventional sputtering processes. In HiPIMS, the power is applied to the target using high peak voltages and very high peak powers at low duration, which results in low average power and low duty cycle. This mode of operation results in the generation of ultra-dense plasmas with unique properties, such as a high degree of ionization of the sputtered atoms. These features make possible the deposition of dense and smooth coatings on complex-shaped substrates, and provide new and added parameters to control direction and energy of the sputtering flux (ANDERS, 2014; SARAKINOS *et al.*, 2010).

The HiPIMS technology is also reported to improve target utilization (HOVSEPIAN *et al.* 2014) and is proven to be suitable for obtaining as-deposited crystalline coatings, including those on temperature sensitive substrates, as the low duty imparts a lower thermal flux to the substrate compared to DC or pulsed DC sputtering at the same time-averaged power (KELLY *et al.*, 2014; RATOVA *et al.*, 2014). Selected research papers on photocatalytic coatings deposited by HiPIMS are summarized in Table 2.5.

**Table 2.5 - Summary of selected data on photocatalytic coatings deposited by HiPIMS.**

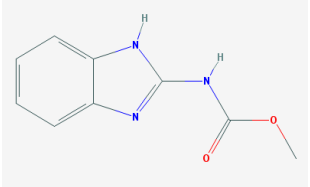
Surface	Main methodology	Main results	Reference
N doped ZnO thin films coated on glass and copper substrates	Reactive HiPIMS of a pure Zn target in Ar/N <sub>2</sub> /O <sub>2</sub> gas mixture with constant mass flow rates of 20, 10 and 1 sccm and a total gas pressure of 6.66 Pa. Unipolar short voltage pulses (10 μs duration), with an amplitude of 1 kV and very high instantaneous power density (~ 4 kW/cm <sup>2</sup> averaged over the racetrack area) were applied to the magnetron cathode, ranging the repetition frequency values over 350–800 Hz. The obtained films were studied in as-deposited state and after annealing at 500 °C in a N <sub>2</sub> atmosphere. The content of N atoms in the deposited films was changed from 0 at.% to 6 at.% by the HiPIMS pulsing frequency. Thin film characterized by AFM, XPS, XRD, UV–Vis and Raman spectroscopy.	The energy band-gap decreased with the content of nitrogen from 3.3 eV to 1.67 eV. Post-deposition annealing of the films improved noticeably the photocatalytic activity. Optimum visible-light photocatalytic activity was achieved by the ZnO <sub>x</sub> N <sub>y</sub> film with 3.4 at.% N. No degradation of pollutants assessed. Only photo-electrochemical and photo-current measurements during visible light on/off irradiation cycles.	(TIRON <i>et al.</i> , 2016 a)
Amorphous titanium oxide (TiO <sub>x</sub> ) thin films with variable stoichiometry (x < 2) Coatings are crystalline and photocatalytically active in as-deposited condition. deposited on quartz and glass substrates	The reactive HiPIMS operated in multi-pulse mode (m-HiPIMS) of a pure Ti target in Ar/O <sub>2</sub> gas mixture (0.2% O <sub>2</sub> of the total mass flow rate). The m-HiPIMS employed a pulsing scheme consisting in repetition with low frequency (400–800 Hz) of sequences of three consecutive very short individual micro-pulses (5 μs in width) spaced by a delay time of 50 μs. Contact angle measurements.	At the repetition frequency of 800 Hz, the m-HiPIMS deposition produced TiO <sub>x</sub> thin films with a high deficit of oxygen, enhanced electrical conductivity and strong absorption of visible light. The as-deposited thin films showed a weak photocatalytic activity. However, after isothermal treatment at 723 K, in argon, the photocatalytic activity has been considerably improved. This improvement may be attributed to the formation of TiO <sub>2</sub> anatase and Ti <sub>4</sub> O <sub>7</sub> phases in the deposited films.	(TIRON <i>et al.</i> , 2016 b)
W-doped and pure titania coatings deposited in HiPIMS mode onto soda lime glass substrates	Ti-5 at.% W alloy target. Ar:O <sub>2</sub> atmosphere at a pressure of 0.33 Pa, with the gases flow fixed as 2:3, respectively. Pulse frequency of 200 Hz and pulse width of 100 μs. The mean power during the pulse was varied from 30 to 44 kW. Photocatalytic activity was assessed in terms of the degradation rate of methylene blue dye.	The coatings were weakly crystalline and showed mixed anatase/rutile structures in the as-deposited condition. W-doped coatings showed enhanced activity in fluorescent and visible light due to shift on band-gap.	(RATOVA <i>et al.</i> , 2014)
Titania coatings deposited onto soda lime glass substrate and after com polymeric substrates (polyethylene terephthalate and polycarbonate)	Ti target. Sputtering was carried out in an Ar:O <sub>2</sub> atmosphere of 2:3 (10 sccm of Ar and 15 sccm of O <sub>2</sub> ). Pressure: 0.13 to 0.93 Pa. Pulse frequency: 100–300 Hz. Pulse width: 50–200 μs. Photocatalytic activity was assessed in terms of the degradation rate of methylene blue dye.	The ability to deposit crystalline titania with photocatalytic functionality at temperatures low enough to enable the use of polymer substrates is a significant advancement in the field. It could potentially allow the production of high volumes of photocatalytic material on flexible and inexpensive substrates.	(RATOVA, <i>et al.</i> , 2014b)

## 2.5 Model Contaminants of Emerging Concern: Carbendazim and Caffeine

Carbendazim or methyl N-(1H-benzimidazol-2-yl) carbamate (CBZ - C<sub>9</sub>H<sub>9</sub>N<sub>3</sub>O<sub>2</sub>) is a systemic benzimidazole fungicide highly consumed worldwide (YANG *et al.*, 2017). Under natural environmental conditions, it is very stable and it has been frequently detected in waters (from 0.000165 µg.L<sup>-1</sup> to 156 µg.L<sup>-1</sup>) (CAMPO *et al.*, 2013; GROS *et al.*, 2017; MONTAGNER *et al.*, 2014a; YANG, Y. *et al.*, 2017) and its utilization is currently prohibited in the European Union (ROUSIS *et al.*, 2017). CBZ is considered as a “priority hazard substance” by the Water Framework Directive of the European Commission (SAIEN & KHEZRIANJOO, 2008) and it is also classified as Group C - Possible Human Carcinogen by (USEPA, 2006).

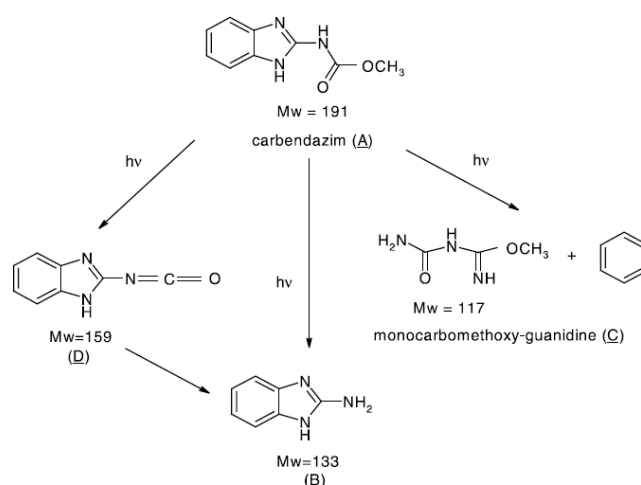
Moreover, it increases estrogen production in humans and therefore may have endocrine disruptor properties (MCKINLAY *et al.*, 2008; MORINAGA *et al.*, 2004). This endocrine disruptor potential was investigated in vitro through aromatase activity of a human ovarian granulosa-like tumor cell line test (MORINAGA *et al.*, 2004) and intensification of estrogen production was observed. Table 2.6 presents the main physical-chemical properties of CBZ.

**Table 2.6** – Physico-chemical properties of carbendazim.

<i>Properties</i>	<i>Carbendazim</i>
Molecular structure	
CAS number	58-08-2
Molecular formula	C <sub>9</sub> H <sub>9</sub> N <sub>3</sub> O <sub>2</sub>
Molecular weight	191.187 g·mol <sup>-1</sup>
Solubility in water (20°C)	8 mg·L <sup>-1</sup>
pKa	4.29

Even though CBZ is a stable molecule in the dark or in environmental conditions, Boudina *et al.* (2003) studied the photochemical behavior of CBZ in aqueous solution by photolysis using both UV light source (high-pressure mercury arc lamp) and a solar light simulator (xenon arc lamp). The authors proposed a photodegradation pathway, which is shown in Figure 2.7 (BOUDINA *et al.*, 2003).

**Figure 2.7-** Proposition of photodegradation pathway of carbendazim in aqueous solution, reproduced from Boudina *et al.*, (2003).



One of the byproducts commonly found in CBZ photochemical degradation is identified as the 2-aminobenzimidazole (2-AB) and presents protonated mass ( $M+H^+$ ),  $m/z$ , of 134 ( $M_w=133$  in Figure 2.7). Boudina and coworkers also found protonated molecular ion peak ( $M+H^+$ ) at  $m/z$  160, that can be attributed to the Benzimidazole isocyanate ( $M-CH_3OH$ ) degradation product ( $C_8H_6N_3O$ ;  $M_w=159$  in Figure 2.7).

Monocarbomethoxy-guanidine is also a reported byproduct of photochemical transformation of CBZ ( $M_w=117$  in Figure 2.7) and can also persist in the environment (BOUDINA *et al.*, 2003; MALLAT *et al.*, 1997; TOMLIN, 2004). Table 2.7 summarizes researches involving the occurrence of this pesticide in different real water matrices, showing that this molecule really persists in the aquatic environment.

**Table 2.7** – Summary of selected data on the occurrence of Carbendazim in diverse water matrices.

Water Matrix	Location	Concentration ( $\mu\text{g}\cdot\text{L}^{-1}$ )	Reference
Surface water	Júcar River basin, Spain	7.939	(AGUILAR <i>et al.</i> 2017)
Wastewater and surface waters	Spain and Italy	Identified but not quantified	(ROUSIS <i>et al.</i> 2017)
Irrigation waters	Peri-urban area of Barcelona, Spain	0.053 – 2.411	(MARGENAT <i>et al.</i> 2017)
Surface water	Dourados, Brazil	N.D.	(ROCHA <i>et al.</i> 2015)
Surface and drinking waters	São Paulo, Brazil	0.003 – 0.781 (surface water) 0.009 (drinking water)	(MONTAGNER <i>et al.</i> 2014a)
Saline water	Adriatic sea	0.000165 – 0.00113	(LOOS <i>et al.</i> 2013)
Surface water	São Lourenço, Brazil	N.D. – 12	(RIBEIRO <i>et al.</i> 2013)
Surface and ground waters	La Rioja, Spain	N.D.	(HERRERO-HERNÁNDEZ <i>et al.</i> 2013)
Surface water	Uruguay and Spain	N.D. – > 0.5	(PAREJA <i>et al.</i> 2011)

Water Matrix	Location	Concentration ( $\mu\text{g}\cdot\text{L}^{-1}$ )	Reference
Surface and ground waters	Belgrade, Serbia	0.0076 – 0.216	(DUJAKOVIĆ <i>et al.</i> 2010)
Surface water	Lyon, France	0.1 ± 0.2	(RABIET <i>et al.</i> 2010)
Wastewater	Emmental e Chevilly, Switzerland	0.004 – 0.982	(BURKHARDT <i>et al.</i> 2007)
Surface water	Andalusia, Spain	0.16 – 5.50	(VEGA <i>et al.</i> 2005)
Surface water	Southern Chile	N.D. – 4.5	(PALMA <i>et al.</i> 2004)
Groundwater	Patagonia, Argentina	N.D. – 156.00	(LOEWY <i>et al.</i> 1999)

It is noteworthy that even though the use of carbendazim in European Union is not legalized since 2016 (ROUSIS *et al.*, 2017), it can be seen in Table 2.7 that it occurred in European countries (Spain and Italy) in recent works.

Caffeine (1,3,7-trimethylpurine-2,6-dione -  $\text{C}_8\text{H}_{10}\text{N}_4\text{O}_2$ ), on the other hand, is a natural alkaloid produced by many plant species and is the most used central nervous system stimulant (HSU, 2015). It is a constituent of a variety of beverages (coffee, tea, mate, guarana and caffeinated soft drinks) and of numerous food products (chocolate and pastries, for example), as well as many pharmaceutical products (RODRÍGUEZ-GIL *et al.* 2018). Although the human body is efficient at metabolizing this stimulant, between 0.5 – 10% (wt%) is excreted unchanged, mostly in urine (RODRÍGUEZ-GIL *et al.* 2018). In addition, caffeine from domestic use may reach the sewer system directly due to the disposal of unconsumed drinks (FERREIRA *et al.*, 2005).

Due to its important consumption, caffeine has been detected in wastewater (RODRÍGUEZ-GIL *et al.* 2018; VIVIANO *et al.* 2017; TERNES, 2001), surface water (RODRÍGUEZ-GIL *et al.* 2018; LOOS *et al.* 2017; LIN *et al.*, 2016), groundwater (LOOS *et al.* 2010), marine waters (PAÍGA & DELERUE-MATOS, 2017; ALI *et al.* 2017; GOH *et al.* 2017) and drinking water (LARDY-FONTAN *et al.* 2017; STACKELBERG *et al.* 2004) worldwide.

Table 2.8 summarizes researches involving the occurrence of this stimulant in different water matrices. It is interesting that concentrations of the stimulant vary in a wide range of concentrations, from below the limit of detection of the analytical method to  $147 \mu\text{g}\cdot\text{L}^{-1}$ .

**Table 2.8-** Summary of selected data on the occurrence of caffeine in diverse water matrices.

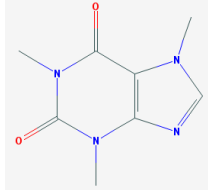
Water Matrix	Location	Concentration ( $\mu\text{g}\cdot\text{L}^{-1}$ )	Reference
Surface water	Danube River	0.087	(LOOS <i>et al.</i> 2017)
Saline water	Portuguese coastal waters	0.018 – 0.525	(PAÍGA & DELERUE-MATOS, 2017)
Saline water	Coastal waters of the Red Sea – Saudi Arabia	Higher than 3 (upper LOD)	(ALI <i>et al.</i> 2017)
Saline water	Coastal Singapore	From <LOD to 0.847	(GOH <i>et al.</i> 2017)
Wastewater	Northern Italy	$0.52 \pm 0.06$ to $21.8 \pm 9$	(VIVIANO <i>et al.</i> 2017a)
Drinking (bottled) water	France and other European countries	0.115	(LARDY-FONTAN <i>et al.</i> 2017)
Surface water	Taihu Lake, China	0.038	(LIN <i>et al.</i> , 2016)
Drinking water	Portugal	0.046	(GAFFNEY <i>et al.</i> , 2015)
Surface and drinking waters	United States of America	0.159 (surface water) and 0.116 (drinking water)	(PADHYE <i>et al.</i> 2014)
Groundwater	Europe	0.189	(LOOS <i>et al.</i> 2010)
Wastewaters and saline water	Atlantic Canada	From <LOD – 2.1	(COMEAU <i>et al.</i> 2008)
Surface, drinking, and waste waters	South Korea	0.01 – 0.194 (surface water) 0.023 - 0.776 (wastewater)	(KIM <i>et al.</i> 2007)
Surface waters	Romania	0.43 – 9.7	(MOLDOVAN, 2006)
Drinking water	United States of America	0.119	(STACKELBERG <i>et al.</i> 2004)
Saline water	North Sea	From <LOD - 0.0161	(WEIGEL <i>et al.</i> 2002)
Wastewater	Germany	147	(TERNES, 2001)

LOD = limit of detection of the analytical method.

Caffeine has been demonstrated to be chemically and photolytically stable and its content is not significantly reduced through traditional wastewater treatment (PADHYE *et al.* 2014; STACKELBERG *et al.* 2004). However, its removal by advanced processes is not completely known (FERREIRA *et al.*, 2005). It is noteworthy that carbendazim and caffeine present low quantum yield for solar photolysis degradation, which justifies its persistence in the environment (Tables 2.7 and 2.8).

Tertiary wastewater treatment efficiency must be evaluated by parameters different than COD (Chemical Oxygen Demand) and BOD (Biochemical Oxygen Demand) since organic matter is present at low concentrations. However, instead of monitoring dozens of different persistent pollutants by expensive analytical methods, caffeine molecule has been used as an indicator of anthropogenic pollution (DANESHVAR *et al.*, 2012; PAÍGA & DELERUE-MATOS, 2017; PEELER *et al.*, 2006; RODRÍGUEZ-GIL *et al.*, 2018; SEILER *et al.*, 1999; VIVIANO *et al.*, 2017) and, therefore, may be used as an indicator of photocatalytic tertiary wastewater treatment performance. Table 2.9 presents the main physical-chemical properties of caffeine.

**Table 2.9-** Physico-chemical properties of caffeine.

<i>Properties</i>	<i>Caffeine</i>
Molecular structure	
CAS number	10605-21-7
Molecular formula	C <sub>8</sub> H <sub>10</sub> N <sub>4</sub> O <sub>2</sub>
Molecular weight	194.194 g·mol <sup>-1</sup>
Solubility in water (25°C)	21600 mg·L <sup>-1</sup>
pKa (25°C)	14

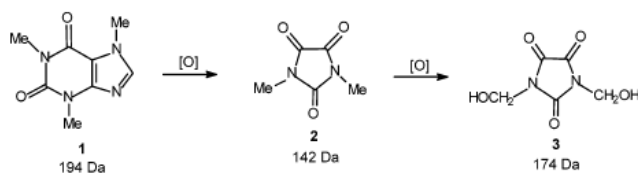
Dalmázio and coworkers (DALMÁZIO *et al.*, 2005) studied the effect of different advanced oxidation processes (UV/H<sub>2</sub>O<sub>2</sub>, TiO<sub>2</sub>/UV, and Fenton) on the degradation of caffeine and used electrospray ionization mass (ESI-MS) and high accuracy MS measurements to show that caffeine is first oxidized to N-dimethylparabanic acid likely via initial OH insertion to the C4dC8 caffeine double bond (DALMÁZIO *et al.*, 2005).

A second degradation intermediate, di(N-hydroxymethyl)parabanic acid, has been identified by ESI-MS and characterized by ESI-MS/MS and high accuracy mass measurements. This polar and likely relatively unstable compound is likely formed via further oxidation of N-dimethylparabanic acid at both of its N-methyl groups and constitutes an unprecedented intermediate in the degradation of caffeine. The proposed photodegradation pathway is divided into 3 schemes, which are shown in Figure 2.8.

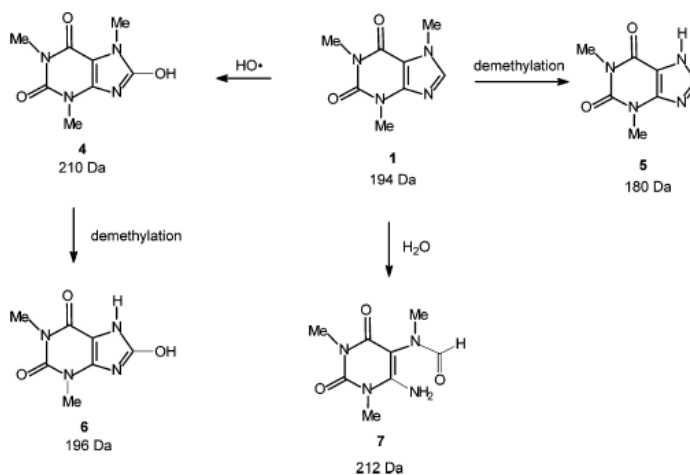


**Figure 2.8** – Photodegradation pathway proposed by Dalmázio *et al.* (2005).

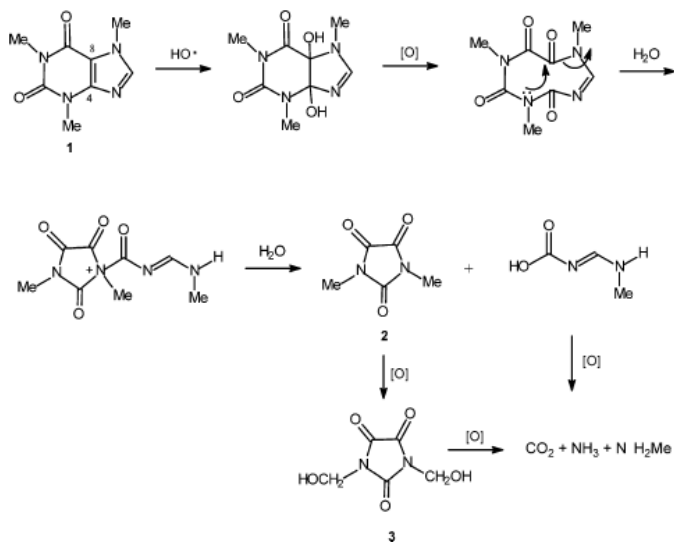
**SCHEME 1**



**SCHEME 2**



**SCHEME 3**



Selected research papers on photocatalytic degradation of the model pollutants of this research (carbendazim and caffeine) are summarized in Table 2.10.

**Table 2.10** - Summary of selected data on photocatalytic degradation of the studied model pollutants (carbendazim or caffeine) aqueous solutions.

Photocatalyst	Main methodology	Main results	Reference
Titania nanotubes films with 5–20 $\mu\text{m}$ length synthesized under galvanostatic anodization	Catalyst characterization: Scanning electron microscopy (SEM), Micro-Raman spectroscopy, diffuse reflectance spectra (Tauc-plot/band-gap). Degradation of 4 mL of aqueous solution of CAF ( $15 \text{ mg L}^{-1}$ ) for 4 hours. Irradiation source: four UV-A lamps – Sylvania GTE F15W/T8, 350–390 nm, $0.5 \text{ mW cm}^{-2}$	50% photocatalytic CAF degradation. Small dependence of photocatalytic efficiency on solutions pH attained. Titania nanotubes give reproducible activity after 10 photocatalytic cycles.	(ARFANIS <i>et al.</i> 2017)
Fe doped $\text{TiO}_2$ (suspended catalyst)	UV-A ( $\lambda_{\text{max}} = 365 \text{ nm}$ ) or solar radiation ( $600 \text{ W}\cdot\text{m}^{-2}$ , 11AM - 1PM). Catalyst load: $1 \text{ g}\cdot\text{L}^{-1}$ (2% Fe), pH = 6,3 (natural), $8 \text{ mg}\cdot\text{L}^{-1}$ CBZ, 300 minutes under solar radiation.	98% of CBZ degradation and 90% of TOC removal.	(KAUR <i>et al.</i> 2016)
$\text{ZnO}$ or $\text{TiO}_2$ - P25 Evonik Degussa (suspended catalysts)	Catalyst characterization: SEM, transmission electron microscopy (TEM), X-ray diffraction (XRD), FTIR Spectrometry and BET experiments ( $\text{N}_2$ adsorption-desorption isotherms). 100 mL of CAF aqueous solution ( $48.9 \text{ mg}\cdot\text{L}^{-1}$ )	$\text{ZnO}$ proved to be a fairly stable catalyst as its repeated use only resulted in a limited decrease of catalyst activity. CAF degradation-rate constant per specific surface area was $34 \times 10^5 \text{ g min}^{-1} \text{ m}^{-2}$ .	(BITENC <i>et al.</i> 2013)
Composites prepared with multi-walled carbon nanotubes and three different $\text{TiO}_2$ materials (suspended catalyst)	Catalyst characterization: Diffuse reflection infrared Fourier transformed (DRIFT), XRD, $\text{N}_2$ adsorption-desorption isotherms (BET), TEM and SEM. Irradiance: UV-A lamp $-\lambda > 350 \text{ nm}$ ; $50 \text{ mW cm}^{-2}$ for 3 hours. Catalyst load: $1 \text{ g}\cdot\text{L}^{-1}$ .	Films prepared with these composites revealed higher photocatalytic activity than films of commercial $\text{TiO}_2$ (Evonik). CAF degradation under photocatalysis.	(MARQUES <i>et al.</i> 2013)
$\text{TiO}_2$ (rutile) nanoparticles (suspended catalyst)	Catalyst characterization: XRD, BET, UV-vis spectrometry, TEM, FTIR. $50 \text{ mg L}^{-1}$ CAF solution under UV/Vis illumination source ( $\lambda > 350 \text{ nm}$ ; $27 \text{ mW}\cdot\text{cm}^{-2}$ ). $7.5 \text{ mg}$ of a $\text{TiO}_2$ sample was mixed with $7.5 \text{ mL}$ of the CAF aqueous solution inside a $10 \text{ mL}$ quartz reactor.	Synthesized rutile particles showed superior activity than commercial rutile particles in the presence of oxygen as an electron acceptor (oxygen flow). No photocatalytic activity was seen without the electron acceptor effect.	(KRIVEC <i>et al.</i> 2013)
$\text{TiO}_2$ -based solar photocatalysis (suspended catalyst)	Tertiary treatment to remove nine emerging pollutants ( $\text{ng}\cdot\text{L}^{-1}$ ) from wastewater treatment plant effluents, including CAF on $\text{TiO}_2$ photocatalysis resulted in significant removal of all CPC solar reactor. Real wastewater spiked with $5 \text{ mg}\cdot\text{L}^{-1}$ of each the emerging pollutants. In addition to this, the percentages CEC. Catalyst load: $0.2\text{-}0.5 \text{ g}\cdot\text{L}^{-1}$ . CAF was used as model of fecal bacteria elimination were close to 100% compound at laboratory scale.		(BERNABEU <i>et al.</i> 2011)

As seen in Table 2.10, there has been an interest in using caffeine as a model pollutant for photocatalytic activity experiments, since it is a photostable compound directly related to anthropogenic pollution. Carbendazim has also been used as a model contaminant of emerging concern in some works due to its inherent hazard. The majority of the published works, however, study the photocatalytic process with suspended catalyst (slurry reactor), where high efficiencies were achieved. The work of Arfanis et al. (2017), on the other hand, used photocatalytic films of titania nanotubes and was able to reach 50% of caffeine degradation under UV-A irradiation.

## 2.6 Photocatalytic Thin Film Characterization

### 2.6.1 Crystallographic characterization by Grazing Incidence X-ray Diffraction (GIXRD)

X-ray diffraction is a non-destructive technique used to measure the atomic arrangement of materials and therefore study the structure of crystalline materials (BIBI *et al.*, 2017; DUTTA *et al.*, 2000; GUO *et al.*, 2014). When a monochromatic X-ray beam hits a sample, in addition to absorption and other phenomena, the occurrence of coherent X-ray scattering is observed whereas X-ray scattering with the same wavelength as the incident beam is detected (HE, 2003). The coherent scattering of X-ray from a sample is a function of the electron distribution in the sample. As such, the intensity and spatial distributions of the scattered X-rays form a specific diffraction pattern which is the “fingerprint” of the sample (CHIU *et al.*, 2008; HE, 2003; HINRICHS, 2014).

This technique provides crystallographic information on phase identification, texture (orientation), unit cell (lattice) dimensions, crystal structure, etc., and it is widely used for crystallographic characterization of catalysts and photocatalytic surfaces (ÖSTERLE *et al.*, 2013; RATOVA *et al.*, 2017). Phase identification is one of the most important uses of X-ray diffraction techniques in materials characterization. The diffraction patterns of unknown samples can be identified by comparing them with the standard line patterns of the Powder Diffraction File Database (PDF) (TSENG *et al.*, 2015).

Conventional X-ray diffraction (XRD) consists of illuminating flat and polycrystalline samples with a monochromatic x-ray beam at different angles of incidence ( $\theta$ ) and evaluating the presence (or absence) of these x-rays in a detector installed in an angular position equivalent to that of illumination ( $\theta$  in relation to the surface of the sample and  $2\theta$  in relation to the incident beam) (HINRICHS, 2014).

Insofar as the angle of incidence and the angle of the detector change simultaneously (HE, 2003), only the crystallographic planes of the grains which are parallel to the surface and respect Bragg's equation (Eq. 2.2) contribute to the diffractogram. The Bragg's law equation (Eq. 2.2) allows calculation of the value of the crystal lattice spacing  $d$  by measuring the diffracted beam angle in XRD analysis:

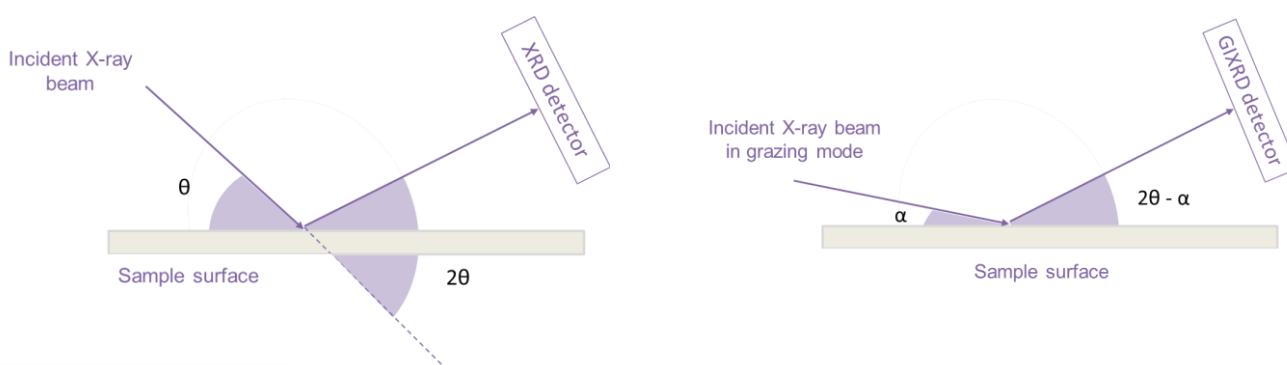
$$2d\sin\theta = n\lambda \tag{2.2}$$

where  $n$  is the diffraction order (usually 1);  $\lambda$  is the wavelength of the X-ray beam;  $d$  is crystal interplanar distance and  $\theta$  is the diffraction angle.

In a GIXRD measurement, the angle of incidence of the X-ray beam with respect to the sample surface,  $\alpha$ , is kept constant at a low value (between  $0.5^\circ$  and  $5^\circ$ ) and the detector is moved by a  $\beta$  angle through the angular range to be analyzed (SIMEONE *et al.*, 2013).  $\beta$  angle corresponds to  $2\theta - \alpha$ , but the obtained diffractogram is presented in the same form of conventional XRD, with  $2\theta$  in the abscissa, so that it can be compared with conventional X-ray diffraction results and PDF database can be used (HINRICHS, 2014).

A schematically simplified comparison of XRD and GIXRD techniques is illustrated in Figure 2.9. Note that on XRD analysis (a), the angle of incidence ( $\theta$ ) and the angle of the detector ( $2\theta$ ) change simultaneously, keeping the same correspondence while in GIXRD the angle of incidence of the X-ray beam ( $\alpha$ ) is kept constant and the detector is moved through the angular range to be analyzed.

**Figure 2.9** – Schematic illustration of XRD (a) and GIXRD (b) incident X-ray beam on the sample surface and detector positioning.



In GIXRD, the lower the angle of incidence, the lower the X-ray penetration depth in the sample, which can then be tuned by varying the incident angle (SIMEONE *et al.*, 2013). It is then possible to probe either near-surface layers (a few nanometers) or thicker layers in coplanar asymmetric reflection conditions (HINRICHS, 2014; SIMEONE *et al.*, 2013).

Therefore, GIXRD technique exhibits advantages over conventional XRD, especially when dealing with polycrystalline samples that are not able to be grounded, such as thin films. Mainly, no sample preparation is needed to analysis the near-surface layer and it is possible to

tune the thickness of the probed layer by adjusting the incident angle of the X-ray beam (SIMEONE *et al.*, 2013).

Regarding the drawbacks of X-ray diffraction techniques (XRD and GIXRD), it is noteworthy that only crystals are usually detected. If the material presents an amorphous fraction, it will not exhibit any diffraction peak and therefore it is not trivial to identify and quantify the amorphous portion of the material (OHTANI, 2010).

Another significant impediment is in the fact that it is hard to set global standard samples of each crystal, since smaller crystallites may exhibit lower peak intensity and therefore it may be complicated to detect and to precisely determine the crystalline content of nanocrystalline materials, for example (OHTANI, 2010; OHTANI *et al.*, 1997; THAMAPHAT *et al.*, 2008; ZHANG *et al.*, 2003).

### **2.6.2 Crystallographic characterization by Raman spectroscopy**

Raman spectroscopy is based on inelastic scattering of light and it provides information about molecular vibrations, rotations and other lower low-frequency modes that can be used for materials identification and quantification (MAZZOLINI *et al.*, 2016; ZHANG *et al.*, 2000). The technique measures the energy difference between an incident photon (shining a monochromatic light source) and the photon scattered off the molecules of interests.

The majority of the scattered light is of the same frequency as the excitation source; this is known as Rayleigh or elastic scattering. A very small amount of the scattered light (ca.  $10^{-6}$  times the incident light intensity) is shifted in energy from the laser frequency due to interactions between the incident electromagnetic waves and the vibrational energy levels of the molecules in the sample. Plotting the intensity of this shifted light versus frequency results in a Raman spectrum of the sample.

In a Raman spectroscopy process, a sample is illuminated with the light source, the light is collected with the lens and directed through the monochromator. The wavelengths close to the one of the laser are filtered out to eliminate those due to the elastic Rayleigh scattering. The rest of the light goes to a detector in order to observe the Raman effect. The Raman effect is observed when a photon excites a molecule from its ground state to some virtual energy state, then it relaxes and emits the photon returning to a different rotational or vibrational state. The

energy difference between the initial state of the molecule and its new state causes the shift in the emitted photon frequency compared to the wavelength of excitation. Raman shifts are typically measured in wavenumbers and typically expressed in  $\text{cm}^{-1}$ .

Raman spectroscopy is an important tool to understand thin film structure and its influence on functional properties of the studied material. It is also used in phase identification. Concerning  $\text{TiO}_2$ -based materials, Raman peaks are well-known and largely reported in the literature (MAZZOLINI *et al.*, 2016; OHSAKA *et al.*, 1978; ZHANG, W. F. *et al.*, 2000).

The anatase structure is tetragonal and it presents six anatase Raman modes, which are reported with the following reference values:  $E_g(1)$  at  $144 \text{ cm}^{-1}$ ,  $E_g(2)$  at  $197 \text{ cm}^{-1}$ ,  $B_{1g}(1)$  at  $399 \text{ cm}^{-1}$ ,  $B_{1g}(2)$  at  $519 \text{ cm}^{-1}$ ,  $A_{1g}$  at  $513 \text{ cm}^{-1}$ , and  $E_g(3)$  at  $638 \text{ cm}^{-1}$  (MAZZOLINI *et al.*, 2016; OHSAKA *et al.*, 1978). The overlapping between  $B_{1g}(2)$  and  $A_{1g}$  may prevent the detection of the weaker  $A_{1g}$  mode in unpolarized measurements at room temperature. The anatase  $E_g(1)$  Raman peak at  $144 \text{ cm}^{-1}$  is the most intense and largely the most investigated in the literature for anatase phase identification (MAZZOLINI *et al.*, 2016). The rutile structure, in another hand, is tetragonal, and it presents four Raman active modes:  $A_{1g}$  at  $612 \text{ cm}^{-1}$ ,  $B_{1g}$  at  $143 \text{ cm}^{-1}$ ,  $B_{2g}$  at  $826 \text{ cm}^{-1}$  and  $E_g$  at  $447 \text{ cm}^{-1}$  (LI BASSI *et al.*, 2005; PORTO *et al.*, 1967).

Raman spectra of brookite are not clearly established and 36 Raman active modes ( $9A_{1g}$ ,  $9B_{1g}$ ,  $9B_{2g}$ , and  $9B_{3g}$ ) are expected from symmetry considerations (ILIEV *et al.*, 2013). The brookite Raman behavior was theoretically and experimentally measured by Iliev *et al.* (2013) where the main obtained modes were  $A_{1g}$ : 125, 152, 194, 246, 324, 412, 492, 545 and  $640 \text{ cm}^{-1}$ ;  $B_{1g}$ : 169, 212, 283, 327, 381, 449 and  $622 \text{ cm}^{-1}$ ;  $B_{2g}$ : 160, 254, 325, 366, 391, 460 and  $584 \text{ cm}^{-1}$ ; and finally  $B_{3g}$ : 132, 212, 318, 416 and  $500 \text{ cm}^{-1}$  modes.

It is noteworthy that it is difficult to produce single-phase crystals (OHTANI, B., 2010) and that in mixed-phase materials, the overlapping of modes may hinder the phase identification process, as in anatase  $E_g(1)$  and rutile  $B_{1g}$  peaks, for example.

Poly(ethylene terephthalate) – PET – can exist in three possible phase structures: amorphous, ordered amorphous and crystalline structure (ADAR; NOETHER, 1985; BISTRICÍĆ *et al.*, 2015; FLEMING; CHAN; KAZARIAN, 2004; IMAI *et al.*, 1992; MURTHY; CORREALE; MINOR, 1991). The amorphous phase has *gauche* glycol groups and disordered terephthalate units. The ordered amorphous structure has a *trans* glycol conformation with disordered

terephthalate groups. The crystalline structure has carbonyl groups coplanar with the benzene ring and *trans* glycol units (BISTRČIĆ *et al.*, 2015). The vibrational spectrum of PET polymer obtained in the literature is presented in Table 2.11 together with its assignments, classification, and corresponding reference.

**Table 2.11** - The vibrational spectrum of PET referenced in the literature.

Wavelengths (cm <sup>-1</sup> )	Classification (S-strong, M-moderate, W-weak, V-very, Sh-shoulder)	Assignments	Laser Wavelength (nm)	Reference
272	W	C-C stretching (ring), CCC bending (ring)	514.5	(BISTRČIĆ <i>et al.</i> , 2015)
633	S	CCC in plane bending (ring)	514.5	(BISTRČIĆ <i>et al.</i> , 2015)
797	W	CH out of plane bending (ring)	514.5	(BISTRČIĆ <i>et al.</i> , 2015)
859	Sh, W	C-C stretching (ring breathing), C-O stretching	Unknown	(ELLIS <i>et al.</i> , 1995)
890	VW	CH <sub>2</sub> rocking	514.5	(BISTRČIĆ <i>et al.</i> , 2015)
1038	VW	C-C stretching (glycol)	514.5	(BISTRČIĆ <i>et al.</i> , 2015)
1097	M	C-C stretching (ring), C(O)-O stretching (ester) and C-C stretching (ethylene glycol)	Unknown	(ELLIS <i>et al.</i> , 1995)
1117	W	CH in plane bending (ring), C-O stretching	514.5	(BISTRČIĆ <i>et al.</i> , 2015; ELLIS <i>et al.</i> , 1995)

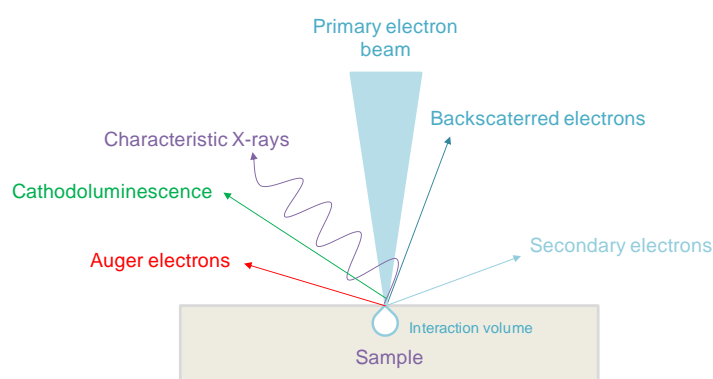


1175	W	CH in plane bending (ring)	514.5	(BISTRÍČÍĆ <i>et al.</i> , 2015)
1245	Sh, W	C-C stretching (ring), C-O stretching	514.5	(BISTRÍČÍĆ <i>et al.</i> , 2015)
1270	M	C-C stretching (ring), C-O stretching	514.5	(BISTRÍČÍĆ <i>et al.</i> , 2015)
1282	M	C-C stretching (ring), C-O stretching	514.5	(BISTRÍČÍĆ <i>et al.</i> , 2015)
1370	VW	CH <sub>2</sub> wagging	514.5	(BISTRÍČÍĆ <i>et al.</i> , 2015)
1412	VW	C-C stretching (ring)	514.5	(BISTRÍČÍĆ <i>et al.</i> , 2015)
1450	W	CH deformation	514.5	(BISTRÍČÍĆ <i>et al.</i> , 2015)
1615	S	C=C stretching (ring)	514.5	(BISTRÍČÍĆ <i>et al.</i> , 2015)
1730	M	C=O stretching	514.5	(BISTRÍČÍĆ <i>et al.</i> , 2015)
2960	W	CH <sub>2</sub> stretching	514.5	(BISTRÍČÍĆ <i>et al.</i> , 2015)
3000	W	CH stretching	514.5	(BISTRÍČÍĆ <i>et al.</i> , 2015)
3068	W	CH stretching	514.5	(BISTRÍČÍĆ <i>et al.</i> , 2015)
3082	W	CH stretching	514.5	(BISTRÍČÍĆ <i>et al.</i> , 2015)

### 2.6.3 Elementary composition by Energy Dispersive Spectroscopy (EDS)

Energy Dispersive Spectroscopy (EDS) is a chemical microanalysis technique (GOLDSTEIN *et al.*, 2003) used in conjunction with Scanning Electron Microscopy (SEM). This method uses the characteristic X-ray spectrum of a solid sample hit by a focused beam of electrons. During an EDS analysis, the specimen is placed inside the scanning electron microscope and bombarded with a high-energy electron beam (Figure 2.10).

**Figure 2.10** - Schematic illustration of electron beam interaction with the sample in a Scanning Electron Microscope. Characteristic X-rays are used by EDS detector.



By the interaction of the electrons from the primary beam with the atoms of the sample (Figure 2.10), secondary electrons, backscattered electrons, characteristic X-ray photons, etc., are generated. Different detectors of the microscope can provide different information, such as surface and topography micrographs (secondary electrons detector), atomic number information and contrast (backscattered electrons detector) and detailed information about the chemical elementary composition of a given measurement spot or area by the X-ray spectrometer (GOLDSTEIN *et al.*, 2003, 2012).

The incoming high-energy electron beam ejects core electrons of the sample, therefore, generating holes in the inner shell of the specimen atoms. The holes in the inner shell will be filled with outer shell electrons. The excessive energy of the electron transfer from the outer shell to the inner shell is emitted as characteristic X-ray photons. The energy of the X-ray is characteristic of specimen atomic number and is measured by EDS detectors (RATOVA *et al.*, 2013).

EDS can detect all the elements with energy higher than 1 keV (due to absorption of the lower energies by beryllium window separating the microscope and spectrometer). Therefore, light elements ( $Z < 10$ ) detection may not be accurate (MIGUENS *et al.*, 2010). The qualitative elementary analysis is based on the identification of the spectrum characteristic lines. Titanium, for example, can be detected by EDS by K line electrons, mainly  $K\alpha$  (4.51 eV) and L line electrons, mainly  $L\alpha$  (0.45 eV) peaks. In order to determine the concentration of each element in a specimen (quantitative analysis) line intensities of each element are measured and compared with calibration samples containing the same elements in known compositions (RATOVA *et al.*, 2013), and usually, only K line electrons are utilized for titanium quantification.

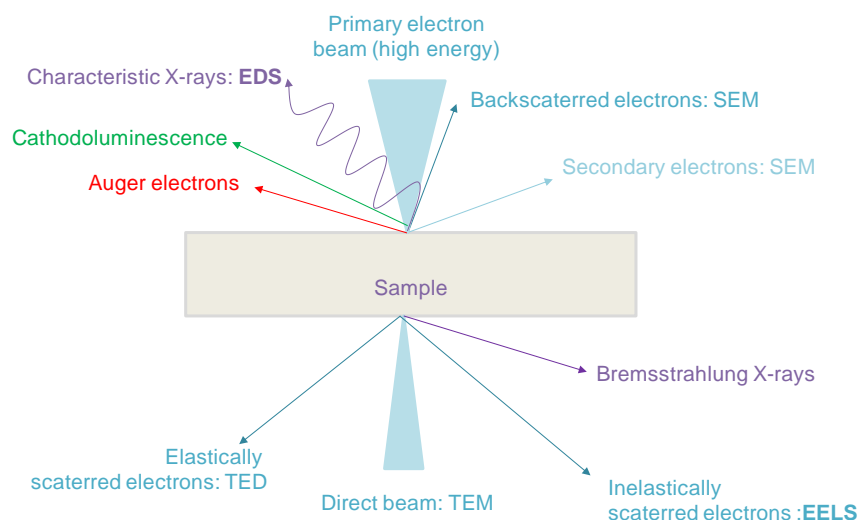
Chemical mapping of a given measurement spot or area can also be performed in an EDS microanalysis. An X-ray spectrum point-by-point is accumulated and evaluated to determine the content of predefined chemical elements. Each resulting element map represents the two-dimensional concentration distribution of the regarding element over the sample surface (selected area or spot). EDS analyzers are generally able to generate maps simultaneously for a great number of different chemical elements (BRUKER NANO GMBH, 2011).

It is noteworthy that EDS supplies general information of element distribution (Titanium atoms distribution, for example) on the specific measured spot or area, and do not give further details on chemical states (it is not clear if Titanium is arranged as titanium dioxide, for example). Different analytical techniques, for instance, electron energy-loss spectroscopy (EELS) or X-ray photoelectron spectroscopy (XPS), must be used in order to obtain further information (BRUKER NANO GMBH, 2011; EGERTON, 2011; MIGUENS *et al.*, 2010; ZHANG, W. *et al.*, 2014).

#### **2.6.4 Electron Energy-Loss Spectroscopy (EELS) microanalysis**

Another interesting technique of analytical electron microscopy is Electron Energy-Loss Spectroscopy (EELS), used in conjunction with Transmission Electron Microscopy (TEM). This method uses the energy loss of inelastically scattered electrons transmitted through a thin sample bombarded by a focused high-energy beam of electrons (HOFER *et al.*, 2016) while EDS microanalysis uses the emitted characteristic X-ray photons (Figure 2.11). EELS is significantly more sensitive for light elements than EDS (LEAPMAN & HUNT, 2014; SAKULICH & LI, 2011).

**Figure 2.11** - Schematic illustration of electron beam interaction with the sample in a Transmission Electron Microscope. Inelastically scattered electrons are used for microanalysis by EELS detector.



EELS detectors measure the amount of energy that fast electrons lose while inelastically interacting with a sample. The energy distribution of all the inelastically scattered electrons provides information about the local environment of the atomic electrons which in turn relates to the physical and chemical properties of the specimen. The transmission electron microscope (TEM) EELS detectors can provide structural and chemical information about a specimen, even down to atomic resolution (HOFER *et al.*, 2016; LEAPMAN; HUNT, 2014).

Due to the broad range of inelastic interactions of the high-energy electrons with the specimen atoms, EELS can be used to map the elemental composition of a specimen, but also for studying the physical and chemical properties of a wide range of materials (HOFER *et al.*, 2016).

Qi *et al.* (2016) used EELS technique in order to study the local chemical states of prepared anatase (TiO<sub>2</sub>) nanoparticles and fullerene (C<sub>60</sub>)-modified anatase TiO<sub>2</sub> nanocomposites. As a result of employing this technique, authors were able to identify TiO<sub>2</sub> structures and observed EELS Ti and O near-edge structures suggested that the phase and crystal structure of TiO<sub>2</sub> was anatase.

Diaz-Egea and coworkers (2015), in another hand, used an improved EELS imaging technique in order to extract plasmon maps with nanometer resolution in TiO<sub>2</sub> thin films embedded with gold nanoparticles. Spatially resolved electron energy-loss spectroscopy was

performed in a scanning transmission electron microscope (STEM) in the Spectrum Imaging (SI) mode. Authors were able to study elementary composition, chemical states, and plasmonic effects through EELS technique, since the resulting maps showed the intensity and the energy spatial dependence of the plasmonic modes sustained by the nanoparticles embedded in the titania thin films coated onto glass and silicon substrates.

### **2.6.5 Coating morphology by Scanning Electron Microscopy (SEM)**

Scanning electron microscopy (SEM) is an important technique for morphology evaluation and it is based on the interaction of an incident electron beam with the sample surface, as illustrated at EDS section and Figures 2.9 and 2.10. Interaction volume is the region of the sample in which the electron beam travel and deposit energy (GOLDSTEIN *et al.*, 2003) and therefore is the studied region. High-resolution surface and topography micrographs can be obtained by secondary electrons (SE) detection while atomic number information and contrast imaging can be analyzed with backscattered electrons (BSE) detection (GOLDSTEIN *et al.*, 2012).

Typical (high vacuum) scanning electron microscopy is the most common configuration of SEM equipment. It requires a dry and conductive sample (often achieved by applying a thin layer of metal or carbon to the surface). The sample must be able to withstand a high vacuum. This type of machine is used for routine imaging, using either SE or BSE.

In a conventional SEM configuration, an electron beam is thermionically emitted from a cathode filament (usually tungsten or LaB<sub>6</sub>) and it is attracted to an anode. The electrons are focused into a fine spot size of circa 5 nm by using two condenser lenses. As the electrons are condensed onto a fine spot size, an objective lens, which contains a pair of scanning coils, is used to deflect the beam in a linear or raster method onto an area of the sample surface, promoting the scanning electron microscopy process (BANYAMIN, 2014).

As the high-energy (up to 50 keV) electrons strike the sample surface, the primary electrons decelerate and begin to lose energy inelastically to the sample atomic electrons and the lattice. Meanwhile, the beam begins to spread across the sample surface due to random scattering events, creating a huge number of electron excitation and the interaction volume is formed. The excited electrons leave the sample surface and emit X-rays characteristic photons, light, electrons and heat (Figures 2.9 and 2.10). The appropriate detectors on the SEM equipment

will be able to identify and differentiate these signals to convert into an image (BANYAMIN, 2014).

SEM micrographs of the photocatalytic surfaces can be used to determine the surface topography and to evaluate its morphology after repeated use and weathering. Coupled with EDS detectors, it can also provide elementary composition information and chemical mapping which can be analyzed alone or combined with SE morphology images.

## **2.6.6 Coating superficial morphology, roughness and specific area by Atomic Force Microscopy (AFM)**

Atomic Force Microscopy (AFM) is a microscopy technique invented by Binnig and coworkers (1986) and it is used to study three-dimensional topography and perform diverse surface measurements. It can generate images at atomic resolution with angstrom scale resolution height information, with minimum sample preparation.

AFM is one class of scanning probe microscopes, which are designed to measure local properties with a probe. To acquire an image, equipment scans this sensor over a small area of the sample, measuring the local properties simultaneously and creating a topographical map of the scanned surface. It operates by measuring force (e.g. van der Waals, magnetic, capacitance, etc.) between its probe and the sample, and the probe is able to determine the topography since its soft cantilever is mounted with a sharp tip at its free end.

Moreover, AFM is widely used for surface roughness characterization (HU *et al.*, 2015; LEPRINCE-WANG & YU-ZHANG, 2001; PASSERI *et al.*, 2013; RATOVA *et al.*, 2017; TIRON *et al.*, 2016). The surface roughness can be quantitatively identified by the root-mean-square roughness ( $R_{rms}$ ).  $R_{rms}$  is given by the standard deviation of the data from AFM topography micrographs, and determined using equation 2.3 (LEPRINCE-WANG & YU-ZHANG, 2001):

$$R_{rms} = \sqrt{\frac{\sum_{n=1}^N (z_n - \bar{z})^2}{N - 1}} \quad (2.3)$$

where  $z_n$  represents the height of the  $n$ th data,  $\bar{z}$  is the mean height of  $z_n$  in AFM topography and  $N$  is the number of the data analyzed.

### **2.6.7 Morphology, composition and thickness determination by Transmission Electron Microscopy (TEM)**

Transmission electron microscopy (TEM) is of great interest in thin film characterization because it can provide structural information with increased spatial resolution (down to atomic dimensions) via high-resolution TEM imaging and electron diffraction (HOFER *et al.*, 2016).

It is a technique that utilizes a high-energy beam of electrons transmitted through an ultra-thin specimen; the beam interacts with the specimen as it passes through. The interaction of electrons transmitted through the specimen (Figure 2.10) forms the image that can be magnified and focused onto the imaging device (RATOVA, 2014).

More than a high-resolution imaging device, TEM can also be used for obtaining diverse types of information about the sample, such as morphology, structural properties, grain size, coating thickness, chemical composition, etc. (MA *et al.*, 1998; MEI *et al.*, 2016; QUYNH *et al.*, 2016; THAMAPHAT *et al.*, 2008).

Sample preparation is crucial to TEM analysis. Thin sections of the specimen may be prepared by a range of methods, such as mechanical polishing, electropolishing, ion-beam thinning, focused ion beam (FIB) cutting, ultramicrotomy, crio-ultramicrotomy, etc. (RATOVA, 2014).

TEM has been used for different photocatalytic surfaces characterization, including TiO<sub>2</sub>-based materials (KRIVEC *et al.*, 2013; LEPRINCE-WANG & YU-ZHANG, 2001; THAMAPHAT *et al.*, 2008), doped TiO<sub>2</sub> thin films (RATOVA *et al.*, 2013; WU & CHEN, 2004) and other visible-light sensitive catalysts (HUANG *et al.*, 2015; NANAKKAL & ALEXANDER, 2017; PENGFEI *et al.*, 2010), for example.

### **2.6.8 Thickness measurement with Profilometry**

A stylus profilometer (or a contact profilometer) measures step heights or trench depths on a surface. It is, therefore, a simple technique that can be used for the thickness evaluation of a coating (KARTHIK *et al.*, 2017; KELLY *et al.*, 2014; MIETTINEN *et al.*, 2015; VRIELINK *et al.*, 2012).

The thickness of the coating is measured by traversing the sample under a stationary stylus and then determining the step height between the substrate and the coating. The step is formed by masking a part of the substrate during the deposition (RATOVA, 2014).

### 2.6.9 Optical band-gap calculation by Tauc-Plot method

Band-gap ( $E_g$ ) indicates the difference in energy between the top of the valence band filled with electrons and the bottom of the conduction band vacant of electrons.  $E_g$  is related to the electric conductivity of the materials and is an important characteristic of photocatalytic surfaces characterization (CAPASSO, 1987; RTIMI *et al.*, 2013; ZHAO *et al.*, 2015).

There is generally no band-gap in conductors (metals, for example), in contrast with insulator materials which are characterized by large band-gap values. Semiconductors typically present intermediate  $E_g$  values. Anatase-TiO<sub>2</sub> phase typically presents band-gap energy of 3.2 eV while  $E_g$  for rutile polymorph is of 3.02 eV. There is no consensus, however, on brookite and TiO<sub>2</sub>-B phases values. The reported experimental  $E_g$  values of brookite range from 3.1 to 3.4 eV while the value of  $E_g$  of TiO<sub>2</sub>-B is reported in the range of 3.1–4.1 (MONAI *et al.*, 2017; OHTANI, 2010).

UV-Vis transmittance (RATOVA *et al.*, 2017) or UV-Vis diffuse reflectance (SARAVANAN *et al.*, 2017) data can be used to obtain the optical band-gap values of the coatings using the Tauc-plot method (TAUC *et al.*, 1966), one of the most widely used for determination of the optical band-gap energy of semiconductors (GRIGOROV *et al.*, 2011; RATOVA, 2014).

For wide band-gap semiconductors, the optical band-gap energy value ( $E_g$ ) can be obtained using the absorption coefficient  $\alpha$  from Tauc-plot method (eq. 2.4):

$$\alpha h\nu = (h\nu - E_g)^{\frac{1}{n}} \quad (2.4)$$

where  $\alpha$  is the absorbance coefficient,  $h$  is the Plank constant,  $\nu$  is the frequency of vibration,  $E_g$  is the energy band-gap and  $n$  is the exponent that denotes the nature of sample transition. For the indirect allowed transition, as in the case of titanium dioxide,  $n = 2$  (RATOVA *et al.*, 2017; SARAVANAN *et al.*, 2017).



Using equation 2.5 (GRIGOROV *et al.*, 2011), the surface transmittance data can be used for band-gap calculation with Tauc method:

$$T = e^{-\alpha d} \quad (2.5)$$

Where  $d$  is the thickness of the coating. Thus, the coatings optical band-gaps can be calculated by plotting  $(\alpha h\nu)^{1/2}$  versus  $h\nu$  and then extrapolating the linear region to the abscissa (RATOVA *et al.*, 2013).

#### 2.6.10 Photoinduced wettability via water droplet contact angle

Photoinduced hydrophilicity is a surface phenomenon that can be indicative of photocatalytic activity. Hydrophilicity can be analytically experimented via water droplet contact angles technique. Contact angles above  $90^\circ$  indicate hydrophobicity of the surface, whereas contact angles below  $90^\circ$  indicate hydrophilicity (FUJISHIMA *et al.*, 2008; STEVENS *et al.*, 2003; VILLANOVA *et al.*, 2015).

Briefly, the liquid droplet contact angle ( $\phi$ ) is a quantitative measurement of the wettability of a material, and it is defined by the intersection of two planes tangent to the liquid: the solid surface and air (VILLANOVA *et al.*, 2015). Wettability is a surface phenomenon and can be defined as the propensity of liquid to spread on a solid surface (KUBIAK *et al.*, 2011). A liquid droplet deposited onto a solid surface, under gravity, has a tendency to spread until the cohesion (internal forces) of the liquid, the gravity forces and the capillary (surface tension) forces are in balance, and an equilibrium state is reached (KUBIAK *et al.*, 2011).

The angle between a drop of liquid with a known surface tension (i.e. pure water) and a solid surface (sample) depends on the relationship between the adhesive forces (surface) and cohesive forces (liquid) and can be measured once the above-mentioned equilibrium is achieved (KUBIAK *et al.*, 2011; VILLANOVA *et al.*, 2015). The equilibrium corresponds to the minimal energy state among the three phases (solid surface, liquid droplet, and air), which can be ideally described by the Young (FUJISHIMA *et al.*, 2008; KUBIAK *et al.*, 2011) equation (eq. 2.6):

$$\gamma_{SG} = \gamma_{SL} + \gamma_{LG} \cdot \cos\theta \quad (2.6)$$

where  $\gamma_{SG}$  is the surface tension coefficient of solid–gas,  $\gamma_{SL}$  of solid-liquid and  $\gamma_{LG}$  of liquid-gas interfaces.

TiO<sub>2</sub> surface, for example, is originally less hydrophilic in the dark, and it becomes highly hydrophilic by its band-gap excitation via UV light irradiation and gradually reverts to originally less hydrophilic in the dark. This photoinduced wettability or photoinduced hydrophilicity phenomenon and has been already investigated and detailed by many researchers (BANERJEE *et al.*, 2015; FUJISHIMA *et al.*, 2008; SAKAI *et al.*, 2003; ZHANG *et al.*, 2012).

Therefore, water droplet contact angle is a simple characterization analysis that can be performed on photocatalytic surfaces in order to understand their wettability behavior in the dark and under irradiation, and therefore relate observed phenomena with photocatalytic activity (BANERJEE *et al.*, 2015; RATOVA *et al.*, 2017). It is noteworthy, however, that this theory and eq. 2.6 are only valid for ideally smooth and homogeneous solid surfaces. In the case of surfaces with high superficial roughness, the observed contact angle may not match the value seen on ideal surfaces and further studies relating wettability and roughness must be considered, such as investigated by Kubiak and coworkers (2011).

### **CHAPTER 3. CHARACTERIZATION OF TiO<sub>2</sub> THIN FILMS COATED ON PET BY HIGH POWER IMPULSE MAGNETRON SPUTTERING**

As already mentioned in the introduction (Chapter 1), the PET-coated surfaces have been developed in partnership with MMU (UK) from the work of Ratova *et al.* (2014) and Delfour-Peyrethon (2018), where the authors found that titania coatings deposited by HiPIMS directly on polymeric substrates showed relatively high levels of activity in their as-deposited state.

The photocatalytic surfaces were characterized at UFMG. This chapter presents the analytical techniques used for the characterization of the photocatalytic coatings discussed in this thesis. Brief background information, the usability of each analytical technique to the current research project were presented in Chapter 2 (Fundamentals) and the methodology employed is provided in the present chapter. Results, discussion, and conclusion are also presented here.

The characterization of the studied photocatalytic surfaces is of great importance for understanding the materials properties, evaluating the deposition method and understanding their relation with photocatalytic activity. However, since the present research is dealing with photocatalytic surfaces, this characterization deals with superficial and interfacial phenomena, rather than only bulk material analysis.

Many of the analytical studies were underpinned by techniques refined (or adapted) from mainstream analytical sciences and originally applied to the study of the bulk material phase. However, especially when working with photocatalytic thin films coated onto polymeric substrates, materials characterization can be challenging since interfacial properties (rather than bulk features) dominate.

Inevitably, newer techniques have been studied and added to the lexicon. However, some studied techniques were not successfully conclusive (or not sufficiently available) and are not presented here, meanwhile, other analysis showed that the studied surfaces were highly contaminated with undesired materials and that those resources had to be forgotten.

A range of different analytical techniques was used for investigating the properties of studied photocatalytic surfaces. The adopted methods were chosen based on their usability on the

current project and mainly availability for utilization. The presented analyses were performed in different locations, as can be seen in details in the following sections.

This chapter is structured as follows: Section 3.1 presents the thin film deposition methodology performed at MMU (UK) while section 3.2 presents material and method information on the analytical techniques employed for crystallographic characterization and elementary composition. Section 3.3 details the analytical techniques for morphological and textural characterization. Section 3.4, on the other hand, presents optical characterization methods studied in this work while Section 3.5 addresses the obtained results and Section 3.6 discusses the obtained conclusions.

### **3.1 Thin Film Deposition**

The thin film deposition process was studied and optimized by the MMU Research Center on Surface Engineering (DELFOUR-PEYRETHON, 2018). The abovementioned research group had also performed mechanical characterization (such as hardness and adhesion) of the coatings that were not presented here since they were not the objective of this thesis. The samples utilized in this work were deposited as described hereafter.

Titanium dioxide thin films were deposited onto PET substrates at MMU (UK) by reactive magnetron sputtering in the HiPIMS mode in a single stage vacuum process from a 99.5% pure Ti target (300mm x 100mm) in an argon/oxygen atmosphere (3.0 sccm O<sub>2</sub> and 50 sccm Ar) at 3 mTorr (0.4 Pa) vacuum. The oxygen flow rate was controlled by optical emission monitoring to provide stoichiometric TiO<sub>2</sub> coatings. The HiPIMS power supply (Huettinger HMP1/1\_P2) was operated at 700 Hz pulse frequency with a 50 µs duration pulse and the voltage was set around 540 V.

The coatings were deposited onto 1 m-long, 100 µm thick food-grade PET sheets, which were ultrasonically pre-cleaned in propanol prior to deposition. The substrates were mounted on a rotating drum substrate holder (1 m circumference) that was electrically floating. The deposition time was 30 min for all the PET samples.

## **3.2 Crystallographic Characterization and Elementary Composition**

### **3.2.1 X-ray diffraction (XRD and GIXRD)**

The evaluation of crystallographic information of the surface was attempted at the Crystallographic Laboratory at the Department of Physics at the *Universidade Federal de Minas Gerais* (UFMG) with X-ray diffraction in conventional geometry (XRD) and in grazing incidence mode (GIXRD). The equipment used was an Empyrean (PANalytical, Netherlands) diffractometer with CuK $\alpha$ 1 radiation ( $\lambda = 1.542 \text{ \AA}$ ) and operated with a 45 kV X-ray tube voltage in grazing mode at  $1^\circ$  angle of incidence.

### **3.2.2 Raman spectroscopy**

A first round of Raman spectroscopy analysis was performed in the Department of Chemistry at the *Universidade Federal de Minas Gerais* (UFMG) using a Senterra Raman spectrometer from Bruker (USA) with a CCD detector equipped with an optical microscope (Olympus BX51) and a 785 nm laser (ELaser = 1.58 eV) at room temperature. Good signal-to-noise ratios were obtained with 10 scans accumulation and an acquisition time of 10 s for each sample using a laser power of 10 mW to avoid heating effects. The obtained data were compared with Raman spectra of pure minerals (anatase and rutile) provided by the RRUFF™ database (<http://rruff.info/>).

In order to better understand the effect of the substrate of PET in the Raman spectra, the second round of Raman spectroscopy was performed in the same conditions but with a different laser ( $\lambda = 532 \text{ nm}$  and ELaser = 2.33 eV) at room temperature. The results were compared with the PET characteristic modes referenced in the literature and summarized in Table 2.11 (Chapter 2 – Fundamentals).

### **3.2.3 Energy Dispersive Spectroscopy (EDS)**

Elementary composition of the samples was investigated via scanning electron microscopy (SEM) coupled with EDS in the Center of Microscopy at the *Universidade Federal de Minas Gerais*, Belo Horizonte, MG, Brazil (<http://www.microscopia.ufmg.br>).

The first round of EDS analysis was performed at JSM - 6360LV scanning electron microscope (JEOL, USA) equipped with an EDS detector (Bruker, Germany) at 15 kV and magnification of 5000x. After adjusting sample preparation parameters, EDS and chemical mapping were also performed at Quanta FEG 3D FEI scanning electron microscope (ThermoFisher scientific) with EDS detector (Bruker, Germany) at 10 kV and magnification of 2500x and 3250x.

### **3.2.4 Electron Energy-Loss Spectroscopy (EELS)**

Elementary composition and chemical state of the samples was investigated via transmission electron microscopy (TEM) coupled with EELS in the Center of Microscopy at the *Universidade Federal de Minas Gerais*, Belo Horizonte, MG, Brazil (<http://www.microscopia.ufmg.br>).

EELS analysis were performed at Tecnai G2-20 - SuperTwin FEI - 200 kV transmission electron microscope coupled with EELS detector. Obtained EELS spectra were compared with TiO<sub>2</sub> standard provided by The EELS Data Base (available at <https://eelsdb.eu/>).

### **3.3 Morphological and textural characterization**

#### **3.3.1 Scanning Electron Microscopy (SEM)**

The coating superficial morphology was evaluated through scanning electron microscopy (SEM) analyses which were performed in the Center of Microscopy at the *Universidade Federal de Minas Gerais*, Belo Horizonte, MG, Brazil (<http://www.microscopia.ufmg.br>) at JSM - 6360LV scanning electron microscope (JEOL, USA) and Quanta FEG 3D FEI scanning electron microscope (ThermoFisher scientific). Samples were prepared and transformed conductors by controlled-sputtering of a 15 nm (approximately) carbon coating on each sample surface and mounting with conductive paint. This step is crucial since the first round of material prepared with a thinner carbon coating suffered high charging during SEM sections, which suspended the analysis.

#### **3.3.2 Atomic Force Microscopy (AFM)**

Superficial morphology, roughness, and specific area were evaluated through atomic force microscopy (AFM) in the Center of Microscopy at the *Universidade Federal de Minas Gerais*, Belo Horizonte, MG, Brazil (<http://www.microscopia.ufmg.br>) at a Cypher ES (Asylum Research) equipment with scanning area of  $900\mu\text{m}^2$  with an AC160TS silicon cantilever (Olympus) operating in the AFM-AC mode (tapping mode) under ambient conditions. No specific sample preparation was required, although size (max.  $1\text{ cm}^2$  sample) and cleaning restrictions exist. The surface roughness was quantified by the root-mean-square roughness ( $R_{\text{rms}}$ ), as detailed in the AFM background section (2.6.6). Each sample was analyzed in four different locations and  $R_{\text{rms}}$  presented (in the results section) are the mean of these four different results for each sample.

#### **3.3.3 Transmission Electron Microscopy (TEM)**

The coating cross-sectioned morphology and thickness were evaluated through transmission electron microscopy (TEM) analyses which were performed in the Center of Microscopy at the *Universidade Federal de Minas Gerais*, Belo Horizonte, MG, Brazil (<http://www.microscopia.ufmg.br>) at Tecnai G2-20 - SuperTwin FEI - 200 kV TEM microscope. Ultra-thin cross-sections of the samples for transmission analysis were prepared by ultramicrotomy, embedding and screen mounting. Sample preparation was challenging due

to the high flexibility of the PET substrate. Conventional preparations (mainly grinding and mounting) of the sample was not possible since the surface of the sample had to be preserved.

### **3.3.4 Coating thickness**

The thickness of the coating onto the PET substrate was measured with Dektak 2 surface profilometer at Manchester Metropolitan University (MMU, UK) and verified by transmission electron microscopy (TEM) at the *Universidade Federal de Minas Gerais* (UFMG, Brazil).



### **3.4 Optical Characterization**

#### **3.4.1 UV-Vis transmittance and Tauc-Plot method**

An Ocean Optics USB4000 spectrometer was used for the UV-Vis transmittance measurements of this transparent coated material. Transmittance data was used to obtain the optical band-gap values of the coatings using the Tauc plot method (TAUC et al., 1966). According to this method, the optical band-gap of a semiconductor can be calculated using the Tauc equation by plotting  $(\alpha h\nu)^{1/2}$  as a function of  $h\nu$  and extrapolating the linear region to the abscissa (where  $\alpha$  is the absorbance coefficient,  $h$  is Plank's constant,  $\nu$  is the frequency of vibration).

#### **3.4.2 Photoinduced wettability via water droplet contact angle**

The measurements of photoinduced wettability were performed via water droplet contact angles ( $\phi$ ) measured at the surface of the films using a contact angle goniometer at the Department of Metallurgical and Materials Engineering (model Digidrop DI, GBX Instruments, France) at room temperature. Ten microliters of water were gently dropped on the surface of the coating using a microsyringe.

Samples were kept in the dark for 24 h prior to the contact angles measurements and irradiated with UV-A lamps (4 x 9 W bulbs with  $\lambda_{\max} = 370$  nm) for 2 h before the contact angle measurements.

All of the droplets were released from 1 cm above the surface to minimize the inconsistency between each measurement. The angle between the tangent line and the coating surface from the goniometric scale was measured 30 s after the release of each droplet onto the surface. Ten consecutive measurements were performed, using the Surface Energy mode of the software, which enables a direct measurement of the contact angle (in degrees).

### **3.5 Results and Discussion**

An extensive characterization of the polyethylene terephthalate (PET) sheet coated with TiO<sub>2</sub> (PET-TiO<sub>2</sub>) by reactive High Power Impulse Magnetron Sputtering (HiPIMS) is provided and discussed in this section. Moreover, in order to evaluate the reusability of the proposed materials and the surface modification occasioned by the coating methodology, some characterization techniques were performed in comparison of brand new PET-TiO<sub>2</sub>, used PET-TiO<sub>2</sub> and uncoated PET substrate.

#### **3.5.1 X-ray diffraction (XRD and GIXRD)**

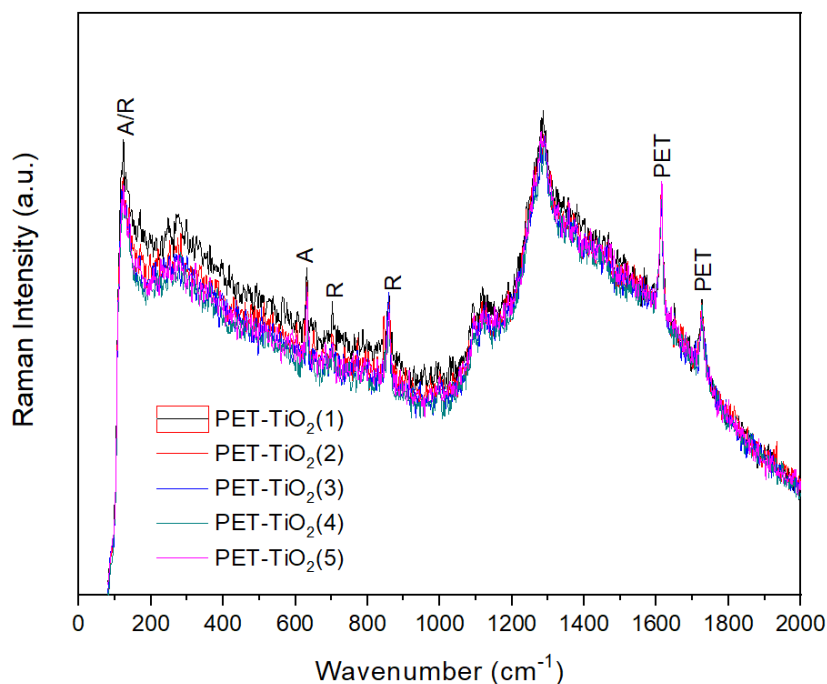
Crystallographic evaluation by X-ray diffraction was performed with uncoated PET substrate and PET coated with TiO<sub>2</sub>. Unfortunately, with conventional X-ray diffraction, XRD, it was not possible to identify titania crystal peaks, since the uncoated PET presented crystalline structure and showed XRD peak in the same angle of expected anatase peak, in agreement with PET-XRD patterns already described in the literature (PANDIYARAJ *et al.*, 2008). Therefore, X-ray diffraction in grazing incidence mode was assessed in order to try to obtain crystallographic information from these samples. Obtained diffractograms, however, were not conclusive and therefore were not presented in this thesis project. Again, uncoated PET samples showed an intense peak where anatase main diffraction was expected. A slight change between coated and uncoated PET samples diffractograms was observed, but LabCri specialists stated it was not possible to guarantee that this change was occasioned by TiO<sub>2</sub> coating and therefore the results were considered not conclusive. It is interesting to note that the diffraction pattern peak intensity of the TiO<sub>2</sub> decreases with decreasing particles size, as already reported on literature (OHTANI, 2010; THAMAPHAT *et al.*, 2008) and discussed on the background section. If the material is arranged as TiO<sub>2</sub> nanocrystals, the peak intensity can be lower than PET diffraction pattern peak intensity. Therefore, PET X-ray diffraction peak at 25° maybe hiding titania nanocrystals main peak at the same angle and further investigation by Raman spectroscopy was necessary.

#### **3.5.2 Raman spectroscopy**

Structural properties of the uncoated PET substrate and of the PET-TiO<sub>2</sub> were investigated by Raman spectroscopy and obtained spectra of 5 scans is presented in Figure 3.1. The Raman spectra obtained corresponded to different polymorphs of nanophase titania, already described in literature (MAZZOLINI *et al.*, 2016; RATOVA *et al.*, 2014; THAMAPHAT *et al.*, 2008)

and obtained results suggest that the thin film investigated developed a mixed titania nanophase crystal structure with characteristic Raman modes of anatase and rutile. PET characteristic modes were also visible in this Figure 3.1.

**Figure 3.1** - Raman spectra excited using 785 nm laser of PET-TiO<sub>2</sub> thin film and uncoated PET sheet. Anatase (A), rutile (R) and PET main characteristic peaks are highlighted.



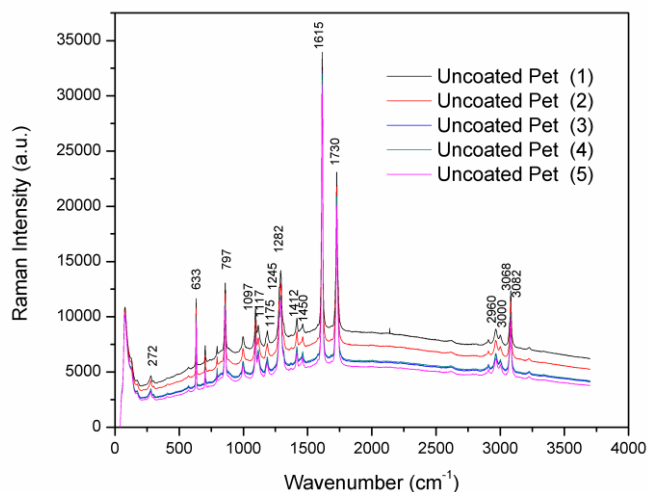
Therefore, it can be seen that PET-TiO<sub>2</sub> presents characteristic features from the nanocrystalline anatase (A) and rutile (R) phases, and some PET modes were also identified. The structure of the titania coating was identified as a mixed anatase/rutile phase with some broad peaks as a result of the overlapping of characteristic modes of different phases. It is noteworthy that in mixed anatase-rutile phases material, the overlapping of anatase E<sub>g</sub>(1) and rutile B<sub>1gb</sub> peaks may hinder the phase identification process.

These result confirmed the viability of the proposed process regarding the deposition of anatase coatings directly onto flexible polymeric substrates in a single stage process without high temperature and/or post-deposition annealing requirements.

It is important to register that it was not easy to get to the results presented in Figure 3.1. Earlier attempts did not clearly show the PET expected Raman modes which were referenced at the literature and shown in Table 2.11. Therefore, another round of experiments was

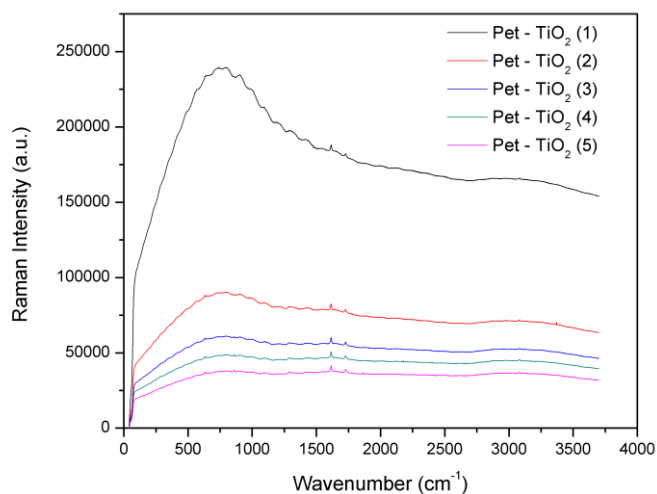
performed using a different laser ( $\lambda = 532$  nm) in order to verify the PET Raman spectrum. The obtained results of the 5 performed scans of the uncoated PET sample are shown in Figure 3.2.

**Figure 3.2** - Raman spectra excited using 532 nm laser of the uncoated PET sheet. PET main characteristic peaks are highlighted.



The obtained spectra agreed with the referenced characteristic modes of pure PET presented in Table 2.11 (Chapter 2 - Fundamentals). However, when the PET-TiO<sub>2</sub> sample was analyzed in the same conditions (laser of  $\lambda = 532$  nm), there was a luminescence effect which disabled the obtainment of conclusive data, as can be seen in Figure 3.3.

**Figure 3.3** - Raman spectra excited using 532 nm laser of the PET-TiO<sub>2</sub> sample.



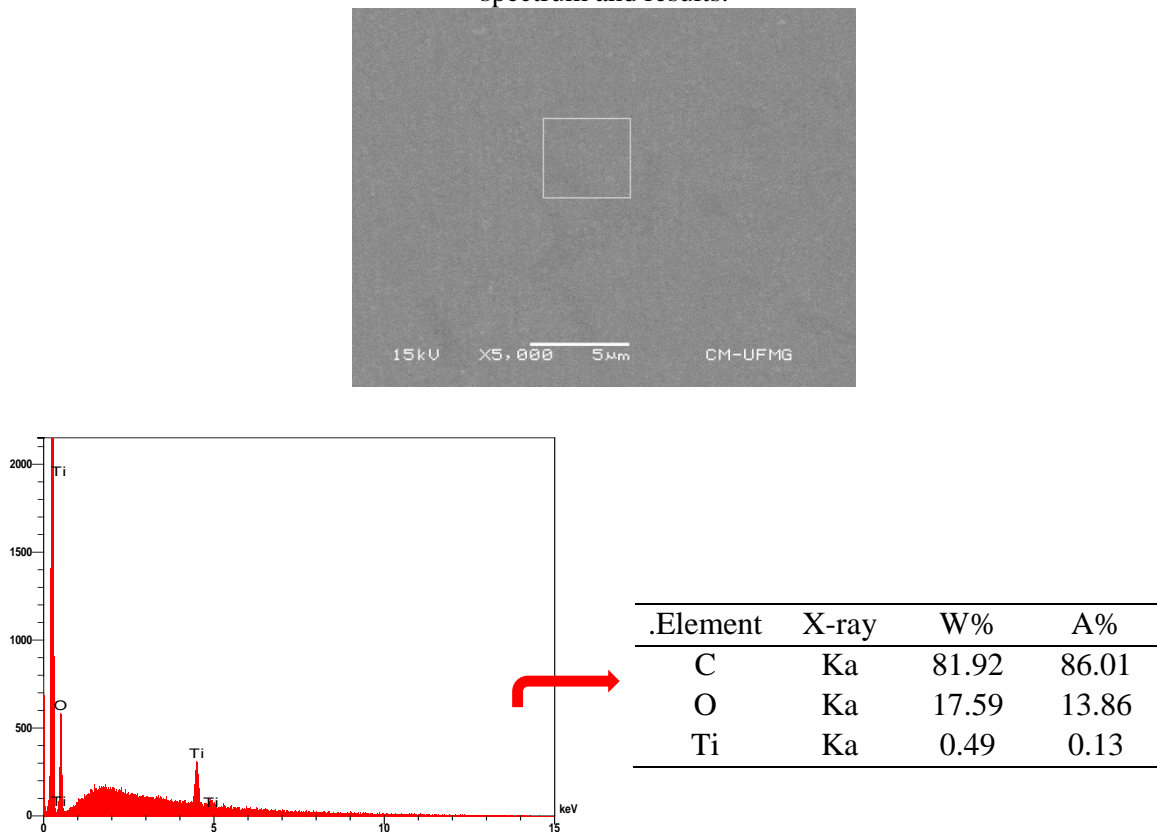
Therefore, due to the photoluminescence of the PET-TiO<sub>2</sub> sample during the scans with the higher energy laser (laser of  $\lambda = 532$  nm and 2.33 eV), it was not possible to clearly see the TiO<sub>2</sub> crystalline structure with this methodology. Indeed, the effect of photoluminescence in titanium dioxide nanocrystals was reported in the literature (ZHANG, W. F.; ZHANG; *et al.*, 2000) under 2.41–2.71 eV laser irradiation. Zhang and coauthors studied the photoluminescence properties of anatase TiO<sub>2</sub> nanocrystals and observed strong visible emission bands with maxima from 2.15 to 2.29 eV even at low excitation power (  $0.06\text{W}\cdot\text{cm}^{-2}$ , for example). The authors concluded that the observed visible luminescence in the anatase TiO<sub>2</sub> nanocrystals is governed by the recombination via the localized levels within the forbidden gap of some defect-related centers which indicates that these anatase TiO<sub>2</sub> nanocrystals could have potential applications in photocatalysis and solar energy conversion (ZHANG, W. F.; ZHANG; *et al.*, 2000). Therefore, these photoluminescence effects could indicate a possible activity of the material under this visible light source (laser of  $\lambda = 532$  nm and 2.33 eV).

As a result, another round of experiments was performed with a laser of  $\lambda = 785$  nm and after careful attempts, it was possible to reach a group of results which minimized the photoluminescence effect and it was able to visualize both coating and substrate characteristic modes. These results were the ones presented in Figure 3.1.

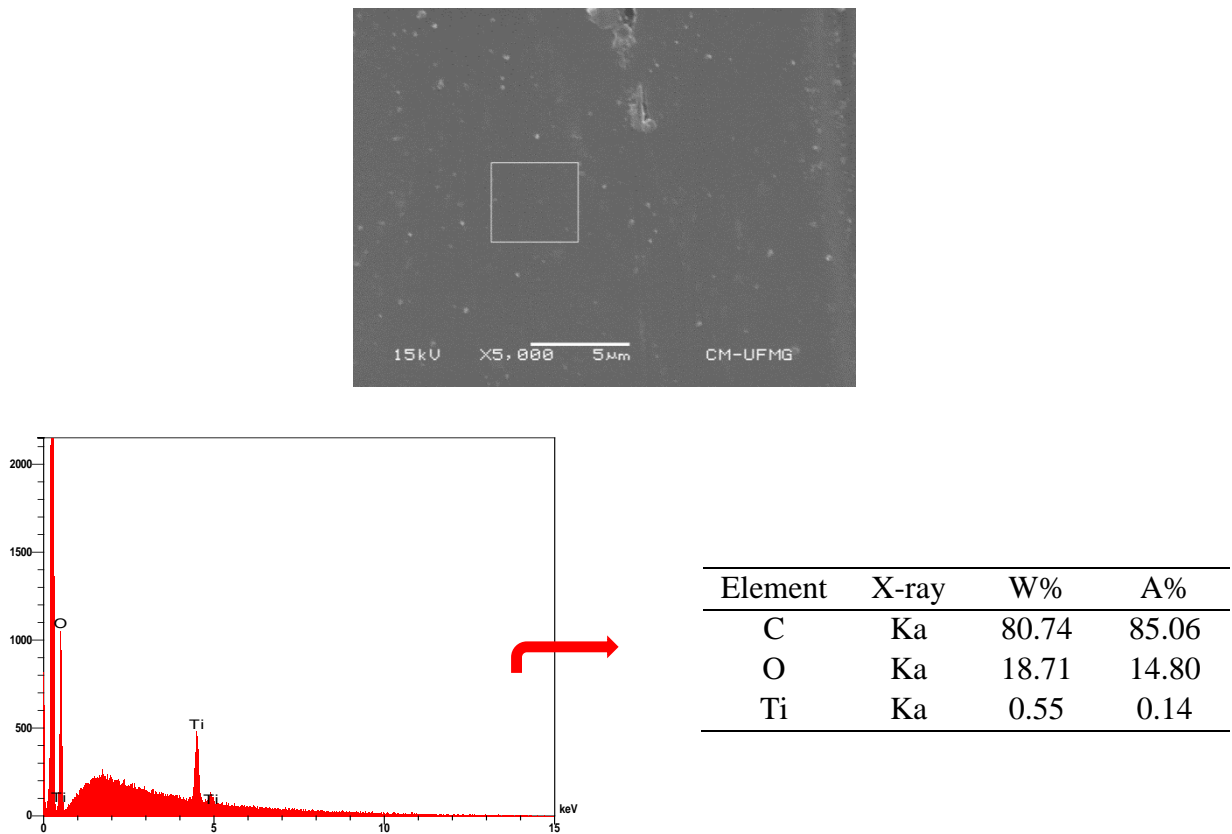
### 3.5.3 Scanning Electron Microscopy (SEM) coupled with Energy Dispersive Spectroscopy (EDS)

In order to evaluate the surface morphology, elementary composition and reusability of the proposed materials, SEM analysis coupled with EDS were performed for the brand new PET-TiO<sub>2</sub> in comparison with the five times used PET-TiO<sub>2</sub> at Jeol JSM-6360LV scanning electron microscope equipped with EDS detector at 15 kV and magnification of 5000 times. Figures 3.4 and 3.5 show SEM micrographs of PET-TiO<sub>2</sub> surfaces (brand new and five times used) with the area where EDS measurements were performed in detail, as well as the EDS absolute data obtained from the analysis.

**Figure 3.4** - SEM micrograph of the brand new titania-coated PET surface with corresponding EDS spectrum and results.



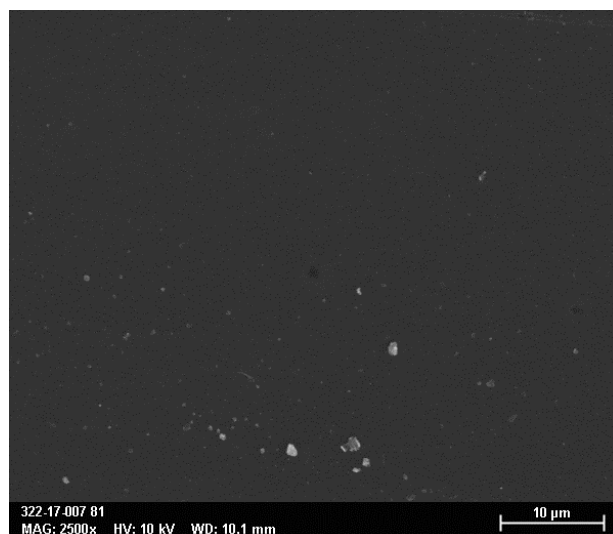
**Figure 3.5** - SEM micrograph of the 5 times used titania-coated PET surface with corresponding EDS spectrum and results.



SEM and EDS results shown in Figures 3.4 and 3.5 indicate that both samples presented similar surface morphology and similar titanium ( $K\alpha$ - 4.51 eV) content (in weight - W% and in atomic counts- A%), which indicates that the studied photocatalytic surfaces did not suffer expressive morphologic and chemical surfaces changes while being in use for five different cycles. The high content of Carbon indicates that the matrix effect plays an important role since the interaction volume comprises both the  $TiO_2$  thin film and the PET substrate. It is also noteworthy that the Ti content of 5-times used surface was slightly higher than that of the brand new surface. These results, however, are in the same order of magnitude and this difference may be occasioned by different measured areas and imprecision in the analytical methodology. EDS is a semi-quantitative technique and high quantitative precision is not expected at this point.

Surface morphology can be evaluated by improved micrographs obtained by Quanta FEG 3D FEI scanning electron microscope at 10 kV and magnification of 2500 times shown in Figure 3.6.

**Figure 3.6** - SEM secondary electrons micrograph of the titania-coated PET surface for surface morphology evaluation.



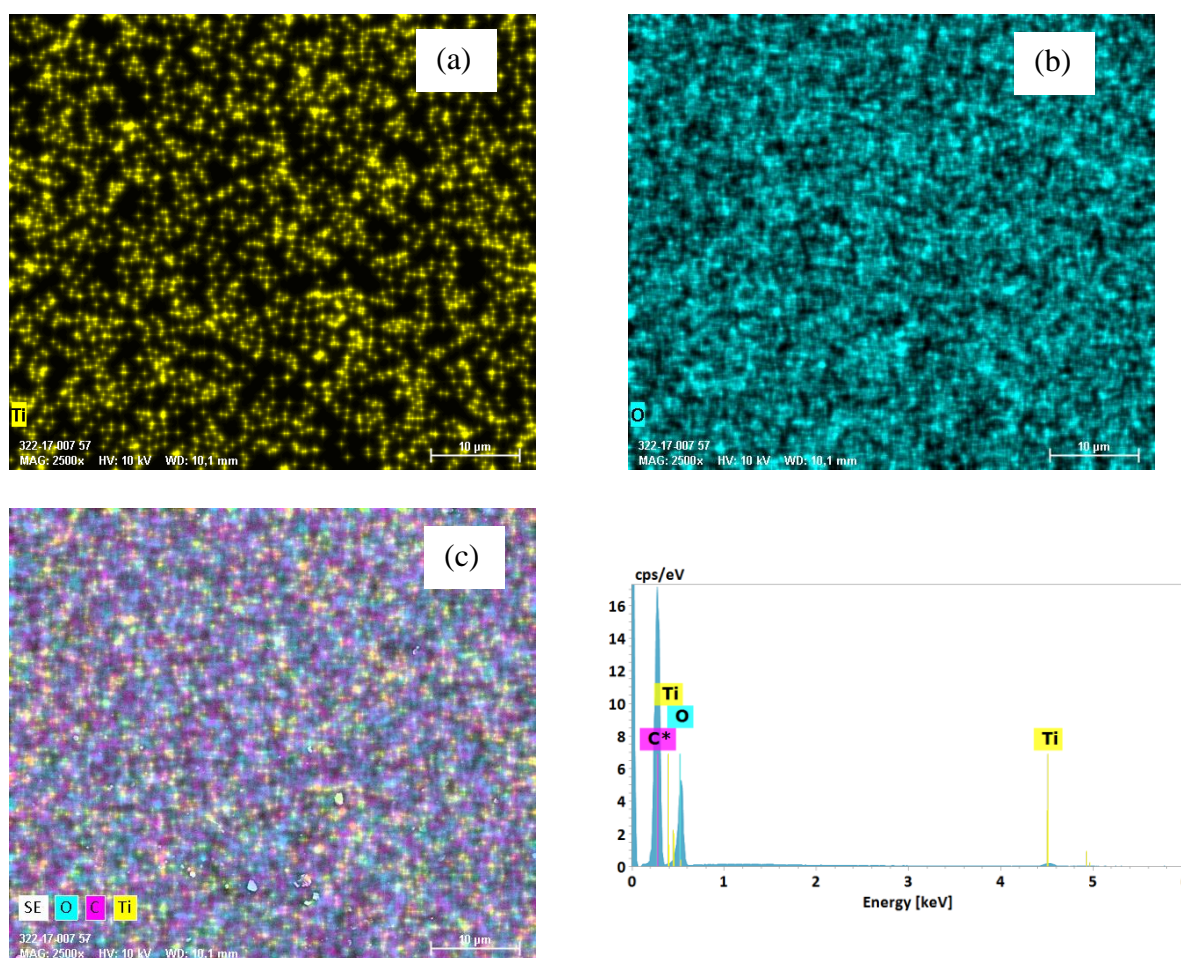
It can be seen from Figure 3.6, as well as from Figures 3.4 and 3.5, that the photocatalytic surfaces presented homogenous, smooth and dense surface with the presence of some punctual clear structures which are supposed to be dirt and dust which were in contact with the surface. The surface morphology and roughness was further evaluated by atomic force microscopy (AFM), which will be discussed in a posterior section.

Dense microstructure and smooth surface were already expected, since different authors have reported such characteristics of TiO<sub>2</sub> coatings deposited by HiPIMS (ALAMI *et al.*, 2009; KONSTANTINIDIS *et al.*, 2006; LATTEMANN *et al.*, 2010; NOUVELLON *et al.*, 2012; RATOVA *et al.*, 2014; SARAkinOS *et al.*, 2010; SARAkinOS *et al.*, 2007; TIRON *et al.*, 2016). Sarakinos *et al.* (2007), for example, deposited TiO<sub>2</sub> films from ceramic TiO<sub>1.8</sub> target and found that HiPIMS-grown films exhibit significantly smoother and denser surfaces than the coatings deposited by pulsed (DC) magnetron sputtering (SARAkinOS *et al.*, 2007). The same effect was observed for TiO<sub>2</sub> films grown by metallic Ti targets, as reported by Konstantinidis and coworkers (2006).

Chemical mapping and EDS of the mainly interested elements were also performed by Quanta FEG 3D FEI scanning electron microscope at 10 kV and magnification of 2500 times in the area presented in Figure 3.6. Results of titanium, oxygen, mixed elements (titanium, oxygen, and carbon) mapping, as well as corresponding EDS spectra, are presented in Figure 3.7.



**Figure 3.7** - SEM chemical mapping micrographs of the titania-coated PET surface: (a) Titanium map, (b) Oxygen map, (c) secondary electron, titanium, oxygen, and carbon mixed map with corresponding EDS spectrum.



It can be seen from Figure 3.7 that titanium is homogeneously distributed on the surface and that it was detected by K $\alpha$  (4.51 eV) and L $\alpha$  (0.45 eV) characteristic peaks. Moreover, only titanium, oxygen and carbon elements were detected on the surface, as expected.

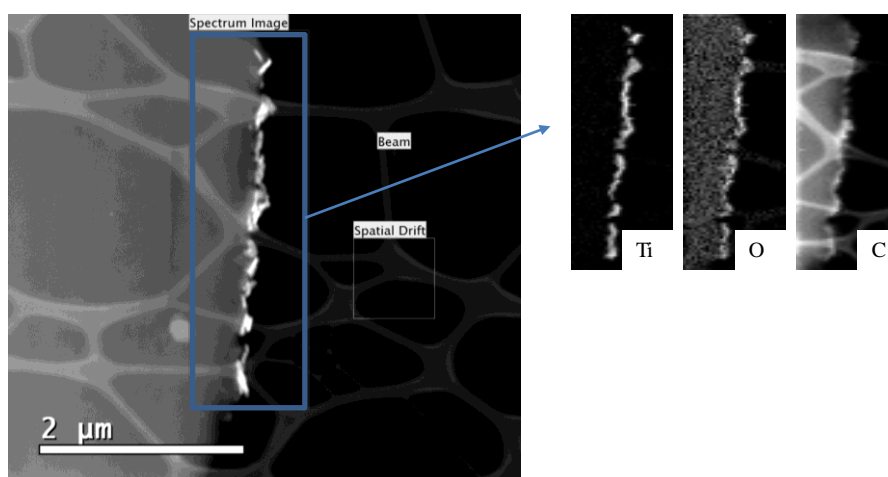
### 3.5.4 Transmission Electron Microscopy (TEM) coupled with Electron Energy-Loss Spectroscopy (EELS)

TEM and EELS analysis were performed at Tecnai G2-20-SuperTwin FEI-200 kV microscope coupled with EELS detector of ultra-thin cross-sections of the coating samples prepared by ultramicrotomy, embedding and screen mounting (honey carbon). Due to the high flexibility of the PET substrate, sample preparation was challenging and aggressive to the

material. The processes of sample preparation were complex and many attempts were performed until the final sample was mounted.

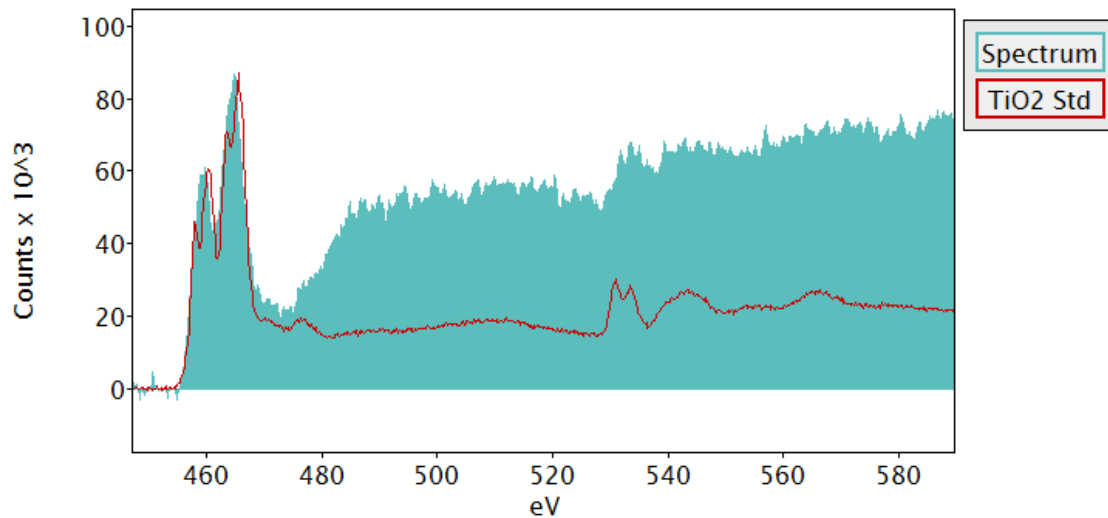
The resulting TEM mounted specimen was not uniform, with different sized and shaped cross-sections. During the TEM experiment, it was difficult to find the titania film, and it looked like it had been ripped off the sample during the ultramicrotomy preparation. A heterogeneous film was visualized and Electron Energy-Loss Spectroscopy (EELS) analysis with elementary chemical mapping were performed in that region in order to confirm if it was a part of the destroyed  $\text{TiO}_2$  coating. The TEM micrograph of the abovementioned region and detailed titanium (Ti), oxygen (O) and carbon (C) mapping is shown in Figure 3.8.

**Figure 3.8** - TEM micrograph of the cross-sectioned  $\text{TiO}_2$  thin film coated onto PET substrate with detailed titanium (Ti), oxygen (O) and carbon (C) mapping.



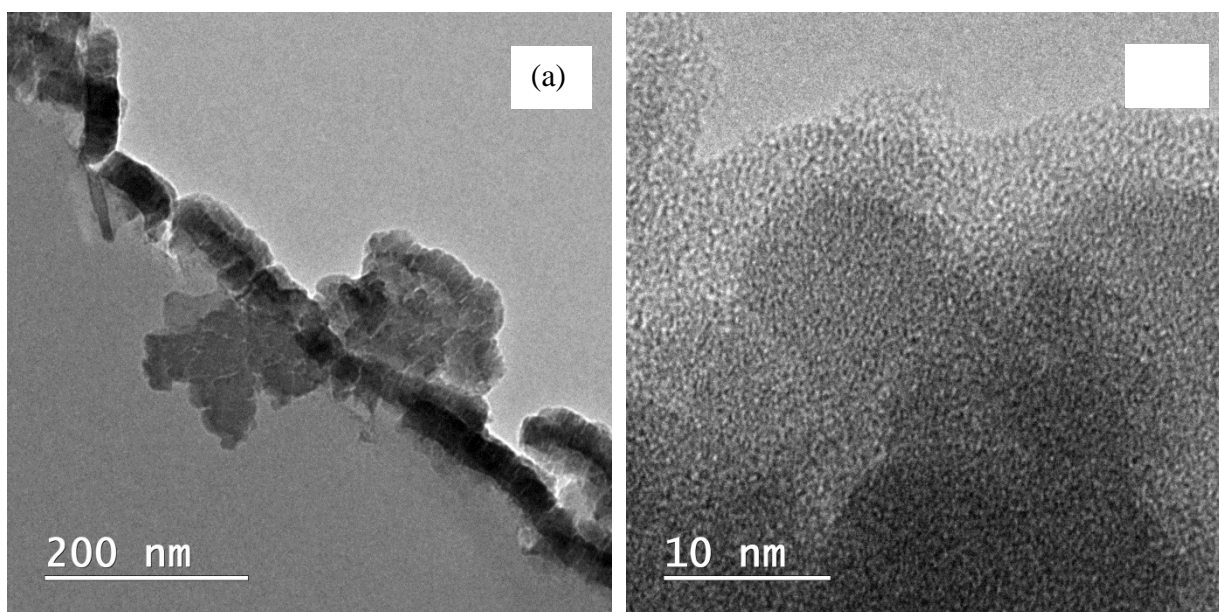
Therefore, although it has been damaged in sample preparation, it was confirmed that the white colored region is the cross-section of the  $\text{TiO}_2$  thin film coated onto the PET substrate. One of the obtained EELS spectra of this region is presented in Figure 3.9 and it was compared with  $\text{TiO}_2$  standard provided by The EELS Data Base (available at <https://eelsdb.eu/>) in order to confirm the chemical state of the titanium detected by the EELS mapping.

**Figure 3.9** - Electron Energy-Loss Spectroscopy (EELS) spectrum of the cross-sectioned TiO<sub>2</sub> thin film coated onto PET substrate.



This result presented in Figure 3.9 corroborates with the hypothesis that the white colored region shown in Figure 3.8 is the cross-section of the TiO<sub>2</sub> thin film coated onto PET substrate. The coating thickness in this heterogeneous region was also measured and values ranged from 50 to 200 nm (due to the damage caused by the ultramicrotomy). Micrographs in nanometric scale were obtained and selected ones are presented in Figure 3.10, where it is possible to visualize the coating thickness distribution (a) and the tendency of crystallinity on the surface of the analyzed cross-section image with near-atomic resolution (b).

**Figure 3.10** - Selected nanometric micrographs of the cross-sectioned TiO<sub>2</sub> thin film coated onto PET substrate: (a) example of heterogeneous coating thickness distribution and (b) tendency of crystallinity on the surface of the analyzed cross-section image with near-atomic resolution.



After the ultramicrotomy experience, it was necessary to find another preparation technique of cross sections of the samples which could better preserve the coating. A published manuscript compared ultramicrotomy and focused-ion-beam (FIB) for the preparation of TEM and STEM cross section of organic solar cells whose substrates was flexible PET. The authors observed that ultramicrotomy was more aggressive than focused-ion-beam for the preparation of the cross-sectioned samples (CORAZZA *et al.*, 2016).

Therefore, another round of sample preparations was performed in order to try to have a less damaged cross-sectioned material to perform STEM analysis. Firstly, the uncoated PET and PET-TiO<sub>2</sub> were prepared for SEM using carbon glue and sputtering of 15 nm carbon film. Afterward, an SEM section in a scanning electron microscope equipped with FIB nanofabrication equipment was used in order to cut the sample and prepare STEM lamels using an ion beam.

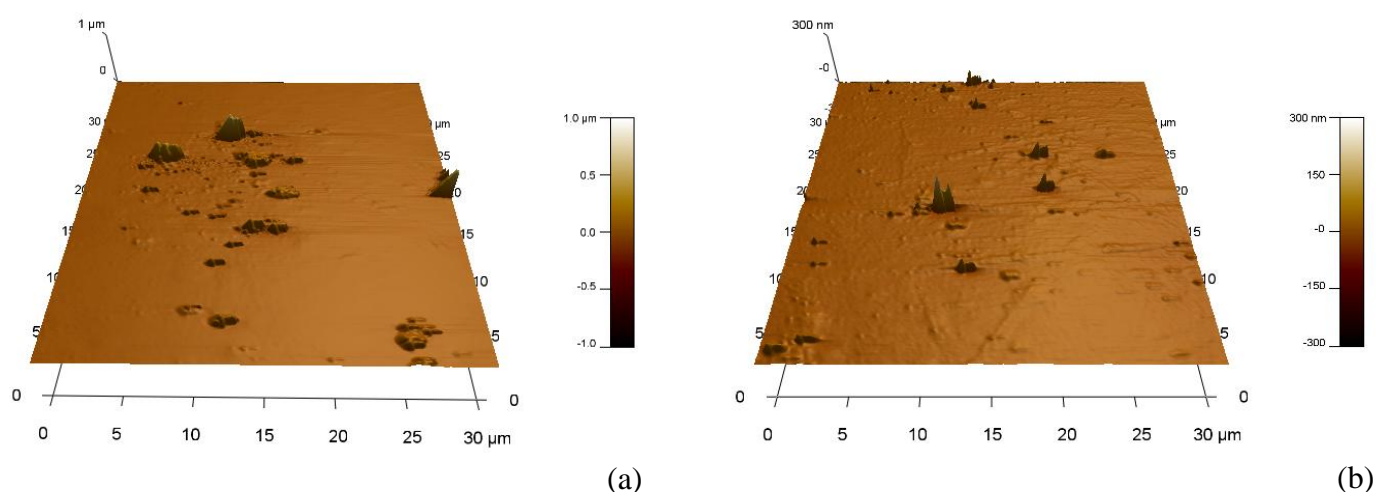
### 3.5.5 Atomic Force Microscopy (AFM)

In order to evaluate superficial morphology, roughness and the reusability of the proposed material, AFM analyses were performed with a Cypher ES (Asylum Research) equipment at a scanning area of  $900\mu\text{m}^2$  of brand new  $\text{TiO}_2$ -coated PET in comparison with five times used  $\text{TiO}_2$ -coated PET. The surface roughness was quantified by the root-mean-square roughness ( $R_{\text{rms}}$ ), as detailed in the AFM background section (2.5.6).

Selected AFM 3D topography micrographs of  $900\mu\text{m}^2$  regions of the uncoated PET and of the brand new  $\text{TiO}_2$ -coated PET are presented in Figure 3.11. AFM micrographs show that the samples presented moderate to low  $R_{\text{rms}}$  roughness, with an average value of 4.48 nm ( $\pm 0.92$  nm) of the uncoated PET against 4.53 nm ( $\pm 0.87$  nm) for brand new  $\text{TiO}_2$  surfaces, respectively. These values are similar and statistical analysis showed that there is no significant difference between the two groups of results under the confidence interval of 95% ( $p=0.09$ ).

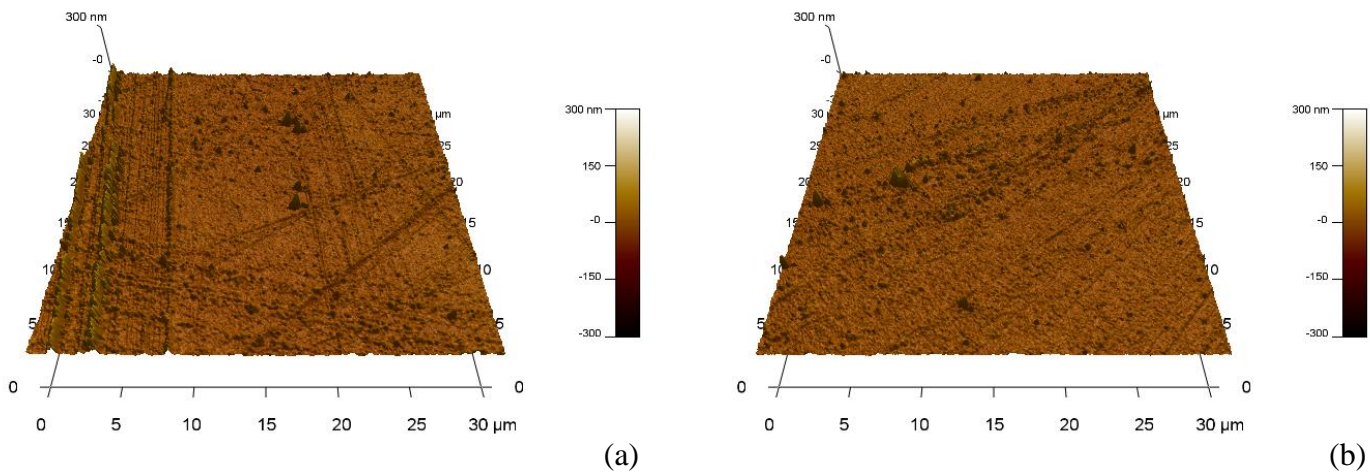
It can be seen from Figure 3.11, in agreement with SEM micrographs, that the photocatalytic surfaces presented homogeneous, smooth and dense surface with the presence of some punctual clear structures which are supposed to be dirt and dust which were in contact with the surface.

**Figure 3.11-** Selected AFM 3D topography micrographs of  $900\mu\text{m}^2$  regions of: (a) the uncoated PET and (b) the brand new  $\text{TiO}_2$ -coated PET.



Selected AFM 3D topography micrographs of two different  $900\mu\text{m}^2$  regions of the five times used  $\text{TiO}_2$ -coated PET are presented in Figure 3.12. The samples presented moderate to low  $R_{\text{rms}}$  roughness, with an average value of  $4.75\text{ nm}$  ( $\pm 1.04\text{ nm}$ ).

**Figure 3.12-** Selected AFM 3D topography micrographs of two different  $900\mu\text{m}^2$  regions of the five times used  $\text{TiO}_2$ -coated PET

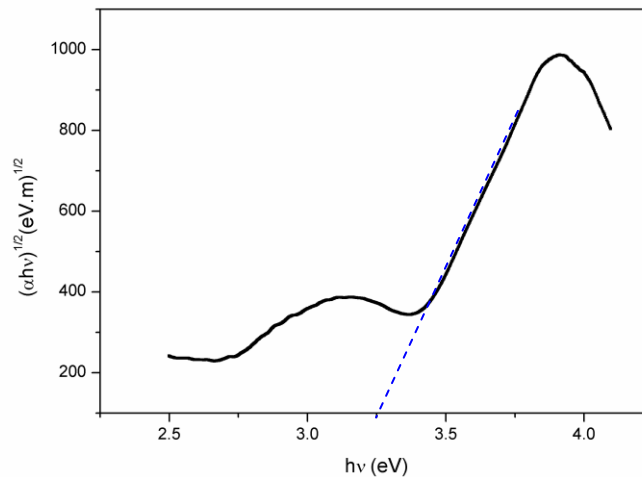


Comparing Figure 3.12 to Figure 3.11, it is possible to see that the surface of the used titania photocatalytic coating is less smooth, although the obtained  $R_{\text{rms}}$  roughness value is similar to the one obtained for the new surface. In this case, statistical analysis showed that the  $R_{\text{rms}}$  results of the brand-new and five times used surface are in the limit of significant difference under the confidence interval of 95% ( $p=0.051$ ).

### 3.5.6 UV-Vis transmittance and Tauc-Plot method for optical band-gap calculation

The optical band-gap ( $E_g$ ) was calculated using the Tauc-Plot method, as described previously. The obtained UV-Vis Tauc-Plot is shown in Figure 3.13.

**Figure 3.13-** Tauc-Plot graphical obtaining of band-gap energy of the titania thin film deposited on PET substrate.

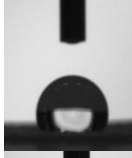

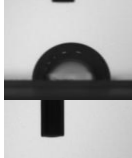
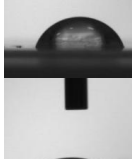
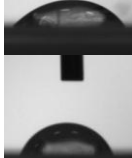
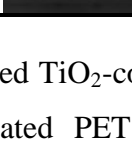


The  $E_g$  value obtained for the studied PET coated with  $\text{TiO}_2$  is in good agreement with literature references, where the band-gap of anatase thin films is typically reported to be around 3.2 eV (LIU et al., 2016; RATOVA et al., 2017) against approximately 3.25 eV of the current material (Figure 3.14), which gives a light adsorption edge of approximately 388 nm (UV-A irradiation). Therefore, it is important to use photosensitization as a method of improving the solar spectrum efficiency and therefore enabling solar photocatalytic process, and this approach will be discussed in the next chapter.

### 3.5.7 Photoinduced Wettability via Water droplet contact angle

As already discussed in previous topics, photoinduced hydrophilicity can be an indicator of photocatalytic activity. Therefore, water droplet contact angles were measured and results with the wettability classification are presented in Table 3.1. Contact angles above  $90^\circ$  indicate hydrophobicity of the surface, whereas contact angles below  $90^\circ$  indicate hydrophilicity.

**Table 3.1-** Water droplet contact angles and wettability classification

<i>Surface description</i>	<i>Water droplet</i>	<i>Contact angle, °</i>	<i>Wettability Classification</i>
Coated PET after 24 hours at the dark		98.3 ± 2.0	Hydrophobic
Uncoated PET after 24 hours at the dark		98.9 ± 1.7	Hydrophobic
Uncoated PET after 2 hours of UV-A irradiation		88.3 ± 2.0	Hydrophilic/Hydrophobic limit
Brand new coated PET after 2 hours of UV-A irradiation		63.1 ± 0.5	Hydrophilic
Coated PET (used one time) after 2 hours of UV-A irradiation		48.4 ± 1.0	Hydrophilic
Coated PET (5 times used) after 2 hours of UV-A irradiation		63.2 ± 2.0	Hydrophilic

It can be seen from Table 3.1 that irradiated TiO<sub>2</sub>-coated PET surfaces presented hydrophilic behavior, while uncoated PET and coated PET kept at the dark presented near the hydrophobic performance. These results may indicate that a photoinduced wettability phenomenon happened and, therefore, the surface may present photocatalytic activity. Moreover, the contact angle of the brand new surface is comparable to the contact angle of the surface used five times. This may also indicate that the material preserved its photocatalytic activity after five cycles of use.

### 3.5.8 Thickness, phase, surface and optical properties of the photocatalytic surface


The coating thickness was determined by profilometry and confirmed with transmission electron microscopy. Profilometry results indicate that the thickness is around 100 nm while TEM results confirmed that they may be in the range of 50-200 nm. The catalyst load per area was estimated by weighing the coated and uncoated PET sheet of a known area. An attempt



of estimating the catalyst load by oxidizing the PET substrate of the PET-TiO<sub>2</sub> material in a muffle oven at 500°C was made, but the results were not conclusive.

In order to recapitulate the obtained results, sample visual appearance, surface, phase and optical properties of the studied TiO<sub>2</sub>-coated PET photocatalytic surface are summarized in Table 3.2.

**Table 3.2** - Phase, surface and optical properties of the TiO<sub>2</sub> photocatalytic surface coated onto 100 µm PET by HiPIMS.

<i>Sample visual appearance</i>	<i>Major crystal phase</i>	<i>Catalyst load per area, mg·cm<sup>-2</sup></i>	<i>Coating thickness, nm</i>	<i>Band-gap, eV</i>	<i>Absorption edge, nm</i>	<i>Surface roughness, nm</i>
	Anatase, Rutile and Brookite	0.785	100	3.25	388	4.53
<i>Methodology</i>	<i>Raman spectroscopy</i>	<i>Weighing</i>	<i>Profilometry</i>	<i>Tauc-plot</i>	<i>Tauc-plot</i>	<i>AFM</i>

Despite the advance on the development of new catalytic materials, it is still important to mention the continuous necessity of the improvement of characterization techniques and their understanding. Even though the catalysis and material sciences have undergone dramatic paradigm changes over the past 3 decades as new characterization techniques became available, such as X-ray Diffraction (XRD), X-ray Photoelectron Spectroscopy (XPS), Fourier Transform Infrared (FTIR) Spectroscopy, Raman Spectroscopy, Solid-state Nuclear Magnetic Resonance (NMR), High-resolution Transmission Electron Microscopy (HR-TEM), UV–Vis Diffuse Reflectance Spectroscopy (DRS), etc. (WACHS, 2005; ALHAJI *et al.*, 2017; STRUNK *et al.*, 2017), there are still challenges involving the identification and quantification of nanocrystalline structures, composites and mixed metal oxide catalytic materials, especially in complex catalysts where multi-crystalline/amorphous phases are present (OHTANI *et al.*, 1997; OHTANI, 2010; OHTANI, 2014).

Mechanical characterization and coating adhesion assays are also important for the complete characterization of the proposed material. These results were not presented in this thesis since

they are subject of work of the Surface Engineering Group (MMU), which has been working towards the improvement of these properties for more than a decade (KELLY, P. J. *et al.*, 2012).

### **3.6 Conclusions**

Characterization results indicate that the studied surface of the PET sheet coated with TiO<sub>2</sub> presented phase characterization referent to a mixed anatase/rutile/brookite phase and characteristic band-gap of anatase, suggesting the strongest presence of anatase polymorph. The morphology and topographic evaluation showed a dense, smooth and homogeneous coating, although some strange particles (probably dust and/or dirt) were observed on the surface of the studied materials.

These result confirmed the viability of the proposed surface engineering process performed at MMU UK - high power impulse magnetron sputtering (HiPIMS) - regarding the deposition of crystalline and dense coatings directly onto flexible polymeric substrates in a single stage process without high temperature and/or post-deposition annealing requirements.

Moreover, the water droplet contact angle showed that the surfaces showed activity under UV-A radiation. Finally, repeated characterization analysis showed that the studied photocatalytic surfaces performed with reproducible behavior after five cycles of utilization, which shows that the supported thin photocatalytic film may be able to be reused in the water treatment process.

## CHAPTER 4. APPLICATION OF TiO<sub>2</sub> THIN FILMS COATED ON PET BY HIGH POWER IMPULSE MAGNETRON SPUTTERING AT LABORATORY SCALE FOR CARBENDAZIM DEGRADATION

This chapter discusses the application of the HiPIMS-coated PET photocatalytic surfaces against carbendazim as a colorless and photostable model pollutant under simulated solar radiation (UV-A and Visible Radiation) at laboratory scale. The main principles of photocatalysis, band-gap engineering, and surface engineering were presented in Chapter 2, while the surface overview and characterization was discussed in Chapter 3. Chapter 4, therefore, presents an introduction, the methodology used and discusses the results obtained for the photocatalytic degradation of carbendazim. The tests were also performed in the presence of food-grade turmeric as a natural photosensitizer.

### 4.1 Introduction

The photocatalytic activity of titanium dioxide (TiO<sub>2</sub>) was perceived almost a century ago. Since then, heterogeneous photocatalysis has been widely studied for multiple environmental applications (REDDY *et al.*, 2016). In parallel, endocrine disruptors and other contaminants of emerging concern (CEC) have been detected in surface waters and in treated wastewaters (BUTKOVSKYI *et al.*, 2016; GROS *et al.*, 2017), at concentrations varying between some ng L<sup>-1</sup> and several µg L<sup>-1</sup>. Owing to the development and dissemination of analytical techniques, the world has become aware of the occurrence of CECs. This awareness, coupled with the fact that the removal rates of CECs in urban wastewater treatment plants (WWTP) are rather low, compounds the need for improvements in treatment techniques in order to achieve improved water quality (BUTKOVSKYI *et al.*, 2016; GROS *et al.*, 2017) and provide a safe aquatic environment (THOMAIDI *et al.*, 2015; VAN DEN BRINK *et al.*, 2000).

In photocatalytic processes, the use of a catalyst in its powdered form results in higher surface areas, but poses some difficulties to recover the powder after treatment. In order to avoid the need for an extra operation to recover the catalyst after photocatalytic treatment, many studies have been made of ways to support the catalysts in different matrices (DE BRITES-NÓBREGA *et al.*, 2013; MUNOZ *et al.*, 2017; RAMASUNDARAM *et al.*, 2017).

Surface engineering is playing an important role, while providing different techniques, including magnetron sputtering, for photocatalytic thin film deposition. Magnetron sputtering is being used for the deposition of a wide range of functional films, including photocatalytic

coatings (KELLY *et al.*, 2014; RATOVA *et al.*, 2017). Titania coatings directly deposited by conventional magnetron sputtering, however, tend to have an amorphous microstructure. For the anatase structure to develop, substrate heating or post-deposition thermal treatment is usually required, with the anatase crystal phase generally forming at temperatures in excess of 400 °C (RATOVA *et al.*, 2014; THAMAPHAT *et al.*, 2008).

Consequently, conventional magnetron sputtering may not be able to deposit anatase materials onto polymeric supports, due to high temperature and/or post-deposition annealing requirements (SINGH *et al.*, 2013). Alternatively, high power impulse magnetron sputtering (HiPIMS), a relatively recently introduced variant of the process, has proven able to deposit photocatalytically active titania coatings directly onto flexible polymeric substrates in a single stage process (KELLY *et al.*, 2014; KELLY *et al.*, 2012; RATOVA *et al.*, 2014) and was, therefore, selected to coat flexible and transparent PET supports used in this research.

Organic polymers have wide applicability as substrates for photocatalytic films deposition (KELLY *et al.*, 2012; RAMASUNDARAM *et al.*, 2017). Polyethylene terephthalate (PET) is a thermoplastic polyester considered one of the most important engineering plastics owing to its interesting properties, such as excellent tensile and impact strength, chemical resistance, clarity, processability, colorability and reasonable thermal stability. Moreover, PET it is reportedly the most recyclable polymer and, therefore, transparent PET substrate was selected to support photocatalytic thin films used in this research.

Photosensitization is a reaction to radiation that is mediated by a light-absorbing molecule, which is not the ultimate target. It can enhance the visible-light harvesting and promote charge separation by effective interface charge transfer between the photosensitizer and the catalyst - TiO<sub>2</sub> (GHAFOOR *et al.*, 2017). Therefore, photosensitization has been widely used to extend the photo-response of semiconductor photocatalysts into the visible region (NANAKKAL *et al.*, 2017). Non-toxic turmeric, a natural source of curcumin (AL-ASMARI *et al.*, 2017), was selected to be used in this project in order to mediate the photocatalytic degradation of the fungicide carbendazim (CBZ) in aqueous solution.

The use of oxidative processes to degrade organic compounds may arise a concern regarding the toxicity of the treated wastewater since the oxidation intermediates can be more toxic than the parent compounds (PRIETO-RODRIGUEZ *et al.*, 2013). In this sense, acute toxicity assessment with *Aliivibrio fischeri* has been used to investigate waterbody contamination

problems and it is considered a reliable fast method compared with other bioassays that employ fish or invertebrates, for example (JACOB *et al.*, 2016a; STARLING *et al.*, 2017).

In this context, this chapter presents data on the performance of photocatalytic thin films of TiO<sub>2</sub> deposited on a PET support via HiPIMS, photosensitized by a natural curcumin source (turmeric), free of hazardous chemicals and a straightforward solution for the degradation of CECs from water sources, utilizing carbendazim as a model pollutant for photocatalytic activity evaluation.

## **4.2 Material and Methods**

### **4.2.1 HiPIMS thin film deposition**

Titanium dioxide thin films were deposited onto PET substrates by reactive High Power Impulse Magnetron Sputtering (HiPIMS) mode in a single stage vacuum process at Manchester Metropolitan University (MMU, United Kingdom).

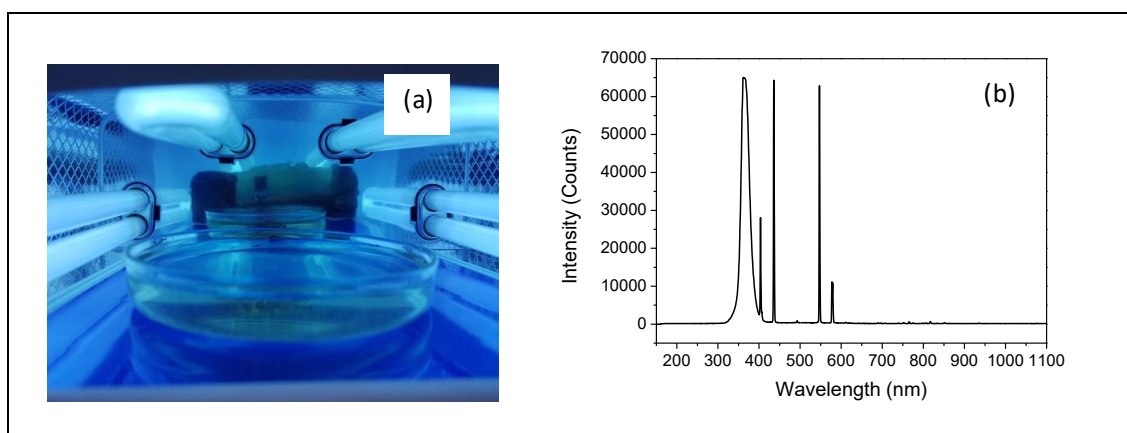
Based on the Surface Engineering Research Group (MMU) expertise and previous works (KELLY *et al.*, 2012; RATOVA *et al.*, 2014), titanium solid target with 99.5% of purity (300mm x 100mm) was utilized in an argon/oxygen atmosphere (3.0 sccm O<sub>2</sub> and 50 sccm Ar) at 3 mTorr vacuum. The oxygen flow rate was controlled by optical emission monitoring. The HiPIMS power supply was operated at 700 Hz pulse frequency with a 50  $\mu$ s duration pulse and the voltage was set around 540 V.

The coatings were deposited onto PET 1 meter-long, 100  $\mu$ m thick PET sheets, which were ultrasonically pre-cleaned in propanol prior to deposition. The substrates were mounted on a rotating drum substrate holder that was electrically floating. The deposition time was 30 min for all the PET samples.

### **4.2.2 Photocatalytic activity assessment**

Photocatalytic activity of the titania coated PET support was assessed by degradation of CBZ (the model pollutant studied in this Chapter) in aqueous solution in the UV-A photoreactor shown in Fig. 4.1(a) for 7 h at room temperature and natural pH. The reactor is equipped with four 9 W (36 W of total power) UV-A bulbs ( $\lambda_{\text{max}} = 370$  nm). The reaction vessel (Petri Plate, D = 9 cm and H = 3 cm) is housed in a 9 x 22 x 25 lamp support, as shown in shown in Fig. 4.1(a). The emission spectrum of the lamps was measured at the Optics Laboratory (Department of Physics, UFMG) with a USB2000+XR1-ES (Ocean Optics) high-resolution spectrometer and the result is presented in Figure 4.1 (b). Temperature and pH were monitored during the experiments.

**Figure 4.1** – (a) The interior of the UV-A/Vis photocatalytic reactor and (b) the corresponding lamps emission spectrum.



In order to study photosensitization to improve visible light activity, the reaction was also performed in the presence of food grade Turmeric (*Curcuma longa*), a natural source of curcumin. The photosensitizer was added at the beginning of each experiment and it was completely removed by the end of the assessment.

An analytical standard of CBZ (Sigma-Aldrich, USA) was used to prepare a 15.6  $\mu\text{M}$  solution with ultrapure water. Natural (food grade) turmeric (Kitano, Brazil) was used as a photosensitizer, limited to its solubility at the concentration of 50  $\text{mg}\cdot\text{L}^{-1}$  previously dissolved in ethanol (final ethanol concentration: 1% m/v).

Photocatalytic degradation of the reactants (CBZ and turmeric) was investigated by UV-Vis spectrophotometry (Micronal AJX-3000PC spectrophotometer). Measurements were taken before irradiation and then at selected time intervals for a total time of 7 h. Adsorption experiments were also performed in the dark for the same total length.

The first round of experiments consisted of turmeric-mediated photolysis, in order to investigate the effect of curcumin and UV-A radiation on the removal of the pesticide carbendazim. Afterward, photocatalytic experiments were performed in the same conditions with the additional presence of the titania coated PET sheet. In order to evaluate the reusability of the immobilized photocatalyst, the same PET-TiO<sub>2</sub> sample was subjected to 5 consecutive photocatalytic runs with CBZ as a model pollutant. After each cycle, the film was washed thoroughly with water, and a fresh solution of CBZ was added before the next photocatalytic run.



The effluents from the 1st, 2nd and 5th runs were submitted to atomic absorption spectrometry – AAS for titanium (VARIAN AA240FS, using nitrous oxide/acetylene and synthetic air/acetylene atmospheres), in order to assess if there were TiO<sub>2</sub> particles detached from the PET substrate.

Moreover, in order to evaluate the behavior of the UV-A light lamps radiation emission during the 7 h assay, global UV irradiance (280-400 nm) was measured with a Kipp & Zonen CMP10 radiometer connected to a data logger (METEON), which records incident UV radiation (W·m<sup>-2</sup>) measured at every one minute. Actinometry investigation was also performed.

The accumulated UV radiation (Q<sub>UV</sub>) was measured and quantified (kJ·L<sup>-1</sup>), according to Eq. 4.1.

$$Q_{UV,n} = \frac{A}{V_t} \int I_{G,UV}(t) dt = Q_{UV,n-1} + \Delta t_n \overline{UV}_{G,n} \frac{A_r}{V_t} \quad (\text{Eq. 4.1})$$

where Q<sub>UV</sub> is the total accumulated incident UV radiation per liter of water solution, (kJ·L<sup>-1</sup>), t represents the time interval (s), I<sub>G,UV</sub> is the global UV irradiance (W·m<sup>-2</sup>), A is the irradiated area (m<sup>2</sup>), and V<sub>t</sub> is the total volume of treated wastewater (L).

#### 4.2.3 Organic matter assessment

Organic matter mineralization after each photocatalytic assessment was monitored through Dissolved Organic Carbon (DOC) analysis. Samples were filtered with C40 quantitative filter paper (125mm) to remove suspended solids and subsequent analyses of DOC were performed in TOC-V CPN equipment (Shimadzu).

#### 4.2.4 CBZ oxidation study via ESI-MS

The CBZ oxidation was also studied by mass spectroscopy with a micrOTOF-QII (Bruker, USA) working in positive mode (ESI-MS). Samples were analyzed by direct injection into the ESI source with a syringe pump at a flow rate of 180 μL h<sup>-1</sup>. ESI assessment used a heated capillary temperature of 180°C, sheath gas (N<sub>2</sub>) at 0.4 bar and flow rate of 5 L·min<sup>-1</sup>, while spray voltage of 4.5 kV was adopted with 8.0 eV of collision energy.

#### 4.2.5 Acute ecotoxicity assessment

Finally, in order to investigate the toxicity of possible by-products formed during the photocatalytic reaction, acute ecotoxicity tests were conducted using the luminescent marine bacteria *Aliivibrio fischeri* and a Microtox® model 500 analyzer (SDI) according to the methodology described by (DA COSTA *et al.*, 2018; JACOB *et al.*, 2016b; STARLING *et al.*, 2017) and by following the protocol described by the software (Microtox® Omni Software, version 4.1) of the equipment. During the tests, resuspended bacteria were exposed to non-treated CBZ aqueous solution and to wastewater treated by photocatalysis assisted by turmeric. Bacteria luminescence was analyzed after 5, 15 and 30 min of exposure to each sample in different dilutions and results are presented in median effective concentration ( $EC_{50}$ ) which corresponds to the concentration that has an effect on 50% of the population. Thus, the lower the  $EC_{50}$ , the higher is the toxicity (DA COSTA *et al.*, 2018).

In addition, an  $EC_{50}$  above 81.9% (maximum sample concentration) is considered as non-toxic and values of  $EC_{50}$  below 81.9% are considered toxic. In order to express toxicity results as a direct measurement, results were converted to and expressed in terms of acute toxicity unit (a.T.U. =  $100/EC_{50}$ ). Therefore, the higher the a.T.U., the higher the toxicity. Moreover, converting the maximum  $EC_{50}$  (81.9%) used in the test to a.T.U. results in 1.21. Therefore, values above this one may be classified as toxic (DA COSTA *et al.*, 2018; STARLING *et al.*, 2017).

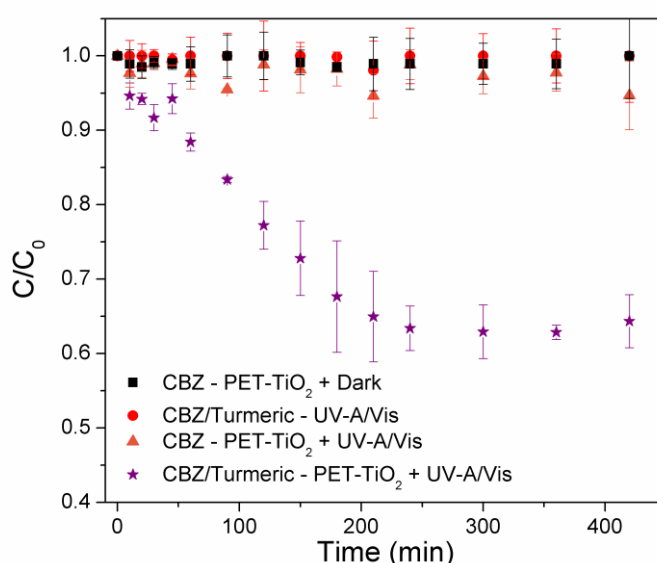
### 4.3 Results and Discussion

In this chapter, the photocatalytic activity of the titania HiPIMS-coated PET was assessed in terms of the degradation of a contaminant of emerging concern: carbendazim in laboratory scale under UVA-Vis irradiation. The assessment includes the monitoring of the pollutant concentration through UV-Vis spectrophotometry, the evaluation of dissolved organic matter through DOC analysis, the confirmation of the oxidation through ESI-MS and the toxicity assessment with *Aliivibrio fischeri* of the treated and untreated wastewater.

#### 4.3.1 Photocatalytic degradation of CBZ under UV-A/Vis irradiation

Firstly, a round of experiments in the dark showed that adsorption of the CBZ molecule onto three different new samples of the studied photocatalytic surface for 420 min (experiments were done in triplicate,  $n=3$ ), as can be seen in Figure 4.2, promoted less than 10% of variation of CBZ concentration during the 7 h adsorption experiments (Figure 4.2 – black squares). Statistical analysis (t-test,  $\alpha=0.05$ ) showed there is no significant difference between the means of the populations of CBZ water solution effluent from the adsorption experiment and the initial CBZ water solutions.

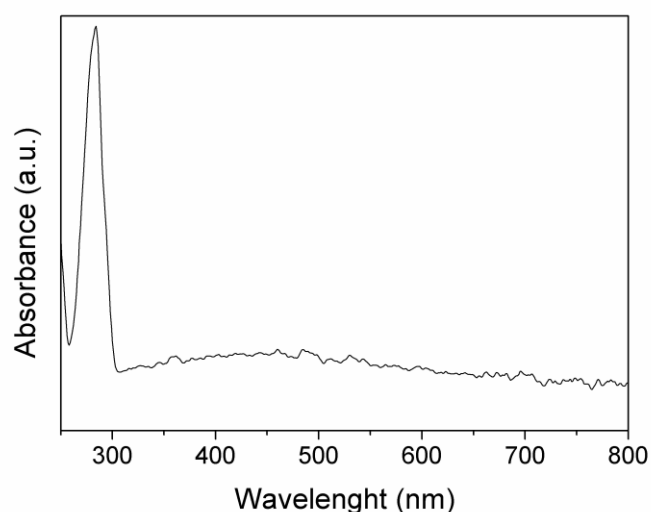
**Figure 4.2** - CBZ removal during adsorption (PET-TiO<sub>2</sub>+ Dark), photocatalysis (PET-TiO<sub>2</sub> + UV-A/Vis), photolysis assisted by turmeric (Turmeric - UV-A/Vis) and photocatalysis assisted by turmeric (Turmeric - PET-TiO<sub>2</sub> - UV-A/Vis) ( $n=3$ ).



These adsorption results are important since it is known that an effective adsorption process can enhance the overall photocatalytic degradation (MIARALIPOUR *et al.*, 2018a). Since the material presented dense and smooth morphology (Chapter 3), since it did not present high surface area and roughness (Chapter 3) and since it did not show a strong capability of adsorbing the model pollutant (Fig. 4.2- black squares), it can be inferred that the improvement of these adsorption properties could enhance the overall process.

After the adsorption experiments, photolysis experiments mediated by turmeric under UV-A irradiation were performed (Fig. 4.2 – red circles) Results show a high photostability of the CBZ molecule which can also be predicted by the UV-Vis spectrophotometry scan shown in Figure 4.3.

**Figure 4.3** - UV-Vis spectrum of CBZ aqueous solution.



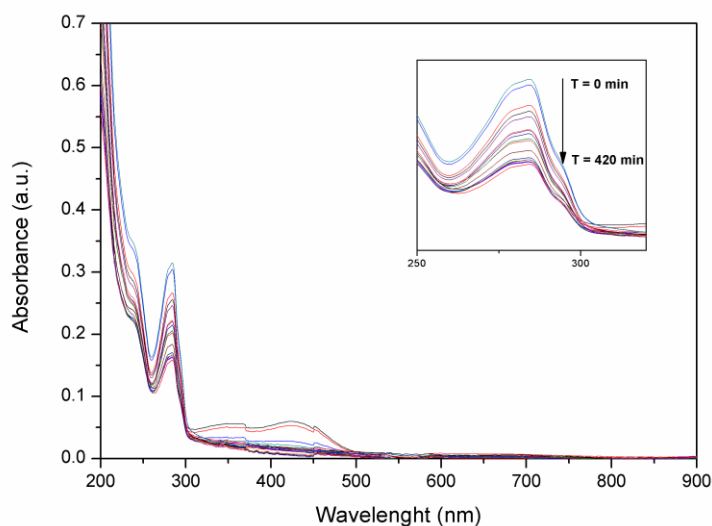
It is possible to see that the CBZ does not significantly absorb UV-A or visible radiation of wavelengths >300 nm. Indeed, photolysis experiments confirmed the expectations and CBZ molecules remained stable during the 7 h photolysis experiment (Fig. 4.2 – red circles), with less than 10% of variability of their concentration. The reactor optical behavior was also studied through actinometry and the quantum yield ( $\phi$ ) of the fungicide photodegradation was calculated at  $1.28 \cdot 10^{-4}$  which agree with the photostability of the pesticide molecule already reported (SAIEN; KHEZRIANJOO, 2008; VAN DEN BRINK *et al.*, 2000).

Photocatalytic tests of the degradation of CBZ under UV-A and visible irradiation in the presence of the coated PET-TiO<sub>2</sub> showed that the reactions did not present fast kinetics

(orange triangles in Fig. 4.2) and the addition of a natural photosensitizer, turmeric, was evaluated in order to improve the degradation of the recalcitrant model pollutant.

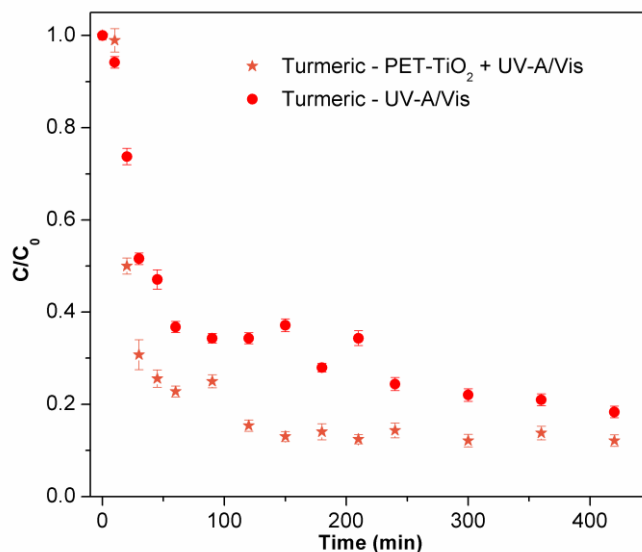
As can be seen by the purple stars shown in Fig. 4.2, the photocatalytic experiments in the presence of the PET-TiO<sub>2</sub> combined with the turmeric sensitizer achieved a relevant reduction of the characteristic peak of CBZ, and a synergetic effect of photocatalysis with photosensitization was observed. It is notable that there was a 35% average removal of the CBZ peak with this sample in a non-hazardous process. These results can be clearly seen by the UV-Vis scan (200-900 nm) of the turmeric-CBZ aqueous solution shown in Fig. 4.4.

**Figure 4.4** - UV-Vis spectrum of CBZ aqueous solution during the photocatalytic reaction assisted by turmeric and detail of the CBZ peak reduction.



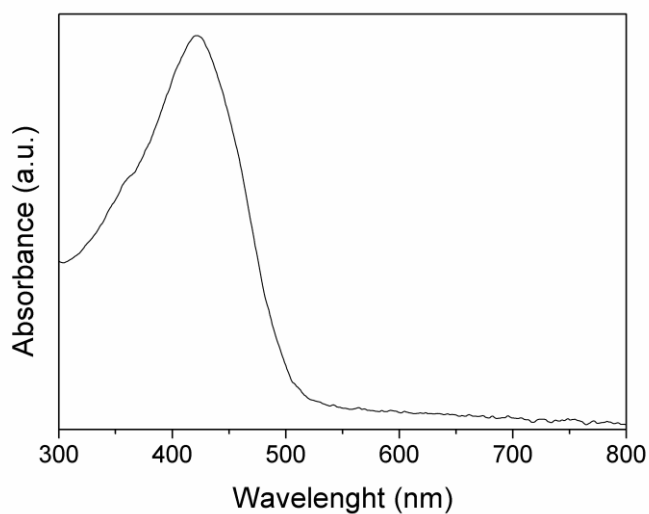
These results are comparable to other studies applying supported TiO<sub>2</sub>, such as the study of Manassero and coworkers which used TiO<sub>2</sub>-coated glass rings in order to promote the photocatalytic degradation of the pharmaceutical drug clofibric acid (MANASSERO; SATUF; ALFANO, 2017a). The authors performed the reaction for 660 min and achieved similar removals (30-40 %) of the CEC concentration in the reaction time of 420 min. Figure 4.5 shows the turmeric concentration behavior during photolysis and photocatalysis experiments.

**Figure 4.5** - Turmeric removal during photolysis (Turmeric - UV-A/Vis) and photocatalysis assisted by turmeric (Turmeric - PET-TiO<sub>2</sub> - UV-A/Vis) (n=3).



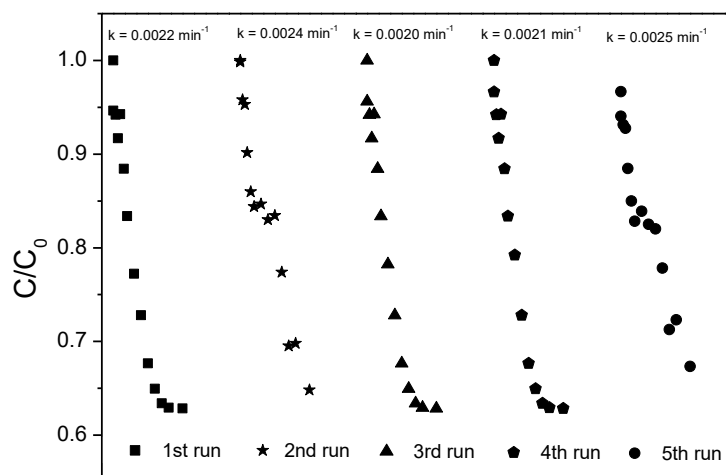
As can be seen in Fig. 4.5, the turmeric concentration suffered a substantial decay during both photolysis and photocatalysis experiments with a visual and spectrophotometric removal of the yellowish color after 2 h of reaction. This was expected, since curcumin, the main yellow bioactive component of turmeric presents an intense characteristic absorption band in the 350–480 nm wavelength region (PATRA & BARAKAT, 2011), which can be confirmed by the turmeric UV-Vis spectrum presented in Figure 4.6.

**Figure 4.6** - UV-Vis spectrum of turmeric aqueous solution.



The recycling of the photocatalytic coatings up to the 5th cycle is seen in Figure 4.7. It proceeds with no significant loss in activity, with the carbendazim removal kinetics remaining approximately the same.

**Figure 4.7** - The reusability of the titania-coated thin film: carbendazim decay curves of the 5 cycles of use with detail to the pseudo-first-order rate constants.



The pseudo-first-order rate constants for each cycle (Fig. 4.7) varied from 0.0020 and 0.0025  $\text{min}^{-1}$ , respectively, with a mean rate constant of 0.0024  $\text{min}^{-1}$  (standard deviation = 0.000207).

Moreover, during 5 cycles, no significant loss of  $\text{TiO}_2$  was verified by EDS and AAS results (all the AAS results were below the detection limit). These results suggest that the proposed process could be used in a passive operation (OKA et al., 2017), where sustained conditions could be achieved without the need of continuous interference processes, such as catalyst addition, catalyst separation or chemical cleaning, for example.

#### 4.3.2 Organic matter removal

Organic matter removal was assessed through DOC analysis. Since it is necessary to filter the samples before the analysis in order to preserve the equipment from suspended particles, the analysis is called dissolved organic carbon (DOC) instead of total organic carbon (TOC). These analyses were challenging due to the low values of the CBZ pure aqueous solution.

Theoretically, the CBZ solution at the concentration of 15.6  $\mu\text{M}$  would present a total organic carbon (TOC) of 1.68  $\text{mg}\cdot\text{L}^{-1}$ , which is a value in the lower limit of the equipment detection capability. The water matrix could slightly increase the organic matter content, but not in an extensive range since ultrapure water was used as the aqueous phase for the bench experiments. The addition of the turmeric, however, increased the initial DOC of the solution and raised it to a better threshold of analytical performance. The DOC results are summarized in Table 4.1.

**Table 4.1** – Summary of organic matter removal of the CBZ aqueous solution through DOC measurements by the different processes.

Sample	Initial ( $\text{mg}\cdot\text{L}^{-1}$ )	Final ( $\text{mg}\cdot\text{L}^{-1}$ )	Removal (%)
Adsorption assisted by turmeric (turmeric + PET-TiO <sub>2</sub> + Dark)	73.92	71.72	2.98
Photolysis assisted by turmeric - (turmeric + UV-A/Vis)	75.03	70.64	5.85
Photocatalysis (PET-TiO <sub>2</sub> + UV-A/Vis)	4.18	3.85	7.89
Photocatalysis assisted by turmeric - (turmeric + PET-TiO <sub>2</sub> + UV-A/Vis)	81.56	16.87	79.31

Similarly to what as observed with the CBZ concentration (Fig. 4.2), it is possible to see that adsorption and photolysis assisted by turmeric were not able to reduce the organic matter content (Table 4.1) of the turmeric-CBZ solution. Table 4.1 also shows the effect of DOC increasing due to the addition of turmeric to the solution. The initial DOC concentration of the CBZ solution (without turmeric) in the photocatalysis process was analyzed at 4.18  $\text{mg}\cdot\text{L}^{-1}$  while the initial DOC concentration of the turmeric-CBZ solution was measured at 73.92-81.56  $\text{mg}\cdot\text{L}^{-1}$ . Nevertheless, there was a significant organic matter removal by the photocatalytic process assisted by turmeric, achieving 79.31% of DOC abatement.



### 4.3.3 CBZ oxidation study via ESI-MS

The Carbendazim (CBZ) photocatalytic degradation process was also monitored by electrospray ionization (ESI-MS). CBZ ( $C_9H_9N_3O_2$ ) presents a molecular weight of  $191.187 \text{ g}\cdot\text{mol}^{-1}$  and the protonated CBZ molecule ( $M+H^+$ ) can be identified as the ion of  $m/z = 192$ .

Figure 4.8 shows the ESI-(+)-MS spectrum from the carbendazim standard solution at the same concentration adopted in the photocatalytic treatment, used to establish the conditions for all analyses, with an intense ion of  $m/z = 192$ , corresponding to protonated carbendazim.

**Figure 4.8** - ESI-(+)-MS spectrum from the Carbendazim standard solution.

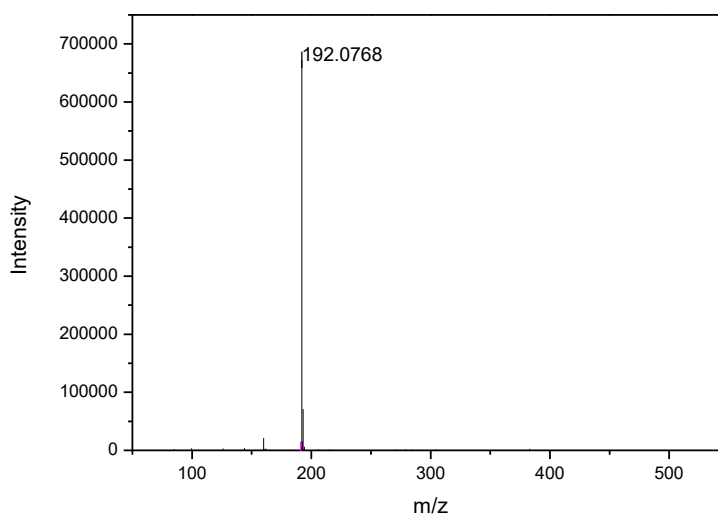


Figure 4.9 shows the ESI-(+)-MS spectrum from the turmeric solution at the same concentration adopted in the photocatalytic treatment, where is possible to see an intense ion of  $m/z = 255$  and a variety of less intense ions.

**Figure 4.9** - ESI-(+)-MS spectrum from the turmeric solution.

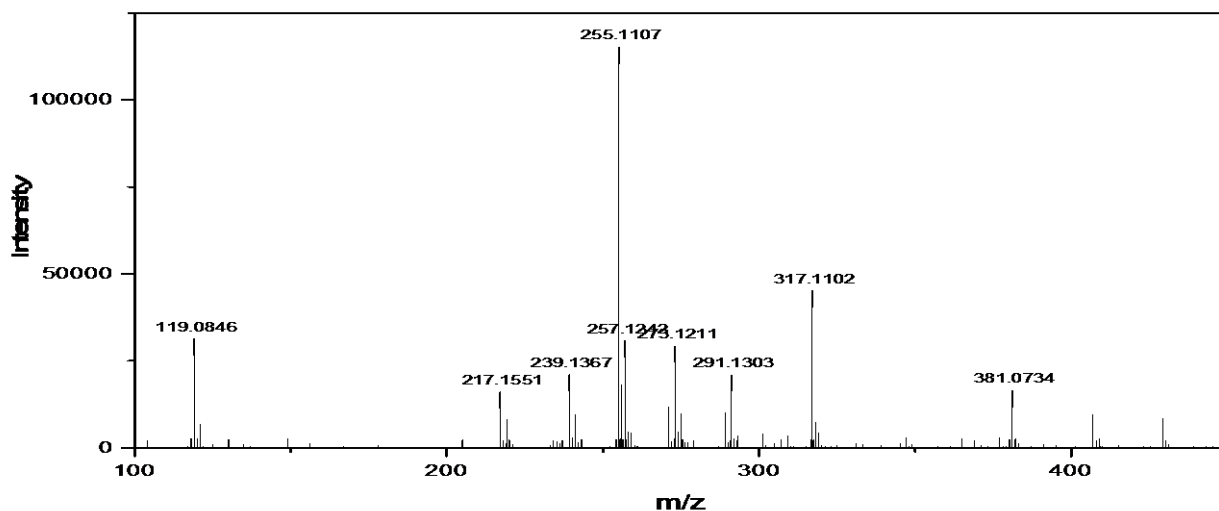
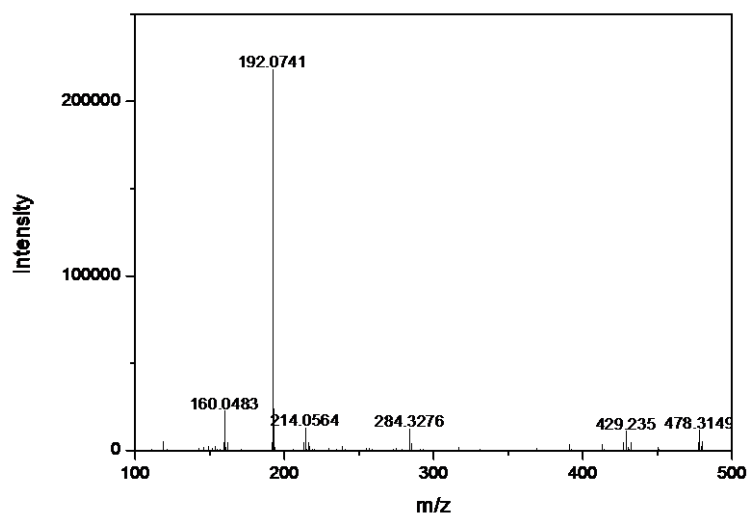


Figure 4.10 shows the ESI-(+)-MS spectrum from the carbendazim with turmeric solution submitted to the photocatalytic treatment with the TiO<sub>2</sub>-coated PET sheets.

**Figure 4.10** - ESI-(+)-MS spectrum from the photocatalytically-treated solution of carbendazim assisted with turmeric.



The photocatalytic degradation in the presence the PET-TiO<sub>2</sub> surface and turmeric resulted in a high loss of the m/z = 192 signal intensity, associated with CBZ oxidation, in agreement with the data observed by absorbance decay (Fig. 4.2).

#### 4.3.4 Acute ecotoxicity assessment

Toxicity assessment was performed in order to verify if the photocatalytic process assisted with turmeric was able to remove the initial toxicity of the CBZ aqueous solution and the possibility of the appearance of toxic byproducts. Actually, ecotoxicity results by *Aliivibrio fischeri* showed no significant changes in the CBZ aqueous solution toxicity after the photocatalytic treatment assisted by turmeric.

The CBZ aqueous solution presented initial a.T.U. value of 3.36 (EC<sub>50</sub> = 29.76) which is considered toxic and after the photocatalytic treatment, a.T.U. was slightly reduced to 3.27 (EC<sub>50</sub> = 30.58), which is still toxic. Da Costa and coworkers found a similar value for a.T.U. toxicity for their non-treated CBZ water solution and the authors observed an increase of toxicity for UV photolysis and UV-H<sub>2</sub>O<sub>2</sub> processes and a decrease for photo-Fenton processes (DA COSTA *et al.*, 2018).

#### **4.4 Concluding Remarks**

The results presented in this chapter suggests the viability of the proposed process regarding the use of the titania-coated polymeric substrates characterized in Chapter 3 as photocatalytic materials for water treatment, degrading a contaminant of emerging concern without increasing the water solution initial toxicity.

It was possible to use band-gap engineering with a natural non-toxic colored compound in order to promote photosensitization and therefore enhance the photocatalytic degradation of a recalcitrant pollutant of emerging concern in water under UV-A/Vis irradiation.

Finally, repeated photocatalytic experiments and characterization analysis (presented in Chapter 3) showed that the studied photocatalytic surfaces performed with reproducible results in five cycles of utilization, which shows that the supported thin photocatalytic film can be reused in the water treatment process.

The proposed process with photocatalytic surfaces photosensitized with natural turmeric may be a hazardous chemical-free, sustainable and straightforward passive solution for the degradation of emerging contaminants from water sources.

## CHAPTER 5. APPLICATION OF TiO<sub>2</sub> THIN FILMS COATED ON PET BY HIGH POWER IMPULSE MAGNETRON SPUTTERING AT LABORATORY SCALE FOR CAFFEINE DEGRADATION

This chapter discusses the application of the HiPIMS-coated PET photocatalytic surfaces against caffeine as a colorless and photostable model pollutant under simulated solar radiation (UV-A-Vis photoreactor and Suntest CPS+ solar simulator) at laboratory scale. The main principles of photocatalysis, band-gap engineering, and surface engineering were presented in Chapter 2, while the surface overview and characterization was discussed in Chapter 3. In Chapter 4, the photocatalytic degradation of Carbendazim assisted by turmeric was assessed at laboratory scale and Chapter 5, therefore, discusses the photocatalytic degradation of caffeine, an anthropogenic pollution indicator, as a model pollutant, in the presence of food-grade turmeric as a natural photosensitizer. The tests were also performed in a Solar Simulator Chamber (Suntest CPS+) with the presence of hydroxyl radicals and holes scavengers, in order to elucidate which of the two processes was the most important to the reaction.

### 5.1 Introduction

Owing to the development and dissemination of analytical techniques, the world has become aware of the occurrence of Contaminants of Emerging Concern (CECs). This awareness, coupled with the fact that the removal rates of CECs in urban wastewater treatment plants (WWTP) can be rather low, compounds the need for improvements in treatment techniques in order to achieve improved water quality (BUTKOVSKYI *et al.*, 2016; GROS *et al.*, 2017; LOOS, R. *et al.*, 2017) and provide a safe aquatic environment (RODRÍGUEZ-GIL *et al.*, 2018; THOMAIDI *et al.*, 2015) and advanced treatment based on photocatalysis is a potential solution for CEC removal.

In photocatalytic processes, the use of a catalyst in its powdered form results in higher surface areas, but poses some difficulties in recovering the powder after treatment. Therefore, it is important to study and develop different methodologies to support solar-activated photocatalysts onto inexpensive substrates.

The selection of a model pollutant for photocatalytic activity evaluation may be a complicated task. Since it is not analytically trivial to monitor all CEC and related by-products that may be present in real water and wastewater matrix, a model molecule (or a group of specifically

designated molecules) may be selected in order to verify the proposed treatment efficiency. An ideal model pollutant must be photochemically stable, colorless and environmentally relevant.

Caffeine is a natural alkaloid produced by many plant species and is the most used central nervous system stimulant (HSU, 2015). It is a constituent of a variety of beverages (coffee, tea, mate, guaraná and caffeinated soft drinks), of numerous food products (chocolate and pastries, for example) and of many pharmaceutical products.

Due to its important consumption, caffeine has been detected in wastewater (RODRÍGUEZ-GIL *et al.*, 2018; TERNES, 2001; VIVIANO *et al.*, 2017), surface water (LIN *et al.*, 2016; LOOS *et al.*, 2017; RODRÍGUEZ-GIL *et al.*, 2018), groundwater (LOOS *et al.*, 2010), marine waters (PAÍGA & DELERUE-MATOS, 2017) and drinking water (LARDY-FONTAN *et al.*, 2017) worldwide. The caffeine molecule is colorless in aqueous solution and has been demonstrated to be chemically and photochemically stable and its content is not significantly reduced through traditional wastewater treatment (PADHYE *et al.*, 2014).

Caffeine molecule has been used as an indicator of anthropogenic pollution (DANESHVAR *et al.*, 2012; PAÍGA & DELERUE-MATOS, 2017; PEELER *et al.*, 2006; RODRÍGUEZ-GIL *et al.*, 2018; SEILER *et al.*, 1999; VIVIANO *et al.*, 2017b) and may, therefore, be used as an indicator of photocatalytic tertiary wastewater treatment performance. It was selected in this chapter as a model pollutant to test the photocatalytic activity of a TiO<sub>2</sub> thin film deposited on PET substrates (PET-TiO<sub>2</sub>) by high power impulse magnetron sputtering (HiPIMS) in a single step process.

## **5.2 Material and Methods**

As already presented in earlier chapters, TiO<sub>2</sub> thin films were deposited on PET substrates at MMU (UK) by reactive HiPIMS in a single stage vacuum process from a 99.5% pure Ti target in an argon/oxygen atmosphere at 0.4 Pa vacuum. The HiPIMS power supply (Huettinger HMP1/1\_P2) was operated at 700 Hz pulse frequency with a 50 μs duration pulse and the voltage was set to 540 V. A detailed description was presented in the topic “4.2.1 HiPIMS thin film deposition”.

### **5.2.1 Photocatalytic degradation of CAF under UV-A/Vis irradiation**

At UFMG, after the photocatalytic/photosensitization experiments presented in Chapter 4, the photocatalytic activity of the titania-coated PET was also assessed by degradation of the caffeine (15.5 μM aqueous solution) as a model pollutant in a lab-scale UV-A/Vis photoreactor for 7 h at room temperature and natural pH. The reactor is equipped with four 9W (36W of total power) UV-A/Vis bulbs ( $\lambda_{\text{max}} = 365$  nm). The interior of the UV-A/Vis photocatalytic reactor and the emission spectrum of the UV-A/Vis fluorescent lamps is the same shown in Figure 4.1.

Samples were periodically collected in order to verify the caffeine (CAF) concentration through UV-Vis spectrophotometry (Micronal AJX-3000PC spectrophotometer). Temperature and pH were monitored during the experiments. In order to study photosensitization to improve visible light activity, the reaction was also performed in the presence of food grade turmeric, a natural source of curcumin, and the sensitizer concentration was also evaluated by UV-Vis spectrophotometry (Micronal AJX-3000PC spectrophotometer).

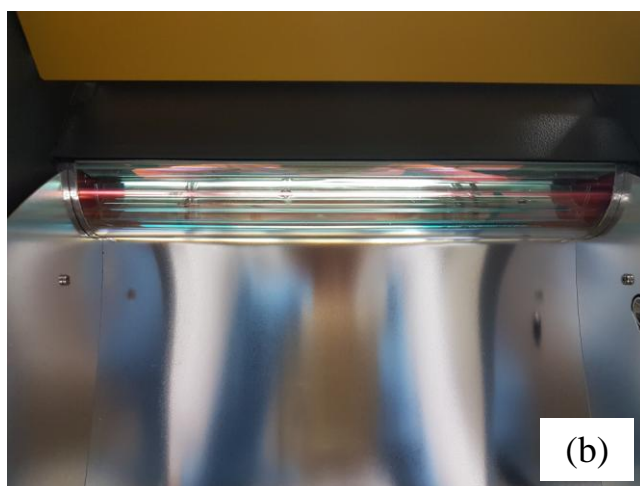
Measurements were taken before irradiation and then at selected time intervals for a total time of 7 h. Adsorption experiments were performed in the dark for the same total length and turmeric-mediated photolysis experiments were performed to investigate the effect of curcumin and UV-A-Vis radiation on the removal of the pharmaceutical CAF.

The photocatalytically treated wastewaters were submitted to atomic absorption spectrometry – AAS, for titanium analysis (VARIAN AA240FS, using nitrous oxide/acetylene and synthetic air/acetylene atmospheres), in order to assess if any TiO<sub>2</sub> particles had detached from the PET substrate.

## 5.2.2 Photocatalytic degradation of CAF under simulated solar irradiation

After the experiments at the UV-A/Vis photoreactor, another round of tests was performed at the bench scale solar simulator chamber, Suntest CPS+ (Atlas, USA). The solar simulator features an air-cooled 1500 W xenon lamp (CIE85 sun referenced) and it is shown in Figure 5.1. The global (300-800 nm) irradiance was set at  $270 \text{ W}\cdot\text{m}^{-2}$ . This value corresponds to  $30 \text{ W}\cdot\text{m}^{-2}$  of broad UV irradiation, which is the average irradiation during sunny days in Belo Horizonte.

**Figure 5.1** – (a) The benchtop solar simulator chamber and (b) the detail of the xenon lamps with daylight filters.



The experiments were similar to the rounds performed at the UV-A/Vis reactor. Measurements were taken before irradiation and then at selected time intervals for a total time of 7 h. Adsorption experiments were performed in the dark for the same total length and



photolysis experiments were performed to investigate the effect simulated solar radiation on the removal of the pharmaceutical CAF.

### 5.2.3 Elucidation of involved radical species via trapping reactions

In order to understand the radical species involved in the photocatalytic reaction, photocatalytic experiments of CAF degradation were also conducted employing hole (1 mM ethylenediaminetetraacetic acid, EDTA), hydroxyl radical (1 mM dimethyl sulfoxide, DMSO) and superoxide radical (1 mM benzoquinone, BQ) scavengers. EDTA, DMSO, and BQ are well known effective scavengers for  $h^+$  (MARQUES *et al.*, 2013; MINERO *et al.*, 2000),  $HO^\bullet$  (DONG *et al.*, 2013; POLYAKOV *et al.*, 2010) and  $^{\bullet}O_2^-$  (DONG *et al.*, 2013). The radical trapping concentrations were selected proportionally based on the work of Marques *et al.* (2013).

Firstly, a serie of photocatalytic radicals trapping experiments was performed by adding DMSO, EDTA and BQ scavengers individually to the CAF solution. The solution was then submitted to a photocatalytic run with the PET-TiO<sub>2</sub> surface in the same conditions of the previous experiments in the Suntest CPS+ solar simulator. Afterward, another run of photocatalytic experiments was performed adding the photosensitizer turmeric to the solution, assessing DMSO, EDTA and BQ scavengers individually.

### 5.2.4 Organic matter assessment

Organic matter mineralization after each photocatalytic assessment was monitored through Dissolved Organic Carbon (DOC) analysis. Samples were filtered with C40 quantitative filter paper (125mm) to remove suspended solids and subsequent analyses of DOC were performed in TOC-V CPN equipment (Shimadzu).

### 5.2.5 Acute toxicity assessment

Finally, in order to investigate the toxicity of possible by-products formed during the photocatalytic reaction, acute ecotoxicity tests were conducted using the luminescent marine bacteria *Aliivibrio fischeri* (Microtox®) according to the methodology detailed in Chapter 4. Toxicity results were analyzed using the a.T.U. (30 minutes) values.

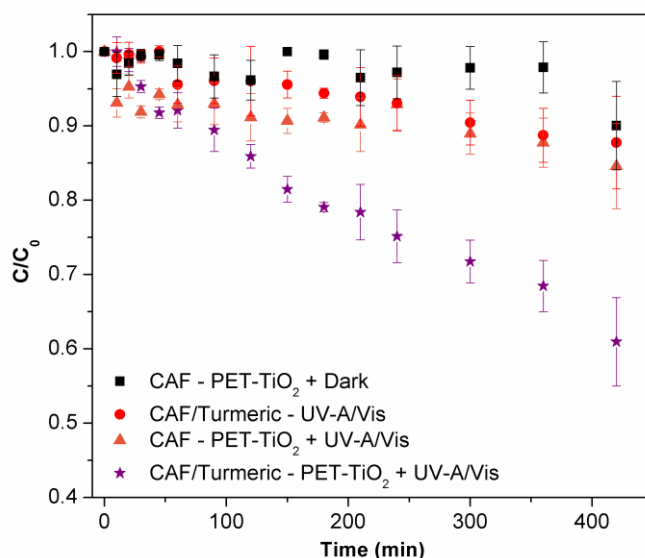
### 5.3 Results and Discussion

In this chapter, the photocatalytic activity of the titania HiPIMS-coated PET was assessed in terms of the degradation of caffeine in laboratory scale under UVA-Vis irradiation and under solar simulator. The assessment includes the monitoring of the pollutant concentration through UV-Vis spectrophotometry, the evaluation of dissolved organic matter through DOC analysis, the confirmation of the oxidation through ESI-MS and the toxicity assessment with *Aliivibrio fischeri* of the treated and untreated water solution.

#### 5.3.1 Photocatalytic degradation of caffeine under UV-A/Vis irradiation

The photocatalytic activity of the studied material was evaluated in terms of the degradation of caffeine (CAF), an indicator of anthropogenic pollution, mediated by the photosensitizer curcumin (from natural turmeric). Firstly, a round of experiments in the dark showed that there was no significant effect of adsorption of the CAF molecule on three different new samples of the studied photocatalytic surface for 420 min, as can be seen in Figure 5.2. Less than 12% of variability of the caffeine concentration was observed during the 7 h adsorption experiments (Figure 5.2 – black squares).

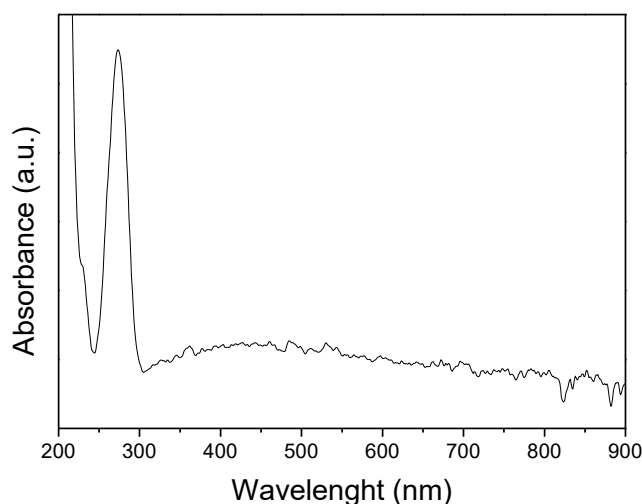
**Figure 5.2-** CAF removal during adsorption (PET-TiO<sub>2</sub>+ Dark), photocatalysis (PET-TiO<sub>2</sub> + UV-A/Vis), photolysis assisted by turmeric (Turmeric - UV-A/Vis) and photocatalysis assisted by turmeric (Turmeric - PET-TiO<sub>2</sub> - UV-A/Vis) (n=3).



In agreement with the results achieved with the model pollutant CBZ in the previous Chapter, the adsorption capabilities of the material are rather low, therefore, it is expected that the improvement of these properties could enhance the overall photocatalytic process. This subject, however, is not discussed in this research.

A UV-Vis spectrophotometry scan of the caffeine solution (Fig. 5.3) predicted the caffeine molecule photostability already reported in the literature (PADHYE *et al.*, 2014). The caffeine molecule has a strong absorbance peak at 273 nm but does not significantly absorb radiation in the UV-A/Vis region. Therefore, it is expected that the caffeine molecule does not suffer photolysis by the radiation emitted by the lamps used in this work (Fig. 4.1).

**Figure 5.3** - UV-Vis spectrum of the caffeine aqueous solution.



The reactor optical behavior was studied through actinometry and the quantum yield ( $\phi$ ) of the stimulant photodegradation was calculated at  $1.34 \cdot 10^{-4}$ . These results agree with the literature concerning the high photostability of the caffeine molecule (PADHYE *et al.*, 2014; STACKELBERG *et al.*, 2004). Indeed, photolysis experiments also confirmed the expectations and the caffeine molecule remained stable during the seven-hour photolysis experiment (Fig. 4.2 – red circles).

Photocatalytic degradation of CAF under UV-A-Vis irradiation in the presence of the coated PET-TiO<sub>2</sub> showed that the reactions did not present fast kinetics (orange triangles in Fig. 5.2) and the addition of a natural photosensitizer, turmeric, was evaluated in order to improve the degradation of the recalcitrant model pollutant.

In agreement with what was observed in Chapter 4, the photocatalytic degradation of CAF in the presence of both turmeric and the titania-coated PET, on the other hand (Fig. 5.2 – purple stars), achieved a relevant reduction of the characteristic peak of caffeine (up to 39%) as well as almost a complete visible reduction of the turmeric peak.

The pseudo-first-order rate constants for the photocatalysis process assisted by turmeric averaged 0.0027 min<sup>-1</sup> (standard deviation = 0.000186). These results are in the same order of magnitude of the ones obtained by a P25 TiO<sub>2</sub> (Evonik) film studied by (MARQUES *et al.*, 2013).

The turmeric peak ( $\lambda_{\max}$ = 420 nm) suffered a substantial decay during both photolysis and photocatalysis experiment and there was a visual and spectrophotometric removal of the yellowish color after 2 hours of photolysis. This was expected since curcumin, the main yellow bioactive component of turmeric, presents a strong and intense characteristic absorption band in the 350–480 nm wavelength region (PATRA & BARAKAT, 2011).

These results indicate that photosensitization of titania thin films with natural turmeric showed a synergistic effect on the removal of both model pollutants: the fungicide CBZ (studied in Chapter 4) and the pharmaceutical CAF. It was possible to use a natural non-toxic colored compound in order to promote photosensitization and therefore enhance the photocatalytic degradation of the different recalcitrant pollutant of emerging concern in water, achieving similar results.

Indeed, some authors have already used curcumin in order to improve photocatalytic processes, and Abou-Gamra & Ahmed (2016) synthesized-TiO<sub>2</sub> coupled with curcumin in its inner structure. The authors realized that the addition of curcumin into the titania structure can shift the apparent optical band-gap of the semiconductor to the visible region (ABOU-GAMRA & AHMED, 2016). In this sense, Polyakov and coworkers studied that water-soluble complexes of carotenoids could enhance the photocatalytic activity of TiO<sub>2</sub> nanoparticles under visible light (POLYAKOV *et al.*, 2010).

The photocatalytic experiments were performed at mild and environment-friendly conditions, without the addition of strong chemicals and reactants. Regarding pH and temperature monitoring, there was a slight decrease of pH values (starting at around 8 and ending at around 7) as well as an increase in aqueous solution temperature (starting at about 18°C - room temperature - and ending at 23°C).

These types of photocatalytic PET surfaces could be easily scalable and utilized in polishing ponds at wastewater treatment plants (WWTP) as a passive treatment for CEC removals, for example. Moreover, low-cost photoreactors, such as Raceway Ponds (CARRA; GARCÍA SÁNCHEZ; *et al.*, 2014), can be designed and constructed with these materials, since PET is flexible and easily molded into irregularly shaped features. Moreover, this system can take advantage of renewable solar irradiance, providing a straightforward solution to the degradation of CECs from water sources using a sustainable and economical process.

### 5.3.2 Study of CAF oxidation via ESI-MS

The CAF oxidation was also monitored by electrospray ionization (ESI-MS). CAF ( $C_8H_{10}N_4O_2$ ) presents a molecular weight of  $194.194 \text{ g}\cdot\text{mol}^{-1}$  and the protonated CAF molecule ( $M+H^+$ ) can be identified as the ion of  $m/z = 195$ .

Figure 5.4 shows the ESI-(+)-MS spectrum from the caffeine standard solution at the same concentration adopted in the photocatalytic treatment, used to establish the conditions for all analyses, with an intense ion of  $m/z = 195$ , corresponding to protonated caffeine. It is also noticeable an intense peak at  $m/z = 217$ , which correspond to Caffeine+Sodium ( $M+Na^+$ ).

**Figure 5.4** – ESI-(+)-MS spectrum from the caffeine standard solution.

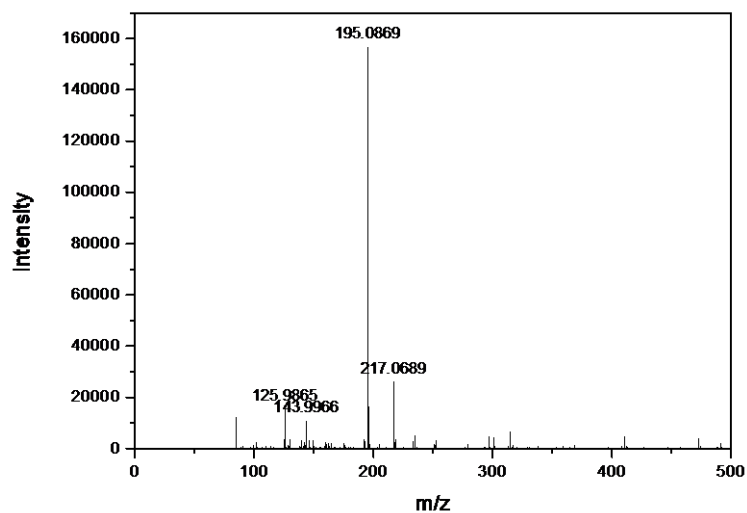
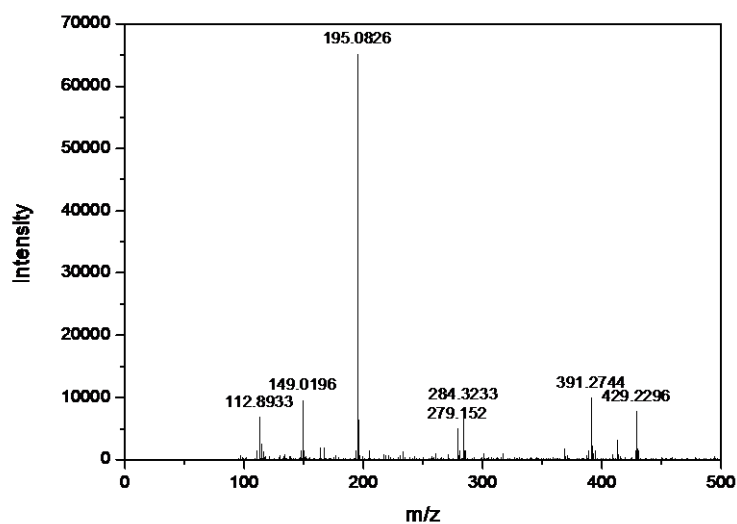


Figure 5.5 shows the ESI-(+)-MS spectrum from the caffeine with turmeric solution submitted to the photocatalytic treatment with the TiO<sub>2</sub>-coated PET sheets.

**Figure 5.5** - ESI-(+)-MS spectrum from the photocatalytically-treated solution of caffeine and turmeric.



Comparing Fig. 5.5 with Fig. 5.4, it is possible to see that the photocatalytic degradation of CAF in the presence the PET-TiO<sub>2</sub> surface and turmeric resulted in a high loss of the m/z =

195 signal intensity, associated with CAF oxidation, in agreement with the data observed by absorbance decay (Fig. 5.2).

### 5.3.3 Organic matter removal

Organic matter removal was assessed through DOC analysis. Similarly, with what was observed in Chapter 4, these analyses were challenging due to the low values of the CAF pure aqueous solution. Theoretically, the CAF solution at the concentration of 15.5  $\mu\text{M}$  would present a total organic carbon (TOC) of 1.48  $\text{mg}\cdot\text{L}^{-1}$ , which is a value in the lower limit of the equipment detection capability. The water matrix could slightly increase the organic matter content, but not in an extensive range since ultrapure water was used as the aqueous phase for the bench experiments. The addition of the turmeric, however, increased the initial DOC of the solution and raised it to a better threshold of analytical performance. The DOC results are summarized in Table 5.1.

**Table 5.1** – Summary of organic matter removal of the CAF aqueous solution through DOC measurements by the different processes.

Sample	Initial ( $\text{mg}\cdot\text{L}^{-1}$ )	Final ( $\text{mg}\cdot\text{L}^{-1}$ )	Removal (%)
Adsorption assisted by turmeric (turmeric + PET-TiO <sub>2</sub> + Dark)	82.92	79.25	4.42
Photolysis assisted by turmeric - (turmeric + UV-A/Vis)	86.21	81.64	5.30
Photocatalysis (PET-TiO <sub>2</sub> + UV-A/Vis)	5.29	4.58	13.42
Photocatalysis assisted by turmeric - (turmeric + PET-TiO <sub>2</sub> + UV-A/Vis)	84.37	18.96	77.53

Similarly to what was observed with the CAF absorbance decay (Fig. 5.2), it is possible to see that adsorption and photolysis assisted by turmeric were not able to impressively reduce the organic matter content (Table 5.1) of the turmeric-CBZ solution. Table 5.1 also shows the effect of DOC increasing due to the addition of turmeric to the solution. The initial DOC concentration of the CBZ solution (without turmeric) in the photocatalysis process was analyzed at  $5.29 \text{ mg}\cdot\text{L}^{-1}$  while the initial DOC concentration of the turmeric-CBZ solution was measured at  $82.92\text{-}86.21 \text{ mg}\cdot\text{L}^{-1}$ . Nevertheless, there was a significant organic matter removal by the photocatalytic process assisted by turmeric, achieving 77.53% of DOC abatement.

### 5.3.4 Acute ecotoxicity assessment

In order to verify if the UV-A/Vis photocatalytic process assisted with turmeric was able to remove the initial toxicity of the CAF aqueous solution and in order to evaluate the possibility of an appearance of toxic byproducts, acute ecotoxicity was evaluated by *Aliivibrio fischeri* bioassay.

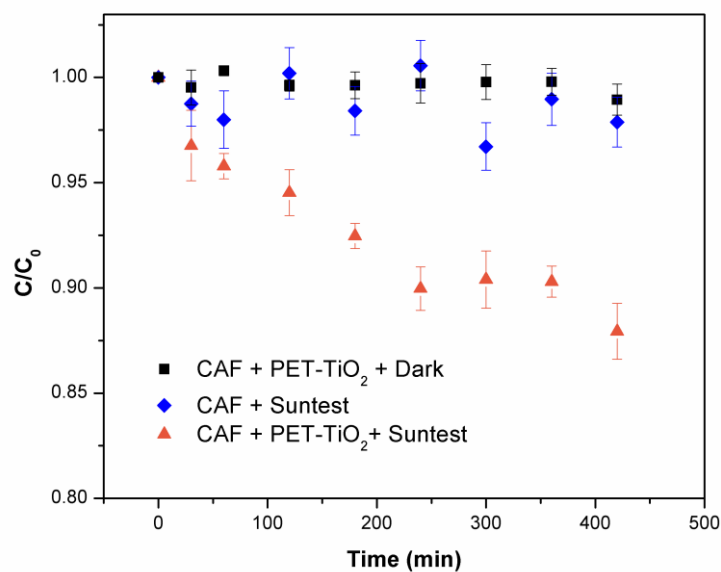
Ecotoxicity results by *Aliivibrio fischeri* showed the photocatalytic treatment assisted by turmeric could remove the toxicity of the initial solution of caffeine. The CAF aqueous solution presented initial a.T.U. value of 3.89 ( $EC_{50} = 25.69$ ) which is considered toxic and after the photocatalytic treatment, a.T.U. was remarkably reduced to 0.23 ( $EC_{50} = 433.30$ ), which is classified as non-toxic. Therefore, in this case, the proposed treatment was able to remove the toxicity of the water solution.

### 5.3.5 Photocatalytic degradation of CAF under simulated solar irradiation

The photocatalytic activity of the PET-TiO<sub>2</sub> was also assessed by the degradation of caffeine in the Suntest CPS+, under daylight simulated solar irradiation. Periodically collected samples were analyzed by UV-Vis spectrophotometry in order to assess the pollutant concentration and the results are shown in Fig. 5.6.

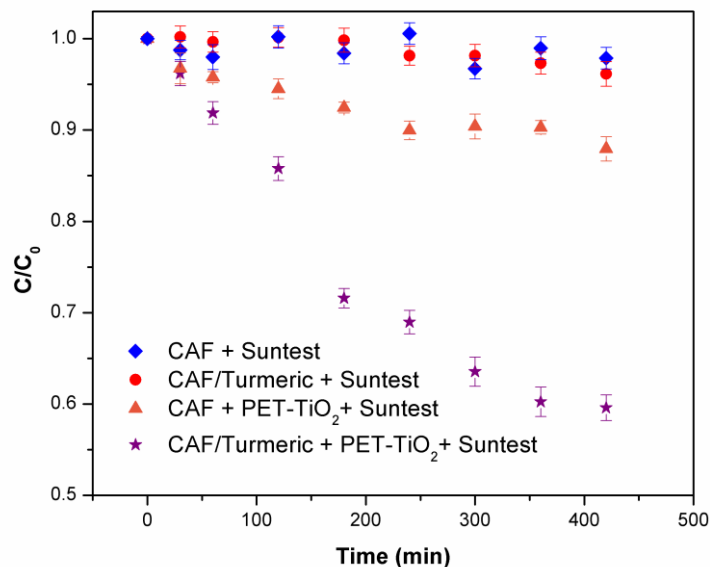


**Figure 5.6-** CAF removal during adsorption (PET-TiO<sub>2</sub>+ Dark), photolysis (Suntest) and photocatalysis (PET-TiO<sub>2</sub> + Suntest) (n=3).



Agreeing with what was observed in the UV-A/Vis photoreactor, the CAF molecule was not adsorbed in the material's surface (Fig. 5.6 – black squares) and it did not suffer significant photolysis (Fig. 5.6 – blue lozenges). In the presence of the photocatalytic surface, it was possible to see a 12% decay of the CAF concentration. This photocatalytic test was also able to slightly minimize the organic matter concentration (DOC) of the sample from 4.79 to 4.08 mg·L<sup>-1</sup>, which corresponds to a 14.82% of DOC abatement. Turmeric assisted photocatalysis was also performed in the Suntest CPS+ chamber. Results are shown in Fig. 5.7.

**Figure 5.7-** CAF removal during photolysis (Suntest), photolysis assisted by turmeric (Turmeric + Suntest), photocatalysis (PET-TiO<sub>2</sub> + Suntest) and photocatalysis assisted by turmeric (Turmeric + PET-TiO<sub>2</sub> + Suntest) (n=3).



In the presence of turmeric as a visible-light photosensitizer, the photocatalytic process was able to remove up to 40% of the CAF initial concentration, as it is shown in Figure 5.7 (purple stars). These results confirm the synergetic effect of the photocatalytic surface (PET-TiO<sub>2</sub>) and the turmeric suggested by the results with the UV-A/Vis photoreactor.

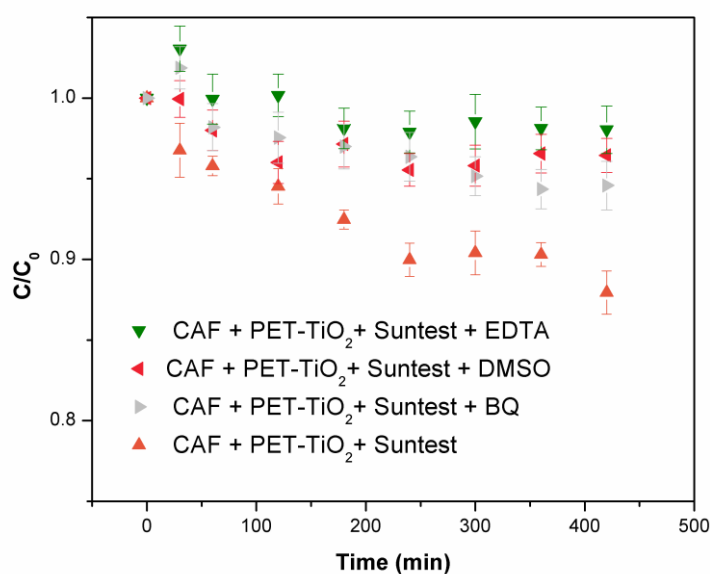
Interestingly, the acute ecotoxicity by *Aliivibrio fischeri* of the CAF water solution was reduced from the a.T.U. value of 3.89 (EC<sub>50</sub> = 25.69) to the value of 1.56 (EC<sub>50</sub> = 64.11). Those two values are considered toxic but the treatment was able to remove 60% of the toxicity of the treated water. The maximum a.T.U. value which the sample is still considered non-toxic is 1.21. Therefore, values above this one may be classified as toxic (DA COSTA *et al.*, 2018; STARLING *et al.*, 2017).

It is important to register that there was evaporation during the experiments in the Suntest CPS+ due to the venting used to cool the lamp and the electronic circuit of the chamber. In order to mitigate this effect, different attempts were tested and the volume was measured and the evaporated water was adjusted with ultrapure water at each sampling time.

### 5.3.6 Elucidation of involved radical species via trapping reactions

The main photoactivated species involved in the photooxidation of organic compounds include superoxide radicals ( $\cdot\text{O}_2^-$ ), hydroxyl radicals ( $\text{HO}\cdot$ ) and photogenerated holes ( $\text{h}^+$ ). In order to elucidate which of these species played the most important roles on the photocatalytic degradation of CAF, the process was studied through the use of  $\text{HO}\cdot$  (dimethyl sulfoxide, DMSO),  $\cdot\text{O}_2^-$  (benzoquinone, BQ) and  $\text{h}^+$  (ethylenediaminetetraacetic acid, EDTA) trapping agents. The results of the trapping reactions with the CAF solution without turmeric are shown in Fig. 5.8.

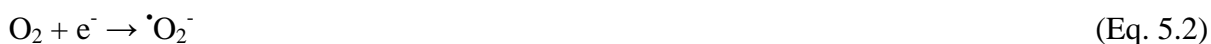
**Figure 5.8-** CAF removal during photocatalysis (PET-TiO<sub>2</sub> + Suntest), photocatalysis with the  $\cdot\text{O}_2^-$  trapping agent (PET-TiO<sub>2</sub> + Suntest + BQ), photocatalysis with the  $\text{HO}\cdot$  trapping agent (PET-TiO<sub>2</sub> + Suntest + DMSO), and photocatalysis with the  $\text{h}^+$  trapping agent (PET-TiO<sub>2</sub> + Suntest + EDTA) (n=3).



From the degradation of CAF aqueous solution over PET-TiO<sub>2</sub> under the simulated solar irradiation presented in Fig. 5.8, it is possible to see that all trapping agents result in, to some extent, suppression of the degradation rate of CAF, which suggests that all 3 species ( $\cdot\text{O}_2^-$ ,  $\text{HO}\cdot$  and  $\text{h}^+$ ) may have been generated on the photocatalytic surface. Even though the kinetics between the different reactions presented in Fig. 5.8 is not so different, it seems that the  $\text{h}^+$  scavenger EDTA (Fig. 5.8 – upside down green triangle) had the most important effect and

therefore results suggest that the photogenerated holes ( $h^+$ ) played a more important role than reactive oxygen species ( $\cdot O_2^-$  and  $HO\cdot$ ) in this case.

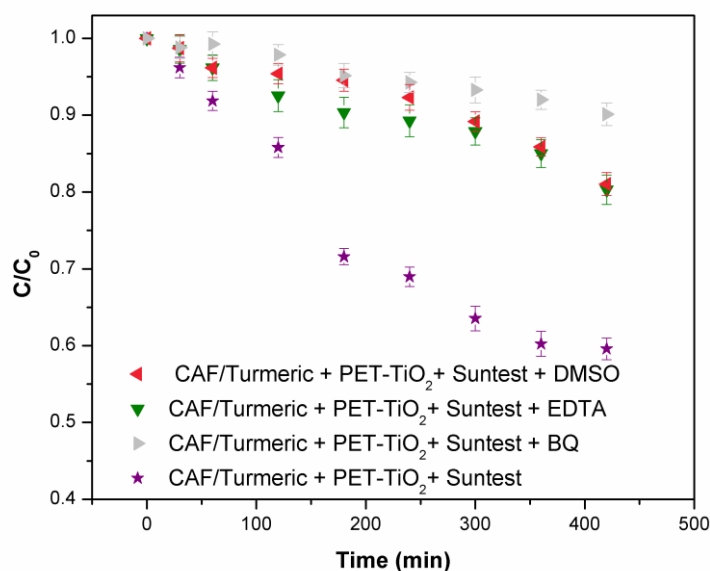
The following simplified photoreactions might occur in the photocatalytic media (DONG *et al.*, 2013):



This simplified model suggests that at the beginning of the photocatalytic reactions, the photogenerated electrons and holes migrate to the surface of the catalyst (PET-TiO<sub>2</sub>). Then the photogenerated electrons are captured by dissolved O<sub>2</sub> in the CAF solution to produce  $\cdot O_2^-$  radicals (Eq. 5.2). The generated  $\cdot O_2^-$  radicals can directly oxidize the CAF molecule (Eq. 5.6) simultaneously as the photogenerated holes (Eq. 5.5). Moreover, the  $h^+$  can also react with H<sub>2</sub>O and/or OH<sup>-</sup> ions to produce HO $\cdot$  (Eq. 5.3 and 5.4), which can also oxidize the CAF (Eq. 5.7) molecule (DONG *et al.*, 2013).

In the presence of the turmeric sensitizer in the reaction media, the results of the trapping reactions with the CAF solution are shown in Fig. 5.9.

**Figure 5.9-** CAF removal during photocatalysis assisted by turmeric (Turmeric + PET-TiO<sub>2</sub> + Suntest), photocatalysis assisted by turmeric with the  $\cdot\text{O}_2^-$  trapping agent (Turmeric + PET-TiO<sub>2</sub> + Suntest + BQ), photocatalysis assisted by turmeric with the HO $\cdot$  trapping agent (Turmeric + PET-TiO<sub>2</sub> + Suntest + DMSO), and photocatalysis assisted by turmeric with the h<sup>+</sup> trapping agent (Turmeric + PET-TiO<sub>2</sub> + Suntest + EDTA) (n=3).



It is again possible to see that all trapping agents result in, to some extent, suppression of the degradation rate of CAF, which suggests that all 3 species ( $\cdot\text{O}_2^-$ , HO $\cdot$  and h<sup>+</sup>) may have been generated on the photocatalytic surface. It is possible to see that the kinetics between the EDTA (Fig. 5.9 – upside down green triangle) and DMSO (Fig. 5.9 – red triangle facing left) reactions presented in Fig. 5.9 is similar, which indicates that the effects of h<sup>+</sup> and HO $\cdot$  are in the same greatest of importance in this sensitized photocatalytic reactions. Fig. 5.9 (gray triangle facing right) shows that the BQ trapping agent ( $\cdot\text{O}_2^-$  scavenger) had the most important effect on the reaction suppression and therefore results suggest that the superoxide radical ( $\cdot\text{O}_2^-$ ) played a more important role than the other species (h<sup>+</sup> and HO $\cdot$ ) in this case.

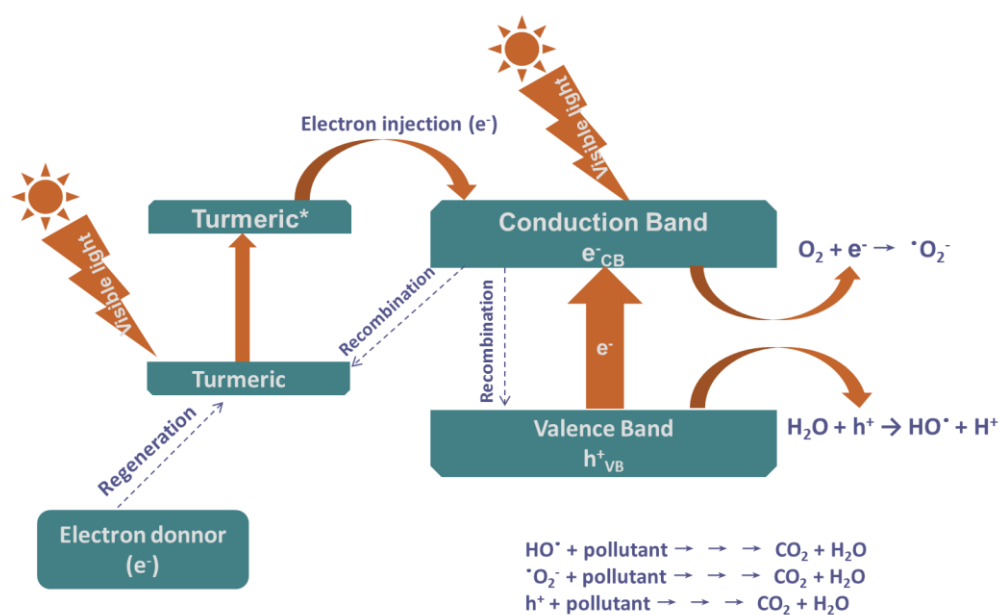
It is reported in the literature that the additional formation of superoxide radicals ( $\cdot\text{O}_2^-$ ) may be responsible for the increase in the quantum yield and photocatalytic activity of sensitized photocatalytic process (ILIEV & TOMOVA, 2002; ZHANG *et al.*, 2016). The visible-light excited photosensitizer particle promotes an electron transfer to the conduction band of TiO<sub>2</sub> catalyst or the Ti(IV) can be converted to Ti(III) by electron capture, and in the presence of

the sensitizer, the holes are trapped by the sensitizer, producing the corresponding radical cation (POLYAKOV *et al.*, 2010) (Eq. 5.8). This electron afterward reacts with solubilized oxygen (Eq. 5.2) promoting the formation of superoxide radicals. The photogeneration of the other involved species may still happen according to equations 5.3, 5.4, 5.5 and 5.7. The process may, therefore, be summarized in the following reactions:



Therefore, the obtained results that the  $\cdot\text{O}_2^-$  played the most important role on the overall photochemical process may indicate that there is a synergetic effect between the photosensitization and photocatalytic process, leading to an increase in the photogeneration of  $\cdot\text{O}_2^-$  radicals and consequently to an increase in the pollutant degradation. A schematic illustration of the combination of the photosensitization and photocatalytic processes is presented in Figure 5.10, adapted from Banerjee *et al.* (2015) and Zhang *et al.* (2016).

**Figure 5.10-** Simplified illustration of the photocatalysis assisted by turmeric process. Adapted from Banerjee *et al.* (2015) and Zhang *et al.* (2016).



The suggested mechanism (Fig. 5.10) includes the photoexcitation of the turmeric photoactive compounds (sensitizer) followed by electron injection into the conduction band of the photocatalyst. In the presence of solubilized oxygen, superoxide radicals may be formed and therefore this species apparently play an important role in photosensitized photocatalysis. Fig. 5.10 also shows possible recombination paths and the formation of hydroxyl radicals ( $\text{HO}^{\bullet}$ ), photogenerated holes ( $\text{h}^+$ ) and superoxide radicals ( $\text{O}_2^{\bullet -}$ ) through the excitation of the semiconductor (photocatalysis).

#### **5.4 Concluding Remarks**

The results presented in this chapter confirmed the viability of the proposed process regarding the use of the titania-coated polymeric substrates characterized in Chapter 3 and tested in Chapter 4 as passive photocatalytic materials for water treatment, degrading a contaminant of emerging concern and decreasing the water solution initial toxicity, achieving the removal of toxicity of CAF aqueous solution in the UV-A/Vis process.

The experiments using simulated solar irradiation agreed with the UV-A/Vis in terms of CAF degradation and therefore suggest that the studied material may be able to perform similarly under natural solar irradiation if equivalent conditions are preserved. The reactions with trapping agents were able to identify that the reactive oxygen species  $\cdot\text{O}_2^-$ ,  $\text{HO}\cdot$  and  $\text{h}^+$  participated in the reaction and that, in the case of the photosensitized process, superoxide radical ( $\cdot\text{O}_2^-$ ) played a more important role, suggesting a possible synergetic effect between photocatalysis and photosensitization.

In conclusion, the presented results corroborate to the thesis that the proposed process with photocatalytic surfaces photosensitized with natural turmeric may be a sustainable and straightforward passive solution for the degradation of emerging contaminants from water sources.



## **CHAPTER 6. APPLICATION OF THE PHOTOCATALYTIC SURFACES AT SEMI-PILOT SCALE UNDER SOLAR IRRADIATION FOR WATER TREATMENT**

This chapter discusses the scale-up of the studied technologies to semi-pilot scale solar reactors. The application of the HiPIMS-coated PET photocatalytic surfaces for water treatment was assessed against caffeine under natural solar radiation in two existing solar reactors in fixed film configurations: Raceway Pond Reactor (RPR) and Compound Parabolic Collector (CPC). The main theoretical principles were already discussed in Chapter 2, while the surface overview and characterization was discussed in Chapter 3 and laboratory tests were presented in Chapters 4 and 5. Chapter 6, therefore, starts with an introduction, presents the methodology and obtained results for the photocatalytic degradation of the pharmaceutical caffeine mediated by the titania-coated PET. The tests were also performed in the presence of food-grade turmeric as a natural photosensitizer.

### **6.1 Introduction**

The applicability of photocatalytic technology for real-scale environmental applications may be still constrained by technical and economic issues that require further investigation. Photoreactor engineering and design may play important roles in enabling the use of this technology in industrial-scale applications.

After the laboratory scale experiments presented in Chapters 4 and 5, it was suggested that the proposed process with photocatalytic surface photosensitized with natural turmeric may be a potential passive solution for the degradation of emerging contaminants from water sources.

In order to study scale-up possibilities from laboratory scale to semi-pilot equipment, the studied photocatalytic surfaces were integrated into solar water treatment reactors already existing in GruPOA (UFMG): a Raceway Pond Reactor (RPR) used by Costa (2017) and coworkers - shown in Figure 6.1(a) - and a Compound Parabolic Collector (CPC) reactor used by Castro and collaborators (2014), shown in Figure 6.1(b). These reactors configurations were selected since they are currently being used by different research groups worldwide and since they are available at GruPOA (UFMG).

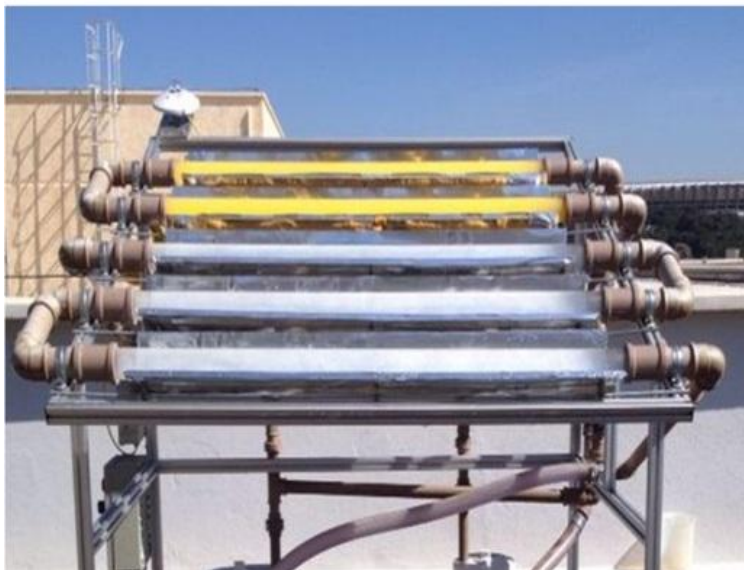
Therefore, the idea of this Chapter is to study the application of the developed process under natural solar radiation in the two semi-pilot solar reactors using caffeine as a model pollutant.

The photocatalytic efficiency will also be evaluated in the presence of turmeric, a natural source of curcumin.

**Figure 6.1(a)** - RPR reactor (GruPOA).



**Figure 6.1(b)** - CPC reactor (GruPOA).



## 6.2 Material and Methods

The photocatalytic degradation of caffeine (15.5  $\mu\text{M}$  aqueous solution) was assessed under natural solar irradiation in the water treatment reactors presented in Figure 6.1(a and b).

A batch fixed film reactor configuration was used in order to evaluate the possibility of passively treating the contaminated water solution with the supported catalytic surface, without the necessity of extra unit operation to separate the catalyst from the treated solution.

Direct solar irradiation experiments were performed on sunny and on partially sunny days (GPS coordinates: S 19 52'10, W 43 57'40, 815 m—WGS84 geodetic datum) for 7 h (420 min) in order to utilize the greatest part of the natural daylight radiation available. Aliquots were collected at given time intervals (0, 30, 60, 120, 180, 240, 300, 360 and 420 min) for UV–VIS (200–900 nm) spectrophotometric evaluation (Micronal AJX-3000PC spectrophotometer, Micronal, Brazil). All experiments were performed at ambient conditions. Temperature and pH were monitored during the experiments.

The global UV irradiance (280–400 nm) was measured with a Kipp & Zonen CMP10 radiometer connected to a data logger (METEON), which records incident UV radiation ( $\text{W}\cdot\text{m}^{-2}$ ) measured at every one minute.

Due to the inherent variation of solar irradiance, the results were also interpreted using accumulated UV energy ( $\text{kJ}\cdot\text{L}^{-1}$ ), in order to compare results obtained in different days and consequently different irradiation conditions. The accumulated UV radiation energy ( $Q_{\text{UV}}$ ) was measured and quantified ( $\text{kJ}\cdot\text{L}^{-1}$ ), according to Eq.6.1.

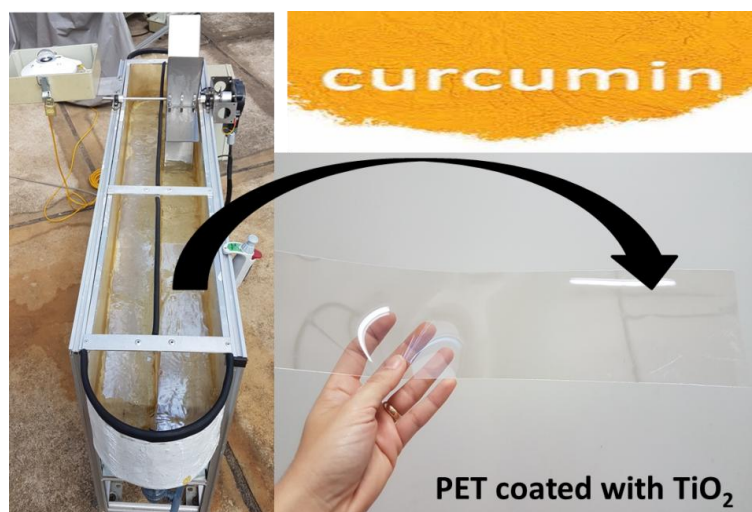
$$Q_{\text{UV},n} = \frac{A}{V_t} \int I_{G,\text{UV}}(t)dt = Q_{\text{UV},n-1} + \Delta t_n \overline{UV}_{G,n} \frac{A_r}{V_t} \quad (\text{Eq 6.1})$$

where  $Q_{\text{UV}}$  is the total accumulated incident UV radiation per liter of water solution, ( $\text{kJ}\cdot\text{L}^{-1}$ ),  $t$  represents the time interval (s),  $I_{G,\text{UV}}$  is the global UV irradiance ( $\text{W}\cdot\text{m}^{-2}$ ),  $A$  is the irradiated area ( $\text{m}^2$ ), and  $V_t$  is the total volume of treated wastewater (L). It is noteworthy that the measurement of the broadband UV radiation (280–400 nm) is considered the most appropriate spectral range to standardize photocatalytic results, as stated by Malato *et al.* (2009).

### 6.2.1 Semi-pilot water treatment assay at RPR solar reactor

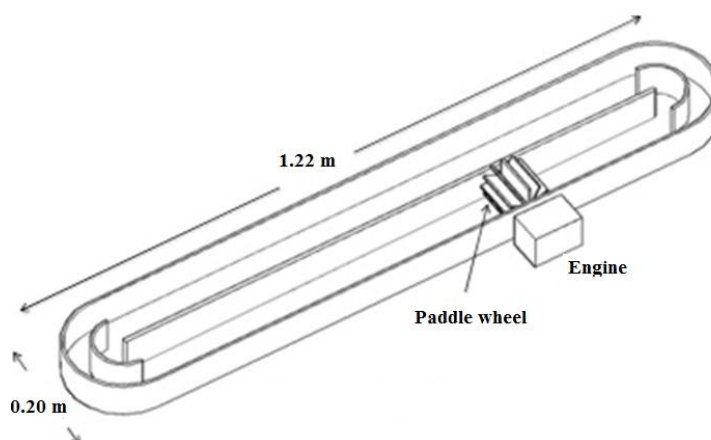
A volume of 12 liters of CAF solution was treated in RPR photoreactor. The bottom of the reactor was completely covered with the catalytic surface (Figure 6.2). The reaction was performed in both the presence and the absence of turmeric.

**Figure 6.2** - RPR reactor with the photocatalytic surface coated with TiO<sub>2</sub>.



The reactor was designed by Costa (2017) and the main dimensions are illustrated in Figure 6.3. Liquid depth, which determines irradiance path length, was set as 5 cm. This value was taken as the common diameter (light path length) used in tubular CPCs reactors (MALATO *et al.*, 2009a; RIVAS *et al.*, 2015). The irradiated area is 0.23 m<sup>2</sup>.

**Figure 6.3** – Illustration of RPR reactor with its main dimensions and components. Adapted from (FREITAS *et al.*, 2017).



The engine of the photoreactor is linked to a variable frequency drive to control the paddles' speed and the rotation was established at around 10 rpm. The reactor was positioned facing the north in order to get the most of incident solar light.

Firstly, a round of experiments under natural sunlight without the PET-TiO<sub>2</sub> was performed in order to access the photolysis. Afterward, a round of experiments with the PET-TiO<sub>2</sub> was performed in the presence and absence of turmeric in order to investigate photocatalysis and photocatalysis assisted by turmeric.

### 6.2.2 Semi-pilot water treatment assay at CPC solar reactor

In the CPC reactor, the photocatalytic surface was cylindrically positioned in the center of one of the reactors' glass tubes, as can be seen in Figure 6.4.

**Figure 6.4(a)** - CPC reactor with cylinder coated with TiO<sub>2</sub>.



**Figure 6.4(b)** – Details of the glass tube of the CPC reactor configured with the cylinder coated with TiO<sub>2</sub>.

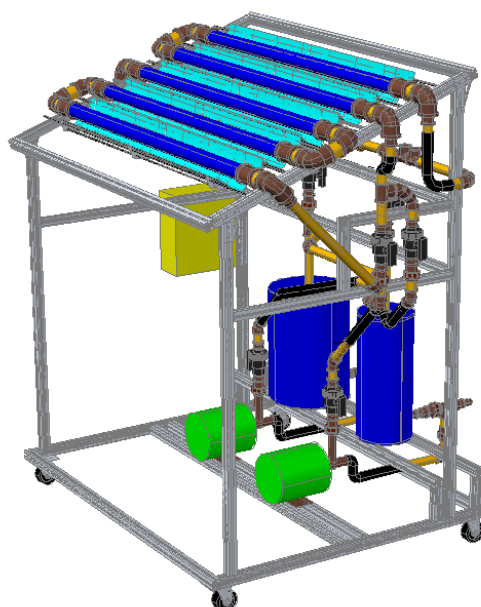


The utilized CPC reactor was dimensioned by Castro *et al.* (2014) and its illustration with its main components is shown in Fig. 6.5. The design of the reactor includes two different water tanks and a *by-pass* system which makes it feasible to work independently with 2 or 3 tubes of the CPC or with all the 5 tubular reactors. In this work, 12 L of CAF solution was selected and the 2 upper tubes were used. In this situation, the irradiated volume corresponds to 4 L.

The reactor has a slope of 20°, which corresponds to the latitude of Belo Horizonte and it was positioned facing the north in order to get the most of incident solar light.

The first step consisted of triplicate experiments under natural sunlight without the PET-TiO<sub>2</sub> in order to verify the effect of solar photolysis on the pollutant concentration. Subsequently, a round of solar experiments with the PET-TiO<sub>2</sub> was performed in the presence and absence of turmeric in order to investigate the effects of both photocatalysis and photocatalysis assisted by turmeric.

**Figure 6.5** – Illustration of CPC reactor with its main components.



### **6.2.3 Organic matter assessment**

Organic matter mineralization of original CAF water solution and after each photocatalytic assessment was monitored through Dissolved Organic Carbon (DOC) analysis. Samples were filtered with C40 quantitative filter paper (125mm) to remove suspended solids and subsequent analyses of DOC were performed in TOC-V CPN equipment (Shimadzu).

### **6.2.4 Acute toxicity assessment**

Finally, in order to investigate the toxicity of possible by-products formed during the photocatalytic reaction, acute ecotoxicity tests were conducted using the luminescent marine bacteria *Aliivibrio fischeri* (Microtox®) according to the methodology detailed in Chapter 4. Toxicity results were analyzed using the a.T.U. (30 minutes) values.

### 6.3 Results and Discussion

This section presents the results of CAF degradation under natural solar irradiation in semi-pilot reactors: RPR and CPC. The results were obtained in the presence and in the absence of turmeric.

#### 6.3.1 Semi-pilot water treatment assay at RPR solar reactor

The solar experiments in the RPR reactor were performed for 7 h in sunny days, even though there were often some clouds around the university which might have lowered the global irradiation received on the catalyst surface.

Firstly, a run of 3 solar photolysis experiments was performed. In these experiments, there was no catalyst added in the reaction, only the 15.5  $\mu\text{M}$  CAF aqueous solution under natural solar irradiation. In this case, due to the larger amount of water involved in the reactions, distilled water was used for the aqueous solution differently than the ultrapure water used in the previous chapters. A photocatalytic run, with the presence of the PET-TiO<sub>2</sub>, was performed after the photolysis series. These results of CAF degradation with time of reaction are summarized in Fig. 6.6.

**Figure 6.6** – CAF removal during photolysis (CAF+ RPR) and photocatalysis (CAF+ PET-TiO<sub>2</sub> + RPR) under natural sunlight in the RPR photoreactor (n=3) in a temporal scale.

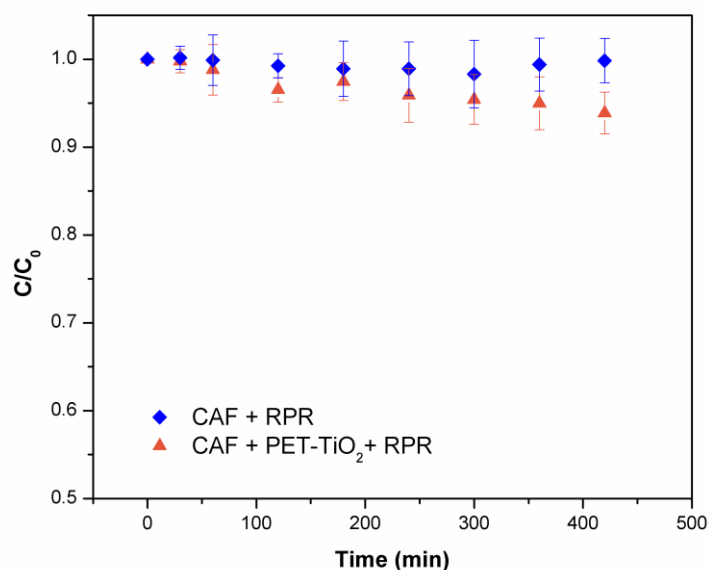
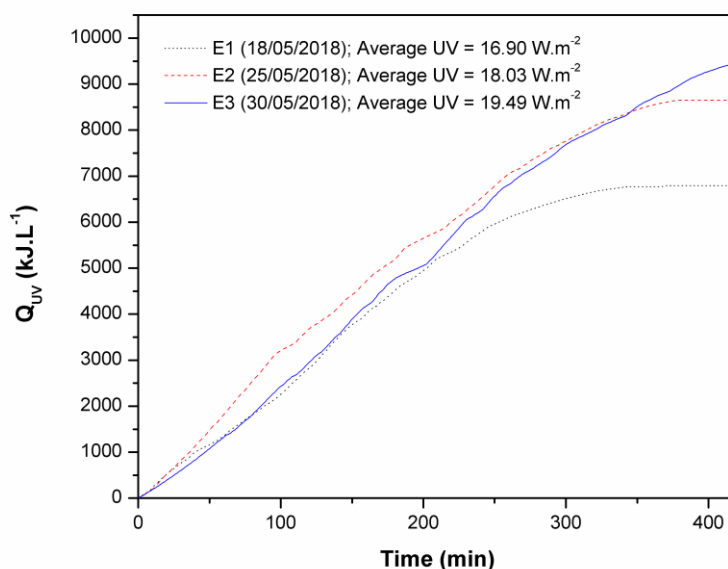


Fig. 6.6 and statistical analysis (t-test,  $\alpha=0.05$ ) showed that there was no significant difference between the means of photolysis (blue lozenges) and photocatalysis (orange triangles) in the RPR reactor for CAF solution without the turmeric in a temporal scale.

Since each experiment was performed in a different day and was therefore submitted to a different solar irradiation condition, the involved energy,  $Q_{UV}$  (Eq. 6.1), which is the total accumulated incident UV radiation per liter of water solution, ( $\text{kJ}\cdot\text{L}^{-1}$ ), was measured at each experiment. The accumulated solar UV radiation  $Q_{UV}$  ( $\text{kJ}\cdot\text{L}^{-1}$ ) is reported with the reaction time for the photocatalytic reaction (CAF+ PET-TiO<sub>2</sub> + RPR) in Figure 6.7.

**Figure 6.7** – Evolution of accumulated solar UV radiation ( $Q_{UV}$ ) during each photocatalysis (CAF + PET-TiO<sub>2</sub> + RPR) experiment (E1, E2, and E3) with reaction time.



It is possible to see in Fig. 6.7 that experiment 3 (E3) received the highest amount of accumulated radiation while experiment 1 (E1) received the lowest. It is also important to note here that these experiments received average UV irradiance below  $20 \text{ W}\cdot\text{m}^{-2}$ , which is lower than expected. In the Suntest CPS+ experiments, for example, the irradiance was set to an average of around  $30 \text{ W}\cdot\text{m}^{-2}$ . In order to simplify the comparison between the 3 different experiments, a figure of merit of CAF removal divided by the accumulated energy  $Q_{UV}$  ( $\text{kJ}\cdot\text{L}^{-1}$ )<sup>1)</sup> was calculated and the results are presented in Fig. 6.8.



**Figure 6.8** – Evaluation of CAF removal per accumulated solar UV radiation ( $Q_{UV}$ ) during each photocatalysis (CAF + PET-TiO<sub>2</sub> + RPR) experiment (E1, E2, and E3).

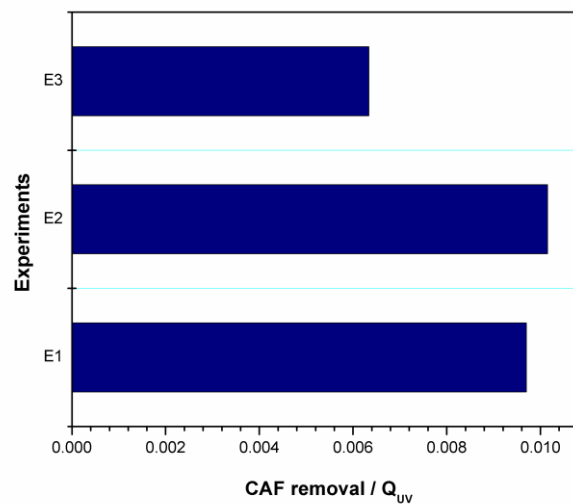
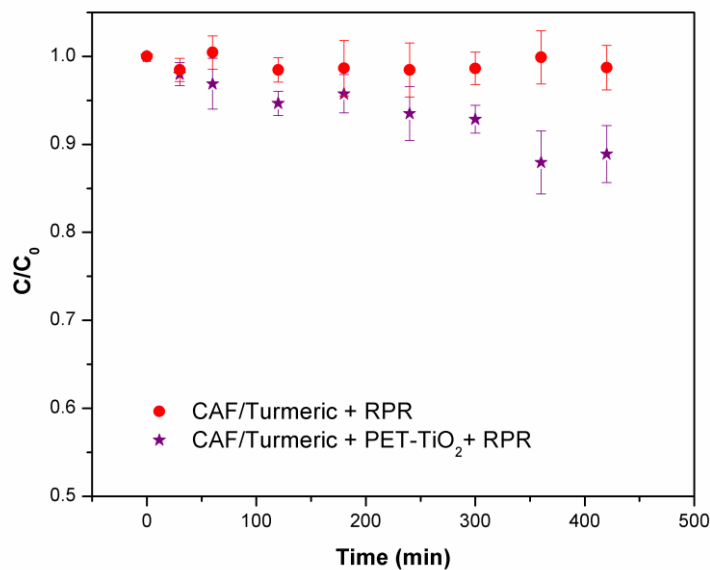


Figure 6.8 shows that experiment 2 (E2) of photocatalysis under natural sunlight in the RPR reactor provided the best CAF removal per accumulated solar UV energy ( $Q_{UV}$ ) received.

Consequently, a run of 3 solar photolysis assisted by turmeric experiments was performed, followed by a photocatalysis assisted by turmeric run (with the presence of the PET-TiO<sub>2</sub>). These results of CAF degradation with time of reaction are summarized in Fig. 6.9.

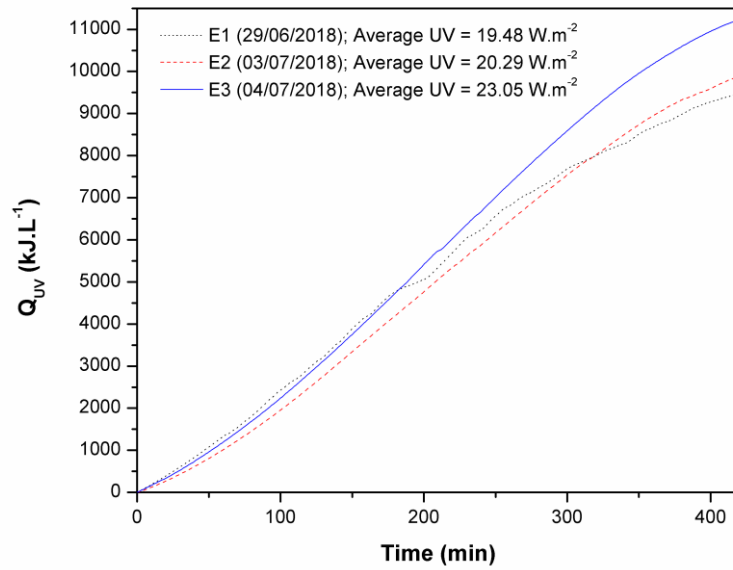
**Figure 6.9** – CAF removal during photolysis assisted by turmeric (CAF/Turmeric + RPR) and photocatalysis assisted by turmeric (CAF/Turmeric + PET-TiO<sub>2</sub> + RPR) under natural sunlight in the RPR photoreactor (n=3) in a temporal scale.



Results shown in Fig. 6.8 demonstrated that photocatalysis assisted by turmeric overperformed photolysis assisted by turmeric. Indeed, statistical analysis of the means (t-test,  $\alpha=0.05$ ) showed a significant difference between the two groups. However, the photocatalysis process assisted by turmeric under natural sunlight did not perform similarly to the observed in previous experiments (Chapter 5), where the experiments achieved around 40% of CAF degradation under simulated solar irradiation. This difference might be explained by the irradiation difference, by the different water matrix, and by the optical path. While in the RPR reactor the optical path length was set at 5 cm, in the Suntest CPS+ experiment, the path length was 2 cm.

The involved energy in each experiment  $Q_{UV}$ , which is the total accumulated incident UV radiation per liter of water solution, ( $\text{kJ}\cdot\text{L}^{-1}$ ), was measured and it is reported with the reaction time for the photocatalytic reaction assisted by turmeric (CAF/Turmeric + PET-TiO<sub>2</sub> + RPR) in Figure 6.10.

**Figure 6.10** – Evolution of accumulated solar UV radiation ( $Q_{UV}$ ) during each photocatalysis assisted by turmeric (CAF/Turmeric + PET-TiO<sub>2</sub> + RPR) experiment (E1, E2, and E3) with reaction time.



It is possible to see in Fig. 6.10 that experiment 3 (E3) received the highest amount of accumulated radiation while experiment 1 (E1) was pretty similar to experiment 2 (E2). In general, the 3 experiments behaved similarly. In order to simplify the comparison between the 3 different experiments, a figure of merit of CAF removal divided by the accumulated energy  $Q_{UV}$  ( $\text{kJ}\cdot\text{L}^{-1}$ ) was calculated and the results are presented in Fig. 6.11.

**Figure 6.11** – Evaluation of CAF removal per accumulated solar UV radiation ( $Q_{UV}$ ) during each photocatalysis assisted by turmeric (CAF/Turmeric + PET-TiO<sub>2</sub> + RPR) experiment (E1, E2, and E3).

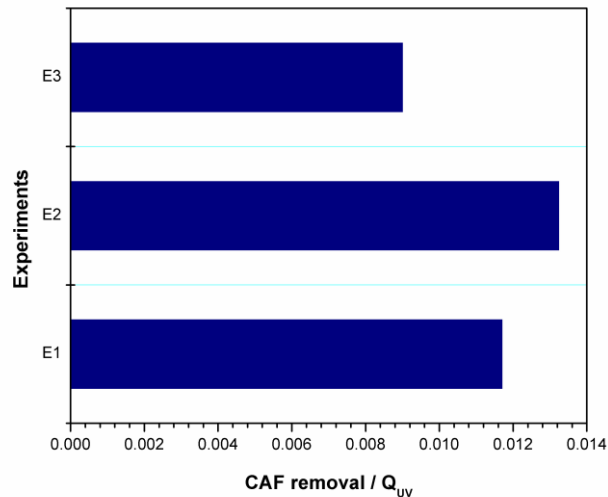
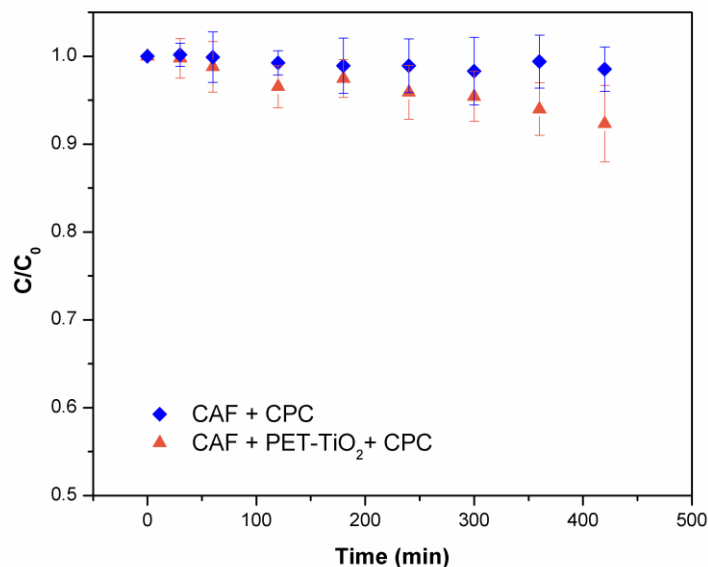


Figure 6.11 shows that experiment 2 (E2) of photocatalysis assisted by turmeric under natural sunlight in the RPR reactor provided the best CAF removal per energy received (accumulated solar UV radiation,  $Q_{UV}$ ).

### 6.3.2 Semi-pilot water treatment assay at CPC solar reactor

The solar experiments in the CPC reactor were performed for 7 h in sunny and partially sunny days. Firstly, a run of 3 solar photolysis experiments was performed, without the addition of the photocatalytic surface, only the 15.5  $\mu\text{M}$  CAF aqueous solution (with distilled water) under natural solar irradiation. After the photolysis series, a photocatalytic run of 3 experiments with the presence of the cylindrical tube coated with  $\text{TiO}_2$  was performed. These results of CAF degradation with time of reaction are summarized in Fig. 6.12.

**Figure 6.12** – CAF removal during photolysis (CAF+ CPC) and photocatalysis (CAF + Tube- $\text{TiO}_2$  + CPC) under natural sunlight in the RPR photoreactor (n=3) in a temporal scale.

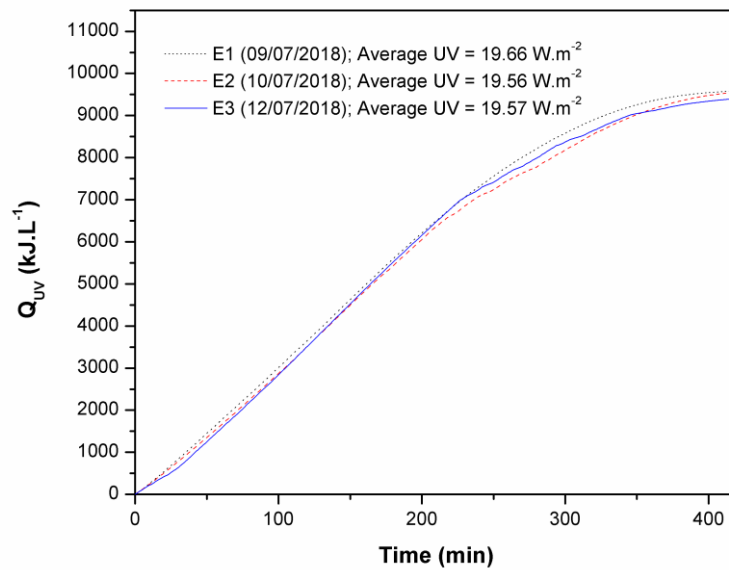


Similarly with what was observed in Fig. 6.6, Fig. 6.12 shows that there was not a significant difference between the photolysis (blue lozenges) and photocatalysis (orange triangles) in the CPC reactor for CAF solution without the turmeric in a temporal scale.

It is noteworthy that there was an impressive temperature elevation during the solar experiments in the CPC reactor. Temperature starts around 20 °C and reached 70°C. Even though the reactor is supposedly closed, the increase in the temperature promoted evaporation of part of the water through an opening in the water tank lid, which hindered the results interpretation. The experiments were repeated and the final volume was measured in an attempt to minimize the evaporation effects.

Since each of the 3 photolysis and 3 photocatalysis experiments was performed in a different day and was therefore submitted to a different solar irradiation condition, the involved energy ( $Q_{UV}$ ) was measured at each experiment. The accumulated solar UV radiation  $Q_{UV}$  ( $\text{kJ}\cdot\text{L}^{-1}$ ) is reported with the reaction time for the photocatalytic reaction (CAF+ Tube-TiO<sub>2</sub> + CPC) in Figure 6.13.

**Figure 6.13** – Evolution of accumulated solar UV radiation ( $Q_{UV}$ ) during each photocatalysis (CAF + Tube-TiO<sub>2</sub> + CPC) experiment (E1, E2, and E3) with reaction time.



It is possible to see in Fig. 6.13 that the 3 experiments were performed under very similar accumulated irradiations. It is also important to note here that these experiments received average UV irradiance below  $20 \text{ W}\cdot\text{m}^{-2}$ , which is lower than expected. In order to simplify the comparison between the 3 different experiments, a figure of merit of CAF removal divided by the accumulated energy  $Q_{UV}$  ( $\text{kJ}\cdot\text{L}^{-1}$ ) was calculated and the results are presented in Fig. 6.14.

**Figure 6.14** – Evaluation of CAF removal per accumulated solar UV radiation ( $Q_{UV}$ ) during each photocatalysis (CAF + Tube-TiO<sub>2</sub> + CPC) experiment (E1, E2, and E3).

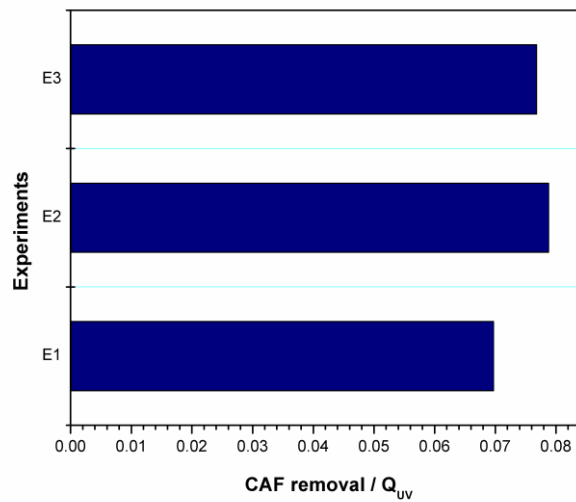
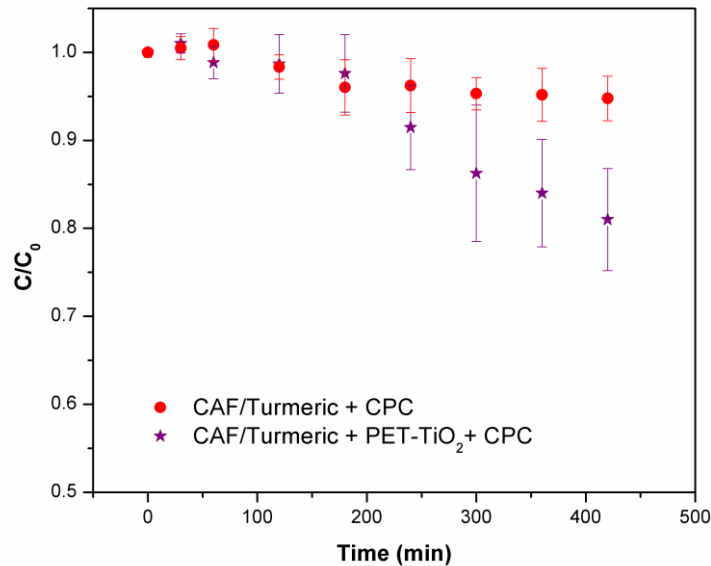


Figure 6.14 shows that experiment 2 (E2) of photocatalysis under natural sunlight in the CPC reactor provided the best CAF removal per energy received (accumulated solar UV radiation,  $Q_{UV}$ ).

Afterward, a run of 3 solar photolysis assisted by turmeric experiments was performed, followed by a photocatalysis assisted by turmeric run (with the presence of the Tube-TiO<sub>2</sub>). These results of CAF degradation with time of reaction are summarized in Fig. 6.15.

**Figure 6.15** – CAF removal during photolysis assisted by turmeric (CAF/Turmeric + CPC) and photocatalysis assisted by turmeric (CAF/Turmeric + Tube-TiO<sub>2</sub> + CPC) under natural sunlight in the CPC photoreactor (n=3) in a temporal scale.

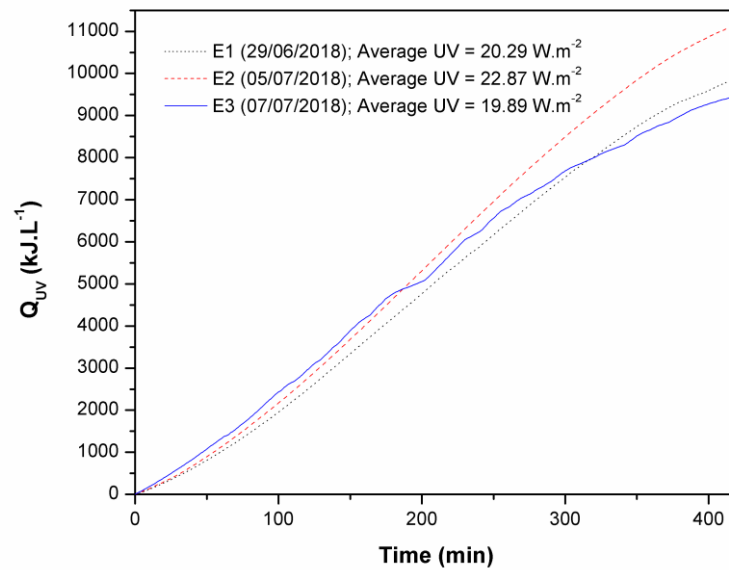


Results shown in Fig. 6.15 demonstrate that photocatalysis assisted by turmeric outperformed photolysis assisted by turmeric and that these experiments also exceeded the results obtained in the RPR reactor in terms of CAF removal. However, the photocatalysis process assisted by turmeric under natural sunlight did not perform similarly to the observed in the solar simulator chamber, where the experiments achieved around 40% of CAF degradation. This difference might be explained by the irradiation difference, by the different water matrix, and by the optical path. While in the CPC reactor the optical path length was set at 5 cm, in the Suntest CPS+ experiment, the path length was 2 cm.

The involved energy in each experiment  $Q_{UV}$ , which is the total accumulated incident UV radiation per liter of water solution, ( $\text{kJ}\cdot\text{L}^{-1}$ ), was measured and it is reported with the reaction time for the photocatalytic reaction assisted by turmeric (CAF/Turmeric + Tube-TiO<sub>2</sub> + CPC) in Figure 6.16.



**Figure 6.16** – Evolution of accumulated solar UV radiation ( $Q_{UV}$ ) during each photocatalysis assisted by turmeric (CAF/Turmeric + Tube-TiO<sub>2</sub> + CPC) experiment (E1, E2, and E3) with reaction time.



It is possible to see in Fig. 6.16 that accumulated UV irradiation behaved similarly during the experiments 1 and 3. The higher accumulated irradiation was achieved in experiment 2. In order to simplify the comparison between the 3 different experiments, a figure of merit of CAF removal divided by the accumulated energy  $Q_{UV}$  ( $\text{kJ}\cdot\text{L}^{-1}$ ) was calculated and the results are presented in Fig. 6.17.

**Figure 6.17** – Evaluation of CAF removal per accumulated solar UV radiation ( $Q_{UV}$ ) during each photocatalysis assisted by turmeric (CAF/Turmeric + Tube-TiO<sub>2</sub> + CPC) experiment (E1, E2, and E3).

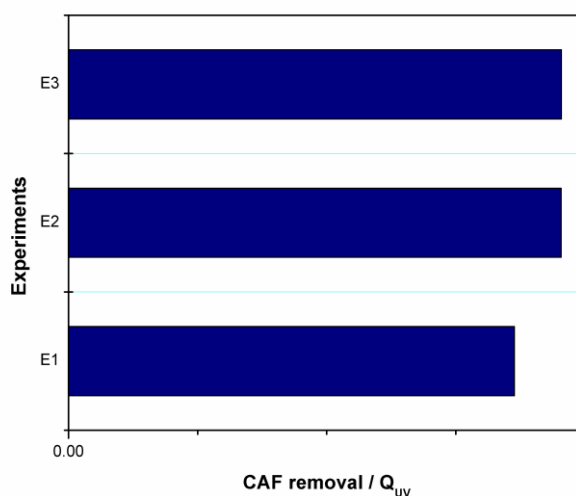
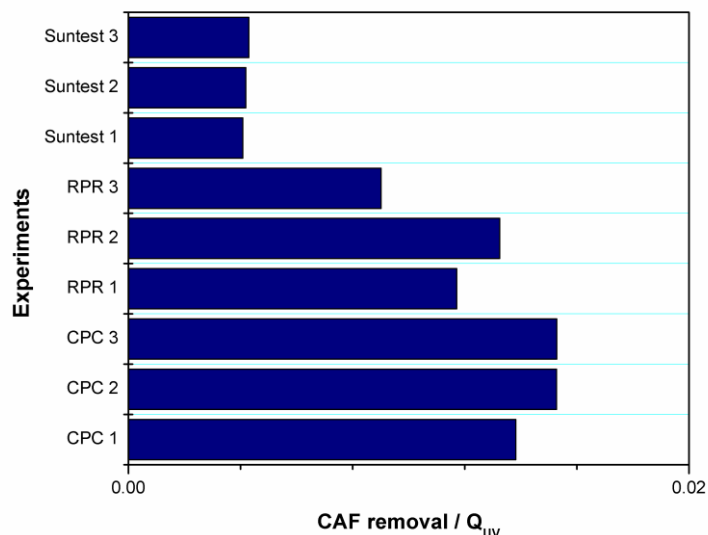


Figure 6.17 shows that experiment 2 (E2) of photocatalysis assisted by turmeric under natural sunlight in the CPC reactor provided the best CAF removal per energy received (accumulated solar UV radiation,  $Q_{UV}$ ).

In order to compare all solar reactors photocatalysis assisted by turmeric experiments, Fig. 6.18 shows the removal of caffeine per accumulated energy  $Q_{UV}$  ( $\text{kJ}\cdot\text{L}^{-1}$ ) for the Suntest CPS+, RPR and CPC reactors, as a form of comparing the CAF removal in relation to the received global UV energy.

**Figure 6.18** – Evaluation of CAF removal per accumulated solar UV radiation ( $Q_{UV}$ ) during each photocatalysis assisted by turmeric experiment in Suntest CPS+ (Suntest1, Suntest2, and Suntest3), RPR reactor (RPR1, RPR2 and RPR3) and CPC reactor (CPC1, CPC2 and CPC3).



Even though the solar photoreactors did not achieve the same degradation observed in the laboratory scale experiments, when we compare the CAF removal per accumulated irradiation, the solar reactors in semi-pilot scale outperformed the laboratory reactors, as it can be seen in Fig. 6.18. This was achieved since the calculation of the accumulated UV irradiation (Eq. 6.1) considers the irradiated area and irradiated volume and the semi-pilot reactors present higher areas and volumes.

These results are similar to what was observed by Leblebici *et al.* (2015) where the authors stated the figure of merit PSTY (Eq. 2.1) to compare different continuous reactors. The author's idea was to compare the efficiency of pollutant treatment considering the kinetics of pollutant removal, the treatment capacity (volume per day) and the lamp power, as it was explained in Chapter 2. Similarly, larger reactors scored higher than laboratory scale reactors (LEBLEBICI *et al.*, 2015).

### 6.3.3 Organic matter assessment

Organic matter removal was assessed through DOC analysis. The DOC results are summarized in Table 6.1.

**Table 6.1** – Summary of organic matter removal of the CAF aqueous solution through DOC measurements by the different processes.

Sample	Initial ( $mg \cdot L^{-1}$ )	Final ( $mg \cdot L^{-1}$ )	Removal (%)
Photocatalysis (PET-TiO <sub>2</sub> + RPR)	14.39	7.62	47.05
Photocatalysis assisted by turmeric - (turmeric + PET-TiO <sub>2</sub> + RPR)	78.01	42.19	45.92
Photocatalysis (Tube-TiO <sub>2</sub> + CPC)	12.98	4.20	67.64
Photocatalysis assisted by turmeric - (turmeric + PET-TiO <sub>2</sub> + CPC)	86.56	28.67	66.88

Table 6.1 shows that the DOC removal of the CAF solution in the photocatalysis process was higher in the CPC reactor than in the RPR reactor. These results indicate that the concentration of irradiation promoted by the CPC reactor might have played an important role in organic matter removal. These results also agree with the results presented in Fig. 6.18.

### 6.3.4 Acute ecotoxicity assessment

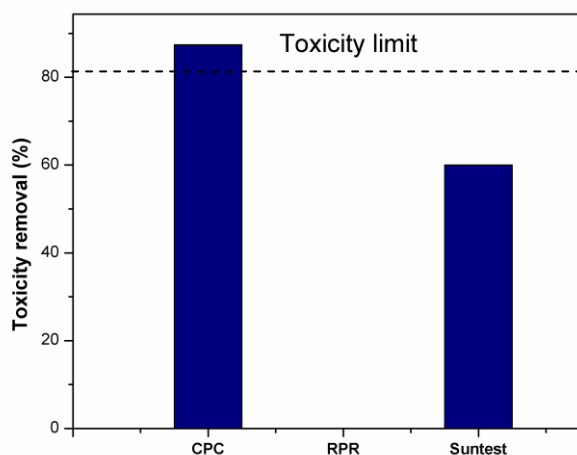
In order to verify if the solar photocatalytic processes in RPR and CPC reactors assisted with turmeric were able to remove the initial toxicity of the CAF aqueous solution and in order to evaluate the possibility of the appearance of toxic byproducts, acute ecotoxicity was evaluated by *Aliivibrio fischeri* bioassay.

Ecotoxicity results by *Aliivibrio fischeri* showed the photocatalytic treatment assisted by turmeric could remove the toxicity of the initial solution of caffeine in the CPC reactor experiments. The CAF aqueous solution presented initial a.T.U. value of 3.89 ( $EC_{50} = 25.69$ ) which is considered toxic and after the photocatalytic treatment assisted by turmeric in the CPC reactor, a.T.U. was remarkably reduced to 0.49 ( $EC_{50} = 201.9$ ), which is classified as

non-toxic. Therefore, in this case, the proposed treatment was able to remove the toxicity of the water solution. In the case of the RPR reactor, the results test showed that the treatment was not able to remove the water solution initial toxicity, suggesting that the toxic compounds were not removed or that a toxic by-product was formed during the reaction. These phenomena should be better investigated in future works.

In order to compare the results of toxicity assessment of all the proposed treatments, Fig. 6.19 summarizes all the obtained results.

**Figure 6.19** – Summary of toxicity assessment results from the CAF solutions treated by solar photocatalysis assisted by turmeric: CPC reactor, RPR reactor, and Suntest CPS+ solar simulator.



In general, the photocatalysis assisted by turmeric treatment promoted a good reduction and removal of toxicity, as can be seen in Fig. 6.19. Except in the case of RPR reactor, in which the toxicity was not removed, both CPC and Suntest solar photocatalytic processes were able to remove the toxicity and, in the case of the CPC reactor, the treated wastewater is considered non-toxic.

## **CHAPTER 7. CONCLUSIONS AND FUTURE WORK SUGGESTIONS**

This chapter gives a summary of the work presented in this thesis, discusses the way research objectives presented in the Introduction Chapter (Chapter 1) were achieved and suggests some aspects of relevant research that might be used in future activities and projects.

The main findings, achievements, and conclusions of the project are summarized in Section 7.1. The topics which require additional work and directions for further research in this project area are discussed in Section 7.2.

### **7.1 Conclusions**

After the literature review presented in Chapter 2, it has been understood that efforts have been made in order to develop an efficient process to utilize visible (sunlight) irradiation to promote photocatalysis for environmental applications. The main approaches involve band-gap engineering, a group of different methodologies to narrow the band-gap of photocatalysis to the visible/near-infrared region, and reactors designs with improved photons absorption, in order to optimize the utilization of the photons emitted by visible energy sources.

Moreover, current researches are willing to support catalysts in different matrices, in order to avoid an extra operation to recover the suspended catalyst after photocatalytic treatment. Surface engineering is playing an important role while providing different techniques for thin films depositions and these processes can add to the development of fixed-film reactors for environmental applications.

Characterization results indicate that the studied PET sheet coated with TiO<sub>2</sub> presented band-gap and phase characterization referent to a mixed anatase/rutile/brookite phase, with the strongest presence of anatase polymorph and characteristic band-gap. The morphology and topographic evaluation showed a dense, smooth and homogeneous coating. Moreover, the water droplet contact angle showed the surfaces activity under UV-A radiation.

These result confirmed the potentiality of the High Power Impulse Magnetron Sputtering (HiPIMS) process regarding the deposition of crystalline and dense coatings directly onto flexible polymeric substrates in a single stage process without high temperature and/or post-deposition annealing requirements.

However, the surface area of the material is not high enough to guarantee strong photocatalytic efficiency, and this may be a drawback of the studied material that could be improved in future works. Moreover, the thin titania film coated onto PET substrate is very difficult to characterize and therefore a huge effort was made in this sense during the development of this research.

Repeated photocatalytic experiments (presented in Chapters 4 and 5) and characterization analysis (presented in Chapter 3) showed that the studied photocatalytic surfaces performed with reproducible results in five cycles of utilization, which shows that the supported thin photocatalytic film can be reused in the water treatment process.

In addition, the study of reactive oxygen species and electrogenerated hole through trapping reactions (Chapter 5) suggested that all the 3 studied species ( $h^+$ ,  $\cdot O_2^-$  and  $HO\cdot$ ) participated in the photocatalytic reactions, with a prevalence of the electrogenerated hole ( $h^+$ ) in the pure photocatalytic process with the PET-TiO<sub>2</sub> surface, while in the photosensitized process, the superoxide radical ( $\cdot O_2^-$ ) played a more important role. A possible simplified mechanism was proposed in Chapter 5.

Photocatalytic experiments at laboratory scale (Chapters 4 and 5) indicated that it was possible to use band-gap engineering approach with a natural non-toxic colored compound in order to promote photosensitization and therefore enhance the photocatalytic degradation of two recalcitrant pollutants of emerging concern (carbendazim and caffeine) in water under UV-A/Vis irradiation with similar results.

The scale-up studied in Chapter 6 showed that, even though the laboratory scale process achieved higher pollutants removal, the semi-pilot reactors achieved higher efficiencies when the processes were compared through the pollutant removal per accumulated UV energy. These results, therefore, suggest the potential of the utilization of these technologies in scaled-up processes and also arises the necessity to continue the study reactors engineering and catalysis in order to achieve high performing technologies.

The results of Chapters 4, 5 and 6 also showed organic matter mineralization of almost 80% and the reduction of acute toxicity to *Aliivibrio fischeri* from treated pollutants solutions, which eliminates the possibility of formation of degradation by-products more toxic than the original pollutants.

The proposed process with photocatalytic surfaces photosensitized with natural turmeric may be a hazardous chemical-free, sustainable and straightforward solution for the degradation of emerging contaminants from water sources.

In conclusion, results indicate that the proposed process was efficient and the studied material proved to be active for the degradation of recalcitrant organic pollutants. However, for this technology to be used in real scale, some characteristics of the material need to be improved in order to maximize the overall efficiency of the system.

## **7.2 Future work suggestions**

Based on the experience acquired during the conduction of this research and on the valuable suggestions of reviewers and evaluators, including its main findings and weaknesses, the following directions may be suggested for future work.

- Improvement of the superficial area of the photocatalytic material. This could be achieved with a different substrate or with a different coating process, which may include TiO<sub>2</sub> nanotubes prepared by anodization, for example;
- Assessment of natural photosensitizers which are soluble in water, such as chlorophyll and investigation of its optimum concentration and application strategy;
- Development of colored PET substrate or colored coatings;
- Development of photocatalytic coating of the (colored) PET substrate with different photocatalysts. The solar process could be achieved with narrow band-gap semiconductors, such as bismuth materials, for example;
- Assessment of photocatalytic treatment with real water (or wastewater) utilizing analytical techniques which could verify the pollutants concentrations and treatment efficiency in real situations (regarding the low concentrations in which the contaminants of emerging concern happen in real waters and the complexity of water matrix and a mixture of pollutants).
- Assessment of an economic evaluation in order to verify the economic feasibility of the proposed process for water polishing



## LIST OF PUBLICATIONS

### Journal Publications:

1. Marcelino, R. B. P. & Amorim, C.C. Towards visible-light photocatalysis for environmental applications: band-gap engineering versus photons absorption—a review. *Environmental Science and Pollution Research International*, 2018. <https://doi.org/10.1007/s11356-018-3117-5>
2. Marcelino, R. B. P.; Queiroz, M. T. A. ; Amorim, C. C. ; Leão, M. M. D. ; Brites-Nóbrega, F. F. Solar energy for wastewater treatment: review of international technologies and their applicability in Brazil. *Environmental Science and Pollution Research International*, v. 22(2), p. 762-773, 2015.

### Journal Publications not Related to this PhD Research:

1. Ratova, M. ; Marcelino, R. B. P. ; Souza, P. ; Amorim, Camila Costa ; Kelly, P. Reactive Magnetron Sputter Deposition of Bismuth Tungstate Coatings for Water Treatment Applications under Natural Sunlight. *Catalysts*, v. 7, p. 283, 2017.
2. Norte, T.H.O.; Marcelino, R.B.P.; Moreira, R.P.L.; Binatti, I.; Starling, M.C.V.M.; Amorim, C.C.; Pereira, E.S.; Rocha, W.R.; Lago, R.M. ESI-MS, UV-Vis, and Theoretical Investigation of Fe<sup>3+</sup>-Amoxicillin Complexation during Coagulation. *Journal of Environmental Engineering*, 144(3), 04018001, 2018.
3. Norte, T.H.O.; Marcelino, R.B.P.; Medeiros, F.H.A.; Moreira, R.P.L.; Amorim, C.C.; Lago, R.M. Ozone oxidation of  $\beta$ -lactam antibiotic molecules and toxicity decrease in aqueous solution and industrial wastewaters heavily contaminated. *Ozone-Science & Engineering*, v. 41, p. 1-7, 2018.

### Oral Communications:

1. Marcelino, R. B. P.; Ratova, M.; Starling, M.C. V. M. ; Castro, L. A. S.; Ribeiro, M. C. M. ; Simões, F. M.; Yukawa, Y. N.; Tenenwurcel, M. A.; Kelly, P.; Amorim, C.C. *Solar semiconductor Photocatalysis For Advanced Water Treatment: Performance Of Novel Catalysts Activated By Sunlight*. The 14th IWA Leading Edge Conference on Water and Wastewater Technologies, Florianópolis, Brazil, 2017.
2. Marcelino, R. B. P.; Ratova, M.; Castro, L. A. S; Simões, F. M.; Kelly, P.; Amorim, C.C. *Fotocatálise para polimento de água: desempenho de superfícies catalíticas à base de Bi/W*

*ativadas pela radiação solar*. 19º Congresso Brasileiro de Catálise (Cbcacat) e IX Congresso Mercosul de Catálise (Mercocat), Ouro Preto, Brazil, 2017.

3. Marcelino, R. B. P.; Ratova, M.; Simões, F. M.; Kelly, P.; Amorim, C.C. *TiO<sub>2</sub> thin films coated onto PET by high power impulse magnetron sputtering for photocatalytic degradation of Carbendazim photosensitized by turmeric in aqueous solutions*. 3rd Iberoamerican Conference on Advanced Oxidation Technologies (III CIPOA), Guatapé, Colombia, 2017.

#### **Poster Presentations:**

1. Marcelino, R.B.P.; Ratova, M.; Kelly, P.; Amorim, C.C. Towards Sustainable Photocatalytic Degradation of Emerging Contaminant Using Caffeine as Model Pollutant. 10th European meeting on Solar Chemistry and Photocatalysis: Environmental Applications (SPEA10), 2018, Almería, 2018.

2. Marcelino, R. B. P.; Ratova, M.; Castro, L. A. S; Simões, F. M.; Yukawa, Y. N.; Ribeiro, M. C. M. ; Kelly, P.; Amorim, C.C. Towards the development of titanium dioxide and niobium pentoxide solar photocatalytic coatings for water treatment. 5th European Conference on Environmental Applications of Advanced Oxidation Processes (EAAOP5), Prague, 2017.

3. Andrade, L. N. ; Marcelino, R. B. P. ; Amorim, C. C. . In Situ Chemical Oxidation With Sodium Persulfate in a Soil Rich in Iron: Behavior of the Oxidation/Reduction Potential. 9th European meeting on Solar Chemistry and Photocatalysis: Environmental Applications (SPEA9), Strasbourg, France, 2016.

4. Ribeiro, M. C. M. ; Leão, M. M. D. ; Moreira, R. F. P. M. ; Cortes, N. S. ; Barbosa, M. L. T. ; Marcelino, R. B. P. ; Amorim, C.C. Desenvolvimento de uma rota inovadora para produção de fotocatalisador de Fe/Nb ativado por radiação solar. 19º Congresso Brasileiro de Catálise (Cbcacat) e IX Congresso Mercosul de Catálise (Mercocat), Ouro Preto, Brazil, 2017.

## REFERENCES

- ABOU-GAMRA, Z. M.; AHMED, M. A. Synthesis of mesoporous TiO<sub>2</sub>-curcumin nanoparticles for photocatalytic degradation of methylene blue dye. *Journal of Photochemistry and Photobiology B: Biology*, v. 160, n. Supplement C, p. 134–141, 2016. Disponível em: <<http://www.sciencedirect.com/science/article/pii/S1011134416302123>>.
- ADAR, F.; NOETHER, H. Raman microprobe spectra of spin-oriented and drawn filaments of poly(ethylene terephthalate). *Polymer*, v. 26, n. 13, p. 1935–1943, 1985.
- AL-ASMARI, F.; MEREDDY, R.; SULTANBAWA, Y. A novel photosensitization treatment for the inactivation of fungal spores and cells mediated by curcumin. *Journal of Photochemistry and Photobiology B: Biology*, v. 173, p. 301–306, 2017. Disponível em: <<http://www.sciencedirect.com/science/article/pii/S1011134417305067>>.
- ALAMI, J.; BOLZ, S.; SARAQUINOS, K. High power pulsed magnetron sputtering: Fundamentals and applications. *Journal of Alloys and Compounds*, v. 483, n. 1, p. 530–534, 2009. Disponível em: <<http://www.sciencedirect.com/science/article/pii/S0925838808019063>>.
- ALEX, S.; SANTHOSH, U.; DAS, S. Dye sensitization of nanocrystalline TiO<sub>2</sub>: Enhanced efficiency of unsymmetrical versus symmetrical squaraine dyes. *Journal of Photochemistry and Photobiology A: Chemistry*, v. 172, n. 1, p. 63–71, 2005.
- ALFANO, O. . *et al. Photocatalysis in water environments using artificial and solar light*. [S.l: s.n.], 2000. v. 58. Disponível em: <<http://www.sciencedirect.com/science/article/pii/S0920586100002522>>.
- ALHAJI, M. H. *et al. Recent developments in immobilizing titanium dioxide on supports for degradation of organic pollutants in wastewater- A review*. *International Journal of Environmental Science and Technology*. [S.l: s.n.], 2017
- ALI, A. M. *et al. Occurrence of pharmaceuticals and personal care products in effluent-dominated Saudi Arabian coastal waters of the Red Sea*. *Chemosphere*, v. 175, p. 505–513, 2017.

AMIRI, H. *et al.* Response surface methodology modeling to improve degradation of Chlorpyrifos in agriculture runoff using TiO<sub>2</sub> solar photocatalytic in a raceway pond reactor. *Ecotoxicology and Environmental Safety*, v. 147, p. 919–925, 2018.

ANDERS, A. A review comparing cathodic arcs and high power impulse magnetron sputtering (HiPIMS). *Surface and Coatings Technology*, v. 257, p. 308–325, 2014. Disponível em: <<http://www.sciencedirect.com/science/article/pii/S0257897214007531>>.

ARFANIS, M. K. *et al.* Photocatalytic degradation of salicylic acid and caffeine emerging contaminants using titania nanotubes. *Chemical Engineering Journal*, v. 310, p. 525–536, 2017.

AUGUGLIARO, V. *et al.* Determination of Photoadsorption Capacity of Polychrystalline TiO<sub>2</sub> Catalyst in Irradiated Slurry. In: HUGO, I. DE L.; BENITO SERRANO, R. (Org.). *Advances in Chemical Engineering*. [S.l.]: Academic Press, 2009. v. Volume 36. p. 1–35. Disponível em: <<http://www.sciencedirect.com/science/article/pii/S0065237709004013>>.

AWAJA, F.; PAVEL, D. *Recycling of PET*. *European Polymer Journal*. [S.l.: s.n.], 2005

BAHOME, M. C. *et al.* Fischer-Tropsch synthesis over iron catalysts supported on carbon nanotubes. *Applied Catalysis A: General*, v. 287, n. 1, p. 60–67, 2005.

BANERJEE, S.; DIONYSIOU, D. D.; PILLAI, S. C. *Self-cleaning applications of TiO<sub>2</sub> by photo-induced hydrophilicity and photocatalysis*. *Applied Catalysis B: Environmental*, 176–177, p. 396–428, 2015.

BANYAMIN, Z. Y. *Novel Photovoltaic Solar Power Generating Diode*. 2014. Manchester Metropolitan University, 2014.

BAUDYS, M. *et al.* Weathering tests of photocatalytic facade paints containing ZnO and TiO<sub>2</sub>. *Chemical Engineering Journal*, v. 261, p. 83–87, 2015.

BERBERIDOU, C. *et al.* Study of the decomposition and detoxification of the herbicide bentazon by heterogeneous photocatalysis: Kinetics, intermediates and transformation pathways. *Applied Catalysis B: Environmental*, v. 200, p. 150–163, 2017.

- BERNABEU, A. *et al.* Solar photocatalysis as a tertiary treatment to remove emerging pollutants from wastewater treatment plant effluents. *Catalysis Today*, v. 161, n. 1, p. 235–240, 2011.
- BETHI, B. *et al.* *Nanomaterials-based advanced oxidation processes for wastewater treatment: A review. Chemical Engineering and Processing: Process Intensification.* [S.l: s.n.], 2016
- BIBI, I. *et al.* Green and eco-friendly synthesis of cobalt-oxide nanoparticle: Characterization and photo-catalytic activity. *Advanced Powder Technology*, v. 28, n. 9, p. 2035–2043, 2017.
- BINNIG, G.; QUATE, C. F. Atomic Force Microscope. *Physical Review Letters*, v. 56, n. 9, p. 930–933, 1986.
- BISTRIČIĆ, L. *et al.* Raman spectra, thermal and mechanical properties of poly(ethylene terephthalate) carbon-based nanocomposite films. *Journal of Polymer Research*, v. 22, n. 3, 2015.
- BITENC, M. *et al.* The impact of ZnO load, stability and morphology on the kinetics of the photocatalytic degradation of caffeine and resazurin. *Applied Catalysis B: Environmental*, v. 136–137, p. 202–209, 2013.
- BOUDINA, A. *et al.* Photochemical behaviour of carbendazim in aqueous solution. *Chemosphere*, v. 50, n. 5, p. 649–655, 2003.
- BOYJOO, Y. *et al.* A review on photocatalysis for air treatment: From catalyst development to reactor design. *Chemical Engineering Journal*, v. 310, p. 537–559, 2017a. Disponível em: <<http://www.sciencedirect.com/science/article/pii/S138589471630897X>>.
- BOYJOO, Y. *et al.* *A review on photocatalysis for air treatment: From catalyst development to reactor design. Chemical Engineering Journal.* [S.l: s.n.], 2017b
- BRUKER NANO GMBH. *Introduction to EDS analysis.* . [S.l: s.n.], 2011.
- BURKHARDT, M. *et al.* Release of biocides from urban areas into aquatic systems. *6th International Conference NOVATECH*, p. 1483–1489, 2007.

BUTKOVSKYI, A. *et al.* Fate of personal care and household products in source separated sanitation. *Journal of Hazardous Materials*, v. 320, p. 427–434, 2016. Disponível em: <<http://www.sciencedirect.com/science/article/pii/S0304389416307816>>.

CABRERA-REINA, A. *et al.* Comparison of different detoxification pilot plants for the treatment of industrial wastewater by solar photo-Fenton: Are raceway pond reactors a feasible option? *Science of the Total Environment*, v. 648, p. 601–608, 2019.

CABRERA REINA, A. *et al.* Modelling the photo-Fenton oxidation of the pharmaceutical paracetamol in water including the effect of photon absorption (VRPA). *Applied Catalysis B: Environmental*, v. 166, n. Supplement C, p. 295–301, 2015. Disponível em: <<http://www.sciencedirect.com/science/article/pii/S0926337314007243>>.

CAI, Q.; HU, J. Decomposition of sulfamethoxazole and trimethoprim by continuous UVA/LED/TiO<sub>2</sub> photocatalysis: Decomposition pathways, residual antibacterial activity and toxicity. *Journal of Hazardous Materials*, v. 323, p. 527–536, 2017. Disponível em: <<http://www.sciencedirect.com/science/article/pii/S0304389416305611>>.

CÁMARA, R. M. *et al.* Photocatalytic activity of TiO<sub>2</sub> films prepared by surfactant-mediated sol-gel methods over commercial polymer substrates. *Chemical Engineering Journal*, v. 283, p. 535–543, 2016.

CAMPO, J. *et al.* Occurrence and removal efficiency of pesticides in sewage treatment plants of four Mediterranean River Basins. *Journal of Hazardous Materials*, v. 263, p. 146–157, 2013. Disponível em: <<http://www.sciencedirect.com/science/article/pii/S030438941300705X>>.

CAO, S. *et al.* Polymeric Photocatalysts Based on Graphitic Carbon Nitride. *Advanced Materials*, v. 27, n. 13, p. 2150–2176, 2015.

CAPASSO, F. Band-gap engineering: from physics and materials to new semiconductor devices. *Science (New York, N.Y.)*, v. 235, n. 4785, p. 172–176, 1987.

CARRA, I. *et al.* Degradation and monitoring of acetamiprid, thiabendazole and their transformation products in an agro-food industry effluent during solar photo-Fenton treatment in a raceway pond reactor. *Chemosphere*, v. 130, p. 73–81, 2015.

CARRA, I.; SANTOS-JUANES, L.; *et al.* New approach to solar photo-Fenton operation. Raceway ponds as tertiary treatment technology. *Journal of Hazardous Materials*, v. 279, p. 322–329, 2014. Disponível em: <<http://www.sciencedirect.com/science/article/pii/S0304389414005718>>.

CARRA, I.; GARCÍA SÁNCHEZ, J. L.; *et al.* Phenomenological study and application of the combined influence of iron concentration and irradiance on the photo-Fenton process to remove micropollutants. *Science of The Total Environment*, v. 478, p. 123–132, 2014. Disponível em: <<http://www.sciencedirect.com/science/article/pii/S0048969714000758>>.

CASTRO, L. A. S. ; MARCELINO, R B P ; STARLING, M. C. V. ; AMORIM, CAMILA COSTA ; LEAO, M. M. D. FOTO REATOR SOLAR PARA REMOÇÃO DE POLUENTES E DESINFECÇÃO DE ÁGUA: CRITÉRIOS DE PROJETO E MONTAGEM. 2014, [S.l: s.n.], 2014.

CASTRO, R. H. R. On the thermodynamic stability of nanocrystalline ceramics. *Materials Letters*, 2013.

CASTRO, R. H. R.; WANG, B. The hidden effect of interface energies in the polymorphic stability of nanocrystalline titanium dioxide. *Journal of the American Ceramic Society*, 2011.

CHAI, S. Y.; KIM, Y. J.; LEE, W. I. Photocatalytic WO<sub>3</sub>/TiO<sub>2</sub> nanoparticles working under visible light. 2006, [S.l: s.n.], 2006. p. 909–912.

CHEN, L. *et al.* Recent advances in bismuth-containing photocatalysts with heterojunctions. *Cuihua Xuebao/Chinese Journal of Catalysis*. [S.l: s.n.], 2016

CHIU, M. Y. *et al.* Simultaneous use of small- and wide-angle X-ray techniques to analyze nanometerscale phase separation in polymer heterojunction solar cells. *Advanced Materials*, v. 20, n. 13, p. 2573–2578, 2008.

CHUNG, H. T.; WON, J. H.; ZELENAY, P. Active and stable carbon nanotube/nanoparticle composite electrocatalyst for oxygen reduction. *Nature Communications*, v. 4, 2013.

COLMENARES, J. C.; VARMA, R. S.; NAIR, V. Selective photocatalysis of lignin-inspired chemicals by integrating hybrid nanocatalysis in microfluidic reactors. *Chem. Soc. Rev.*, 2017.

Disponível em: <<http://xlink.rsc.org/?DOI=C7CS00257B>>.

COMEAU, F. *et al.* The occurrence of acidic drugs and caffeine in sewage effluents and receiving waters from three coastal watersheds in Atlantic Canada. *Science of the Total Environment*, v. 396, n. 2–3, p. 132–146, 2008.

CORAZZA, M. *et al.* Comparison of ultramicrotomy and focused-ion-beam for the preparation of TEM and STEM cross section of organic solar cells. *Applied Surface Science*, v. 389, p. 462–468, 2016.

COSTA, E. P. DA. *Degradação de carbendazim em água por foto-fenton solar em um fotoreator semipiloto do tipo RPR*. 2017. Universidade Federal de Minas Gerais, 2017.

COTTINEAU, T. *et al.* One step synthesis of niobium doped titania nanotube arrays to form (N,Nb) co-doped TiO<sub>2</sub> with high visible light photoelectrochemical activity. *Journal of Materials Chemistry A*, v. 1, n. 6, p. 2151–2160, 2013. Disponível em: <<http://dx.doi.org/10.1039/C2TA00922F>>.

DA COSTA, E. P. *et al.* Degradation of carbendazim in water via photo-Fenton in Raceway Pond Reactor: assessment of acute toxicity and transformation products. *Environmental Science and Pollution Research*, 2018. Disponível em: <<https://doi.org/10.1007/s11356-018-2130-z>>.

DA COSTA FILHO, B. M. *et al.* Intensification of heterogeneous TiO<sub>2</sub> photocatalysis using an innovative micro-meso-structured-photoreactor for n-decane oxidation at gas phase. *Chemical Engineering Journal*, v. 310, p. 331–341, 2017.

DA SILVA, A. L.; HOTZA, D.; CASTRO, R. H. R. Surface energy effects on the stability of anatase and rutile nanocrystals: A predictive diagram for Nb<sub>2</sub>O<sub>5</sub>-doped-TiO<sub>2</sub>. *Applied Surface Science*, v. 393, p. 103–109, 2017.

DALMÁZIO, I. *et al.* Advanced oxidation of caffeine in water: On-line and real-time monitoring by electrospray ionization mass spectrometry. *Environmental Science and Technology*, v. 39, n. 16, p. 5982–5988, 2005.

DANESHVAR, A. *et al.* Evaluating pharmaceuticals and caffeine as indicators of fecal



contamination in drinking water sources of the Greater Montreal region. *Chemosphere*, v. 88, n. 1, p. 131–139, 2012.

DANION, A. *et al.* Characterization and study of a single-TiO<sub>2</sub>-coated optical fiber reactor. *Applied Catalysis B: Environmental*, v. 52, n. 3, p. 213–223, 2004. Disponível em: <<http://www.sciencedirect.com/science/article/pii/S0926337304002656>>.

DANION, A. *et al.* Malic acid photocatalytic degradation using a TiO<sub>2</sub>-coated optical fiber reactor. *Journal of Photochemistry and Photobiology A: Chemistry*, v. 190, n. 1, p. 135–140, 2007. Disponível em: <<http://www.sciencedirect.com/science/article/pii/S1010603007001797>>.

DE BRITES-NÓBREGA, F. F. *et al.* Evaluation of photocatalytic activities of supported catalysts on NaX zeolite or activated charcoal. *Journal of Hazardous Materials*, v. 263, p. 61–66, 2013. Disponível em: <<http://www.sciencedirect.com/science/article/pii/S0304389413005402>>.

DE JESUS GAFFNEY, V. *et al.* Occurrence of pharmaceuticals in a water supply system and related human health risk assessment. *Water Research*, v. 72, p. 199–208, 2015.

DE LASA, H. *et al.* Efficiency Factors in Photocatalytic Reactors: Quantum Yield and Photochemical Thermodynamic Efficiency Factor. *Chemical Engineering and Technology*, v. 39, n. 1, p. 51–65, 2016.

DELFOUR-PEYRETHON, B. *HiPIMS plasma diagnostic to study the repeatability of low temperature deposition of crystalline titania*. 2018. Manchester Metropolitan University, 2018.

DI VALENTIN, C. *et al.* N-doped TiO<sub>2</sub>: Theory and experiment. *Chemical Physics*, v. 339, n. 1–3, p. 44–56, 2007.

DIAZ-EGEA, C. *et al.* Mapping the plasmonic response of gold nanoparticles embedded in TiO<sub>2</sub> thin films. *Nanotechnology*, v. 26, n. 40, 2015.

DIEHM, C. *et al.* Spatial Resolution of Species and Temperature Profiles in Catalytic Reactors. In Situ Sampling Techniques and CFD Modeling. *Advances in Chemical*

*Engineering*, v. 45, p. 41–95, 2014.

DONG, H. *et al.* A novel high-efficiency visible-light sensitive Ag<sub>2</sub>CO<sub>3</sub> photocatalyst with universal photodegradation performances: Simple synthesis, reaction mechanism and first-principles study. *Applied Catalysis B: Environmental*, v. 134–135, p. 46–54, 2013.

DRUNKA, R.; GRABIS, J.; KRŪMIŅA, A. Preparation of Au, Pt, Pd and Ag Doped TiO<sub>2</sub> Nanofibers and their Photocatalytic Properties under LED Illumination. *Key Engineering Materials*, v. 762, p. 283–287, 2018.

DUJAKOVIĆ, N. *et al.* Determination of pesticides in surface and ground waters by liquid chromatography–electrospray–tandem mass spectrometry. *Analytica Chimica Acta*, v. 678, n. 1, p. 63–72, 2010. Disponível em: <<http://www.sciencedirect.com/science/article/pii/S0003267010010184>>.

DUNCAN, W. R.; PREZHDO, O. V. Theoretical studies of photoinduced electron transfer in dye-sensitized TiO<sub>2</sub>. *Annual review of physical chemistry*, v. 58, p. 143–184, 2007.

DUTTA, P. Grazing incidence X-ray diffraction. *Current Science*, v. 78, n. 12, p. 1478–1483, 2000.

EGERTON, R. F. *Electron Energy-Loss Spectroscopy in the Electron Microscope*. [S.l.: s.n.], 2011. v. 72. Disponível em: <<http://stacks.iop.org/0034-4885/72/i=1/a=016502?key=crossref.f635c25c2b0bdba48559a535ef56c541%5Cnhttp://link.springer.com/10.1007/978-1-4419-9583-4>>.

ELLIS, G. *et al.* FT Raman study of orientation and crystallization processes in poly(ethylene terephthalate). *Spectrochimica Acta Part A: Molecular Spectroscopy*, v. 51, n. 12, p. 2139–2145, 1995.

FARAHANI, N. *et al.* An Investigation into W or Nb or ZnFe<sub>2</sub>O<sub>4</sub> Doped Titania Nanocomposites Deposited from Blended Powder Targets for UV/Visible Photocatalysis. *Coatings*, v. 3, n. 3, p. 153–165, 2013. Disponível em: <<http://www.mdpi.com/2079-6412/3/3/153/>>.

FARALDOS, M.; BAHAMONDE, A. Environmental applications of titania-graphene

photocatalysts. *Catalysis Today*, v. 285, p. 13–28, 2017. Disponível em:  
<<http://www.sciencedirect.com/science/article/pii/S0920586117300299>>.

FERREIRA, A. P.; DE LOURDES, C.; DA CUNHA, N. Anthropogenic pollution in aquatic environment: Development of a caffeine indicator. *International Journal of Environmental Health Research*, v. 15, n. 4, p. 303–311, 2005. Disponível em:  
<<http://dx.doi.org/10.1080/09603120500155898>>.

FLEMING, O. S.; CHAN, K. L. A.; KAZARIAN, S. G. FT-IR imaging and Raman microscopic study of poly(ethylene terephthalate) film processed with supercritical CO<sub>2</sub>. 2004, [S.l.: s.n.], 2004. p. 3–7.

FREITAS, A. M. *et al.* Ecotoxicity evaluation of a WWTP effluent treated by solar photo-Fenton at neutral pH in a raceway pond reactor. *Environmental Science and Pollution Research*, v. 24, n. 2, p. 1093–1104, 2017.

FUJISHIMA, A.; ZHANG, X.; TRYK, D. A. *TiO<sub>2</sub> photocatalysis and related surface phenomena*. *Surface Science Reports*. [S.l.]: North-Holland. Disponível em:  
<<http://www.sciencedirect.com.ez27.periodicos.capes.gov.br/science/article/pii/S0167572908000757>>. Acesso em: 16 out. 2017. , 15 dez. 2008

GANIYU, S. O. *et al.* Coupling of membrane filtration and advanced oxidation processes for removal of pharmaceutical residues: A critical review. *Separation and Purification Technology*. [S.l.: s.n.], 2015

GAR ALALM, M.; TAWFIK, A.; OOKAWARA, S. Enhancement of photocatalytic activity of TiO<sub>2</sub> by immobilization on activated carbon for degradation of pharmaceuticals. *Journal of Environmental Chemical Engineering*, v. 4, n. 2, p. 1929–1937, 2016.

GARZA-CAMPOS, B. *et al.* Salicylic acid degradation by advanced oxidation processes. Coupling of solar photoelectro-Fenton and solar heterogeneous photocatalysis. *Journal of Hazardous Materials*, v. 319, p. 34–42, 2016. Disponível em:  
<<http://www.sciencedirect.com/science/article/pii/S0304389416301777>>.

GHAFOOR, S. *et al.* Photosensitization of TiO<sub>2</sub> nanofibers by Ag<sub>2</sub>S with the synergistic effect of excess surface Ti<sup>3+</sup> states for enhanced photocatalytic activity under simulated

sunlight. *Scientific Reports*, v. 7, n. 1, p. 255, 2017. Disponível em:

<<https://doi.org/10.1038/s41598-017-00366-7>>.

GHAFOORI, S.; MEHRVAR, M.; CHAN, P. K. Photoreactor scale-up for degradation of aqueous poly(vinyl alcohol) using UV/H<sub>2</sub>O<sub>2</sub> process. *Chemical Engineering Journal*, v. 245, n. 0, p. 133–142, 2014. Disponível em:

<<http://www.sciencedirect.com/science/article/pii/S1385894714000801>>.

GOH, S. G. *et al.* Occurrence and distribution of bacteria indicators, chemical tracers and pathogenic vibrios in Singapore coastal waters. *Marine Pollution Bulletin*, v. 114, n. 1, p. 627–634, 2017.

GOLDSTEIN, J. *et al.* *Scanning Electron Microscopy and X-Ray Microanalysis: A Text for Biologists, Materials Scientists, and Geologists. Scanning Electron Microscopy and X-Ray Microanalysis - A Text for Biologists, | Springer*. [S.l: s.n.]. Disponível em:

<<https://books.google.com/books?hl=en&lr=&id=25nxBwAAQBAJ&pgis=1>>. , 2012

GOLDSTEIN, J. *et al.* *Scanning Electron Microscopy and X-ray Microanalysis*. [S.l: s.n.], 2003. v. 44.

GORGES, R.; MEYER, S.; KREISEL, G. Photocatalysis in microreactors. *Journal of Photochemistry and Photobiology A: Chemistry*, v. 167, n. 2–3, p. 95–99, 2004.

GRÄTZEL, M. *Photoelectrochemical cells*. *Nature*. [S.l: s.n.]. , 2001

GRIGOROV, K. G. *et al.* Optical and morphological properties of N-doped TiO<sub>2</sub> thin films. *Surface Science*, v. 605, n. 7–8, p. 775–782, 2011.

GROS, M. *et al.* Screening and prioritization of micropollutants in wastewaters from on-site sewage treatment facilities. *Journal of Hazardous Materials*, v. 328, p. 37–45, 2017.

Disponível em: <<http://www.sciencedirect.com/science/article/pii/S0304389416311967>>.

GUO, S.; ZHANG, G.; WANG, J. Photo-Fenton degradation of rhodamine B using Fe<sub>2</sub>O<sub>3</sub>-Kaolin as heterogeneous catalyst: Characterization, process optimization and mechanism. *Journal of Colloid and Interface Science*, v. 433, p. 1–8, 2014.

- HAN, M. Y. *et al.* Energy band-gap engineering of graphene nanoribbons. *Physical Review Letters*, v. 98, n. 20, 2007.
- HANAOR, D. A. H.; SORRELL, C. C. *Review of the anatase to rutile phase transformation. Journal of Materials Science*. [S.l: s.n.], 2011
- HE, B. B. Introduction to two-dimensional X-ray diffraction. *Powder Diffraction*, v. 18, n. 02, p. 71–85, 2003.
- HERRERO-HERNÁNDEZ, E. *et al.* Occurrence of pesticides and some of their degradation products in waters in a Spanish wine region. *Journal of Hydrology*, v. 486, p. 234–245, 2013.
- HERRMANN, J. M. *et al.* Environmental green chemistry as defined by photocatalysis. *Journal of Hazardous Materials*, v. 146, n. 3, p. 624–629, 2007. Disponível em: <<http://www.sciencedirect.com/science/article/pii/S0304389407005559>>.
- HINRICHS, R. Difração de raios X com incidência rasante (GIXRD). In: IGEO/UFRGS (Org.). . Porto Alegre: [s.n.], 2014. p. 159–172.
- HOFER, F. *et al.* Fundamentals of electron energy-loss spectroscopy. 2016, [S.l: s.n.], 2016.
- HOMA, P.; TRYBA, B.; GĘSIKIEWICZ-PUCHALSKA, A. Impact of paint matrix composition and thickness of paint layer on the activity of photocatalytic paints. *Polish Journal of Chemical Technology*, v. 19, n. 1, p. 113–119, 2017.
- HOVSEPIAN, P. E. *et al.* Effect of the degree of high power impulse magnetron sputtering utilisation on the structure and properties of TiN films. *Thin Solid Films*, v. 562, p. 132–139, 2014.
- HSU, E. S. Central nervous system stimulants. *Essentials of Pharmacology for Anesthesia, Pain Medicine, and Critical Care*. [S.l: s.n.], 2015. p. 381–396.
- HU, W. *et al.* Atomic-scale control of TiO<sub>6</sub> octahedra through solution chemistry towards giant dielectric response. *Scientific Reports*, v. 4, n. 1, p. 6582, 2015. Disponível em: <<http://www.nature.com/articles/srep06582>>.

HUANG, H. *et al.* Fabrication of Multiple Heterojunctions with Tunable Visible-Light-Active Photocatalytic Reactivity in BiOBr–BiOI Full-Range Composites Based on Microstructure Modulation and Band Structures. *ACS Applied Materials & Interfaces*, v. 7, n. 1, p. 482–492, 2015. Disponível em: <<http://dx.doi.org/10.1021/am5065409>>.

HURUM, D. C. *et al.* Explaining the Enhanced Photocatalytic Activity of Degussa P25 Mixed-Phase TiO<sub>2</sub> Using EPR. *The Journal of Physical Chemistry B*, v. 107, n. 19, p. 4545–4549, 2003. Disponível em: <<http://pubs.acs.org/doi/abs/10.1021/jp0273934>>.

IBHADON, A. O.; FITZPATRICK, P. Heterogeneous photocatalysis: Recent advances and applications. *Catalysts*, Cited By :62Export Date: 11 January 2016, v. 3, n. 1, p. 189–218, 2013. Disponível em: <<http://www.scopus.com/inward/record.url?eid=2-s2.0-84885083724&partnerID=40&md5=01f5498517adf4c04b329906fa2b5828>>.

ILIEV, M. N.; HADJIEV, V. G.; LITVINCHUK, A. P. Raman and infrared spectra of brookite (TiO<sub>2</sub>): Experiment and theory. *Vibrational Spectroscopy*, v. 64, p. 148–152, 2013.

ILIEV, V.; TOMOVA, D. Photocatalytic oxidation of sulfide ion catalyzed by phthalocyanine modified titania. *Catalysis Communications*, v. 3, n. 7, p. 287–292, 2002.

ILIEV, V.; TOMOVA, D.; BILYARSKA, L. Promoting the oxidative removal rate of 2,4-dichlorophenoxyacetic acid on gold-doped WO<sub>3</sub>/TiO<sub>2</sub>/reduced graphene oxide photocatalysts under UV light irradiation. *Journal of Photochemistry and Photobiology A: Chemistry*, v. 351, p. 69–77, 2018.

IMAI, M. *et al.* Structural formation of poly (ethylene terephthalate) during the induction period of crystallization: 1. Ordered structure appearing before crystal nucleation. *Polymer*, v. 33, n. 21, p. 4451–4456, 1992.

INDERMÜHLE, C. *et al.* Modelling of UV optical ageing of optical fibre fabric coated with TiO<sub>2</sub>. *Applied Catalysis B: Environmental*, v. 182, p. 229–235, 2016. Disponível em: <<http://www.sciencedirect.com/science/article/pii/S0926337315301648>>.

INFINITYPV. *Solar spectral efficiency of a semiconductor*. Disponível em: <<https://infinitypv.com/l/Bandgap.php>>. Acesso em: 1 jan. 2017.

JACOB, R. S. *et al.* A toxicity assessment of 30 pharmaceuticals using *Aliivibrio fischeri* : a comparison of the acute effects of different formulations. *Environmental Technology*, v. 37, n. 21, p. 2760–2767, 2016a. Disponível em: <<https://www.tandfonline.com/doi/full/10.1080/09593330.2016.1164249>>.

JACOB, R. S. *et al.* A toxicity assessment of 30 pharmaceuticals using *Aliivibrio fischeri* : a comparison of the acute effects of different formulations. *Environmental Technology*, v. 37, n. 21, p. 2760–2767, 2016b.

JAMDAR, V. *et al.* Recycling of PET wastes using Electron beam radiations and preparation of polyurethane coatings using recycled material. *Progress in Organic Coatings*, v. 107, p. 54–63, 2017.

KALE, M. J.; AVANESIAN, T.; CHRISTOPHER, P. *Direct photocatalysis by plasmonic nanostructures*. *ACS Catalysis*. [S.l: s.n.], 2014

KARTHIK, M.; GOHIL, J. M.; SURESH, A. K. Probing the thickness and roughness of the functional layer in thin film composite membranes. *International Journal of Hydrogen Energy*, v. 42, n. 42, p. 26464–26474, 2017.

KAUR, T. *et al.* Utilization of solar energy for the degradation of carbendazim and propiconazole by Fe doped TiO<sub>2</sub>. *Solar Energy*, v. 125, p. 65–76, 2016.

KAUR, T.; TOOR, A. P.; WANCHOO, R. K. Parametric study on degradation of fungicide carbendazim in dilute aqueous solutions using nano TiO<sub>2</sub>. *Desalination and Water Treatment*, v. 54, n. 1, p. 122–131, 2015.

KAYANI, Z. N. *et al.* Deposition of porous titanium oxide thin films as anti-fogging and anti-reflecting medium. *Optik*, v. 127, n. 12, p. 5124–5127, 2016.

KELLY, P. *et al.* Structural Formation and Photocatalytic Activity of Magnetron Sputtered Titania and Doped-Titania Coatings. *Molecules*, v. 19, n. 10, p. 16327, 2014. Disponível em: <<http://www.mdpi.com/1420-3049/19/10/16327>>.

KELLY, P. J. *et al.* Deposition of photocatalytic titania coatings on polymeric substrates by HiPIMS. *Vacuum*, v. 86, n. 12, p. 1880–1882, 2012. Disponível em:

<<http://www.sciencedirect.com/science/article/pii/S0042207X12002710>>.

KIM, S. D. *et al.* Occurrence and removal of pharmaceuticals and endocrine disruptors in South Korean surface, drinking, and waste waters. *Water Research*, v. 41, n. 5, p. 1013–1021, 2007.

KONSTANTINIDIS, S.; DAUCHOT, J. P.; HECQ, M. Titanium oxide thin films deposited by high-power impulse magnetron sputtering. *Thin Solid Films*, v. 515, n. 3, p. 1182–1186, 2006.

KOUZNETSOV, V. *et al.* A novel pulsed magnetron sputter technique utilizing very high target power densities. *Surface and Coatings Technology*, v. 122, n. 2, p. 290–293, 1999.  
Disponível em: <<http://www.sciencedirect.com/science/article/pii/S0257897299002923>>.

KRIVEC, M.; ŽAGAR, K.; *et al.* Highly efficient TiO<sub>2</sub>-based microreactor for photocatalytic applications. *ACS Applied Materials and Interfaces*, v. 5, n. 18, p. 9088–9094, 2013.

KRIVEC, M.; SEGUNDO, R. A.; *et al.* Low-temperature synthesis and characterization of rutile nanoparticles with amorphous surface layer for photocatalytic degradation of caffeine. *Applied Catalysis B: Environmental*, v. 140–141, p. 9–15, 2013.

KUBIAK, K. J. *et al.* Wettability versus roughness of engineering surfaces. *Wear*, v. 271, n. 3–4, p. 523–528, 2011.

LARDY-FONTAN, S. *et al.* Validation of a method to monitor the occurrence of 20 relevant pharmaceuticals and personal care products in 167 bottled waters. *Science of the Total Environment*, v. 587–588, p. 118–127, 2017.

LATTEMANN, M.; HELMERSSON, U.; GREENE, J. E. Fully dense, non-faceted 111-textured high power impulse magnetron sputtering TiN films grown in the absence of substrate heating and bias. *Thin Solid Films*, v. 518, n. 21, p. 5978–5980, 2010.

LEAPMAN, R. D.; HUNT, J. Comparison of detection limits for EELS and EDXS. *Microsc. Microanal. Microstruct.*, v. 2, p. 231–244, 2014.

LEARY, R.; WESTWOOD, A. *Carbonaceous nanomaterials for the enhancement of TiO<sub>2</sub>*



*photocatalysis. Carbon*. [S.l: s.n.]. , 2011

LEBLEBICI, M. E.; STEFANIDIS, G. D.; VAN GERVEN, T. Comparison of photocatalytic space-time yields of 12 reactor designs for wastewater treatment. *Chemical Engineering and Processing: Process Intensification*, v. 97, p. 106–111, 2015. Disponível em: <<http://www.sciencedirect.com/science/article/pii/S025527011530101X>>.

LEPRINCE-WANG, Y.; YU-ZHANG, K. Study of the growth morphology of TiO<sub>2</sub> thin films by AFM and TEM. *Surface and Coatings Technology*, v. 140, n. 2, p. 155–160, 2001.

LEVCHENKO, A. A. *et al.* TiO<sub>2</sub> stability landscape: Polymorphism, surface energy, and bound water energetics. *Chemistry of Materials*, v. 18, n. 26, p. 6324–6332, 2006.

LI BASSI, A. *et al.* Raman spectroscopy characterization of titania nanoparticles produced by flame pyrolysis: The influence of size and stoichiometry. *Journal of Applied Physics*, v. 98, n. 7, 2005.

LIN, T.; YU, S.; CHEN, W. Occurrence, removal and risk assessment of pharmaceutical and personal care products (PPCPs) in an advanced drinking water treatment plant (ADWTP) around Taihu Lake in China. *Chemosphere*, v. 152, p. 1–9, 2016.

LIN, Y.-C. *et al.* TiS<sub>2</sub> transformation into S-doped and N-doped TiO<sub>2</sub> with visible-light catalytic activity. *Applied Surface Science*, v. 359, p. 1–6, 2015. Disponível em: <<http://www.sciencedirect.com/science/article/pii/S0169433215024010>>.

LIU, W. *et al.* Simultaneous removal of Cr(VI) and 4-chlorophenol through photocatalysis by a novel anatase/titanate nanosheet composite: Synergetic promotion effect and autosynchronous doping. *Journal of Hazardous Materials*, v. 317, p. 385–393, 2016. Disponível em: <<http://www.sciencedirect.com/science/article/pii/S030438941630557X>>.

LOEWY, M. *et al.* Groundwater contamination by azinphos methyl in the Northern Patagonic Region (Argentina). *Science of The Total Environment*, v. 225, n. 3, p. 211–218, 1999. Disponível em: <<http://www.sciencedirect.com/science/article/pii/S0048969798003659>>.

LOOS, R. *et al.* Analysis of emerging organic contaminants in water, fish and suspended particulate matter (SPM) in the Joint Danube Survey using solid-phase extraction followed by

UHPLC-MS-MS and GC-MS analysis. *Science of the Total Environment*, v. 607–608, p. 1201–1212, 2017.

LOOS, R. *et al.* Analysis of emerging organic contaminants in water, fish and suspended particulate matter (SPM) in the Joint Danube Survey using solid-phase extraction followed by UHPLC-MS-MS and GC-MS analysis. *Science of the Total Environment*, v. 607–608, 2017.

LOOS, R. *et al.* Analysis of polar organic contaminants in surface water of the northern Adriatic Sea by solid-phase extraction followed by ultrahigh-pressure liquid chromatography-QTRAP® MS using a hybrid triple-quadrupole linear ion trap instrument. *Analytical and Bioanalytical Chemistry*, v. 405, n. 18, p. 5875–5885, 2013.

LOOS, R. *et al.* Pan-European survey on the occurrence of selected polar organic persistent pollutants in ground water. *Water Research*, v. 44, n. 14, p. 4115–4126, 2010.

LUTTRELL, T. *et al.* Why is anatase a better photocatalyst than rutile? - Model studies on epitaxial TiO<sub>2</sub> films. *Scientific Reports*, v. 4, n. 1, p. 4043, 2015. Disponível em: <<http://www.nature.com/articles/srep04043>>.

MA, W.; LU, Z.; ZHANG, M. Investigation of structural transformations in nanophase titanium dioxide by Raman spectroscopy. *Applied Physics A-Materials Science & Processing*, v. 66, n. 6, p. 621–627, 1998.

MACHADO, T. C.; LANSARIN, M. A.; RIBEIRO, C. S. Wastewater remediation using a spiral shaped reactor for photochemical reduction of hexavalent chromium. *Photochem. Photobiol. Sci.*, v. 14, n. 3, p. 501–505, 2015. Disponível em: <<http://xlink.rsc.org/?DOI=C4PP00263F>>.

MALATO, S. *et al.* Decontamination and disinfection of water by solar photocatalysis: Recent overview and trends. *Catalysis Today*, v. 147, n. 1, p. 1–59, 2009a. Disponível em: <<http://www.sciencedirect.com/science/article/pii/S0920586109003344>>.

MALATO, S. *et al.* *Decontamination and disinfection of water by solar photocatalysis: Recent overview and trends. Catalysis Today*. [S.l: s.n.], 2009b

MALLAT, E.; BARCELÓ, D.; TAULER, R. Degradation study of benomyl and carbendazim

in water by liquid chromatography and multivariate curve resolution methods.

*Chromatographia*, v. 46, n. 7–8, p. 342–350, 1997.

MANASSERO, A.; SATUF, M. L.; ALFANO, O. M. Evaluation of UV and visible light activity of TiO<sub>2</sub> catalysts for water remediation. *Chemical Engineering Journal*, v. 225, p. 378–386, 2013.

MANASSERO, A.; SATUF, M. L.; ALFANO, O. M. Photocatalytic degradation of an emerging pollutant by TiO<sub>2</sub>-coated glass rings: a kinetic study. *Environmental Science and Pollution Research*, v. 24, n. 7, p. 6031–6039, 2017a.

MANASSERO, A.; SATUF, M. L.; ALFANO, O. M. Photocatalytic reactors with suspended and immobilized TiO<sub>2</sub>: Comparative efficiency evaluation. *Chemical Engineering Journal*, v. 326, p. 29–36, 2017b.

MARCELINO, R. B. *et al.* Solar energy for wastewater treatment: review of international technologies and their applicability in Brazil. *Environmental science and pollution research international*, v. 22, n. 2, 2015.

MARGENAT, A. *et al.* Occurrence of chemical contaminants in peri-urban agricultural irrigation waters and assessment of their phytotoxicity and crop productivity. *Science of the Total Environment*, v. 599–600, p. 1140–1148, 2017.

MARINHO, B. A. *et al.* Intensification of heterogeneous TiO<sub>2</sub> photocatalysis using an innovative micro–meso-structured-reactor for Cr(VI) reduction under simulated solar light. *Chemical Engineering Journal*, v. 318, p. 76–88, 2017.

MARQUES, R. R. N. *et al.* Photocatalytic degradation of caffeine: Developing solutions for emerging pollutants. *Catalysis Today*, v. 209, p. 108–115, 2013.

MARTÍNEZ-HERNÁNDEZ, V. *et al.* Removal of emerging organic contaminants in a poplar vegetation filter. *Journal of Hazardous Materials*, v. 342, p. 482–491, 2018.

MAUČEC, D. *et al.* Titania versus zinc oxide nanoparticles on mesoporous silica supports as photocatalysts for removal of dyes from wastewater at neutral pH. *Catalysis Today*, 2017. Disponível em: <<http://www.sciencedirect.com/science/article/pii/S0920586117303826>>.

MAZELLIER, P.; LEROY, E.; LEGUBE, B. Photochemical behavior of the fungicide carbendazim in dilute aqueous-solution. *Journal of Photochemistry and Photobiology A: Chemistry*, v. 153, n. 1–3, p. 221–227, 2002.

MAZZOLINI, P. *et al.* Vibrational-Electrical Properties Relationship in Donor-Doped TiO<sub>2</sub> by Raman Spectroscopy. *Journal of Physical Chemistry C*, v. 120, n. 33, p. 18878–18886, 2016.

MCKINLAY, R. *et al.* Endocrine disrupting pesticides: Implications for risk assessment. *Environment International*, v. 34, n. 2, p. 168–183, 2008. Disponível em: <<http://www.sciencedirect.com/science/article/pii/S0160412007001444>>.

MEI, D. *et al.* Plasma-photocatalytic conversion of CO<sub>2</sub> at low temperatures: Understanding the synergistic effect of plasma-catalysis. *Applied Catalysis B: Environmental*, v. 182, p. 525–532, 2016. Disponível em: <<http://www.sciencedirect.com/science/article/pii/S0926337315301788>>.

MENG, Z.-D. *et al.* Review for Fullerene Materials Enhanced TiO<sub>2</sub> Photocatalysis. *Journal of Photocatalysis Science*, v. 2, n. 1, p. 29–38, 2011.

MIARALIPOUR, S. *et al.* TiO<sub>2</sub>/porous adsorbents: Recent advances and novel applications. *Journal of Hazardous Materials*, v. 341, n. Supplement C, p. 404–423, 2018a. Disponível em: <<http://www.sciencedirect.com/science/article/pii/S0304389417305861>>.

MIARALIPOUR, S. *et al.* *TiO<sub>2</sub>/porous adsorbents: Recent advances and novel applications. Journal of Hazardous Materials*. [S.l: s.n.], 2018b

MIETTINEN, A. *et al.* Measuring intrinsic thickness of rough membranes: application to nanofibrillated cellulose films. *Journal of Materials Science*, v. 50, n. 21, p. 6926–6934, 2015.

MIGUENS, F. C. *et al.* A new protocol to detect light elements in estuarine sediments by X-ray microanalysis (SEM/EDS). *Journal of Electron Microscopy*, v. 59, n. 5, p. 437–446, 2010.

MILLS, A.; LE HUNTE, S. An overview of semiconductor photocatalysis. *Journal of Photochemistry and Photobiology A: Chemistry*, Export Date: 20 November 2015, v. 108, n.

1, p. 1–35, 1997. Disponível em: <<http://www.scopus.com/inward/record.url?eid=2-s2.0-0031592715&partnerID=40&md5=d173eacda70d5836c57da78da8c16848>>.

MINERO, C. *et al.* Photocatalytic Transformation of Organic Compounds in the Presence of Inorganic Anions. 1. Hydroxyl-Mediated and Direct Electron-Transfer Reactions of Phenol on a Titanium Dioxide–Fluoride System. *Langmuir*, v. 16, n. 6, p. 2632–2641, 2000. Disponível em: <<http://pubs.acs.org/doi/abs/10.1021/la9903301>>.

MIRALLES-CUEVAS, S. *et al.* Combined nanofiltration and photo-Fenton treatment of water containing micropollutants. *Chemical Engineering Journal*, v. 224, n. 0, p. 89–95, 2013. Disponível em: <<http://www.sciencedirect.com/science/article/pii/S1385894712012594>>.

MOLDOVAN, Z. Occurrences of pharmaceutical and personal care products as micropollutants in rivers from Romania. *Chemosphere*, v. 64, n. 11, p. 1808–1817, 2006.

MONAI, M.; MONTINI, T.; FORNASIERO, P. Brookite: Nothing new under the sun? *Catalysts*, v. 7, n. 10, 2017.

MONTAGNER, C. C. *et al.* Trace analysis of pesticides and an assessment of their occurrence in surface and drinking waters from the State of Sao Paulo (Brazil). *Analytical Methods*, v. 6, n. 17, p. 6668–6677, 2014a. Disponível em: <<http://dx.doi.org/10.1039/C4AY00782D>>.

MONTAGNER, C. C. *et al.* Trace analysis of pesticides and an assessment of their occurrence in surface and drinking waters from the State of São Paulo (Brazil). *Analytical Methods*, v. 6, n. 17, p. 6668, 2014b.

MORIKAWA, T. *et al.* Band-Gap Narrowing of Titanium Dioxide by Nitrogen Doping. *Japanese Journal of Applied Physics*, v. 40, n. Part 2, No. 6A, p. L561–L563, 2001. Disponível em: <<http://stacks.iop.org/1347-4065/40/L561>>.

MORINAGA, H. *et al.* A Benzimidazole Fungicide, Benomyl, and Its Metabolite, Carbendazim, Induce Aromatase Activity in a Human Ovarian Granulosa-Like Tumor Cell Line (KGN). *Endocrinology*, 10.1210/en.2003-1182, v. 145, n. 4, p. 1860–1869, 2004. Disponível em: <<http://dx.doi.org/10.1210/en.2003-1182>>.

MOTEGH, M. *et al.* Photocatalytic-reactor efficiencies and simplified expressions to assess their relevance in kinetic experiments. *Chemical Engineering Journal*, v. 207–208, p. 607–615, 2012.

MOZIA, S. Photocatalytic membrane reactors (PMRs) in water and wastewater treatment. A review. *Separation and Purification Technology*, v. 73, n. 2, p. 71–91, 2010.

MUNOZ, M. *et al.* Application of CWPO to the treatment of pharmaceutical emerging pollutants in different water matrices with a ferromagnetic catalyst. *Journal of Hazardous Materials*, v. 331, p. 45–54, 2017. Disponível em:  
<<http://www.sciencedirect.com/science/article/pii/S0304389417300985>>.

MURANYI, P.; SCHRAML, C.; WUNDERLICH, J. Antimicrobial efficiency of titanium dioxide-coated surfaces. *Journal of Applied Microbiology*, v. 108, n. 6, p. 1966–1973, 2010.

MURTHY, N. S.; CORREALE, S. T.; MINOR, H. Structure of the Amorphous Phase in Crystallizable Polymers: Poly(ethylene terephthalate). *Macromolecules*, v. 24, n. 5, p. 1185–1189, 1991.

NAKATA, K.; FUJISHIMA, A. TiO<sub>2</sub> photocatalysis: Design and applications. *Journal of Photochemistry and Photobiology C: Photochemistry Reviews*, v. 13, n. 3, p. 169–189, 2012.

NANAKKAL, A. R.; ALEXANDER, L. K. Graphene/BiVO<sub>4</sub>/TiO<sub>2</sub> nanocomposite: tuning band gap energies for superior photocatalytic activity under visible light. *Journal of Materials Science*, v. 52, n. 13, p. 7997–8006, 2017.

NGUYEN-PHAN, T. D. *et al.* The role of graphene oxide content on the adsorption-enhanced photocatalysis of titanium dioxide/graphene oxide composites. *Chemical Engineering Journal*, v. 170, n. 1, p. 226–232, 2011.

NIDHEESH, Puthiya Veetil. Graphene-based materials supported advanced oxidation processes for water and wastewater treatment: a review. *Environmental Science and Pollution Research*, 2017. , p. 1–23.

NOUVELLON, C. *et al.* Deposition of titanium oxide films by reactive High Power Impulse Magnetron Sputtering (HiPIMS): Influence of the peak current value on the transition from

metallic to poisoned regimes. *Surface and Coatings Technology*, v. 206, n. 16, p. 3542–3549, 2012.

O'REGAN, B.; GRÄTZEL, M. A low-cost, high-efficiency solar cell based on dye-sensitized colloidal TiO<sub>2</sub> films. *Nature*, v. 353, n. 6346, p. 737–740, 1991. Disponível em: <<http://www.nature.com/doi/10.1038/353737a0>>.

OFFICE OF PESTICIDE PROGRAMS HEALTH EFFECTS DIVISION, SCIENCE INFORMATION MANAGEMENT BRANCH, U. S. E. P. A. “Chemicals Evaluated for Carcinogenic Potential”. 2006.

OHKO, Y. *et al.* 17 $\beta$ -estradiol degradation by TiO<sub>2</sub> photocatalysis as a means of reducing estrogenic activity. *Environmental Science and Technology*, v. 36, n. 19, p. 4175–4181, 2002.

OHKO, Y. *et al.* Degradation of bisphenol A in water by TiO<sub>2</sub> photocatalyst. *Environmental Science and Technology*, v. 35, n. 11, p. 2365–2368, 2001.

OHSAKA, T.; IZUMI, F.; FUJIKI, Y. Raman spectrum of anatase, TiO<sub>2</sub>. *Journal of Raman Spectroscopy*, v. 7, n. 6, p. 321–324, 1978.

OHTANI, B. *Photocatalysis A to Z-What we know and what we do not know in a scientific sense. Journal of Photochemistry and Photobiology C: Photochemistry Reviews*. [S.l.: s.n.], 2010

OHTANI, B. Revisiting the fundamental physical chemistry in heterogeneous photocatalysis: its thermodynamics and kinetics. *Physical chemistry chemical physics : PCCP*, v. 16, n. 5, p. 1788–97, 2014. Disponível em: <<http://pubs.rsc.org/en/Content/ArticleHTML/2014/CP/C3CP53653J>>.

OHTANI, B. Titania Photocatalysis beyond Recombination: A Critical Review. *Catalysts*, v. 3, n. 4, p. 942–953, 2013. Disponível em: <<http://www.mdpi.com/2073-4344/3/4/942/>>.

OHTANI, B.; OGAWA, Y.; NISHIMOTO, S. Photocatalytic activity of amorphous-anatase mixture of titanium(IV) oxide particles suspended in aqueous solutions. *Journal of Physical Chemistry B*, v. 101, n. 19, p. 3746–3752, 1997.

OKA, P. A.; KHADEM, N.; Bİ̇½RUBİ̇½, P. R. Operation of passive membrane systems for drinking water treatment. *Water Research*, v. 115, p. 287–296, 2017.

OROMIEHIE, A.; MAMIZADEH, A. Recycling PET beverage bottles and improving properties. *Polymer International*, v. 53, n. 6, p. 728–732, 2004.

ÖSTERLE, W. *et al.* Impact of high energy ball milling on the nanostructure of magnetite-graphite and magnetite-graphite-molybdenum disulphide blends. *Materials Characterization*, v. 86, p. 28–38, 2013.

PADHYE, L. P. *et al.* Year-long evaluation on the occurrence and fate of pharmaceuticals, personal care products, and endocrine disrupting chemicals in an urban drinking water treatment plant. *Water Research*, v. 51, p. 266–276, 2014.

PAÍGA, P.; DELERUE-MATOS, C. Anthropogenic contamination of Portuguese coastal waters during the bathing season: Assessment using caffeine as a chemical marker. *Marine Pollution Bulletin*, v. 120, n. 1–2, p. 355–363, 2017.

PAL, S. *et al.* Self-Cleaning Mineral Paint for Application in Architectural Heritage. *Coatings*, v. 6, n. 4, p. 48, 2016.

PALMA, G. *et al.* Pesticide levels in surface waters in an agricultural-forestry basin in Southern Chile. *Chemosphere*, v. 57, n. 8, p. 763–770, 2004.

PAN, L. *et al.* Water-mediated promotion of dye sensitization of TiO<sub>2</sub> under visible light. *Journal of the American Chemical Society*, v. 133, n. 26, p. 10000–10002, 2011.

PANDIYARAJ, K. N. *et al.* The effect of glow discharge plasma on the surface properties of Poly (ethylene terephthalate) (PET) film. *Surface and Coatings Technology*, v. 202, p. 4218–4226, 2008.

PAREJA, L. *et al.* Trace analysis of pesticides in paddy field water by direct injection using liquid chromatography-quadrupole-linear ion trap-mass spectrometry. *Journal of Chromatography A*, v. 1218, n. 30, p. 4790–4798, 2011.

PASCUAL AGUILAR, J. A. *et al.* Pesticide occurrence in the waters of Júcar River, Spain



from different farming landscapes. *Science of the Total Environment*, v. 607–608, p. 752–760, 2017.

PASSALÍA, C. *et al.* Coated mesh photocatalytic reactor for air treatment applications: comparative study of support materials. *Environmental Science and Pollution Research*, v. 24, n. 7, p. 6382–6389, 2017.

PASSALÍA, C.; ALFANO, O. M.; BRANDI, R. J. *Integral design methodology of photocatalytic reactors for air pollution remediation. Molecules*. [S.l: s.n.], 2017

PASSERI, D. *et al.* Mechanical characterization of polymeric thin films by atomic force microscopy based techniques. *Analytical and Bioanalytical Chemistry*. [S.l: s.n.], 2013

PATRA, D.; BARAKAT, C. Synchronous fluorescence spectroscopic study of solvatochromic curcumin dye. *Spectrochimica Acta Part A: Molecular and Biomolecular Spectroscopy*, v. 79, n. 5, p. 1034–1041, 2011. Disponível em: <<http://www.sciencedirect.com/science/article/pii/S1386142511002502>>.

PEELER, K. A.; OPSAHL, S. P.; CHANTON, J. P. Tracking Anthropogenic Inputs Using Caffeine, Indicator Bacteria, and Nutrients in Rural Freshwater and Urban Marine Systems. *Environmental Science & Technology*, v. 40, n. 24, p. 7616–7622, 2006. Disponível em: <<http://dx.doi.org/10.1021/es061213c>>.

PELAEZ, M. *et al.* A review on the visible light active titanium dioxide photocatalysts for environmental applications. *Applied Catalysis B: Environmental*, v. 125, p. 331–349, 2012. Disponível em: <<http://www.sciencedirect.com/science/article/pii/S0926337312002391>>.

PENGFEEI, J. *et al.* Recent advances in visible light-responsive titanium oxide-based photocatalysts. *Research on Chemical Intermediates*, v. 36, n. 4, p. 327–347, 2010. Disponível em: <<http://search.ebscohost.com/login.aspx?direct=true&db=aph&AN=51548905&lang=pt-br&site=ehost-live&authtype=ip,cookie,uid>>.

PEREIRA, J. O. S. *et al.* Assessment of solar driven TiO<sub>2</sub>-assisted photocatalysis efficiency on amoxicillin degradation. *Environmental Science and Pollution Research*, v. 21, n. 2, p. 1292–1303, 2014. Disponível em: <<http://dx.doi.org/10.1007/s11356-013-2014-1>>.

PETRONELLA, F. *et al.* Nanocomposite materials for photocatalytic degradation of pollutants. *Catalysis Today*, v. 281, p. 85–100, 2017. Disponível em: <<http://www.sciencedirect.com/science/article/pii/S0920586116304096>>.

PITRE, S. P.; YOON, T. P.; SCAIANO, J. C. Titanium dioxide visible light photocatalysis: surface association enables photocatalysis with visible light irradiation. *Chem. Commun.*, v. 53, n. 31, p. 4335–4338, 2017. Disponível em: <<http://dx.doi.org/10.1039/C7CC01952A>>.

POLYAKOV, N. E. *et al.* Enhancement of the photocatalytic activity of TiO<sub>2</sub> nanoparticles by water-soluble complexes of carotenoids. *The journal of physical chemistry. B*, v. 114, n. 45, p. 14200–4, 2010. Disponível em: <<http://www.ncbi.nlm.nih.gov/pubmed/19968316>>.

PORTO, S. P. S.; FLEURY, P. A.; DAMEN, T. C. Raman spectra of TiO<sub>2</sub>, MgF<sub>2</sub>, ZnF<sub>2</sub>, FeF<sub>2</sub>, and MnF<sub>2</sub>. *Physical Review*, v. 154, n. 2, p. 522–526, 1967.

PRIETO-RODRIGUEZ, L. *et al.* Application of solar AOPs and ozonation for elimination of micropollutants in municipal wastewater treatment plant effluents. *Water Research*, v. 47, n. 4, p. 1521–1528, 2013. Disponível em: <<http://www.sciencedirect.com/science/article/pii/S004313541200797X>>.

QI, D. *et al.* Enhanced photocatalytic performance of TiO<sub>2</sub> based on synergistic effect of Ti<sup>3+</sup> self-doping and slow light effect. *Applied Catalysis B: Environmental*, v. 160–161, n. 1, p. 621–628, 2014.

QI, K. *et al.* Enhanced photocatalytic activity of anatase-TiO<sub>2</sub> nanoparticles by fullerene modification: A theoretical and experimental study. *Applied Surface Science*, v. 387, p. 750–758, 2016.

QUYNH, Luu Manh *et al.* Optical and electrical responses of magnetron-sputtered amorphous Nb-doped TiO<sub>2</sub> thin films annealed at low temperature. *Physica B: Condensed Matter*, 2016.

RABIET, M. *et al.* Assessing pesticide concentrations and fluxes in the stream of a small vineyard catchment - Effect of sampling frequency. *Environmental Pollution*, v. 158, n. 3, p. 737–748, 2010.

RAMASUNDARAM, S. *et al.* Preparation, characterization, and application of TiO<sub>2</sub>-

patterned polyimide film as a photocatalyst for oxidation of organic contaminants. *Journal of Hazardous Materials*, v. 340, p. 300–308, 2017. Disponível em: <<http://www.sciencedirect.com/science/article/pii/S0304389417304909>>.

RATOVA, M. *et al.* Enhanced properties of magnetron sputtered photocatalytic coatings via transition metal doping. *Surface and Coatings Technology*, v. 228, n. SUPPL.1, 2013.

RATOVA, M. *Enhanced Properties of Photocatalytic Titania Thin Films via Doping During Magnetron Sputter Deposition*. 2014. Manchester Metropolitan University, 2014.

RATOVA, M.; KLAYSRI, R.; *et al.* Pulsed DC magnetron sputtering deposition of crystalline photocatalytic titania coatings at elevated process pressures. *Materials Science in Semiconductor Processing*, v. 71, p. 188–196, 2017a. Disponível em: <<http://www.sciencedirect.com/science/article/pii/S136980011731795X>>.

RATOVA, M.; KLAYSRI, R.; *et al.* Pulsed DC magnetron sputtering deposition of crystalline photocatalytic titania coatings at elevated process pressures. *Materials Science in Semiconductor Processing*, v. 71, p. 188–196, 2017b.

RATOVA, M. *et al.* Reactive magnetron sputter deposition of bismuth tungstate coatings for water treatment applications under natural sunlight. *Catalysts*, v. 7, n. 10, 2017.

RATOVA, M. *et al.* Reactive Magnetron Sputter Deposition of Bismuth Tungstate Coatings for Water Treatment Applications under Natural Sunlight. *Catalysts*, v. 7, n. 10, p. 283, 23 set. 2017. Disponível em: <<http://www.mdpi.com/2073-4344/7/10/283>>. Acesso em: 11 out. 2017.

RATOVA, M. *et al.* Reactive magnetron sputtering deposition of bismuth tungstate onto titania nanoparticles for enhancing visible light photocatalytic activity. *Applied Surface Science*, v. 392, p. 590–597, 2017. Disponível em: <<http://www.sciencedirect.com/science/article/pii/S0169433216319031>>.

RATOVA, M. *et al.* Synergistic effect of doping with nitrogen and molybdenum on the photocatalytic properties of thin titania films. *Vacuum*, v. 114, p. 205–212, 2015.

RATOVA, M. *et al.* Visible light active photocatalytic C-doped titanium dioxide films

deposited via reactive pulsed DC magnetron co-sputtering: Properties and photocatalytic activity. *Vacuum*, v. 149, p. 214–224, 2018. Disponível em: <<https://doi.org/10.1016/j.vacuum.2018.01.003>>.

RATOVA, M.; WEST, G. T.; KELLY, P. J. HiPIMS deposition of tungsten-doped titania coatings for photocatalytic applications. *Vacuum*, v. 102, p. 48–50, 2014a.

RATOVA, M.; WEST, G. T.; KELLY, P. J. Optimisation of HiPIMS photocatalytic titania coatings for low temperature deposition. *Surface and Coatings Technology*, v. 250, p. 7–13, 2014. Disponível em: <<http://www.sciencedirect.com/science/article/pii/S0257897214001200>>.

RATOVA, M.; WEST, G. T.; KELLY, P. J. Optimisation of HiPIMS photocatalytic titania coatings for low temperature deposition. *Surface and Coatings Technology*, v. 250, p. 7–13, 2014b.

RAY, A. K. Photocatalytic Reactor Configurations for Water Purification: Experimentation and Modeling. In: HUGO, I. DE L.; BENITO SERRANO, R. (Org.). . *Advances in Chemical Engineering*. [S.l.]: Academic Press, 2009. v. Volume 36. p. 145–184. Disponível em: <<http://www.sciencedirect.com/science/article/pii/S0065237709004050>>.

REDDY, P. A. K. *et al.* Recent advances in photocatalytic treatment of pollutants in aqueous media. *Environment International*, v. 91, p. 94–103, 2016. Disponível em: <<http://www.sciencedirect.com/science/article/pii/S0160412016300484>>.

REIS, N. M.; LI PUMA, G. A novel microfluidic approach for extremely fast and efficient photochemical transformations in fluoropolymer microcapillary films. *Chemical Communications*, v. 51, n. 40, p. 8414–8417, 2015. Disponível em: <<http://dx.doi.org/10.1039/C5CC01559F>>.

RIBEIRO, A. C. A. *et al.* Resíduos de pesticidas em águas superficiais de área de nascente do rio São Lourenço - MT: validação de método por extração em fase sólida e cromatografia líquida. *Química Nova*, v. 36, n. 2, p. 284–290, 2013.

RIVAS, G. *et al.* Modelling of the operation of raceway pond reactors for micropollutant removal by solar photo-Fenton as a function of photon absorption. *Applied Catalysis B:*

*Environmental*, v. 178, p. 210–217, 2015. Disponível em:  
<<http://www.sciencedirect.com/science/article/pii/S0926337314005426>>.

ROBERT, D.; KELLER, N.; SELLI, E. Environmental photocatalysis and photochemistry for a sustainable world: a big challenge. *Environmental Science and Pollution Research*, v. 24, n. 14, p. 12503–12505, 2017. Disponível em: <<https://doi.org/10.1007/s11356-017-8935-3>>.

ROCHA, M. P. *et al.* The influence of industrial and agricultural waste on water quality in the Água Boa stream (Dourados, Mato Grosso do Sul, Brazil). *Environmental Monitoring and Assessment*, v. 187, n. 7, p. 442, 2015.

RODRÍGUEZ-GIL, J. L. *et al.* Caffeine and paraxanthine in aquatic systems: Global exposure distributions and probabilistic risk assessment. *Science of The Total Environment*, v. 612, p. 1058–1071, 2018. Disponível em:  
<<http://www.sciencedirect.com/science/article/pii/S0048969717320648>>.

ROSSNAGEL, S. M. Thin film deposition with physical vapor deposition and related technologies. *Journal of Vacuum Science & Technology A: Vacuum, Surfaces, and Films*, v. 21, n. 5, p. S74, 2003. Disponível em:  
<<http://scitation.aip.org/content/avs/journal/jvsta/21/5/10.1116/1.1600450>>.

ROUSIS, N. I. *et al.* Monitoring a large number of pesticides and transformation products in water samples from Spain and Italy. *Environmental Research*, v. 156, p. 31–38, 2017.

RTIMI, S. *et al.* Coupling of narrow and wide band-gap semiconductors on uniform films active in bacterial disinfection under low intensity visible light: Implications of the interfacial charge transfer (IFCT). *Journal of Hazardous Materials*, v. 260, p. 860–868, 2013.  
Disponível em: <<http://www.sciencedirect.com/science/article/pii/S0304389413004196>>.

RUSSO, D.; SPASIANO, D.; VACCARO, M.; ANDREOZZI, R.; *et al.* Direct photolysis of benzoylecgonine under UV irradiation at 254nm in a continuous flow microcapillary array photoreactor. *Chemical Engineering Journal*, v. 283, p. 243–250, 2016.

RUSSO, D.; SPASIANO, D.; VACCARO, M.; COCHRAN, K. H.; *et al.* Investigation on the removal of the major cocaine metabolite (benzoylecgonine) in water matrices by UV254/H<sub>2</sub>O<sub>2</sub> process by using a flow microcapillary film array photoreactor as an efficient

experimental tool. *Water Research*, v. 89, p. 375–383, 2016.

SAIEN, J.; KHEZRIANJOO, S. Degradation of the fungicide carbendazim in aqueous solutions with UV/TiO<sub>2</sub> process: Optimization, kinetics and toxicity studies. *Journal of Hazardous Materials*, v. 157, n. 2, p. 269–276, 2008. Disponível em: <<http://www.sciencedirect.com/science/article/pii/S0304389408000216>>.

SAKAI, N. *et al.* Quantitative Evaluation of the Photoinduced Hydrophilic Conversion Properties of TiO<sub>2</sub> Thin Film Surfaces by the Reciprocal of Contact Angle. *The Journal of Physical Chemistry B*, v. 107, n. 4, p. 1028–1035, 2003. Disponível em: <<http://dx.doi.org/10.1021/jp022105p>>.

SAKULICH, A. R.; LI, V. C. Comparison of the detection limits of EDS and EELS in S/TEM. *33rd Int'l Conf on Cement Microscopy, San Francisco, CA USA*, v. 16, n. Suppl 2, p. 1–10, 2011.

SARAKINOS, K.; ALAMI, J.; KONSTANTINIDIS, S. High power pulsed magnetron sputtering: A review on scientific and engineering state of the art. *Surface and Coatings Technology*, v. 204, n. 11, p. 1661–1684, 2010. Disponível em: <<http://www.sciencedirect.com/science/article/pii/S0257897209009426>>.

SARAKINOS, K.; ALAMI, J.; WUTTIG, M. Process characteristics and film properties upon growth of TiO<sub>x</sub> films by high power pulsed magnetron sputtering. *Journal of Physics D: Applied Physics*, v. 40, n. 7, p. 2108–2114, 2007.

SARAVANAN, R. *et al.* Crystallinity and lowering band gap induced visible light photocatalytic activity of TiO<sub>2</sub>/CS (Chitosan) nanocomposites. *International Journal of Biological Macromolecules*, 2017.

SATUF, M. L. *et al.* Scaling-up of slurry reactors for the photocatalytic degradation of 4-chlorophenol. *Catalysis Today*, v. 129, n. 1, p. 110–117, 2007. Disponível em: <<http://www.sciencedirect.com/science/article/pii/S0920586107004166>>.

SCHULTZ, D. M.; YOON, T. P. *Solar synthesis: Prospects in visible light photocatalysis*. Science. [S.l: s.n.], 2014

SEDDIGI, Z. S. *et al.* Facile synthesis of light harvesting semiconductor bismuth oxychloride nano photo-catalysts for efficient removal of hazardous organic pollutants. *PLoS ONE*, v. 12, n. 2, 2017.

SEILER, R. L. *et al.* Caffeine and Pharmaceuticals as Indicators of Waste Water Contamination in Wells. *Ground Water*, v. 37, n. 3, p. 405–410, 1999. Disponível em: <<http://dx.doi.org/10.1111/j.1745-6584.1999.tb01118.x>>.

SHAHAM-WALDMANN, N.; PAZ, Y. *Away from TiO<sub>2</sub>: A critical minireview on the developing of new photocatalysts for degradation of contaminants in water. Materials Science in Semiconductor Processing*. [S.l: s.n.], 2016

SHI, J. *et al.* The fabrication of TiO<sub>2</sub> supported on slag-made calcium silicate as low-cost photocatalyst with high adsorption ability for the degradation of dye pollutants in water. *Catalysis Today*, v. 281, p. 21–28, 2017. Disponível em: <<http://www.sciencedirect.com/science/article/pii/S092058611630219X>>.

SIMEONE, D. *et al.* Grazing incidence X-ray diffraction for the study of polycrystalline layers. 2013, [S.l: s.n.], 2013. p. 9–13.

SINGH, S.; MAHALINGAM, H.; SINGH, P. K. Polymer-supported titanium dioxide photocatalysts for environmental remediation: A review. *Applied Catalysis A: General*, v. 462, p. 178–195, 2013. Disponível em: <<http://www.sciencedirect.com/science/article/pii/S0926860X13002561>>.

SORNALINGAM, K. *et al.* Photocatalysis of estrone in water and wastewater: Comparison between Au-TiO<sub>2</sub>nanocomposite and TiO<sub>2</sub>, and degradation by-products. *Science of the Total Environment*, v. 610–611, p. 521–530, 2018.

SPASIANO, D. *et al.* Solar photocatalysis: Materials, reactors, some commercial, and pre-industrialized applications. A comprehensive approach. *Applied Catalysis B: Environmental*, v. 170–171, p. 90–123, 2015. Disponível em: <<http://www.sciencedirect.com/science/article/pii/S0926337315000028>>.

STACKELBERG, P. E. *et al.* Persistence of pharmaceutical compounds and other organic wastewater contaminants in a conventional drinking-water-treatment plant. *Science of the*

*Total Environment*, v. 329, n. 1–3, p. 99–113, 2004.

STARLING, M. C. V. M. *et al.* Application of solar photo-Fenton toward toxicity removal and textile wastewater reuse. *Environmental Science and Pollution Research*, v. 24, n. 14, p. 12515–12528, 2017.

STEVENS, N. *et al.* Wettability of photoresponsive titanium dioxide surfaces. *Langmuir*, v. 19, n. 8, p. 3272–3275, 2003.

STRAATHOF, N. J. W. *et al.* Accelerated gas-liquid visible light photoredox catalysis with continuous-flow photochemical microreactors. *Nature Protocols*, v. 11, n. 1, p. 10–21, 2016.

STRUNK, J.; BAÑARES, M. A.; WACHS, I. E. Vibrational Spectroscopy of Oxide Overlayers. *Topics in Catalysis*, v. 60, n. 19–20, p. 1577–1617, 2017.

SUAVE, J. *et al.* TiO<sub>2</sub>/reduced graphene oxide composites for photocatalytic degradation in aqueous and gaseous medium. *Journal of Photochemistry and Photobiology A: Chemistry*, v. 348, p. 326–336, 1 nov. 2017. Disponível em: <[http://www.sciencedirect-com.ez27.periodicos.capes.gov.br/science/article/pii/S1010603016311248](http://www.sciencedirect.com.ez27.periodicos.capes.gov.br/science/article/pii/S1010603016311248)>. Acesso em: 11 out. 2017.

SUAVE, J.; AMORIM, S. M.; MOREIRA, R. F. P. M. TiO<sub>2</sub>-graphene nanocomposite supported on floating autoclaved cellular concrete for photocatalytic removal of organic compounds. *Journal of Environmental Chemical Engineering*, v. 5, n. 4, p. 3215–3223, 2017.

SUN, H. *et al.* A new metal-free carbon hybrid for enhanced photocatalysis. *ACS Applied Materials and Interfaces*, v. 6, n. 19, p. 16745–16754, 2014.

SUN, H. *et al.* Halogen element modified titanium dioxide for visible light photocatalysis. *Chemical Engineering Journal*. [S.l: s.n.], 2010

TAUC, J.; GRIGOROVICI, R.; VANCU, A. Optical Properties and Electronic Structure of Amorphous Germanium. *physica status solidi (b)*, v. 15, n. 2, p. 627–637, 1966. Disponível em: <<http://dx.doi.org/10.1002/pssb.19660150224>>.

TERNES, T. A. Analytical methods for the determination of pharmaceuticals in aqueous



- environmental samples. *TrAC - Trends in Analytical Chemistry*, v. 20, n. 8, p. 419–434, 2001.
- THAMAPHAT, K.; LIMSUWAN, P.; NGOTAWORNCHAI, B. Phase Characterization of TiO<sub>2</sub> Powder by XRD and TEM. *Nature Science*, v. 42, p. 357–361, 2008.
- THOMAIDI, V. S. *et al.* Is there a risk for the aquatic environment due to the existence of emerging organic contaminants in treated domestic wastewater? Greece as a case-study. *Journal of Hazardous Materials*, v. 283, p. 740–747, 2015. Disponível em: <<http://www.sciencedirect.com/science/article/pii/S0304389414008449>>.
- TIRON, V. *et al.* High visible light photocatalytic activity of nitrogen-doped ZnO thin films deposited by HiPIMS. *Surface and Coatings Technology*, 2016. Disponível em: <<http://linkinghub.elsevier.com/retrieve/pii/S025789721631218X>>.
- TIRON, V. *et al.* Reactive multi-pulse HiPIMS deposition of oxygen-deficient TiO<sub>x</sub> thin films. *Thin Solid Films*, v. 603, p. 255–261, 2016.
- TOMLIN, C. (ED. . The e-Pesticide Manual, 13th ed. *BCPC Publications, Alton, Hants, UK*, 2004.
- TRYBA, B. Increase of the photocatalytic activity of TiO<sub>2</sub> by carbon and iron modifications. *International Journal of Photoenergy*, v. 2008, 2008.
- TSENG, Z.-L.; CHIANG, C.-H.; WU, C.-G. Surface Engineering of ZnO Thin Film for High Efficiency Planar Perovskite Solar Cells. *Scientific Reports*, v. 5, n. 1, p. 13211, 2015. Disponível em: <<http://www.nature.com/articles/srep13211>>.
- UR RASHID, H. *et al.* Catalyst Role in Chemical Vapor Deposition (Cvd) Process: a Review. *Rev. Adv. Mater. Sci*, v. 40, p. 235–248, 2015.
- VAIANO, V. *et al.* Photocatalytic removal of spiramycin from wastewater under visible light with N-doped TiO<sub>2</sub> photocatalysts. *Chemical Engineering Journal*, v. 261, p. 3–8, 2015.
- VAN DEN BRINK, P. J. *et al.* Impact of the fungicide carbendazim in freshwater microcosms. II. Zooplankton, primary producers and final conclusions. *Aquatic Toxicology*, v. 48, n. 2–3, p. 251–264, 2000.

VAN GERVEN, T. *et al.* A review of intensification of photocatalytic processes. *Chemical Engineering and Processing: Process Intensification*, v. 46, n. 9 SPEC. ISS., p. 781–789, 2007a.

VAN GERVEN, T. *et al.* A review of intensification of photocatalytic processes. *Chemical Engineering and Processing: Process Intensification*, v. 46, n. 9, p. 781–789, 2007b.  
Disponível em: <<http://www.sciencedirect.com/science/article/pii/S0255270107001924>>.

VEGA, A. B.; FRENICH, A. G.; VIDAL, J. L. V. Monitoring of pesticides in agricultural water and soil samples from Andalusia by liquid chromatography coupled to mass spectrometry. *Analytica Chimica Acta*, v. 538, n. 1–2, p. 117–127, 2005.

VERBRUGGEN, S. W. *TiO<sub>2</sub> photocatalysis for the degradation of pollutants in gas phase: From morphological design to plasmonic enhancement*. *Journal of Photochemistry and Photobiology C: Photochemistry Reviews*. [S.l: s.n.], 2015

VILLANOVA, J. C. O.; AYRES, E.; ORÉFICE, R. L. Design, characterization and preliminary in vitro evaluation of a mucoadhesive polymer based on modified pectin and acrylic monomers with potential use as a pharmaceutical excipient. *Carbohydrate Polymers*, v. 121, n. Supplement C, p. 372–381, 2015. Disponível em:  
<<http://www.sciencedirect.com/science/article/pii/S014486171401248X>>.

VIVIANO, G. *et al.* Combined Use of Caffeine and Turbidity to Evaluate the Impact of CSOs on River Water Quality. *Water, Air, & Soil Pollution*, v. 228, n. 9, p. 330, ago. 2017a.  
Disponível em: <<https://doi.org/10.1007/s11270-017-3505-3>>.

VIVIANO, G. *et al.* Combined Use of Caffeine and Turbidity to Evaluate the Impact of CSOs on River Water Quality. *Water, Air, & Soil Pollution*, v. 228, n. 9, p. 330, ago. 2017b.

VRIELINK, J. A. M. *et al.* Applicability of X-ray fluorescence spectroscopy as method to determine thickness and composition of stacks of metal thin films: A comparison with imaging and profilometry. *Thin Solid Films*, v. 520, n. 6, p. 1740–1744, 2012.

WACHS, I. E. Recent conceptual advances in the catalysis science of mixed metal oxide catalytic materials. 2005, [S.l: s.n.], 2005. p. 79–94.

WANG, P. *et al.* Dye-sensitization-induced visible-light reduction of graphene oxide for the enhanced TiO<sub>2</sub> photocatalytic performance. *ACS Applied Materials and Interfaces*, v. 5, n. 8, p. 2924–2929, 2013.

WANG, Y. *et al.* Carbon nitride nanosheets for photocatalytic hydrogen evolution: remarkably enhanced activity by dye sensitization. *Catalysis Science & Technology*, v. 3, n. 7, p. 1703, 2013. Disponível em: <<http://xlink.rsc.org/?DOI=c3cy20836b>>.

WEI, P.; YANG, Q.; GUO, L. Bismuth oxyhalide compounds as photocatalysts. *Progress in Chemistry*, v. 21, n. 9, p. 1734–1741, 2009. Disponível em: <<http://www.scopus.com/inward/record.url?eid=2-s2.0-70350452180&partnerID=40>>.

WEIGEL, S.; KUHLMANN, J.; HÜHNERFUSS, H. Drugs and personal care products as ubiquitous pollutants: Occurrence and distribution of clofibric acid, caffeine and DEET in the North Sea. *Science of the Total Environment*, v. 295, n. 1–3, p. 131–141, 2002.

WU, J. C. S.; CHEN, C. H. A visible-light response vanadium-doped titania nanocatalyst by sol-gel method. *Journal of Photochemistry and Photobiology A: Chemistry*, v. 163, n. 3, p. 509–515, 2004.

XING, M. *et al.* Self-doped Ti<sup>3+</sup>-enhanced TiO<sub>2</sub> nanoparticles with a high-performance photocatalysis. *Journal of Catalysis*, v. 297, p. 236–243, 2013.

XU, C.; ZHAO, X. S.; RANGAIAH, G. P. Performance analysis of ultraviolet water disinfection reactors using computational fluid dynamics simulation. *Chemical Engineering Journal*, v. 221, p. 398–406, 2013. Disponível em: <<http://www.sciencedirect.com/science/article/pii/S1385894713001848>>.

YAN, X. *et al.* Is methylene blue an appropriate substrate for a photocatalytic activity test? A study with visible-light responsive titania. *Chemical Physics Letters*, v. 429, n. 4–6, p. 606–610, 2006.

YAN, X. *et al.* The interplay of sulfur doping and surface hydroxyl in band gap engineering: Mesoporous sulfur-doped TiO<sub>2</sub> coupled with magnetite as a recyclable, efficient, visible light active photocatalyst for water purification. *Applied Catalysis B: Environmental*, v. 218, p. 20–31, 2017. Disponível em:

<<http://www.sciencedirect.com/science/article/pii/S0926337317305659>>.

YANG, D. *et al.* An efficient photocatalyst structure: TiO<sub>2</sub>(B) nanofibers with a shell of anatase nanocrystals. *Journal of the American Chemical Society*, v. 131, n. 49, p. 17885–17893, 2009.

YANG, Y. *et al.* Effects of superabsorbent polymers on the fate of fungicidal carbendazim in soils. *Journal of Hazardous Materials*, v. 328, p. 70–79, 2017. Disponível em: <<http://www.sciencedirect.com/science/article/pii/S0304389416311980>>.

YE, T. *et al.* Preparation of TiO<sub>2</sub>/graphene composite with appropriate N-doping ratio for humic acid removal. *Journal of Materials Science*, v. 53, n. 1, p. 613–625, 2018.

YI, J. *et al.* AgI/TiO<sub>2</sub> nanobelts monolithic catalyst with enhanced visible light photocatalytic activity. *Journal of Hazardous Materials*, v. 284, p. 207–214, 2015. Disponível em: <<http://www.sciencedirect.com/science/article/pii/S0304389414009273>>.

YOON, T. P.; ISCHAY, M. A.; DU, J. Visible light photocatalysis as a greener approach to photochemical synthesis. *Nature Chemistry*, v. 2, n. 7, p. 527–532, 2010.

ZHANG, G.; KIM, G.; CHOI, W. Visible light driven photocatalysis mediated via ligand-to-metal charge transfer (LMCT): an alternative approach to solar activation of titania. *Energy & Environmental Science*, v. 7, n. 3, p. 954–966, 2014. Disponível em: <<http://dx.doi.org/10.1039/C3EE43147A>>.

ZHANG, J. *et al.* Design and Scaling Up of Microchemical Systems: A Review. *Annual Review of Chemical and Biomolecular Engineering*, v. 8, n. 1, p. 285–305, 2017. Disponível em: <<http://www.annualreviews.org/doi/10.1146/annurev-chembioeng-060816-101443>>.

ZHANG, L. *et al.* Photo-induced hydrophilicity and self-cleaning: models and reality. *Energy & Environmental Science*, v. 5, n. 6, p. 7491–7507, 2012. Disponível em: <<http://dx.doi.org/10.1039/C2EE03390A>>.

ZHANG, L.; ZHU, Y. A review of controllable synthesis and enhancement of performances of bismuth tungstate visible-light-driven photocatalysts. *Catalysis Science & Technology*, v. 2, n. 4, p. 694, 2012. Disponível em: <<http://xlink.rsc.org/?DOI=c2cy00411a>>.

ZHANG, W. *et al.* Raman, EELS and XPS studies of maghemite decorated multi-walled carbon nanotubes. *Spectrochimica Acta - Part A: Molecular and Biomolecular Spectroscopy*, v. 121, p. 715–718, 2014.

ZHANG, W. F.; ZHANG, M. S.; *et al.* Photoluminescence in anatase titanium dioxide nanocrystals. *Applied Physics B: Lasers and Optics*, v. 70, n. 2, p. 261–265, 2000.

ZHANG, W. F.; HE, Y. L.; *et al.* Raman scattering study on anatase TiO<sub>2</sub> nanocrystals. *Journal of Physics D: Applied Physics*, v. 33, n. 8, p. 912–916, 2000.

ZHANG, X. *et al.* Isolation and Characterization of Carbendazim-degrading *Rhodococcus erythropolis* djl-11. *PLoS ONE*, v. 8, n. 10, p. 1–6, 2013.

ZHANG, X.; PENG, T.; SONG, S. Recent advances in dye-sensitized semiconductor systems for photocatalytic hydrogen production. *Journal of Materials Chemistry A*, v. 4, n. 7, p. 2365–2402, 2016.

ZHANG, Z.; ZHOU, F.; LAVERNIA, E. J. On the analysis of grain size in bulk nanocrystalline materials via X-ray diffraction. *Metallurgical and Materials Transactions a-Physical Metallurgy and Materials Science*, v. 34A, n. 6, p. 1349–1355, 2003.

ZHAO, J. *et al.* Novel band gap-tunable K–Na co-doped graphitic carbon nitride prepared by molten salt method. *Applied Surface Science*, v. 332, p. 625–630, 2015. Disponível em: <<http://www.sciencedirect.com/science/article/pii/S0169433215002950>>.